Catalysis in fuel-driven chemical reaction networks

van der Helm, M.P.

DOI
10.4233/uuid:fc85fc09-65a1-4d0f-ac1c-2fe3a7b48ee7

Publication date
2021

Document Version
Final published version

Citation (APA)
van der Helm, M. P. (2021). *Catalysis in fuel-driven chemical reaction networks*. [Dissertation (TU Delft), Delft University of Technology]. https://doi.org/10.4233/uuid:fc85fc09-65a1-4d0f-ac1c-2fe3a7b48ee7

Catalysis in fuel-driven chemical reaction networks

Proefschrift

ter verkrijging van de graad van doctor
aan de Technische Universiteit Delft,
op gezag van Rector Magnificus, Prof. dr. ir. T.H.J.J. van der Hagen
voorzitter van het College voor Promoties,
in het openbaar te verdedigen op

Donderdag 11 maart 2021 om 10:00 uur

door
Michelle Petronella VAN DER HELM

Master of Science in Chemical Engineering
Technische Universiteit Delft, Nederland
geboren te Delft, Nederland

Dit proefschrift is goedgekeurd door de promotoren.

Samenstelling promotiecommissie bestaat uit:

Rector magnificus,	voorzitter
Prof. dr. J.H. van Esch	Technische Universiteit Delft, promotor
Dr. R. Eelkema	Technische Universiteit Delft, promotor

Onafhankelijke leden:

Prof. dr. U. Hanefeld	Technische Universiteit Delft
Prof. dr. J.C.M. van Hest	Technische Universiteit Eindhoven
Prof. dr. A. Walther	Johannes Gutenberg Universiteit Mainz, Duitsland
Prof. dr. N. H. Katsonis	Rijksuniversiteit Groningen
Prof. dr. S.J. Picken	Technische Universiteit Delft, reservelid

Andere leden:

Dr. L. Rossi	Technische Universiteit Delft

The research described in this thesis was performed in the Advanced Soft Matter (ASM) group at Delft University of Technology, Department of Chemical Engineering, Faculty of Applied Sciences. The research has been funded by a consolidator grant (726381) from the European Research Council (ERC).

Cover by:	Pritish Bose and Michelle van der Helm in Blender software with a molecule geometry import script from Scott Hartley
Printed by:	Ipskamp Drukkers, Enschede
ISBN:	978-94-6421-229-7

TABLE OF CONTENTS

GENERAL INTRODUCTION

CHAPTER 1

The research in this thesis falls under the larger field of Systems Chemistry. Traditionally, chemists are educated to look at molecules in isolation, while for Systems Chemists complex mixtures of interacting molecules are of interest. Particular attention is given to the understanding of the complexity of biology by mimicking biochemical reaction networks, which can have emergent properties attributed to the entire system. The research here concentrates on the design of man-made non-equilibrium chemical reaction networks (CRNs) with inspiration taken from signal transduction pathways in living organisms. Since catalysis plays an essential role in cellular signal transduction mechanisms, special attention is given to catalysis in the design of the CRNs. Consequently, the aim of this research is to control individual reaction pathways in out-of-equilibrium fuel-driven CRNs with catalysis. For the design of the catalytic CRNs, organocatalysts are used as they are simple, cheap, recyclable and robust compared to enzymes and frequently less toxic catalysts than metals. Moreover, because organocatalysts can operate under mild conditions, it can encourage future applications in biological environments. Eventually, increased understanding of the design of complex CRNs could be at the basis of the development of artificial signal responsive and interactive materials.

1

Understanding the complexity of biology and the underlying metabolic pathways built from biochemical reaction networks has been a major interest of the past decade. Encouraged by recent efforts in Systems Biology and with the arrival of modern analytics and computational tools, the young field of Systems Chemistry has been established.[1-4] Historically, chemists have been trained to study molecules in isolation. In contrast, a Systems Chemistry approach requires a perspective change by studying complex mixtures of interacting molecules. Using biology as inspiration source Systems Chemistry focuses on the design of artificial chemical reaction networks (CRNs) with emergent properties. Such emergent properties are the result of the interactions and mutual interconversion of the system components.[1, 2] For the research described in this thesis we found inspiration in signal transduction mechanisms of living organisms.

1.1 SIGNAL TRANSDUCTION AND CATALYSIS

Signal transduction in living systems is known as the conversion of information into a chemical change and is the principal process by which communication of living cells occurs over micrometre distances. Cells are equipped with very specific and sensitive signal-transducing mechanisms, which are controlled by protein receptors in the membrane in response to external signals such as antigens, light, hormones, pathogens, hypoxia, pheromones, amongst others. A signal molecule fits in the binding site of a complementary receptor, which then starts a process to amplify the signal i.e. the numbers of molecules increases geometrically in a signalling cascade. Integration with input from other receptors leads to transmission of the information throughout the cells and if the signal perseveres a feedback mechanism called desensitization weakens or ends the response. Multicellular organisms constitute six general categories of signal transducers: 1) G-protein coupled receptors; 2) Receptor tyrosine kinases; 3) Receptor guanylyl cyclases; 4) Gated ion channels; 5) Adhesion receptors and 6) Nuclear receptors (Figure 1.1).[5] By looking only at the countless signal transduction pathways in the human body regulated by enzymes – nature's switchable catalysts – , it is apparent that catalysis plays an essential role in the creation of cellular signal transduction.[6, 7] By definition a catalyst is a substance that accelerates the rate of approach to equilibrium of a chemical reaction without being noticeably consumed and hence does not alter the thermodynamics of the process.[8] Catalysis in signal transduction enables a signal amplification from a minor input signal and can for instance generate a burst release of a small signal molecule[9] (Figure 1.2). The regulation of catalysis is paramount for the health of living organisms. For example deregulation of enzymes involved in signalling cascades, such as tyrosine kinases, can be life-threatening and mark the onset of cancer.[10, 11]

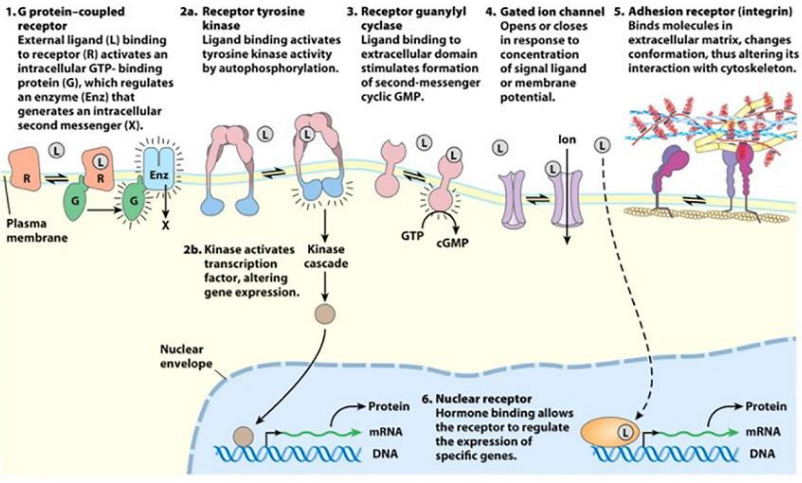

Figure 1.1: The six general types of signal transduction mechanisms in multicellular organisms, reproduced from ref. (5).

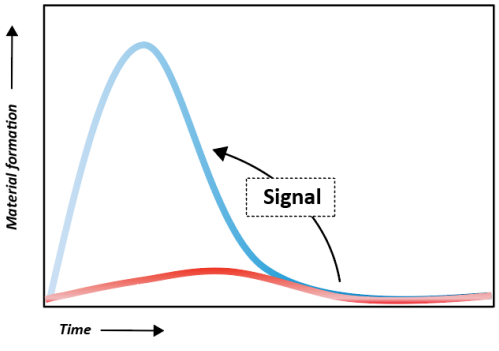

Figure 1.2: Schematic graphical representation of signal amplification in material formation.

1.2 OUT-OF-EQUILIBRIUM (BIO)CHEMICAL REACTION NETWORKS

In addition, signal transduction makes possible functions, such as time-keeping and signal-amplification, which are encoded in out-of-equilibrium (bio)chemical reaction networks (CRNs).[12-14] Typically, such a reaction network consists of at least two competing reactions (formation and degradation), of which the formation reaction is driven by the continued input of a chemical fuel (high-energy molecule).[15-18] In these chemical networks it is not thermodynamic stability that determines critical characteristics of the overall system (such as lifetime), but the reaction kinetics of the individual pathways. The system is maintained in a non-equilibrium condition until it runs out of chemical fuel. When the chemical fuel is depleted, the system falls back to the original thermodynamic equilibrium. Biasing one of the pathways (or both) in a

fuel-driven CRN with ((de)activation of) a catalyst will enable a high degree of control over the system and have a great impact on the system's behaviour. Eventually, coupling fuel-driven CRNs to materials can provide the materials with unique and emergent properties, such as self-assembly (e.g. micelles, peptide hydrogels), replication, feedback, bistability, oscillatory or self-healing behaviour.

1.3 RESEARCH AIM

The aim of this research is to control individual reaction pathways in out-of-equilibrium fuel-driven CRNs with catalysis. A better understanding of such systems and the discovery of new chemistry to design these networks could form the basis for the development of man-made signal responsive and interactive materials. For the design of the CRNs organocatalysts will be used as they are simple, cheap, recyclable and robust compared to biocatalysts and often non-toxic compared to metal-based catalysts. Additionally, as the organocatalysts operate under mild conditions, it would pave the way for future applications in biological settings under physiological conditions.

1.4 THESIS OUTLINE

This thesis comprises seven chapters, which each deal with different aspects of the main research aim and are either theoretical or experimental contributions. After the first introductory chapter, the second chapter deals with organocatalysis in aqueous media and focusses especially on nucleophilic and base catalysis. The third chapter gives an overview of what has been done to date in the field of chemically fuelled supramolecular polymers. The fourth chapter describes the organocatalytic fuel-driven chemical reaction network designed in this research. The fifth chapter builds on chapter 4 by using the organocatalytic CRN to control colloidal interactions. The sixth chapter is a theoretical chapter with simulations and literature examples to show how catalysis can bias pathways in batch and flow out-of-equilibrium systems. The seventh chapter deals with a second fuel-driven chemical reaction network based on non-covalent regulation of catalyst activity. Lastly, a comprehensive summary of all the combined chapters with conclusive statements will be presented. Noteworthy, except for the first and third chapter, extra material for the chapters is provided as Supplementary Information (SI).

1.5 REFERENCES

1. G. Ashkenasy, T. M. Hermans, S. Otto and A. F. Taylor, *Chem. Soc. Rev.*, 2017, **46**, 2543-2554.
2. R. F. Ludlow and S. Otto, *Chem. Soc. Rev.*, 2008, **37**, 101-108.
3. J. R. Nitschke, *Nature*, 2009, **462**, 736.
4. G. M. Whitesides and R. F. Ismagilov, *Science*, 1999, **284**, 89-92.
5. D. L. Nelson, M. M. Cox and A. L. Lehninger, *Lehninger principles of biochemistry*, W.H. Freeman, New York, 2013.
6. E. Whitehead, *Prog. Biophys. Mol. Biol.*, 1970, **21**, 321-397.
7. T. W. Traut, *Allosteric Regulatory Enzymes*, Springer US, Boston, 2008.

8. D. von Lothar, *Chem. unserer Zeit*, 1982, **16**, 186-196.
9. P. Scrimin and L. J. Prins, *Chem. Soc. Rev.*, 2011, **40**, 4488-4505.
10. S. Fernandez, V. Desplat, A. Villacreces, A. V. Guitart, N. Milpied, A. Pigneux, I. Vigon, J.-M. Pasquet and P.-Y. Dumas, *Int. J. Mol. Sci.*, 2019, **20**, 3429.
11. P. Blume-Jensen and T. Hunter, *Nature*, 2001, **411**, 355-365.
12. B. N. Kholodenko, *Nat. Rev. Mol.*, 2006, **7**, 165.
13. J. E. Ferrell Jr., T. Y. C. Tsai and Q. Yang, *Cell*, 2011, **144**, 874-885.
14. S. N. Semenov, A. S. Y. Wong, R. M. van der Made, S. G. J. Postma, J. Groen, H. W. H. van Roekel, T. F. A. de Greef and W. T. S. Huck, *Nat. Chem.*, 2015, **7**, 160.
15. S. A. P. van Rossum, M. Tena-Solsona, J. H. van Esch, R. Eelkema and J. Boekhoven, *Chem. Soc. Rev.*, 2017, **46**, 5519-5535.
16. J. Boekhoven, W. E. Hendriksen, G. J. M. Koper, R. Eelkema and J. H. van Esch, *Science*, 2015, **349**, 1075-1079.
17. L. S. Kariyawasam and C. S. Hartley, *J. Am. Chem. Soc.*, 2017, **139**, 11949–11955.
18. M. Tena-Solsona, B. Rieß, R. K. Grötsch, F. C. Löhrer, C. Wanzke, B. Käsdorf, A. R. Bausch, P. Müller-Buschbaum, O. Lieleg and J. Boekhoven, *Nat. Commun.*, 2017, **8**, 15895.

ORGANOCATALYSIS IN AQUEOUS MEDIA

CHAPTER 2

Even though enzymes are the cornerstones of living systems, it has so far proven difficult to deploy artificial catalysts in a biological setting. Organocatalysts are arguably well-suited artificial catalysts for this purpose because, compared with enzymes and inorganic catalysts, they are simpler, often less toxic and widely accessible. This chapter describes part of the review article (Organocatalysis in aqueous media) on how organocatalysts that operate in aqueous media might enable us to selectively access new chemical transformations and provide new possibilities for chemical biology and biomedicine. Organocatalysts can be categorized according to the mechanisms by which they activate substrates, drawing comparisons with enzymes. In this chapter, the focus is on organocatalysts that work via nucleophilic and general/ specific base catalysis. The attributes of the catalyst (such as functional groups and pK_a values) and the reaction (such as the microenvironment surrounding intermediates) are key considerations when developing efficient organocatalysis in aqueous media. Although we only know of a limited set of organocatalytic reactions with biological potential, on the basis of recent developments we expect a bright future for organocatalysis in biology, to the benefit of chemical biology and biomedicine.

This chapter is based on the published work:
M.P. van der Helm, B. Klemm and R. Eelkema, *Nat. Rev. Chem*, 2019, **3**, 491-508.

2.1 INTRODUCTION

Enzymes are crucial components of living systems. Along with enzyme catalysis, synthetic transition metal catalysis has seen widespread use under biologically relevant conditions.[1-8] By contrast, applications of synthetic organocatalysis in biological systems are only emerging, despite organocatalysis being a powerful tool to selectively access new transformations in chemical biology. For example, by constructing protein conjugates we can gain a better understanding of cellular biochemistry and eventually come closer to the creation of *de novo* life. Organocatalysts are well suited to this and other tasks because, compared with enzymes or inorganic catalysts, they are simpler to design and modify, more accessible and often less toxic. Organocatalysts can even be considered minimalistic biocatalysts because they can often closely approximate the amino acid residues and cofactors that make up an enzyme. Function can follow form, such that organocatalytic mechanisms can closely mimic enzymatic ones. Despite this, although enzymatic reactions commonly proceed in aqueous environments, performing organocatalytic reactions in these solutions remains a considerable challenge.[9-12] H_2O is a solvent with a high surface tension, polarity and hydrogen-bonding ability — properties that can detract from organic reactions. Indeed, the major drawbacks for using H_2O as a solvent are the insolubility of most organic compounds, poor hydrolytic stability of chemical compounds and catalytic intermediates, and destabilization of transition states by disruption of hydrogen bonds.[10, 13, 14] However, landmark studies have shown that these challenges can be overcome (Figure 2.1).

The landmark organocatalysis studies have been reviewed [10-12, 15-19] and we instead focus on aqueous organocatalytic reactions, categorizing each type and providing background and examples, including relevant comparisons with enzymatic reactions. However, in this thesis chapter only nucleophilic and base catalysis will be treated, which are of relevance to other thesis chapters. The organocatalytic reactions that are considered are reactions in which all reactants, co-solvents, reagents and products are homogeneously dissolved in H_2O or aqueous buffer as the major solvent. Attention must also be paid to catalyst loadings, which in the case of organocatalysts are variable and usually higher than those used for enzymes and transition metal catalysts. Altogether, organocatalysts that operate efficiently in aqueous and even biological environments would find applications ranging from smart materials, such as soft robotics or self-healing materials to more biomedically relevant applications, like controlled drug delivery or on-demand drug synthesis in tumour cells. The reaction examples of organocatalysts discussed in this chapter are summarized in Table S2.1 at the end of the chapter.

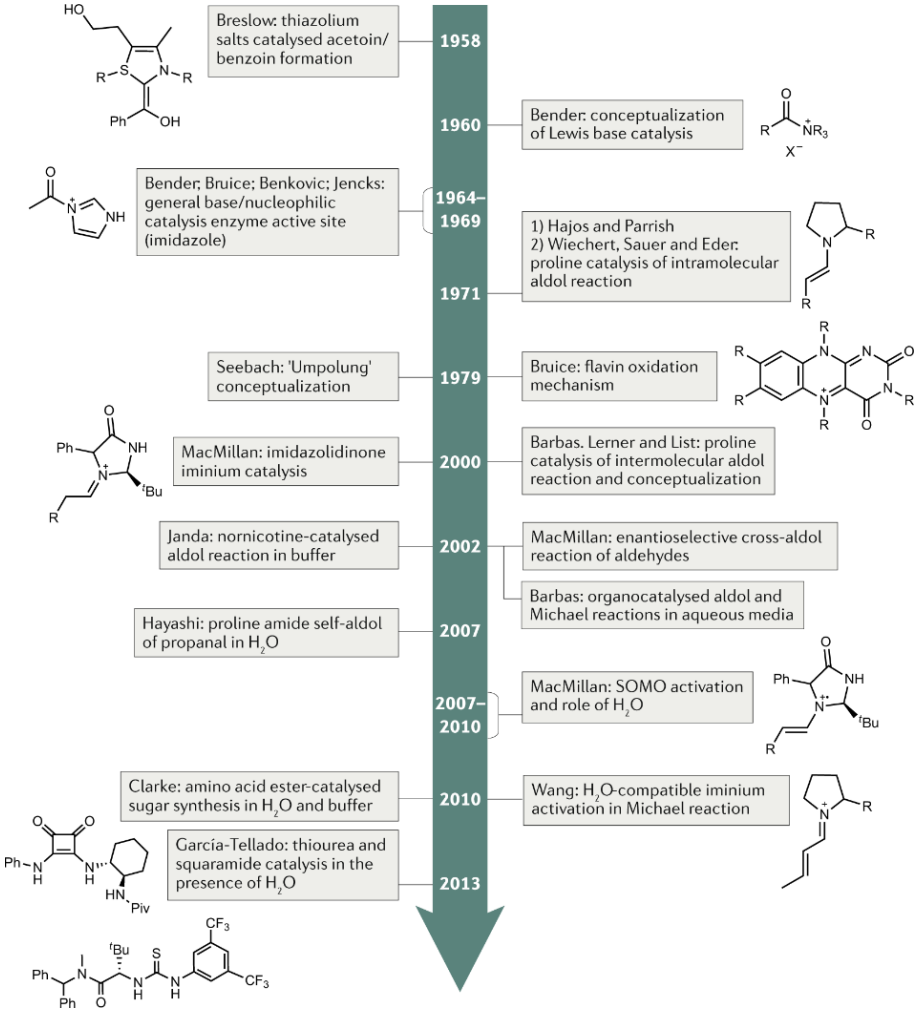

Figure 2.1: Organocatalysis has developed rapidly in little over half a century. Landmark discoveries are either conceptual contributions or examples of organocatalysis in (buffered) H_2O (or H_2O/organic solvent mixtures). SOMO, singly- occupied molecular orbital.

2.2 ORGANOCATALYTIC ACTIVATION

Seminal studies by Barbas, List and MacMillan saw organocatalysis popularized as a third strategy in asymmetric catalysis, next to transition metal and enzymatic catalysis.[20-22] However, examples of organocatalysis extend beyond asymmetric catalysis and we describe here any bond-breaking and bond-forming transformation.

In covalent activation, the catalyst forms a covalent bond to the substrate to afford an activated intermediate. In terms of aqueous reactions, catalysts that activate a carbonyl substrate to form an enamine and iminium, typically as part of an overall asymmetric aldol reaction, have received the most attention.[23, 24] Other activation modes, not often discussed for asymmetric catalysis, but important in a water context, are nucleophilic catalysis, as well as general and specific acid or base catalysis. The majority of organocatalytic reactions featuring covalent activation do so through one of the seven modes depicted below (Table 2.1).[25, 26]

In non-covalent activation, the catalyst accelerates the reaction by non-covalently binding a substrate through one or more modes. Along with singly-occupied molecular orbital activation, these pathways will not be discussed here because they are rarely observed in H_2O, because this solvent competes strongly with substrates for catalyst binding. Supramolecular catalysis in H_2O has been reviewed[27] and will not be discussed here either.

Category	Covalent activation reaction mechanisms	Example reactions
[Enamine – HOMO activation]		
Enamine Catalysis	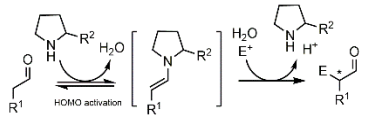	Aldol reaction Michael reaction
[Iminium – LUMO activation]		
Iminium Catalysis	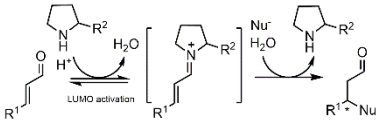	Michael reaction
[Radical cation – SOMO activation]		
SOMO Catalysis	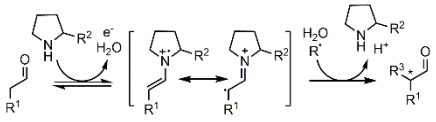	No examples in H_2O
[Breslow intermediate]		
N-heterocyclic carbene Catalysis	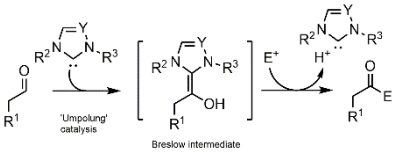	Enal coupling Benzoin condensation
[Lewis base complex]		
Nucleophilic Catalysis	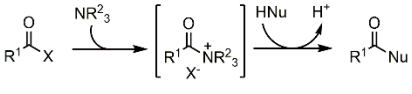	Ester hydrolysis Morita-Baylis-Hillman reaction Acetylation Substitution Hydrazone/ oxime formation Native chemical ligation
[Tetrahedral Intermediate]		
General Base Catalysis	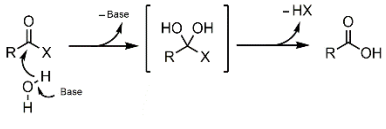	Knoevenagel reaction Multi-component synthesis of azapyrrolizidines
Specific Base Catalysis	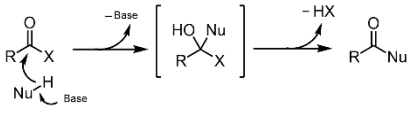	

Table 2.1: Categories of covalent organocatalysis in aqueous media. The examples are sorted according to their mechanisms, each of which is represented by archetypical reactions, where applicable. SOMO, singly- occupied molecular orbital.

2.3 NUCLEOPHILIC AND GENERAL/SPECIFIC BASE CATALYSIS

An organic base can generally act as a Brønsted or Lewis base. In catalysis, the former leads to either general or specific base catalysis, and the latter is important in nucleophilic catalysis.[28] General and specific acid–base catalysis is a much older concept than nucleophilic catalysis, which was described by Bender in 1960.[28] The interest in using small organic molecules as catalysts was furthered by an emerging fascination for enzyme structures and mechanistic elucidation. For example, the discovery of a role for the imidazolyl group of a His residue at the active site of α-chymotrypsin (Figure 2.2A) inspired and aided the understanding of how imidazole performs nucleophilic catalysis in hydrolysis (Table S2.1, reaction 1a) and acyl transfer reactions.[29-38]

α-Chymotrypsin is an example of a serine protease — enzymes that hydrolyse peptides or esters at an active site featuring a His residue near an Asp in a conserved arrangement that enhances the basicity of the His. Thus, the His can deprotonate a proximal Ser residue such that it can attack the substrate at the carbonyl group. Ser receives an acyl group from the substrate[39-41] (Figure 2.2B) to afford an esterified intermediate, which can be hydrolysed to give the acid derivative of the substrate and regenerate serine protease. Once more, His plays a key role by effecting H_2O deprotonation to facilitate the hydrolysis (Figure 2.2B).[42]

Imidazoyl groups are highly polar and amphoteric, and the imidazole–imidazolium conjugate pair can perform general acid–base catalysis. As we now describe, such imidazoyl groups can also perform nucleophilic catalysis. Contemporary with Bender's publication, Jencks formulated three criteria for nucleophilic catalysis: the catalyst must have a higher reactivity towards the substrate than the acceptor molecule; the reactive intermediate should be more susceptible towards attack by the acceptor than the substrate; and the equilibrium constant for forming the reactive intermediate must be smaller than that for the product.[43] If these criteria are satisfied, the catalytic reaction is faster than the uncatalysed background reaction and the catalyst does not remain bound to the reaction products.[43] One reaction that sometimes fulfils these criteria is imidazole catalysed hydrolysis of an ester RCO_2R', which could conceivably proceed through a nucleophilic pathway in which the formation of an *N*-acetyl imidazole intermediate is rate-limiting (Figure 2.2C).[33, 44] The other possibility is the occurrence of a general base mechanism, in which imidazole and H_2O are a source of the nucleophile ^-OH. The most favourable pathway depends on the relative suitability of imidazole and $^-OR'$ as leaving groups.[44] Esters with poorer (more basic) leaving groups are subject to general base catalysis, whereas esters with better (less basic) leaving groups such as substituted phenolates undergo nucleophilic catalysis (Figure 2.2C - top).[29, 31] The

nucleophilic pathway is pH-dependent and is favoured under basic conditions in which imidazole (pK_a ≈ 6.9) is more likely to exist as a neutral species.[45]

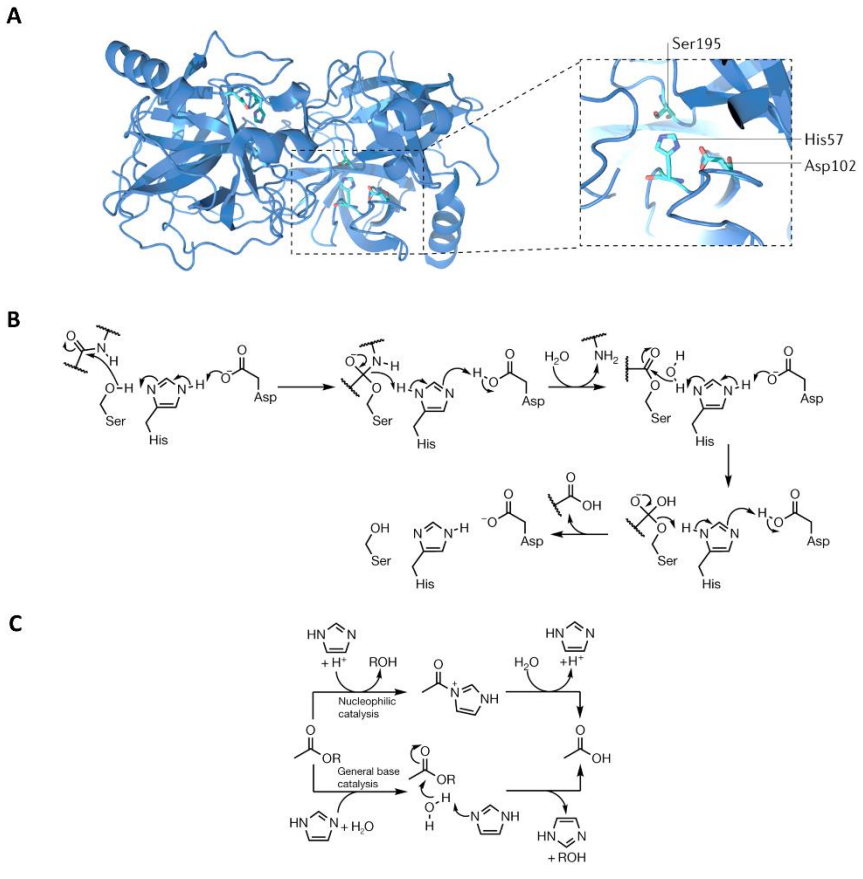

Figure 2.2: Imidazolyls are common bases in enzymatic and synthetic organocatalysis. **(A)**. The X- ray structure of α-chymotrypsin (from *Bos Taurus*, Protein Databank identifier: 4CHA)[46] features an active site with Ser195, His57 and Asp102 as a catalytic triad. Structure visualized using the PyMOL Molecular Graphics System. **(B)**. The general mechanism of serine proteases involves the collective H^+ transfer chain enabling deprotonation of the Ser195 side chain followed by attack on the substrate peptide, which then undergoes hydrolysis. **(C)**. Ester hydrolysis is catalysed by imidazole, either through a nucleophilic (top) or general base (bottom) mechanism, depending on the basicity of the $^-$OR group.[33, 44]

Aside from well-established applications in the hydrolysis of activated esters, the catalysts imidazole (**1**) and/ or histidine are active in other reactions, including the aldol reaction (through an enamine intermediate), hydrolysis of *N*-acetylserinamide, RNA cleavage and thioester hydrolysis.[45] The catalysts can not only take the form of a small molecule or protein[42, 47-49], but also be imidazole-functionalized nanoparticles[50] or polymers[51, 52]. The dipeptide Ser–His was purported as a minimalistic enzyme for the

hydrolysis of phosphate ester bonds of DNA, peptide bonds in proteins[53] and 4-nitrophenyl acetate. However, it was later found that only activated esters such as the latter substrate fall in the scope of the dipeptide (imidazole itself has a similar scope).[54] Thus, the search for *de novo* catalysts for the formation or hydrolysis of amides in H_2O remains a challenging research area.[55] One approach towards this involves direct selection to screen for catalytically active phages through self-assembly of the product.[56] Some of the phages active for ester and amide hydrolysis did not feature Ser–His sequences, and some did not contain His at all. This interesting result indicates that such phages must operate through a mechanism distinct from that described above. Indeed, further experiments gave no evidence for Michaelis–Menten kinetics, leading to the suggestion that the catalytic mechanism resembles that of small-molecule organocatalysis.[56] The selection approach using active phages is an interesting step towards identifying efficient new organocatalysts, although their activity does not yet compare with proteases and esterases developed through natural evolution.[55] To date, the hydrolysis of amide bonds under mild conditions, although a facile reaction when using hydrolytic enzymes, remains difficult for organic small-molecule catalysts. Furthermore, the conceptual and mechanistic relevance of using the hydrolysis of activated esters to mimic that of amides is questionable. [54, 57]

Imidazole is not only a H_2O-soluble catalyst for bond-breaking reactions, but also for bond-formation reactions such as the Morita–Baylis–Hillman (MBH) reaction, in which it serves as a nucleophilic catalyst. Indeed, MBH reactions of aldehydes and cyclic enones, when conducted in the presence of imidazole, afford higher yields in shorter reaction times and have a wider substrate scope that includes typically unreactive and sterically bulky aldehydes.[58] In the case of the MBH reaction of cyclic enones and isatin (Table S2.1, reaction 2), the bicyclic imidazolyl alcohol **3** is an even better catalyst than imidazole.[59-61] Experimental and computational evidence suggest that this high activity is a result of **3** mediating effective intramolecular H^+ transfer.[61] We note that this reaction of cyclic enones and isatin, although conducted in H_2O, requires a surfactant to establish a hydrophobic environment in which the organic reactants combine.

Pyridine (**4**) and its derivatives are the catalysts of choice for acetylations, in which they act as nucleophilic catalysts that form reactive *N*-acetylpyridinium intermediates. Pyridine itself has a modest Brønsted basicity ($pK_a \approx 5.2$), such that in neutral aqueous solutions it exists predominantly as its free base (in contrast to alkylamine catalysts, which are more basic).[62] Consequently, pyridine is an effective catalyst for the hydrolysis of Ac_2O (Table S2.1, reaction 3). Evidence for a nucleophilic catalytic mechanism reaction comes in the relative inactivity of comparably basic, but more hindered 2-methylsubstituted pyridines.[63] However, when the hydrolysis of Ac_2O is conducted in

H_2O, the direct reaction with the solvent dominates the pyridine-mediated pathways. Pyridine has been exploited as a catalyst for the hydrolysis of ArOAc substrates but the rate accelerations are not comparable with pyridine-catalysed acylations using anhydrides or imidazole-catalysed hydrolyses of activated esters.[62, 64] Additionally, pyridine also has been observed to catalyse maleimide polymerization in H_2O through a non-radical pathway.[65] However, this mechanism is unclear and pyridine may rather serve as a nucleophilic initiator, as is the case for other amines in polar solvents.[65, 66]

4-(Dimethylamino)pyridine (DMAP, **5**; pK_a ≈ 9.2) is more reactive and basic than pyridine, such that in neutral aqueous solution it exists in its protonated catalytically inactive form. This protonation can be curbed by incorporating 4-(alkylmethylamino)pyridine groups into surface-crosslinked micelles (**2**), in which hydrophobic microenvironments facilitate efficient catalysis of (phosphate) ester hydrolysis even when the bulk solution is acidic (Table S2.1, reaction 1b).[67] Other recent catalytic applications of DMAP and its derivatives include affinity protein-labelling[68], activation and acetyl transfer from acetyl-coenzyme A to Lys (using peptide appended DMAP analogue featuring a thiol)[69] and the related histone-selective acylation using nucleosome-binding catalysts and acyl donors (a reaction typically performed by histone acetyltransferases)[70]. Outside biology, DMAP-functionalized polyacrylonitrile fibres catalyse the aqueous-phase Gewald reaction, in which a ketone/aldehyde (or its equivalent) condenses with an α-cyanoester and S_8 to give a 3-substituted 2-aminothiophene.[71]

1,4-Diazabicyclo[2.2.2]octane (DABCO, **6**; pK_{a1} ≈ 3.0, pK_{a2} ≈ 8.8) is a versatile tertiary amine organocatalyst that is more basic than imidazole and pyridine, but less basic than DMAP. DABCO-catalysed MBH reactions of PhCHO with acrylonitrile or cyclic enones proceed rapidly in H_2O because this hydrogen-bonding solvent stabilizes the reactive enolate intermediate and/ or activates PhCHO to nucleophilic attack (Table S2.1, reaction 5).[72, 73] This hydrogen-bonding effect is apparently a more important contributor to rate enhancement than are polarity and hydrophobic effects, because both salting-in and salting-out experiments lead to rate enhancement.[72] The related catalyst 3-quinuclidinol (**7**) is even more active than DABCO or DMAP in the MBH reaction.[72]

DABCO has been used in Knoevenagel condensations in H_2O for the formation of α,β-unsaturated carbonyl compounds.[74, 75] In such reactions, DABCO likely acts either as a general base that deprotonates the active methylene compound or as a specific base (Table S2.1, reaction 9) that deprotonates H_2O (these studies included no information on solution pH to distinguish these two mechanisms) to give OH^-, which is known to catalyse such reactions.[76] More generally, a typical problem faced by those

wishing to conduct these condensations in H_2O is the limited solubility of many organic starting materials. The products are usually insoluble in H_2O, such that phase separation drives the reaction to completion. Knoevenagel condensations of highly reactive methylene compounds in H_2O are often fast even in the absence of a catalyst, because the hydrophobic effect[77] causes the organic reactants to partially phase-separate into small droplets[78]. Thus, the rates of reactions with negative activation volumes are greatly increased. Aside from this general effect, hydrogen-bond donation from H_2O can also provide a rate enhancement[79], as has been observed in the MBH reaction catalysed by **7**. [72] The role of DABCO as a nucleophilic catalyst has also been confirmed in the allylic substitution of vinyl phosphonates with N-centred and S-centred nucleophiles (Table S2.1, reaction 4).[80]

The reader will undoubtedly realize the prevalence of nitrogen bases in our discussion so far. It is consequently no surprise that piperidine (**8**) is also catalytically active in the Knoevenagel reaction in H_2O, for example, in a multicomponent reaction affording azapyrrolizidines in high regioselectivity, chemoselectivity and diastereoselectivity (Table S2.1, reaction 10).[81, 82] It is not clear whether piperidine catalyses the reaction by base catalysis or by giving rise to an iminium intermediate. As with some examples above, the products in this reaction are insoluble, making this a heterogeneous reaction system.

Primary amines such as aniline **9** are common nucleophilic organocatalysts for reactions in H_2O. [83] For example, aniline catalyses hydrazone and oxime formation through a transamination mechanism (Figure 2.3A; Table S2.1, reaction 6). These reactions are often applied to bioconjugations, such as functionalization of polymers[84] and biomolecules for *in vitro* and *in vivo* studies[83, 85]. The nucleophilic catalytic mechanism of aniline was elucidated by Cordes and Jencks back in 1962[43] (Figure 2.3A). Aniline condenses with the aldehyde or ketone to give the first reactive tetrahedral intermediate (a carbinolamine), from which H_2O is eliminated to give the Schiff base (imine). The imine is subsequently attacked by the hydrazine or alkoxyamine (or semicarbazide[43]) to afford the second tetrahedral intermediate (a germinal diamine) that extrudes aniline and the hydrazone or oxime product (or semicarbazone[43]).[85] Despite being a carbonyl condensation reaction, the equilibrium favours hydrazone formation in H_2O, and hence fulfils Jencks' criteria for nucleophilic catalysis.[43] The reaction is accelerated by acid catalysis[86], but is slow at neutral pH, such that applications in most biological systems are challenging. High (super-stoichiometric) concentrations of aniline are required to realize significant rate enhancements[87], motivating the development of second-generation and third-generation aniline catalysts for bioconjugation in biological settings[85]. Increasing catalytic efficiency requires closely

studying the pK_a and substituent effects of the catalyst[85, 88-90], and more basic catalysts typically promote protonation of the Schiff base and accelerate the reaction[85, 91]. Aside from engineering the catalyst, the choice of reactants is also crucial and *ortho* substituents on aryl aldehydes can greatly enhance rates (for example, by intramolecular general acid catalysis with phosphate groups[92]).[85, 93] Organocatalysed ligations of peptides by means of hydrazone/ oxime formation at pH 7.0 can experience up to 40-fold rate enhancements in the presence of super-stoichiometric aniline. [91, 94] However, the biocompatibility of aniline is questionable at high concentrations, motivating efforts to search for alternatives such as *p*-aminophenylalanine.[95] Aside from purely synthetic aniline derivatives, bioconjugates have also been investigated. For example, an aniline-terminated DNA strand, when hybridized to a complementary hydrazide-terminated DNA strand, catalyses the condensation of the hydrazide group with 4-nitrobenzaldehyde under physiological conditions.[96] The related amine–acid organocatalyst **10** similarly promotes rapid hydrazone crosslink exchange (Table S2.1, reaction 7) in hyaluronan hydrogels in the presence of human umbilical vein endothelial cells at physiological pH and temperature.[97] A recent study has shown how the aldehyde product of the protein aldol ligation can be further functionalized in a tandem organocatalyst-mediated β-hydroxyoxime ligation catalysed by 4-methoxyaniline at neutral pH.[98] The rate of this organocatalysed oxime formation exhibits an unexpected pH dependence, with the yield of conjugation product being higher at pH 7.5 than at pH 4.5. A possible explanation may be the hydrogen bonding between the β-OH moiety and the protonated aldehyde or Schiff base intermediate.[98] Lastly, it has been demonstrated that *p*-aminophenylalanine can be incorporated into artificial enzymes[99], each with a hydrophobic binding pocket that affords rate enhancements outperforming aniline by a factor of >550 for a model hydrazone formation reaction.[99]

Organocatalysed click reactions are not only limited to hydrazone and oxime formation, as demonstrated by the use of thiol catalysts in native chemical ligation (NCL). NCL is an effective method for the chemoselective formation of a covalently linked ligation product from two unprotected peptides under aqueous conditions.[100, 101] Specifically, a thioester-terminated peptide undergoes transthioesterification with a thiol catalyst, to afford an activated thioester than can undergo a further transthioesterification with another peptide with an N-terminal Cys. After intramolecular acyl transfer from the S atom to the terminal N, one then has a polypeptide with a native amide bond at the ligation site (Table S2.1, reaction 8).[100] Mixed catalyst systems (BnSH/ PhSH) or 2-mercaptoethanesulfonate sodium salt (MESNA) are typical catalysts, but they are slow even for sterically unhindered peptides, which can therefore instead participate in side reactions.[100, 102, 103] Alkylthiols and arylthiols with different pK_a values[100] have been

tested and it appears that whereas arylthiols with higher pK_a values are more effective, the opposite trend is observed for alkylthiols such as MESNA and BnSH. At present, (4-mercaptophenyl)acetic acid (MPAA, **11**) is the best catalyst and also has improved H_2O solubility and no offensive odour.[100] Since the disclosure of its activity, MPAA has been extensively used in NCL reactions, although the quest for better-performing catalysts has not ended. For example, mercaptobenzylsulfonates have been investigated, and although they are not faster than MPAA, their greater polarity leads to greater H_2O solubility and aids the purification process.[104] Akin to aniline catalysis, the thiol-catalysed NCL appears to be an example of nucleophilic catalysis, with a reactive thioester intermediate forming from the starting thioester and thiol catalyst (Figure 2.3B).[100, 102, 105] The rate-determining step for arylthiol catalysts is the first transthioesterification, analogous to aniline-catalysed hydrazone/ oxime formation, having to proceed through the limiting Schiff base formation. However, the opposite holds true for alkylthiols, which have greater basicity, such that the second transthioesterification becomes rate determining.[100, 102] The full mechanistic details of these catalysed NCL reactions have not been elucidated[100] and other studies have focused on catalysts for ligations that use an *N*,*S*-acyl shift reaction. Thus, H_2O-soluble alkyldiselenol catalysts for transthioesterification and ligation have been developed and are superior to MPAA-based systems. They are particularly efficient at pH 4.0, which, although not relevant to *in vivo* or *in vitro* experiments, does enable complex peptide syntheses[106].

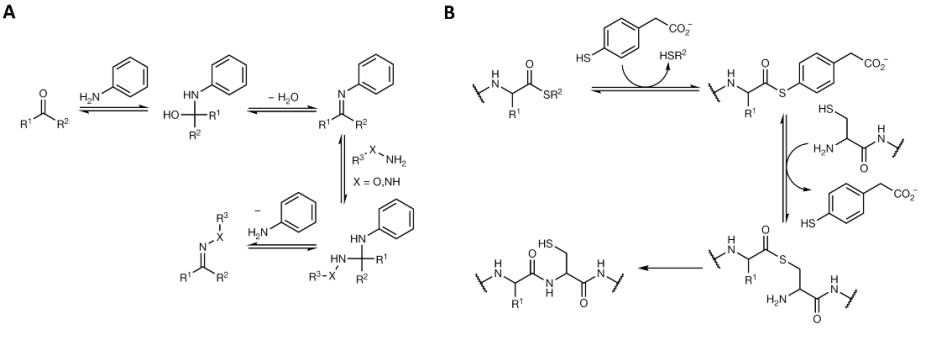

Figure 2.3: Transamination and transthioesterification in organocatalysis. **(A)**. Aniline-catalysed hydrazone and oxime formation involves transamination through a *N*-phenylimine intermediate.[43] **(B)**. Arylthiol-catalysed native chemical ligation proceeds by the catalytic thiol displacing another thiol to give a reactive thioester that is attacked by a Cys thiol.[100] The ligation is completed once the acyl transfers from the S to the N atom of the Cys.

2.4 CONCLUSION AND OUTLOOK

The examples of aqueous organocatalysis described in this chapter highlight the importance of Jencks' criteria, in particular the pK_a and energy of the catalyst–substrate intermediate complex relative to those of the reactants and products.[43] Additionally, organocatalysis in aqueous media is very sensitive to the nature of the catalyst. Thus, the field can benefit from improvements in catalyst design, which might involve simply adding or varying substituents on the catalyst (as is the case for aniline derivatives[85, 88-90]) or engineering the catalyst to establish a favourable active-site microenvironment, such that it can operate under unusual conditions (for example, DMAP in surface-crosslinked micelles[67] or designer enzymes with unnatural catalytic residues[99]). The latter examples take inspiration from natural enzymes, in which a hydrophobic pocket often serves as an optimal chemical environment, as we have seen in the biocatalytic example described here. Organocatalyst engineering is arguably still a young field and there is tremendous potential for organocatalysis to be exploited in biological environments. Altogether, we expect a bright future for rationally designed organocatalytic processes and encourage their application in biology.

2.5 REFERENCES

1. A. Küchler, M. Yoshimoto, S. Luginbühl, F. Mavelli and P. Walde, *Nat. Nanotechol.*, 2016, **11**, 409.
2. S. Schoffelen and J. C. van Hest, *Soft Matter*, 2012, **8**, 1736-1746.
3. F. Wen, Y. Dong, L. Feng, S. Wang, S. Zhang and X. Zhang, *Anal. Chem.*, 2011, **83**, 1193-1196.
4. A. E. Speers and B. F. Cravatt, *Chem. Biol.*, 2004, **11**, 535-546.
5. Y. Bai, J. Chen and S. C. Zimmerman, *Chem. Soc. Rev.*, 2018, **47**, 1811-1821.
6. J. Li, J. Yu, J. Zhao, J. Wang, S. Zheng, S. Lin, L. Chen, M. Yang, S. Jia and X. Zhang, *Nat. Chem.*, 2014, **6**, 352.
7. J. P. Coverdale, I. Romero-Canelón, C. Sanchez-Cano, G. J. Clarkson, A. Habtemariam, M. Wills and P. J. Sadler, *Nat. Chem.*, 2018, **10**, 347.
8. M. Tomás-Gamasa, M. Martínez-Calvo, J. R. Couceiro and J. L. Mascareñas, *Nat. Commun.*, 2016, **7**, 12538.
9. D. G. Blackmond, A. Armstrong, V. Coombe and A. Wells, *Angew. Chem. Int. Ed.*, 2007, **46**, 3798-3800.
10. M. Raj and V. K. Singh, *Chem. Commun.*, 2009, 6687-6703.
11. M. Gruttadauria, F. Giacalone and R. Noto, *Adv. Synth. Catal.*, 2009, **351**, 33-57.
12. P. I. Dalko, *Comprehensive Enantioselective Organocatalysis: Catalysts, Reactions, and Applications, 3 Volume Set*, John Wiley & Sons, 2013.
13. F. Cruz-Acosta, P. de Armas and F. García-Tellado, *Chem. Eur. J.*, 2013, **19**, 16550-16554.
14. J. Clayden, N. Greeves and S. Warren, in *Organic Chemistry*, OUP Oxford, 2012, ch. 12, p. 256.
15. I. Ingram, S. Lawrenson and M. North, in *Encyclopedia of Sustainable Technologies*, 2017, pp. 629-643.
16. C. Jimeno, *Org. Biomol. Chem.*, 2016, **14**, 6147-6164.
17. S. Toma, R. Sebesta and M. Meciarova, *Curr. Org. Chem.*, 2011, **15**, 2257-2281.
18. U. M. Lindström, *Chem. Rev.*, 2002, **102**, 2751-2772.
19. S. Bhowmick, A. Mondal, A. Ghosh and K. C. Bhowmick, *Tetrahedron: Asymmetry*, 2015, **26**, 1215-1244.
20. B. List, R. A. Lerner and C. F. Barbas, *J. Am. Chem. Soc.*, 2000, **122**, 2395-2396.
21. W. Notz and B. List, *J. Am. Chem. Soc.*, 2000, **122**, 7386-7387.
22. K. A. Ahrendt, C. J. Borths and D. W. MacMillan, *J. Am. Chem. Soc.*, 2000, **122**, 4243-4244.
23. J. Mlynarski and J. Paradowska, *Chem. Soc. Rev.*, 2008, **37**, 1502-1511.
24. J. Mlynarski and S. Baś, *Chem. Soc. Rev.*, 2014, **43**, 577-587.
25. D. W. MacMillan, *Nature*, 2008, **455**, 304.
26. M. Silvi and P. Melchiorre, *Nature*, 2018, **554**, 41.
27. M. De Rosa, P. La Manna, C. Talotta, A. Soriente, C. Gaeta and P. Neri, *Front. Chem.*, 2018, **6**, 84.

28. M. L. Bender, *Chem. Rev.*, 1960, **60**, 53-113.
29. T. C. Bruice and G. L. Schmir, *J. Am. Chem. Soc.*, 1957, **79**, 1663-1667.
30. W. P. Jencks and J. Carriuolo, *J. Biol. Chem.*, 1959, **234**, 1280-1285.
31. J. F. Kirsch and W. P. Jencks, *J. Am. Chem. Soc.*, 1964, **86**, 837-846.
32. J. Gerstein and W. P. Jencks, *J. Am. Chem. Soc.*, 1964, **86**, 4655-4663.
33. W. P. Jencks and J. Carriuolo, *J. Biol. Chem.*, 1959, **243**, 1272-1279.
34. W. P. Jencks and J. Carriuolo, *J. Am. Chem. Soc.*, 1961, **83**, 1743-1750.
35. W. P. Jencks, D. G. Oakenfull and K. Salvesen, *J. Am. Chem. Soc.*, 1971, **93**, 188-194.
36. J. F. Kirsch and W. P. Jencks, *J. Am. Chem. Soc.*, 1964, **86**, 833-837.
37. W. P. Jencks, *Catalysis in Chemistry and Enzymology*, Dover Publications, 2 edn., 1987.
38. V. Gold, *Advances in Physical Organic Chemistry APL*, Elsevier Science, 1975.
39. T. A. Steitz and R. G. Shulman, *Annu. Rev. Biophys. Bioeng.*, 1982, **11**, 419-444.
40. P. Carter and J. A. Wells, *Nature*, 1988, **332**, 564.
41. K. Faber, *Biotransformations in organic chemistry*, Springer, 1992.
42. K. L. Duncan and R. V. Ulijn, *Biocatalysis*, 2015, **1**, 67-81.
43. E. H. Cordes and W. P. Jencks, *J. Am. Chem. Soc.*, 1962, **84**, 826-831.
44. F. Schneider, *Angew. Chem. Int. Ed.*, 1978, **17**, 583-592.
45. P. Nieri, S. Carpi, S. Fogli, B. Polini, M. C. Breschi and A. Podestà, *Sci. Rep.*, 2017, **8**, 45760.
46. H. Tsukada and D. Blow, *J. Mol. Biol.*, 1985, **184**, 703-711.
47. L. Schoonen, K. S. Esterik, C. Zhang, R. V. Ulijn, R. J. Nolte and J. C. van Hest, *Sci. Rep.*, 2017, **7**, 14772.
48. M. D. Nothling, A. Ganesan, K. Condic-Jurkic, E. Pressly, A. Davalos, M. R. Gotrik, Z. Xiao, E. Khoshdel, C. J. Hawker and M. L. O'Mara, *Chem*, 2017, **2**, 732-745.
49. S. Bezer, M. Matsumoto, M. W. Lodewyk, S. J. Lee, D. J. Tantillo, M. R. Gagné and M. L. Waters, *Org. Biomol. Chem.*, 2014, **12**, 1488-1494.
50. G. Chadha and Y. Zhao, *Org. Biomol. Chem.*, 2013, **11**, 6849-6855.
51. C. Overberger and K. Dixon, *J. Polym. Sci., Part A: Polym. Chem.*, 1977, **15**, 1863-1868.
52. E. H. Wanderlind, D. G. Liz, A. P. Gerola, R. F. Affeldt, V. Nascimento, L. C. Bretanha, R. Montecinos, L. Garcia-Rio, H. D. Fiedler and F. Nome, *ACS Catal.*, 2018, **8**, 3343-3347.
53. Y. Li, Y. Zhao, S. Hatfield, R. Wan, Q. Zhu, X. Li, M. McMills, Y. Ma, J. Li and K. L. Brown, *Biorg. Med. Chem.*, 2000, **8**, 2675-2680.
54. M. J. MacDonald, L. D. Lavis, D. Hilvert and S. H. Gellman, *Org. Lett.*, 2016, **18**, 3518-3521.
55. Y. Maeda, O. V. Makhlynets, H. Matsui and I. V. Korendovych, *Annu. Rev. Biomed. Eng.*, 2016, **18**, 311-328.
56. Y. Maeda, N. Javid, K. Duncan, L. Birchall, K. F. Gibson, D. Cannon, Y. Kanetsuki, C. Knapp, T. Tuttle and R. V. Ulijn, *J. Am. Chem. Soc.*, 2014, **136**, 15893-15896.
57. F. Menger and M. Ladika, *J. Am. Chem. Soc.*, 1987, **109**, 3145-3146.
58. S. Luo, P. G. Wang and J.-P. Cheng, *J. Org. Chem.*, 2004, **69**, 555-558.
59. J. C. Gomes, M. T. Rodrigues Jr, A. Moyano and F. Coelho, *Eur. J. Org. Chem.*, 2012, **2012**, 6861-6866.
60. J. C. Gomes, J. Sirvent, A. Moyano, M. T. Rodrigues Jr and F. Coelho, *Org. Lett.*, 2013, **15**, 5838-5841.
61. L. Raich, H. Santos, J. C. Gomes, M. T. Rodrigues, R. Galaverna, M. N. Eberlin, F. Coelho, C. Rovira and A. Moyano, *ACS Catal.*, 2018, **8**, 1703–1714.
62. A. R. Fersht and W. P. Jencks, *J. Am. Chem. Soc.*, 1970, **92**, 5432-5442.
63. A. R. Butler and I. H. Robertson, *J. Chem. Soc., Perkin Trans. 2*, 1975, 660-663.
64. M. L. Bender and B. W. Turnquest, *J. Am. Chem. Soc.*, 1957, **79**, 1656-1662.
65. D. Decker, *Macromol. Chem. Phys.*, 1973, **168**, 51-58.
66. M. Azechi, N. Toyota, K. Yamabuki, K. Onimura and T. Oishi, *Polym. Bull.*, 2011, **67**, 631-640.
67. G. Chadha and Y. Zhao, *Chem. Commun.*, 2014, **50**, 2718-2720.
68. T. Tamura and I. Hamachi, in *Site-Specific Protein Labeling*, Springer, 2015, pp. 229-242.
69. Y. Amamoto, Y. Aoi, N. Nagashima, H. Suto, D. Yoshidome, Y. Arimura, A. Osakabe, D. Kato, H. Kurumizaka and S. A. Kawashima, *J. Am. Chem. Soc.*, 2017, **139**, 7568-7576.
70. T. Ishiguro, Y. Amamoto, K. Tanabe, J. Liu, H. Kajino, A. Fujimura, Y. Aoi, A. Osakabe, N. Horikoshi and H. Kurumizaka, *Chem*, 2017, **2**, 840-859.
71. P. Li, J. Du, Y. Xie, M. Tao and W.-Q. Zhang, *ACS Sustain. Chem. Eng.*, 2016, **4**, 1139-1147.
72. V. K. Aggarwal, D. K. Dean, A. Mereu and R. Williams, *J. Org. Chem.*, 2002, **67**, 510-514.
73. J. Augé, N. Lubin and A. Lubineau, *Tetrahedron Lett.*, 1994, **35**, 7947-7948.
74. Y. Q. Yu and Z. L. Wang, *J. Chin. Chem. Soc.*, 2013, **60**, 288-292.
75. M. S. Abaee and S. Cheraghi, *Turk. J. Chem.*, 2014, **38**, 650-660.

76. E. V. Dalessandro, H. P. Collin, M. S. Valle and J. R. Pliego, *RSC Adv.*, 2016, **6**, 57803-57810.
77. F. Bigi and C. Quarantelli, *Curr. Org. Synth.*, 2012, **9**, 31-39.
78. S. Otto and J. B. Engberts, *Org. Biomol. Chem.*, 2003, **1**, 2809-2820.
79. J. J. Gajewski, *Acc. Chem. Res.*, 1997, **30**, 219-225.
80. A. Seingeot, Y. Charmasson, M. Attolini and M. Maffei, *Heteroat. Chem*, 2017, **28**, e21352.
81. B. Rajarathinam, K. Kumaravel and G. Vasuki, *ACS Comb. Sci.*, 2017, **19**, 455-463.
82. B. Rajarathinam and G. Vasuki, *Org. Lett.*, 2012, **14**, 5204-5206.
83. J. Lv, Q. Zhang, M. Cai, Y. Han and S. Luo, *Chem. Asian J.*, 2018, **13**, 740-753.
84. F. Trausel, C. Maity, J. M. Poolman, D. Kouwenberg, F. Versluis, J. H. van Esch and R. Eelkema, *Nat. Commun.*, 2017, **8**, 879.
85. D. K. Kölmel and E. T. Kool, *Chem. Rev.*, 2017, **117**, 10358-10376.
86. W. P. Jencks, *J. Am. Chem. Soc.*, 1959, **81**, 475-481.
87. C. Godoy-Alcántar, A. K. Yatsimirsky and J. M. Lehn, *J. Phys. Org. Chem.*, 2005, **18**, 979-985.
88. P. Crisalli and E. T. Kool, *J. Org. Chem.*, 2013, **78**, 1184-1189.
89. P. Crisalli and E. T. Kool, *Org. Lett.*, 2013, **15**, 1646-1649.
90. D. Larsen, M. Pittelkow, S. Karmakar and E. T. Kool, *Org. Lett.*, 2014, **17**, 274-277.
91. A. Dirksen, T. M. Hackeng and P. E. Dawson, *Angew. Chem. Int. Ed.*, 2006, **45**, 7581-7584.
92. O. Dilek, A. M. Sorrentino and S. Bane, *Synlett*, 2016, **27**, 1335-1338.
93. F. Trausel, B. Fan, S. A. van Rossum, J. H. van Esch and R. Eelkema, *Adv. Synth. Catal.*, 2018, **360**, 2571-2576.
94. A. Dirksen, S. Dirksen, T. M. Hackeng and P. E. Dawson, *J. Am. Chem. Soc.*, 2006, **128**, 15602-15603.
95. A. R. Blanden, K. Mukherjee, O. Dilek, M. Loew and S. L. Bane, *Bioconjugate Chem.*, 2011, **22**, 1954-1961.
96. D. W. Domaille and J. N. Cha, *Chem. Commun.*, 2014, **50**, 3831-3833.
97. J. Lou, F. Liu, C. D. Lindsay, O. Chaudhuri, S. C. Heilshorn and Y. Xia, *Adv. Mater.*, 2018, **30**, e1705215.
98. R. J. Spears, R. Brabham, D. Buddhadev, T. Keenan, S. McKenna, J. Walton, J. A. Brannigan, M. Brzozowski, A. J. Wilkinson and M. Plevin, *Chem. Sci.*, 2018, 5585-5593.
99. I. Drienovská, C. Mayer, C. Dulson and G. Roelfes, *Nat. Chem.*, 2018, **10**, 946.
100. E. C. Johnson and S. B. Kent, *J. Am. Chem. Soc.*, 2006, **128**, 6640-6646.
101. P. E. Dawson, T. W. Muir, I. Clark-Lewis and S. Kent, *Science*, 1994, **266**, 776-779.
102. P. E. Dawson, M. J. Churchill, M. R. Ghadiri and S. B. Kent, *J. Am. Chem. Soc.*, 1997, **119**, 4325-4329.
103. T. W. Muir, *Annu. Rev. Biochem*, 2003, **72**, 249-289.
104. B. Cowper, T. M. Sze, B. Premdjee, A. F. Bongat White, A. Hacking and D. Macmillan, *Chem. Commun.*, 2015, **51**, 3208-3210.
105. K. Mandal, B. L. Pentelute, D. Bang, Z. P. Gates, V. Y. Torbeev and S. B. Kent, *Angew. Chem.*, 2012, **124**, 1510-1515.
106. M. Cargoët, V. Diemer, B. Snella, R. Desmet, A. Blanpain, H. Drobecq, V. Agouridas and O. Melnyk, *J. Org. Chem.*, 2018, **83**, 12584-12594.

2.6 SUPPLEMENTARY INFORMATION

Table S2.1: Overview of organocatalysed reactions: activation mode, catalyst (loading), reaction conditions (pH, T, time, additives), remarks and literature reference.

Activation-mode	Reaction variant	#	Catalyst* (loading)	Reaction conditions (pH, T (°C), time, additives) and remarks	Ref.
Covalent - Nucleophilic base catalysis	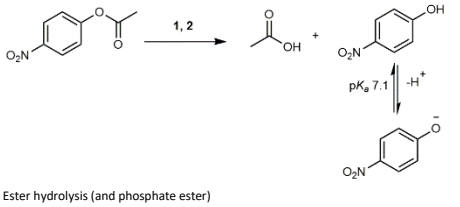 Ester hydrolysis (and phosphate ester)	1a	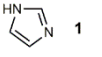 Imidazole (super-stoichiometric)	pH > 7 (basic favourable) T: RT Time: fast (min) Additives: organic co-solvent for ester Remarks: use of imidazole buffers	1-3
		1b	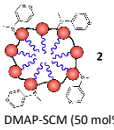 DMAP-SCM (50 mol%)	pH: 4-8 T: 35 Time: fast (min) Additives: organic co-solvent for ester Remarks: use of HEPES buffer	4
	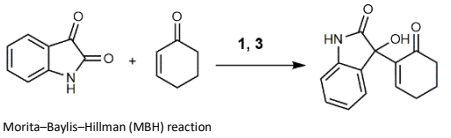 Morita–Baylis–Hillman (MBH) reaction	2	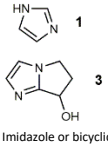 Imidazole or bicyclic imidazolyl alcohol (10 mol%)	pH: n.d. T: RT Time: 4 h Additives: Sodium Dodecyl Sulphate (SDS)	5-7
	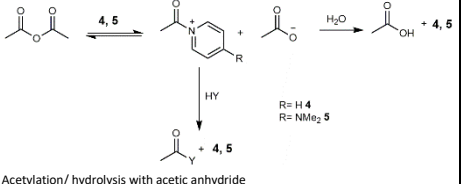 Acetylation/ hydrolysis with acetic anhydride	3	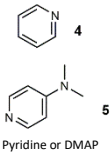 Pyridine or DMAP (super-stoichiometric)	pH: 5.5 T: 25 Time: fast (min) Additives: organic co-solvent for acetic anhydride Remarks: use of pyridine buffers	8, 9
	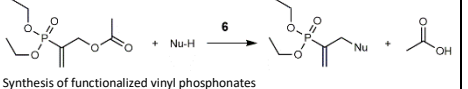 Synthesis of functionalized vinyl phosphonates	4	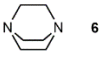 DABCO (20 mol%)	pH: n.d. T: RT Time: overnight Remarks: sulphur and nitrogen-based aliphatic and aromatic nucleophiles	10
	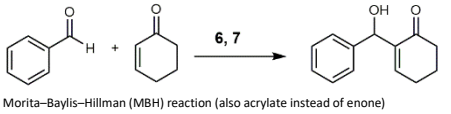 Morita–Baylis–Hillman (MBH) reaction (also acrylate instead of enone)	5	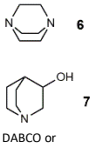 DABCO or 3-hydroxyquinuclidine (stoichiometric)	pH: n.d. T: RT Time: 4 h Remarks: Purification by flash chromatography	11
	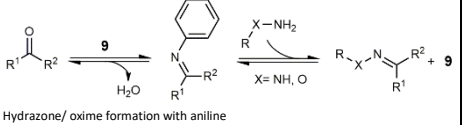 Hydrazone/ oxime formation with aniline	6	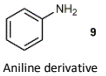 Aniline derivative (super-stoichiometric)	pH: 2.5-7.4 (acidic favourable) T: RT Time: minutes to hours (depending on catalyst and reactants) Additives: some cases co-solvent (DMF) for reactants	12-18

	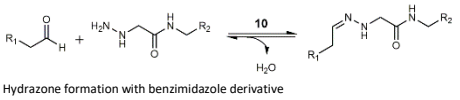 Hydrazone formation with benzimidazole derivative	7	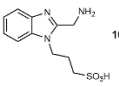 2-(aminomethyl) benzimidazole derivative (super-stoichiometric)	pH: 7.4 T: 37 Time: minutes to hours (depends on concentrations) Remarks: use of PBS buffer	19
	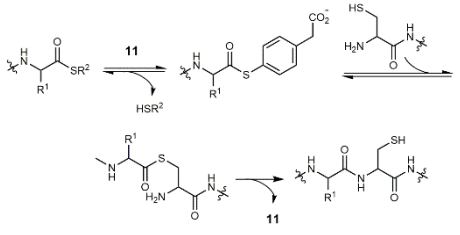 Native chemical ligation (NCL)	8	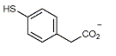 4-mercaptophenyl acetic acid (MPAA) (super-stoichiometric)	pH: 7.0 T: 25 Time: few hours (depending on catalyst and reactants) Additives: TCEP (to maintain thiols in reduced form) Remarks: HPLC purification	20, 21
Covalent – General/ specific base catalysis	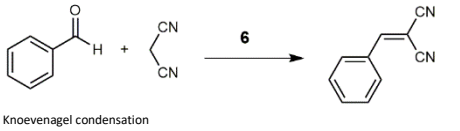 Knoevenagel condensation	9	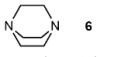 DABCO (10 mol%)	pH: n.d. T: RT Time: 2 min Remarks: recycling of catalyst (six times) by recovery from the filtrate water	22
Covalent – Iminium and/ or base	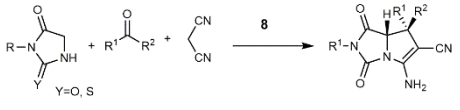 Multi-component reaction	10	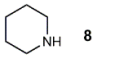 Piperidine (10 mol%)	pH: n.d. T: RT-80 Time: 0.5-8 h	23

Abbreviations: T=temperature, RT=room temperature, n.d. = not determined, Nu-H = nucleophile, SCM=surface-crosslinked-micelle, DMF=N,N-dimethylformamide, TCEP=Tris(2-carboxyethyl)-phosphine, Ar=aryl, Me=methyl, Et=ethyl.
Notes: *Catalysts are numbered regardless of their ionization state or different R-groups.

2.6.1 Supplementary references

1. J. F. Kirsch and W. P. Jencks, *J. Am. Chem. Soc.*, 1964, **86**, 837-846.
2. W. P. Jencks and J. Carriuolo, *J. Biol. Chem.*, 1959, **234**, 1280-1285.
3. T. C. Bruice and G. L. Schmir, *J. Am. Chem. Soc.*, 1957, **79**, 1663-1667.
4. G. Chadha and Y. Zhao, *Chem. Commun.*, 2014, **50**, 2718-2720.
5. J. C. Gomes, M. T. Rodrigues Jr, A. Moyano and F. Coelho, *Eur. J. Org. Chem.*, 2012, **2012**, 6861-6866.
6. J. C. Gomes, J. Sirvent, A. Moyano, M. T. Rodrigues Jr and F. Coelho, *Org. Lett.*, 2013, **15**, 5838-5841.
7. L. Raich, H. Santos, J. C. Gomes, M. T. Rodrigues, R. Galaverna, M. N. Eberlin, F. Coelho, C. Rovira and A. Moyano, *ACS Catal.*, 2018, **8**, 1703–1714.
8. A. R. Butler and I. H. Robertson, *J. Chem. Soc., Perkin Trans. 2*, 1975, 660-663.
9. A. R. Fersht and W. P. Jencks, *J. Am. Chem. Soc.*, 1970, **92**, 5432-5442.
10. A. Seingeot, Y. Charmasson, M. Attolini and M. Maffei, *Heteroat. Chem*, 2017, **28**, e21352.
11. V. K. Aggarwal, D. K. Dean, A. Mereu and R. Williams, *J. Org. Chem.*, 2002, **67**, 510-514.
12. F. Trausel, B. Fan, S. A. van Rossum, J. H. van Esch and R. Eelkema, *Adv. Synth. Catal.*, 2018, **360**, 2571-2576.
13. F. Trausel, C. Maity, J. M. Poolman, D. Kouwenberg, F. Versluis, J. H. van Esch and R. Eelkema, *Nat. Commun.*, 2017, **8**, 879.
14. P. Crisalli and E. T. Kool, *J. Org. Chem.*, 2013, **78**, 1184-1189.
15. P. Crisalli and E. T. Kool, *Org. Lett.*, 2013, **15**, 1646-1649.
16. D. K. Kölmel and E. T. Kool, *Chem. Rev.*, 2017, **117**, 10358-10376.
17. D. Larsen, M. Pittelkow, S. Karmakar and E. T. Kool, *Org. Lett.*, 2014, **17**, 274-277.
18. E. H. Cordes and W. P. Jencks, *J. Am. Chem. Soc.*, 1962, **84**, 826-831.

19. J. Lou, F. Liu, C. D. Lindsay, O. Chaudhuri, S. C. Heilshorn and Y. Xia, *Adv. Mater.*, 2018, **30**, e1705215.
20. E. C. Johnson and S. B. Kent, *J. Am. Chem. Soc.*, 2006, **128**, 6640-6646.
21. B. Cowper, T. M. Sze, B. Premdjee, A. F. Bongat White, A. Hacking and D. Macmillan, *Chem. Commun.*, 2015, **51**, 3208-3210.
22. Y. Q. Yu and Z. L. Wang, *J. Chin. Chem. Soc.*, 2013, **60**, 288-292.
23. B. Rajarathinam, K. Kumaravel and G. Vasuki, *ACS Comb. Sci.*, 2017, **19**, 455-463.

CHEMICALLY FUELLED, TRANSIENT SUPRAMOLECULAR POLYMERS

CHAPTER 3

Supramolecular polymerization is a form of molecular self-assembly, where one-dimensional aggregates are established by non-covalent interactions. The growth mechanisms of supramolecular polymers are primarily isodesmic and cooperative. Taking inspiration from biology, examples are given of microtubule and actin filament assembly, which are important for cellular motility. Next, we shed light on the different thermodynamic regimes of supramolecular polymerization and the nature of the chemical fuel. Together with the polymerization mechanisms, these concepts return in the comprehensive literature overview in this chapter, where all chemically fuelled, transient supramolecular polymer systems are reviewed. Highly popular are the nucleoside triphosphate systems with biocatalysts, next to redox systems and pH-switches. For now, the bigger challenges in this field are to equip the systems with dynamic functions, to sustain the non-equilibrium condition by continuous fuel supply and to increase the degree of control over the non-equilibrium state. Altogether, chemically fuelled, transient supramolecular polymers are considered as vital elements for the development of dynamic and responsive materials, which hold great promise for future applications.

This chapter will be published as a book chapter:
M.P. van der Helm, J.H. van Esch, R. Eelkema, WILEY-VCH, *manuscript submitte*d.

3.1 INTRODUCTION

Molecular self-assembly, a phenomenon where individual molecules unite to form larger clusters, is a concept that is ubiquitously found in chemistry, physics and biology.[1,2] When these clusters form one-dimensional aggregates connected by moderately strong and highly directional secondary interactions, the self-assembly is known as supramolecular polymerization. In more detail, in their seminal contributions E. W. Meijer and co-workers postulated the following definition for supramolecular polymers: *"Supramolecular polymers are defined as polymeric arrays of monomeric units that are brought together by reversible and highly directional secondary interactions, resulting in polymeric properties in dilute and concentrated solution as well as in the bulk. The directionality and strength of the supramolecular bonding are important features of systems that can be regarded as polymers and that behave according to well-established theories of polymer physics."*[2, 3] Hence, supramolecular polymers distinguish themselves from traditional covalent polymers by the non-covalent forces that hold together the individual monomers or repeating units. The interactions, including hydrogen bonding, π-π stacking, metal coordination, dipole moments and host-guest interactions, are weak to moderately strong and directional, making the supramolecular polymerization reversible and giving the self-assembled structures their unique dynamic and stimuli-responsive character.[4, 5] Here, multivalent binding motifs in combination with non-covalent interactions, such as van der Waals, Coulomb and π–π interactions, and solvophobic effects, are key in the development of strong supramolecular polymers.[6]

The foundation for modern synthetic polymer science was laid in 1920 by Herman Staudinger[7], who introduced the concept of macromolecules as being high molecular weight entities, and Wallace H. Carothers in 1931[8], who made a classification for those macromolecules and their polymerization mechanisms. The first supramolecular polymer was only introduced by Jean-Marie Lehn and co-workers in 1990, who synthesized a supramolecular polymer based on complementary, ditopic, triple hydrogen bonding donor (D)–acceptor (A) motifs.[9] Ever since, literature examples of supramolecular polymers have increased exponentially and the three different growth mechanisms, (1) isodesmic, (2) cooperative and (3) ring-chain, have been introduced. Ring-chain polymers, which are formed through an equilibrium between the linear aggregate (also the monomer) and a cyclic structure in the assembly pathway, are a special class of supramolecular polymers, since they only involve ditopic monomers. In contrast, most supramolecular polymers exhibit an isodesmic or a(n) (anti-)cooperative growth mechanism. The isodesmic mechanism or *equal K* model is characterized by a reversible formation of a single non-covalent bond that is identical for all steps in the monomer-to-aggregate transformation. The covalent polymer chemistry counterpart would be a step-by-step reversible polycondensation that follows the "principle of equal

reactivity" from Flory[10]. On the other hand, the cooperative (or nucleation-elongation) mechanism is identified by two stages: the formation of a nucleus (with association constant K_n), followed by elongation of the nucleus (with association constant K_e). Depending on the difference between the association constants the mechanism is called cooperative or anti-cooperative. To initiate the elongation process, a critical temperature, concentration or solvent composition should be overcome. Cooperative supramolecular polymerization shows much resemblance with living ionic or radical covalent polymerizations, yet also polycondensations can be affected by cooperative effects.

Both the isodesmic and cooperative mechanisms are most commonly used to characterize thermodynamically controlled supramolecular polymerizations and in general the focus has been on *under equilibrium conditions*.[2, 11, 12] In the last decades, inspired by life-like systems where structures can reside *out-of-equilibrium*, the attention is shifted towards *non-equilibrium* supramolecular polymerization. Non-equilibrium supramolecular polymerization is characterized by a net exchange of energy and matter between the supramolecular polymer and its surroundings. An important distinction has to be made, though, as non-equilibrium can refer to a kinetically/ metastable (depending on the timescale) state or a dissipative state, where the continuous supply of energy (e.g. a chemical fuel) is required to maintain the non-equilibrium condition.

In this chapter, we focus on the latter condition and discuss chemically fuelled supramolecular polymers, which are thus transient non-equilibrium supramolecular polymers and dissipative systems. The fuel, here, is a high energy molecule (a chemical fuel) and not a photon. Nonetheless, light-driven supramolecular polymerizations have been reported. An illustrative example is the work from Sleiman and co-workers, who exploited *cis-trans* conformational changes in carboxylic acid functionalized azobenzenes to switch between rod-like aggregates and linear tapes under UV light irradiation (from *trans* to *cis*) and thermal relaxation (from *cis* to *trans*). [13] It should be noted that, as for chemical fuel-driven supramolecular polymerization the assembly process is driven by a chemical fuel, the term "self-assembly" is avoided in favour of simply "assembly". For more information on and an overview of supramolecular polymers and their applications under equilibrium and non-equilibrium conditions other than dissipative systems the reader is referred to excellent reviews by Hermans and de Greef[14], Besenius[6, 15], Fernández[16], George[17, 18] and Meijer[4]. Additionally, for an in-depth review of fuel-driven non-equilibrium systems we refer to the recent tutorial review of our group together with the Boekhoven group[19]. Unless mentioned otherwise, we will limit ourselves to the formation of 1D aggregates and fibrillar gel networks, other aggregates, such as micelles and vesicles, are out of scope. In the next section we first motivate the importance of this research area by giving examples of non-linear

behaviour in biology. Then we explain two important concepts, i.e. the energy landscape of supramolecular polymerization and the nature of the chemical fuel leading to different assembly terminology. Afterwards, we go through the various literature examples explaining the underlying chemical reaction networks and subsequently coupled transient supramolecular polymerization. Finally, we state the conclusions and give an outlook for the future direction of chemically fuelled supramolecular polymerization.

3.2 NON-LINEAR BEHAVIOUR; A LESSON FROM BIOLOGY

In contrast to traditional man-made molecular systems, most complex biological systems operate out-of-equilibrium and are thermodynamically unstable. To maintain desired structures and functions these systems are ruled by kinetics rather than thermodynamics and require the constant consumption of energy, which is often in the form of a chemical fuel with a high-energy bond, like the phosphoanhydride bond in adenosine triphosphate (ATP) and guanosine triphosphate (GTP).[19-24] Free energy in these systems is utilized in two complementary ways. Either free energy from a thermodynamically favourable chemical reaction (e.g. ATP hydrolysis) is used to carry out otherwise thermodynamically unfavourable reactions, like protein phosphorylation and transmembrane transport, or the free energy is used for replication purposes, such as ribosomal protein synthesis. [21] In these living systems, the dissipation of energy to the environment to sustain a non-equilibrium structure brings about important consequences.[20] It permits the uncoupling of dynamic and mechanical behaviour, resulting in strong and at the same time dynamic architectures otherwise infeasible. Additionally, energy dissipation enables the formation of stable structures that are kinetically controlled, as life is 'a kinetic state of matter'[23, 25]. The often observed stability of living materials originates from a balance between kinetically controlled formation and degradation pathways.[26] In fact, this non-equilibrium behaviour is at the core of Darwinian evolution. The stability of the non-equilibrium structures emerges from their degree of adaption to the environment and facilitates the process of selection.[27-29]

To give a flavour of how chemical fuel-driven supramolecular polymerization works in biology we will discuss the dynamic behaviour of the actin and microtubule protein filaments. Together with intermediate protein filaments, actin filaments and microtubules form a network that make up the cytoskeleton of eukaryotic cells. The cytoskeleton enables spatial organization of the cells, cellular polarity and diverse mechanical functions. The actin filaments (i.e. microfilaments) are flexible structures with a diameter of 9 nm, while microtubules are stiff, long and hollow cylindrical polymers with an outer diameter of 25 nm. Actin filaments shape the cell's surface and enable locomotion, whereas microtubules position organelles, enable intracellular transport and form the mitotic spindle for chromosome segregation during mitosis. In

collaboration with kinesin and dynein motor proteins entire organelles can be transported along these filaments. Actin and microtubule filaments are built up from individual protein subunits, actin monomers and αβ-tubulin heterodimers respectively, which assemble into helical structures by forming end-to-tail and side-to-side protein connections. They can only assemble after binding to a nucleoside triphosphate molecule (Figure 3.1 for microtubule structure build from individual αβ-tubulin proteins). The intermolecular forces between these proteins are weak and non-covalent, leading to rapid (dis)assembly and providing their dynamic character. Importantly, the (dis)assembly is directly coupled to the hydrolysis of the bound ATP (actin) or GTP (microtubules). Next to that, the subunits are asymmetrical and preferentially combine head-to-tail, giving the resulting polymers structural polarity and making the head and tail ends of the polymer behave differently.

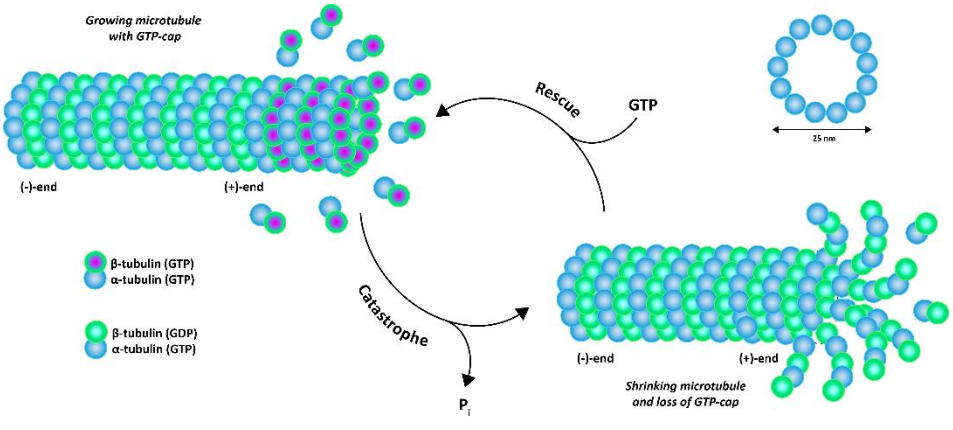

Figure 3.1: Schematic overview of microtubule (dis)assembly. Growth is established by the addition of GTP-tubulin to the (+)-end of the growing microtubule. However, when the GTP cap is lost with the release of inorganic phosphate (P_i), GDP-tubulin is exposed at the microtubule (+)-end and *catastrophe* occurs. The opposite process from shrinkage to growth is called *rescue*.

The polymerizations of actin and tubulin are examples of cooperative supramolecular polymerization. To form a new filament, first an initial aggregate needs to be formed. For actin this is a trimer, whereas the microtubules require a larger nucleus of about thirteen subunits, such as in the centrosome of the cell. After the initial nucleus has been formed, further monomer addition goes rapidly, leading to an elongated helical polymer. In this process the initial nucleation is the kinetic barrier. The coupling of the nucleotide (ATP or GTP) hydrolysis to the polymerization brings about the non-linear behaviour of the filaments. For both filaments, (local) gradients in the chemical fuel and the binding of accessory proteins (e.g. formins, tropomyosins, microtubule-associated proteins (MAPs)) provide them with the necessary adaptation to the environment and enable them to self-organize into macrostructures. In the case of actin, a non-linear

phenomenon called “treadmilling” can be observed. Since the actin filaments are polarized, the kinetic rate constants are much greater at the (+)-end than at the (-)-end, leading to fast polymerization of the (+)-end and fast depolymerization of the (-)-end, depending on the free actin monomer concentration. When the ATP-monomer concentration surpasses a critical concentration, filament elongation proceeds spontaneously by addition of ATP-monomer to a growing polymer chain and a cell can use the released free energy to carry out work. The treadmilling phenomenon is a steady state, where the net assembly of monomers from the (+)-end happens at an identical rate as the net disassembly from the (-)-end. The length of the polymer remains constant, while there is a net flux of monomers.

Similar to actin filaments, the behaviour of microtubules is non-linear and exhibit a phenomenon called “dynamic instability”, where microtubules rapidly switch between a period of slow growth and fast shrinkage (known as *catastrophe*) or vice versa (known as *rescue*) (Figure 3.1). This non-linear behaviour is observed experimentally *in vivo* and *in vitro* as individual microtubule oscillations and/or collective oscillations.[30-32] The rapid interconversion between microtubule growth and shrinkage can be exploited by cells to exert forces, for example to segregate the chromosomes during cell division. The dynamic instability is a direct consequence of the nucleoside triphosphate hydrolysis, which proceeds more rapidly in the assembled state than for the free GTP-tubulin dimer in solution due to its activated GTPase. Depolymerization of the microtubules is much faster at a GDP-tubulin end than at a GTP-tubulin end. Hence, growth is favoured when a GTP cap is present, but when hydrolysed to GDP depolymerization kicks in.[33]

As becomes apparent from the non-linear behaviour in vital cellular processes, the coupling to an irreversible chemical reaction can drive assembly and generate autonomous control in time and space over supramolecular structures. Inspired by these biological examples, researchers have started to design similar networks involving chemical fuel-driven supramolecular polymerization, which will be covered in the rest of this chapter after the discussion of the energy landscape and the nature of the chemical fuel.

3.3 WALKING UPHILL IN THE ENERGY LANDSCAPE

When a system resides in thermodynamic equilibrium, the final state is a result of the Boltzmann distribution and is pathway independent. Equilibrium assemblies reside in the global minimum of the free energy landscape and are thermodynamically stable, which is reflected by a long (infinite) lifetime. Noteworthy, the system is still dynamic and monomers exchange between supramolecular structures and solution. Likewise, energy dissipation does take place during the transformation from monomer-to-aggregate, as this is a spontaneous process.[34]

Second, non-equilibrium kinetically trapped assembled structures are captured in a local minimum of the energy landscape and the product distribution relates to the specific assembly pathway.[35] Different preparation protocols can lead to the occupation of a distinct local minimum and structurally different aggregates. Factors that influence the final aggregate formation are temperature, pH, solvent composition, etc. To get back to the thermodynamic equilibrium, time or activation energy is required. Whether this time is finite or infinite determines if the system is kinetically trapped (infinite with large energy barrier; >> k_BT) or just metastable (finite with energy barrier; ~ k_BT).[14] To describe the presence of different aggregation pathways the term pathway complexity was introduced by Meijer and co-workers and on-pathway vs off-pathway are used to distinguish kinetic outcomes from the thermodynamically stable analogues.[36] As discussed in the introduction, cooperative supramolecular polymerization shows most resemblance with conventional living polymerizations. In the covalent counterpart, control over final molecular weight and polymer dispersity can be achieved by the introduction of dormant states. For supramolecular polymerization this is not trivial, because of rapid nucleation and subsequent random initiation of assembly. However, a dormant state can be introduced by designing a kinetic trap (i.e. metastable state) along the way to thermodynamic equilibrium that postpones the nucleation step. Slow and constant addition of monomers from the metastable state results in controlled polymer growth. Since the polymer growth is controlled in this manner, this strategy is sometimes referred to as "living supramolecular polymerization".[18] However, the analogy does not truly hold, since in conventional living polymerization the control over polydispersity is typically achieved by fast nucleation (chain initiation), slow propagation (chain growth) and the absence of termination.

Finally, a third regime exists, known as non-equilibrium dissipative (or active) assembly or transient supramolecular polymerization (uphill in the energy landscape), for which a continuous energy supply is needed to be maintained. Depletion of the energy source causes the system to disintegrate and eventually convert back to the thermodynamic equilibrium state of the individual building blocks (or a local minimum down the road). In the case of chemically fuel driven systems, assembly of the building blocks is coupled to a chemical reaction network, involving at least two competing reactions (formation and degradation), with the formation being driven by conversion of the chemical fuel. The consumed energy, which is absorbed by the system, is associated with the fuel-to-waste conversion and can either be stored in the system or dissipated to the environment. With a fixed fuel concentration in a batch process this corresponds to an accompanying $\Delta G<0$ for the reaction. The stored energy is used to drive product concentrations away from equilibrium, whereas the dissipated energy leads to the irreversible generation of heat or waste products.[37] Control over the system can be achieved by the supply of the fuel in a batch-wise manner. However, compared to this

batch-wise addition of fuel, continuous energy supply can give rise to unusual features, like oscillations, bifurcations or chaotic behaviour. For example in the renowned Belousov-Zhabotinsky reaction[38, 39], exchange of matter and energy in an open system allows the concentrations of the species to exhibit spatiotemporal oscillations.[19, 21]

For the design of non-equilibrium dissipative systems there are two important aspects that need to be taken care of. First, to achieve steady-state concentrations of the various species (for an assembly process i.e. monomer, activated monomer, activated assembly and deactivated assembly) that are different to those at equilibrium, the process must exhibit a certain directionality. This can be achieved by kinetic asymmetry[37, 40] in the energy consumption pathways and can be best understood by applying the principles of microscopy reversibility[41]. Under stationary conditions the product of the rate constants of the forward reactions (clockwise direction) is equivalent to the product of the rate constants of the backward reactions (anticlockwise direction). However, this changes in a fuel-driven network, because the activation and deactivation steps follow chemically distinct pathways. For example, in the case of assembly, such kinetic asymmetry may arise from the facts that the chemical fuel preferentially activates the monomer and not the aggregate, whereas the fuel-to-waste conversion may be kinetically favoured in the assembly. Out-of-equilibrium, the distribution between the states does not depend on the free energies of the states themselves, but rather on the relative heights of the energy barriers between them (i.e. the kinetic asymmetry), the transition state energies, along with the strength of the non-equilibrium driving force.[42, 43] This also holds true for the net fluxes between the states at non-equilibrium conditions. Thus, the directionality originates from the asymmetry in the relative heights of the energy barriers between the transition and ground states (and not the level of the ground states themselves) and hence an information ratcheting mechanism is at play.[41, 44, 45]

The second requirement is that the high-energy structures should be kinetically stable and the kinetic barrier should be the dissociation step. Thus, a macromolecule, when driven out-of-equilibrium, tries to occupy the most stable kinetic states and not the thermodynamic ones. Moreover, the specific free-energy values of the states do not affect the adaptation to non-equilibrium conditions.[37, 40]

Both these requirements are also present in the microtubule system, which was discussed before. Kinetic asymmetry in the energy consumption pathways is reached by distortion of the Michaelis-Menten parameters caused by the assembly of the activated building blocks (activation of the GTPase due to assembly) and disfavoured binding of fresh GTP in the deactivated assemblies (due to the presence of GDP waste in the assemblies). Overall, this leads to the formation of high-energy microtubules by using thermodynamically activated substrates as chemical fuels. For more detail about how this works and a mathematical explanation with simulations we refer to the recently published perspective from Ragazzon and Prins[37].

3.4 THE NATURE OF THE CHEMICAL FUEL

At the heart of non-equilibrium systems is the energy source, which can either be a high-energy molecule or photon, although light-driven systems are not equal to their chemically driven analogues.[26] Nonetheless using light as the energy source can have the advantage of not producing any waste chemicals. Chemically fuelled networks are interesting because of their ability to selectively couple different processes in one system[20] and because their reaction kinetics can be controlled through a multitude of parameters (e.g. concentration, temperature, catalysts). For chemical fuels, a distinction can be made between a direct and indirect energy source or an external factor.[19]

In the first case, the starting materials react directly with the chemical fuel, generating the building blocks for the transient state. In the second (indirect) case, the consumption of the fuel can lead to the association of starting materials with no part of the fuel being integrated in the final assembled structures. Here, only the energy of the fuel is used by the generation of an active intermediate from the precursor and the fuel, hence decoupling the fuel structure from the system's function.[19] Both cases are examples of "dissipative assembly", where chemical fuel-to-waste conversion is mediated by the building blocks either in a direct or indirect manner, resulting in fuel-driven (non)-covalent modification of monomers. Here, the energy dissipation pathway is coupled to the assembly pathway. Important to mention is that this condition does not guarantee a system that is "driven" away from equilibrium. For that to occur, the kinetic asymmetry criterion needs to be satisfied and hence processes that fulfil this criterion are categorized under "driven assembly". Only in that case, the system operates out-of-equilibrium and continuous energy consumption is required to maintain the non-equilibrium state.

In a third system, it is not the building blocks that mediate the fuel-to-waste conversion, but an external factor, such as an enzyme. This case is defined as "assembly under dissipative conditions". Here, the energy dissipation pathway is entirely disconnected from the assembly pathway. Still, the assembly process responds to the available fuel, which slowly decreases over time, but this process is completely controlled by thermodynamics. While this terminology was recently introduced by Prins[37], another classification was made by George and co-workers in a slightly earlier contribution[17]. They categorized the chemical fuel-driven supramolecular polymerization as fuel-driven covalent or non-covalent modification of the monomers or a changing reaction environment. However, this distinction does not give much insight into the assembly process, nor the non-equilibrium condition. Hence, throughout this chapter we will try to be as specific as possible, when describing the different aspects of the fuel-driven supramolecular polymerization examples and their assembling processes. Still, in general it is not straightforward to arrange the reported systems in the various categories and analyse if the kinetic asymmetry criterion holds, since most of them use

batch-wise fuel additions. The latter makes it difficult to analyse whether the concentrations are different from the equilibrium concentrations and hence if a system truly resides out-of-equilibrium.

3.5 CHEMICALLY FUELLED, TRANSIENT SUPRAMOLECULAR POLYMERIZATION SYSTEMS

Since the report on the first man-made chemical fuel-driven supramolecular polymerization system from our group [46, 47], a considerable number of new systems have been designed or developed by various groups, which will be discussed in this chapter. In the pioneering system, hydrogelator precursors with anionic carboxylates are transformed into esters by reaction with an alkylating agent as a direct chemical fuel (methylation - forward reaction) (Figure 3.2A). In an aqueous environment these esters are not stable and slowly hydrolyse back to the original building blocks (demethylation - backward reaction). The fuel-driven conversion of the water-soluble carboxylates to the hydrophobic esters results in dissipative assembly, i.e. transient supramolecular polymerization. Subsequently, transient fibre formation in an aqueous environment temporarily generates a hydrogel network, which could be observed by a plethora of analysis techniques, such as confocal microscopy, atomic force microscopy (AFM), dynamic light scattering (DLS) and rheology measurements. Gel properties such as lifetime, stiffness and self-healing capability were controlled through reaction kinetics of fuel conversion (influenced by pH of the buffer and the type of methylating agent) and fuel concentrations. Strikingly, the fibres showed non-linear dynamic behaviour, including stochastic collapse and concomitant growth and shrinkage, reminiscent of microtubule assembly.[46] These non-linear dynamics are a strong indication that the system is "driven" away from equilibrium and the system should have kinetic asymmetry.

The group of Barragán used this system for their thermodynamic analysis of non-equilibrium assembly and the understanding of gelation under such conditions. They developed a mesoscopic non-equilibrium thermodynamic model that describes the fuel activation, assembly and disassembly processes. In the model, the generation of a more advanced gel structure is preceded by transient organization in intermediate aggregates. First-order structures (individual linear fibres) with strong interactions and a sequential formation, are distinguished from second-order and higher order structures (gel network), of which the interactions are much weaker and the formation is non-sequential. Fokker-Planck type kinetic equations are used to describe the structural transformation from the initially inactivated precursors to the final agglomerates. With this model the original experimental results of scattering intensity and species concentration over time were very accurately reproduced.[48]

In a follow-up work, Barragán and co-workers shed light on the role of entropy in the establishment of non-equilibrium structures. When described as a function of a structural parameter the architecture of the structures is determined by the entropy produced in the non-equilibrium assembling system. While energy and matter are exchanged in such systems, the system tries to minimize the free energy by creating structures, in that way increasing order, but decreasing entropy. Based on the second law of thermodynamics, the total entropy of a system and its surroundings must increase (or remain constant) and entropy must then be generated and released to the surroundings. Hence, the production rate of entropy is a measure of the energy dissipation in the system. In the non-equilibrium gelation process, the formation of gel structures is found at extreme values of entropy produced and is associated with a maximum. Moreover, they indeed showed that gel structures dissipate the maximum amount of free energy to increase their hierarchical order. Overall, the link between the entropy produced and the architecture of the structures can be a potential selection criterion, showing why disordered components form ordered assembled structures.[49]
Along the same line, a recent theoretical study by Green and co-workers analysed typical stochastic paths in a transient assembly process. The experimentally informed model could reproduce the fibre dynamics with fast fibre growth and stochastic fibre collapse, as observed by confocal microscopy. The model results corroborated the importance of produced entropy and showed that the number of fibres and their local maximum length are correlated with a maximum in entropy production rate and the size of a typical set of non-equilibrium pathways. Interestingly, for the non-equilibrium dissipative hydrogel system the most probable path did not describe the formation of the fibrous structure.[50]

Recently, Boekhoven and co-workers amended the aforementioned system and build a chemical reaction network based on the condensation of dicarboxylate peptide precursors (i.e. Fmoc protected peptide derivatives with a terminal aspartate or glutamate residue) into their corresponding anhydrides (Figure 3.2B). They deployed high-energy carbodiimides as indirect chemical fuels. Hydrophobization of the carboxylates into the anhydrides generated non-equilibrium assembling structures and led to the formation of colloids, self-erasing inks or hydrogels. Specifically, Fmoc-tripeptides precursors showed fibre formation in their anhydride state and depending on the concentration and nature of the precursor formed viscoelastic gels. The lifetime of the transient structures was limited to minutes or hours, since the anhydrides were rapidly hydrolysed in an aqueous environment. Both β-sheet formation and π-orbital overlap were responsible for the transient assembly into fibres, as measured by a Thioflavin-T (THT) assay and fluorescence spectroscopy. Interestingly, Fmoc tripeptides fibre structures based on a Fmoc-AA motif were converted back to the dicarboxylate building block state and turned liquid again. In contrast, fibres generated

from tripeptides starting with Fmoc-AV motifs did not disassemble back to the building blocks, but remained present as fibres, as observed by cryo-transmission electron microscopy (TEM) and shown on circular dichroism (CD) spectra, even though all anhydride groups had been hydrolysed. From these results, the authors concluded that the Fmoc-AV carboxylate fibres were driven into a kinetic trap by the fuel cycle, which converted them temporarily into the anhydride state. Only a heating-cooling cycle could cause the eventual disassembly of the carboxylate fibres.[51] Using the same fuel cycle, they also showed that selection of non-equilibrium products created from a pool of reacting species can be achieved by compartmentalization, as in liquid phase-separation.[52] The anhydride products were generated by the condensation of a library of carboxylic acid derivatives with different lengths. From this abiotic pool, the metastable products that could phase-separate into oil droplets were found to be more stable against deactivation than the non-assembling analogues. In all, pushing a molecular library out-of-equilibrium is a very clever approach en route to obtaining assembled structures with more life-like features.

Exploiting the same chemical reaction network with anhydride formation fuelled by carbodiimides, the group of Hartley reported on the transient formation of macrocycles similar to crown ethers, which demonstrated responsive cation binding behaviour.[53] Building on this work and using the same chemistry, they developed transiently anhydride cross-linked dynamic polymer networks from aqueous polymer solutions. Unlike supramolecular polymerization, the hydrogels generated by this covalent polymer network are much stiffer with maximum storage moduli at least one order of magnitude higher than those observed in the previous supramolecular polymer systems.[54]

Carbodiimides, more specifically 1-Ethyl-3-(3-dimethylaminopropyl)carbodiimide (EDC), as chemical fuels in combination with *p*-nitrophenol were also exploited by Das and co-workers to esterify lipid functionalized histidine amphiphile precursors. The esterification of the carboxylic acid end group led to the formation of a self-supporting gel. Interestingly, the proximity of the histidine imidazole group resulted in a cooperative catalytic effect, enhancing the ester hydrolysis in the assembled state and leading to subsequent disassembly of the fibrous structure.[55] Earlier, these cooperative effects were also reported by Prins and co-workers in a substrate-induced assembling system.[56] While it is typically easier to recognize systems with fuel-driven covalently modified building blocks, also in these non-covalent systems from Das and Prins the building blocks do play a role in the energy dissipation pathway.

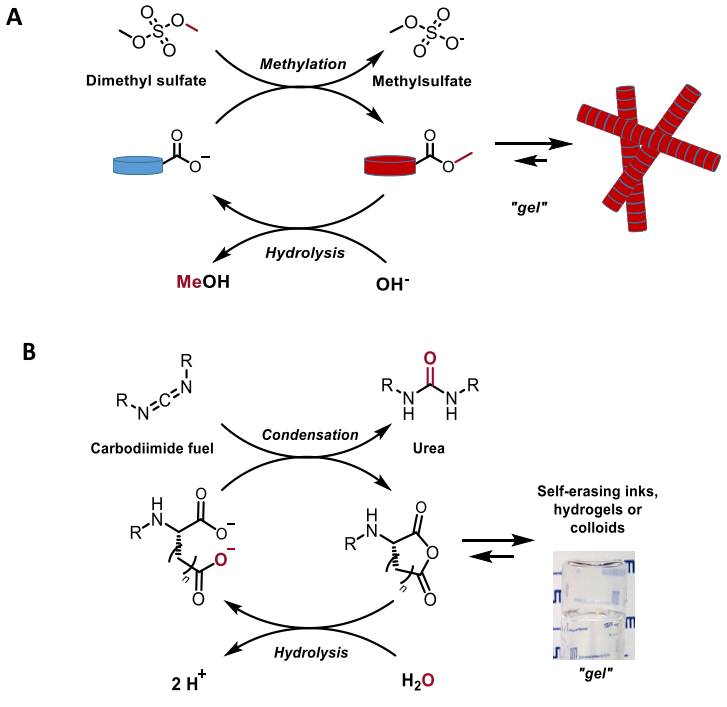

Figure 3.2: (A). Pioneering dissipative chemically fuelled supramolecular polymer system: anionic carboxylate precursors are converted into esters by supply of an alkylating agent (dimethyl sulphate) as a direct chemical fuel (methylation - forward reaction). The esters are transiently stable and slowly hydrolyse back to the original building blocks (demethylation - backward reaction). The increased hydrophobicity leads to the formation of fibres and a transient hydrogel network in aqueous buffered medium (shown in picture). Figure adapted from ref. (46). Copyright 2015 American Association for the Advancement of Science. **(B)**. Dissipative chemically fuelled supramolecular polymerization network based on condensation of dicarboxylate peptide precursors mediated by carbodiimides as indirect chemical fuels. The increased hydrophobicity of the anhydride structures results in the formation of transiently stable colloids, self-erasing inks or hydrogels (shown in picture). Figure adapted from ref. (51). Copyright 2017 Nature Publishing Group.

Different from the earlier abiotic systems, Ulijn and co-workers used a biocatalytic approach to arrive at transient supramolecular polymers. They designed a reaction network based on α-chymotrypsin transacetylation (forward reaction – kinetically controlled) in combination with amide hydrolysis by the same protease (backward reaction – thermodynamically controlled) (Figure 3.3A). This way, transient hydrogels, based on π-stacking and hydrogen bonding interactions, were formed from amine precursors fuelled by a methyl ester amino acid. Although not straightforward, the lifetime of the gel could be controlled by the enzyme concentration (affecting mostly the backward reaction), the pH of the solution with increasing amide hydrolysis under more basic conditions and the fuel concentration. Gel formation could be repeated for up to three times. Afterwards, the build-up of waste products such as methanol most

likely prevented the system from reaching the critical gelation concentration.[57, 58] Fascinatingly, using the same biocatalytic strategy, Ulijn and co-workers showed in a recent publication that they can couple a function to the transient supramolecular structure by the formation of transient conducting nanostructures in aqueous media. The biocatalytic assembly process was controlled by varying the amino acid input, leading to a transient or delayed chiral assembly having tuneable right- or left-handed structures on the nanoscale.[59]

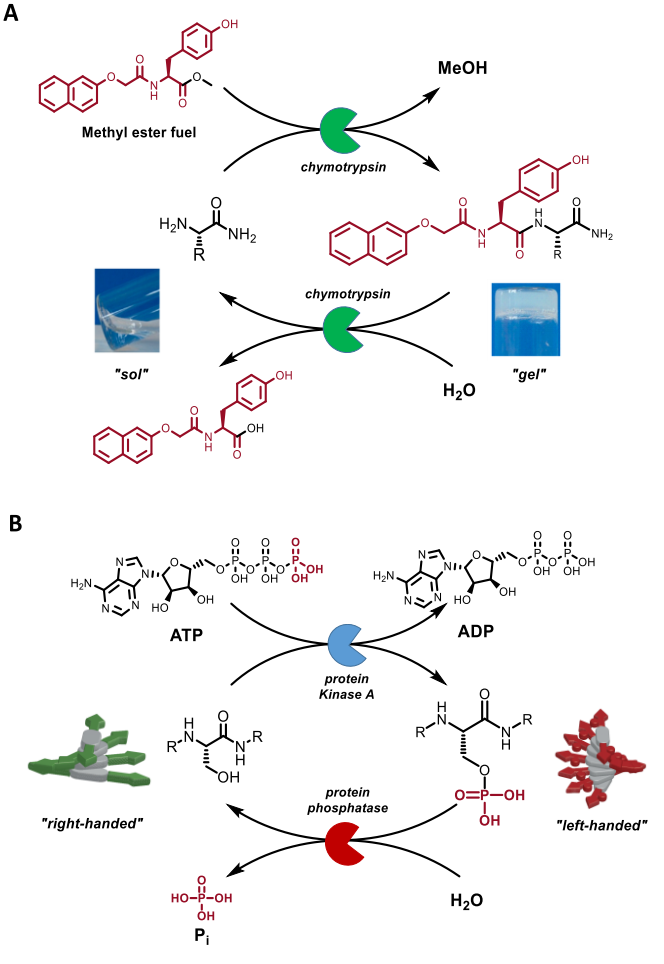

Figure 3.3: (A). Biocatalytic transient supramolecular polymer system involving a reaction network based on α-chymotrypsin transacetylation in combination with amide hydrolysis catalysed by the same enzyme. Transient hydrogels (shown in picture) were generated from different amine precursors fuelled by a methyl ester amino acid. Figure is adapted with permission from ref. (57). Copyright 2013 American Chemical Society. **(B)**. Biocatalytic transient supramolecular polymer system forming a switchable helix conformation based on phosphorylation by protein kinase A (forward reaction) and dephosphorylation by λ-protein phosphatase (backward reaction). ATP is used as the chemical fuel for the phosphorylation of the two serine residues of the symmetric peptide derivative of the PDI. Figure is adapted from ref. (60). Copyright 2017 Nature Publishing Group.

Another system were enzymes play essential roles in dissipative chemically fuelled supramolecular polymerization comes from the group of Hermans, who used phosphorylation by kinase (forward reaction) and dephosphorylation by phosphatase (backward reaction) enzymes to generate switchable supramolecular polymers (Figure 3.3B). Using ATP as a chemical fuel, two serine residues of a symmetric peptide derivative of 3,4,9,10-perylenediimide (PDI) were phosphorylated, catalysed by protein Kinase A. Dephosphorylation of the two phosphate groups was catalysed by λ-protein phosphatase. The addition of the negatively charged phosphate groups to the assembling precursors leads to polymer growth, based on π-stacking, hydrophobic and electrostatic interactions, and switching between a left- and right-handed helical supramolecular polymer in the phosphorylated and dephosphorylated state, respectively. Finding suitable conditions at which both enzymes could work properly was not trivial and batch-wise fuel addition was severely hampered by phosphatase inhibition caused by the generation of inorganic phosphate waste after one fuel cycle. However, by substituting the batch system for a continuous flow membrane reactor this limitation was circumvented. This way, the system could remain operational for days in the membrane reactor as long as the fuel was supplied and the waste removed. Various non-equilibrium steady states could be achieved under the continuous flow conditions, depending on the concentration of ATP supplied and the removal of waste by a dialysis membrane.[60]

In continuation, very recently the same group of Hermans reported on the first man-made supramolecular polymer system featuring oscillations, travelling fronts and large-scale dissipative structures.[61] They used a redox system where PDI's modified with solubilizing ethylene glycol chains and hydrogen bond forming amide groups are chemically reduced by sodium dithionite ($Na_2S_2O_4$) (forward reaction) in buffered medium (Figure 3.4A). The stable dianions that are subsequently formed can be oxidized back by exposure to air (O_2 as oxidizing agent) (backward reaction), establishing a transient network. In earlier work, they demonstrated that the chemical fuel addition could control the assembly/ disassembly cycles in the redox system, which in turn affected the nucleation and growth of the supramolecular polymer (in a cooperative supramolecular polymerization mechanism), leading to different sizes and varying internal order of the final structures.[62] The neutral starting PDIs are partially soluble in water and overtime precipitate by forming π-stacked large colloidal assemblies. Initiated by the redox cycling, however, the PDIs could form helical assemblies with a hierarchical growth process of side-to-side fused assemblies. Although, after more than 7 redox cycles colloidal aggregates were formed again, when the system was not given time for growth. In this way, cycle-dependent pathway selection was achieved in a chemically fuelled redox system. Based on their results, it was concluded that strong kinetic barriers

can eventually be overcome via assembly cycles mediated by chemical fuels and that way strong hydrophobic assembling units, such as PDIs, can be efficiently used in aqueous media. The inherent non-linearities present in this system, i.e. a positive feedback from the nucleation–elongation–fragmentation process and a negative feedback arising from a size-dependent reduction/disassembly of the building block PDI, were seen as key ingredients for the design of their ultimate oscillating system. However, based on modelling results only the positive feedback and a linear chemically fuelled depolymerization sufficed in building the oscillator. In extension to the collective oscillations, they explored the spatiotemporal behaviour of the system and could generate travelling fronts and patterns in a rectangular chip with two parallel glass slides. Both phenomena were due to density differences in assembled and disassembled regions leading to a convection behaviour throughout the system. Remarkably, when compared to other oscillating systems this system is unique as the building blocks are responsible for both the non-linear dynamics and the assembling behaviour. Altogether, this work is seen as a major contribution to the research field, constituting a first step forward toward obtaining more life-like systems by the design of a self-oscillating supramolecular polymer system with large-scale self-organized patterns, reminiscent of most biological systems and observed in for example microtubules.

Another redox system was reported by George and co-workers, who used chemically fuelled viologen redox chemistry to induce conformational changes in an amphiphilic foldamer. The foldamer, consisting of a hydrophobic tail with a viologen-pyranine charge transfer (CT) pair connected through a hydrophilic glycol connector, initially remains in a folded conformation, while after reduction of the viologen moiety with sodium dithionite as a chemical fuel (forward reaction) no CT is possible anymore and it switches to an unfolded conformation. Oxidation of viologen by dissolved oxygen in water (backward reaction) reverts the system back to the original foldamer. However, control over more parameters for the backward reaction was achieved by coupling the oxidation of glucose to glucono-lactone catalysed by glucose oxidase to the redox cycle. The redox enzyme produces H_2O_2, which is a stronger oxidant than oxygen, and subsequent control over the enzyme kinetics led to control over the rate of refolding. Interestingly, by exploiting the transient (un)folding behaviour, switching of the final material structure between vesicles (in the folded state) and 2D-nanosheets (in the unfolded state) was achieved.[63]

Next to redox fuelling, George and co-workers also designed other chemically fuelled supramolecular polymer systems with enzymes to achieve rate control over single pathways. The first system uses ATP as a chemical fuel in combination with two enzymes to afford transient helicity in a supramolecular polymer with tuneable lifetime and

stereomutation rates (Figure 3.4B).[64] In detail, naphthalene diimides derivatives functionalized with zinc(II)-diethylenedipicolylamine (a receptor for adenosine phosphates) are deployed. Upon non-covalent binding with ATP they form a right-handed P-helix (forward reaction), while they form a left-handed M-helix with ADP (backward reaction). The supramolecular polymerization is based on charge neutralization (of zinc cations with phosphate anion) together with π-interactions and hydrophobic effects. To control both ATP formation and degradation pathways, two enzymes were used: creatine phosphokinase and hexokinase. The former generates ATP from phosphocreatine, while the latter uses ATP to phosphorylate glucose, yielding glucose-6-phosphate. Using this tandem enzyme approach, modulation of the kinetics was achieved and subsequent control over helix conformation of the supramolecular polymer, which was observed by CD monitoring of the system. Taking this approach one step further, in a follow-up work, George and co-workers extended the reaction network to realize multi non-equilibrium transient supramolecular polymerization depending on ATP, ADP or AMP binding, respectively.[65] Creatine phosphokinase was used in combination with alkaline phosphatase or apyrase. Binding to ADP leads to the generation of an M-helix (1st non-equilibrium state), while phosphorylation of ADP to ATP by creatine phosphokinase generates the P-helix (2nd non-equilibrium state), subsequent hydrolysis of ATP to ADP and finally to AMP, leads to the reformation of the P-helix with ADP or AMP, respectively (3rd non-equilibrium state). Finally, complete hydrolysis to inorganic phosphate leads to the formation of racemic stacks, as observed by CD and DLS. Additionally, with substitution of the alkaline phosphatase enzyme for apyrase and changing the substrate and enzyme concentrations, control over lifetime of different helices and rates of transient state formation and degradation were achieved. In extension, with this enzyme approach, George and co-workers also realized fuel-driven, temporally controlled supramolecular polymerization.[66] In order to do this, they changed the precursor into an extended π-conjugated monomer functionalized with two zinc(II)-diethylenedipicolylamine phosphate receptors. This molecule features an acceptor-donor-acceptor (A-D-A) electronic structure, which can reside in an intermolecular CT slip-stacked dormant state. Addition of ATP fuel (forward reaction) induces a reorganization of the chromophore and leads to the transition of the slipped CT dormant state to the π-stacked, facilitating elongated assembly into helical supramolecular polymers. Transient assembly is achieved by coupling the enzymatic ATP hydrolysis catalysed by apyrase (backward reaction). In addition, the system has a selectivity for ATP compared to other phosphate fuels and intermolecular hydrogen bonding of the respective adenine bases supports the elongation into a supramolecular polymer. Very interestingly, this system shows a seeded-growth mechanism, akin to actin polymerization, and further additions of ATP and monomer resulted in the addition on pre-grown stacks, instead of creating new nuclei. The seeded cooperative

polymerization was used to control the degree of polymerization and the dispersity. While the above systems from George access non-equilibrium states, it is important to note that fuel-to-waste conversion in these examples is not mediated by the building blocks and hence those system fall under assembly under dissipative conditions. Nevertheless, the systems of George stand out as excellent synthetic analogues of ATP fuelled biological systems.

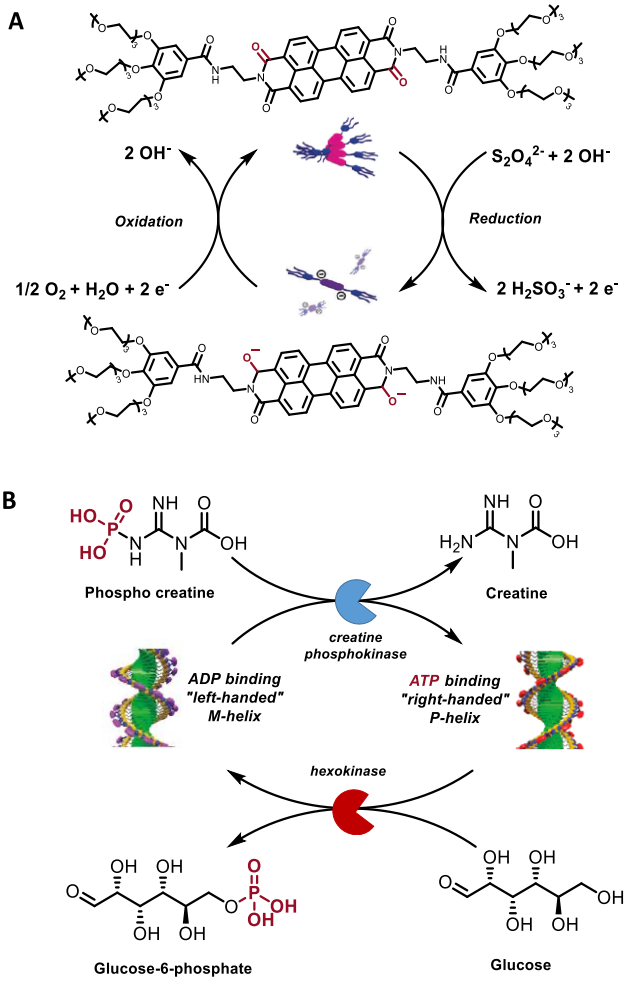

Figure 3.4: (A). Non-equilibrium supramolecular polymer system based on PDIs containing solubilizing ethylene glycol chains and hydrogen-bond forming amide groups. Chemical reduction by sodium dithionite ($Na_2S_2O_4$) (forward reaction) and subsequent oxidation by exposure to air (O_2 as oxidizing agent) (backward reaction), establishes a transient network with the formation of helical assemblies. Figure adapted from ref. (62). Copyright 2016 The Royal Society of Chemistry. **(B)**. Transient supramolecular polymer system based on naphthalene diimides derivatives functionalized with zinc(II)-diethylenedipicolylamine (a receptor for adenosine phosphates). Non-covalent binding with ATP leads to the formation of a right-handed P-helix, while binding to ADP generates an M helix. The ATP formation and degradation are regulated by creatine

phosphokinase, which generates ATP from phosphocreatine (forward reaction), while the ATP degradation is coupled to phosphorylation of glucose by hexokinase, yielding glucose-6-phosphate (backward reaction). Figure adapted from ref. (64).

Non-equilibrium supramolecular polymer systems based on a pH switching were also designed by Walther and co-workers. [67] They utilized a fast acidic activator (acidic buffer) in combination with a slow, biocatalytic, feedback-driven formation of a base ("dormant deactivator"), based on the urease-catalysed hydrolysis of urea to carbon dioxide and ammonia.[68, 69] The enzyme catalysis generates a non-linear time dependent pH change, realizing transient supramolecular polymerization of Fmoc protected dipeptide precursors. Decreasing the pH with the acidic activator leads to the formation of a supramolecular hydrogel, whereas a subsequent slow increase in the pH triggers the disassembly of the precursors. The transient pH profiles, regulated by amongst others the enzyme and urea concentration, were exploited to control the sol to gel transition. Additionally, they also designed a microfluidic system and could control different microfluidic channels by transient channel blocking.[67] The pH-switching approach was further deployed by the Walther group to program transient lifetimes into DNA duplexes[70], design pre-programmable DNA hydrogels with two enzymes with an antagonistic pH-modulating effect[71] and in a photonic device to realize autonomous transient memories, remotely regulated signal propagation and sensing[72].

Another interesting system where the pH plays a crucial role was developed by Miravet and co-workers. In this work, the hydrogel formation of an amide surfactant precursor was linked to the production of carbon dioxide (CO_2) by baker's yeast (*Saccharomyces cerevisiae*) indirectly fuelled by sucrose.[73] The microorganism consumes sucrose, which leads to the production of ethanol and CO_2. In the aqueous environment, the CO_2 is in equilibrium with bicarbonate, acidifying the solution. Protonation of the amphiphilic surfactant building blocks, constituting hydrogen bonding amino acids along with a pH sensitive N-acylated succinate part, results in surfactant assembly and the generation of a fibrillar network. However, as the dissolved CO_2 is always in equilibrium with the air, the gaseous CO_2 leaves the system over time. This leads to deprotonation of the building blocks, causing the hydrogel to disintegrate. This way, transient hydrogelation is achieved mediated by the microorganisms. Additionally, control over hydrogel lifetime was realized by varying the sucrose fuel and yeast concentration and the controlled release of CO_2 from the system, for example by changing the thickness of the cap.

A related system was developed by Besenius and co-workers, who designed transient thermoresponsive gels based on multi-stimuli responsive supramolecular polymerization.[74] Specifically, they deployed β-sheet forming dendritic peptide

monomers containing glutamic acid residues for pH responsiveness and methionine groups for redox responsiveness. Next to that, triethylene glycol chains were incorporated to give the material a thermoresponsive character. By coupling the glucose oxidase-catalysed oxidation of glucose to gluconolactone and H_2O_2 to the assembly process, they could obtain transiently stable supramolecular polymers by using a combination of pH and oxidation triggers, promoted by the release of reactive oxygen species (ROS). The pH shift was realized by slow conversion of gluconolactone to gluconic acid. First, the glucose oxidase catalysed glucose fuelled pH decrease leads to protonation of the glutamic acid residues, facilitating supramolecular polymerization. Secondly, the thioether groups of the methionine residues are oxidized to the more hydrophilic sulfoxide groups by the H_2O_2 (ROS) produced by glucose oxidase, which leads to subsequent collapse of the hydrogel. The gel properties, such as lifetime and stiffness, could be modulated by varying the enzyme and glucose fuel concentrations. Furthermore, by adding reductase repair enzymes the methionine sulfoxide groups were converted back to the thioether form, recovering the original building blocks. Using the same pH-redox responsive supramolecular polymerization chemistry, Besenius and co-workers also designed a peptide-polymer conjugate system of the ABA-type.[75] PEG polymers with varying chain length were fitted with hexapeptide sequences on both sides, which assemble into β-sheet like supramolecular nanorods in aqueous media. Methionine residues in the peptide chain were added for the redox sensitivity and histidine residues for the pH sensitivity. Transient supramolecular hydrogels were obtained by the production of ROS mediated by the glucose oxidase catalysed glucose oxidation. Interestingly, the system could remain operational in a completely autonomous reaction set-up, exhibiting tuneable gel lifetimes of 1–12 h. As ROS are important in a plethora of biological processes, the systems from the group of Besenius show a great potential for application in biological redox microenvironments.

Likewise, Sheiko and co-workers used the same glucose oxidase strategy to obtain time programmable cross-linked hydrogels. By varying the glucose oxidase concentration collapse of the gel network could be tuned from minutes to hours.[76] Other pH triggered transient systems, which will not be discussed in detail here, were developed by the groups of Kuehne (photonic and colloidal microgel systems)[77, 78], Che (redox-pH triggered system)[79], Liu (pH oscillator based on BrO_3-SO_3^{2-}-$Fe(CN)_6^{4-}$)[80], Adams (urease and methyl formate)[81] and Montenegro (base triggered system)[82].

While merely based on solubility principles, Escuder and Araújo designed a triazole-based gelator system capable of forming transient gels in the presence of a copper catalyst in a biphasic system.[83] A “click” reaction between benzylazide and phenylacetylene leads to the formation of the triazole and subsequent supramolecular

polymerization of the amphiphilic gelator, forming a copper(I) coordinated gel. The addition of extra reactants to the metallogel creates a hydrophobic environment that promotes the disassembly of the gel and solubilisation in the apolar organic solvent phase. Upon consumption of the added reactants by the "click reaction" the hydrophobicity of the system is lowered again, leading to subsequent reassembly of the gel. The construction of the metallogel could be repeated for three consecutive times. In this example, however, the non-equilibrium state arises from solubility-driven assembly instead of chemical fuel consumption mediated by the building blocks.

In the quest to obtain adaptive life-like behaviour and inspired by the multitude of cellular functions of microtubules and actin filaments, Huck and co-workers designed a supramolecular polymer system capable of dissipative adaptation[84] and formation of dynamic nanostructures[85]. In detail, they showed the dissipative assembly of FtsZ protein filaments (a bacterial homologue of tubulin) fuelled by GTP within membraneless coacervate compartments. The dissipative adaptation, mediated by dissipative assembly inside the compartments, is a result of a reaction-driven flux of molecules across the interface into the compartment, which ultimately determines the local access to energy from the environment. Fascinatingly, modelling studies demonstrated that the asymmetric distribution of filaments within the compartments can result in a capillary driving force and droplet splitting, analogous to cell division. The asymmetric growth and shrinkage are a direct consequence of the local higher availability of high-energy FtsZ-GTP precursors at the end of the fibrils within the droplets, resulting in supramolecular polymerization and growing filaments. This leads to elongated coacervate droplets and a subsequent change of their shape. On the other hand, the irreversible hydrolysis of GTP to GDP brings about the energy dissipation, causing depolymerization and the disintegration of the oldest filaments in the centre of the fibrils, which eventually leads to splitting of the coacervate droplets. Although the building blocks in this system are not man-made, it is intelligently shown that encapsulation of dissipative elements in open compartments promotes dynamic behaviour of growing and dividing nanostructures capable of dissipative adaption and thus showing life-like behaviour.

Although not strictly forming transient 1D-aggregates, we like to highlight three more smartly designed recent literature examples, where the consumption of fuels drives assembly. Taking inspiration from biology, Franco and Agarwal designed an enzyme-driven DNA-RNA nanosystem capable of controlled assembly/ disassembly at physiological temperature.[86] To this end, they engineered double crossover (DX) DNA tiles building blocks that by addition of RNA fuel could be activated and assemble in micron-long nanotubes. Isothermal control over the kinetics of the distinctive assembly

and disassembly pathways of the DNA-RNA nanostructures was realized by regulating the enzymatic production and decay of tile activation by RNA in transcriptional programmes. Additionally, the RNA fuel production rate could be modulated by changing the promoter sequence, the template, the nucleoside triphosphate fuel (needed for RNA polymerase to produce RNA) or the enzyme concentration. On the other hand, the RNA degradation pathway was controlled by the RNase H concentration, by inclusion of other RNA-degrading enzymes or chemical modification of several nucleobases of the DNA tiles. Unfortunately, the system was limited to only one assembly/ disassembly cycle, as it proved impossible to initiate reassembly after the disassembly promoted by RNase H. This is likely due to the fact that the RNA strands are not fully degraded by RNase H. An incomplete hydrolysis can result in the build-up of small bound RNA molecules to the inactive tiles, creating "waste" tiles that become inaccessible for the RNA trigger. Overall, with this DNA-RNA hybrid dynamic nanosystem they cleverly take advantage of both the stability of DNA systems and the natural roles of RNA molecules in biology, which is seen as a starting point for the design of nanomachines in biological environments.

Liu and co-workers designed a I_2-responsive supra-amphiphile system with a PEGylated poly(amino acid)[87], based on earlier work by Zhang and co-workers[88]. Dissipative assembly was achieved in a batch reactor by coupling to a redox reaction of $NaIO_3$ and thiourea, a well-known chemical oscillator that transiently produces I_2. Reduction of the $NaIO_3$ fuel produces I_2 (forward reaction), which can coordinate to the PEG segment, increases its hydrophobicity and leads to formation and assembly of the supra-amphiphile. Subsequently, the reduction of the I_2 by thiourea, the second chemical fuel, (backward reaction), leads to the disassembly of the supra-amphiphile and disappearance of the aggregates, as observed by time-dependent DLS measurements. As an interesting application example, when the PEG segments are grafted on multiwalled carbon nanotubes in water, upon addition of the chemical fuels their transient aggregation can remove organic impurities from water.

Another transient assembling system was designed by Lee and co-workers.[89] In their system, non-assembling substrates are used as chemical fuels and drive the transient membrane assembly of a pyridine-based amphiphile, based on enhanced hydrophobic interactions. This way, a confined space is generated for acceleration of an aromatic nucleophilic substitution reaction in water. The reaction generates a hydrophobic product and an acid by-product. The latter species in turn protonates the pyridine-based amphiphile, promoting disassembly and concomitant release of the product. Subsequent neutralization with K_2CO_3 of the pyridine moiety can instigate a new assembly/ disassembly cycle with substrate entrapment followed by product release.

This is a cleverly designed system, where an irreversible chemical reaction in confined space is responsible for the dynamic membrane assembly/ disassembly process.

3.6 CONCLUSION AND OUTLOOK

As witnessed by the growing number of chemically fuelled dissipative supramolecular polymer systems designed by different groups, it becomes clear that this young research area is highly important. In this chapter, we have first explained the basics of supramolecular polymerization by quickly recapping the different mechanisms and categorizing the different non-equilibrium states. Afterwards, we have introduced non-linear behaviour in biology, as a great inspiration source for artificial system designs. Next, the energy landscape of supramolecular polymerization was extensively discussed along with the nature of the chemical fuel and a careful examination of the assembly terminology, disclosing the importance of kinetic asymmetry in chemical fuel-driven non-equilibrium systems.[37, 40]

In the different literature examples, we have observed a multitude of non-covalent interactions governing the transient supramolecular polymerization of the mostly initially soluble building blocks. Not for all systems the polymerization mechanism was reported or investigated, but in most cases the building blocks assembled via a cooperative mechanism. We have seen systems with different chemical fuel integration strategies and precursors varying from natural building blocks, such as peptide sequences or DNA, to completely artificial molecules. As a key element usually a change in hydrophobicity of the precursors coupled to an irreversible chemical reaction (the consumption of the chemical fuel) brought about the desired transient assembly behaviour. Moreover, a thermodynamic analysis revealed that the production rate of entropy is a measure of energy dissipation in such systems with gels dissipating the maximum amount of free energy to increase their hierarchical order[48, 49]. Overall, dissipative systems have been designed using natural nucleoside triphosphates as popular fuel candidates, with assistance of catalysis by enzymes, based on redox chemistry or with a cleverly build-in pH-switch.

The next challenge these days is to not only design the dissipative systems, but also provide them with dynamic functions, reminiscent of life-like structures. The first examples of such systems were reported recently by the groups of Ulijn with the formation of transient conducting nanostructures[59], Hermans with a self-oscillating supramolecular polymer system[61] and Huck with supramolecular polymers capable of dissipative adaptation[85]. It is expected that more advanced systems with dynamic functionalities based on chemical fuel consumption will follow to ultimately arrive at the *de novo* synthesis of life. One of the other big challenges in this field is the maintenance of the non-equilibrium state by the continuous supply of energy. This will enable the investigation and application of properties specific to non-equilibrium states and

analyse if a system truly resides out-of-equilibrium. Currently, only few examples of continuous fuel supply systems have been reported and design of more systems of this kind would give more insight in the behaviour of non-equilibrium steady states and could lead to uncommon phenomena, such as chaotic behaviour or bifurcations. Finally, obtaining a higher degree of control over non-equilibrium systems is highly desirable. Here, one could think of pathway biasing in the chemical reaction network by using catalysts or even triggered pre-catalysts[90, 91], or coupling different fuel-driven chemical reaction networks. All in all, while chemically fuelled dissipative supramolecular polymer systems are less than a decade old, they are recognized as one of the key elements to design man-made dynamic and controllable systems, which hold great promise for future applications.

3.7 REFERENCES

1. G. M. Whitesides and B. Grzybowski, *Science*, 2002, **295**, 2418-2421.
2. T. F. De Greef, M. M. Smulders, M. Wolffs, A. P. Schenning, R. P. Sijbesma and E. Meijer, *Chem. Rev.*, 2009, **109**, 5687-5754.
3. L. Brunsveld, B. Folmer, E. W. Meijer and R. Sijbesma, *Chem. Rev.*, 2001, **101**, 4071-4098.
4. T. Aida, E. Meijer and S. I. Stupp, *Science*, 2012, **335**, 813-817.
5. J.-M. Lehn, *Eur. Rev.*, 2009, **17**, 263-280.
6. D. Spitzer and P. Besenius, in *Supramolecular Chemistry in Water*, ed. W.-V. V. G. Co, First Edition edn., 2019, ch. 8 pp. 285-336.
7. H. Staudinger, *Dtsch. Chem. Ges. B*, 1920, **53**, 1073.
8. W. H. Carothers, *Chem. Rev.*, 1931, **8**, 353-426.
9. C. Fouquey, J. M. Lehn and A. M. Levelut, *Adv. Mater.*, 1990, **2**, 254-257.
10. P. J. Flory, *Principles of polymer chemistry*, Cornell University Press, 1953.
11. M. M. Smulders, M. M. Nieuwenhuizen, T. F. de Greef, P. van der Schoot, A. P. Schenning and E. Meijer, *Chem. Eur. J.*, 2010, **16**, 362-367.
12. A. Cifferi, *Supramolecular Polymers*, 6th edition edn., 2005.
13. F. Rakotondradany, M. Whitehead, A. M. Lebuis and H. F. Sleiman, *Chem. Eur. J.*, 2003, **9**, 4771-4780.
14. A. Sorrenti, J. Leira-Iglesias, A. J. Markvoort, T. F. de Greef and T. M. Hermans, *Chem. Soc. Rev.*, 2017, **46**, 5476-5490.
15. P. Besenius, *J. Polym. Sci., Part A: Polym. Chem.*, 2017, **55**, 34-78.
16. J. Matern, Y. Dorca, L. Sánchez and G. Fernández, *Angew. Chem. Int. Ed.*, 2019, **58**, 16730-16740.
17. S. Dhiman and S. George, *Bull. Chem. Soc. Jpn.*, 2018, **91**, 687-699.
18. S. Dhiman, A. Sarkar and S. George, *RSC Adv.*, 2018, **8**, 18913-18925.
19. S. A. P. van Rossum, M. Tena-Solsona, J. H. van Esch, R. Eelkema and J. Boekhoven, *Chem. Soc. Rev.*, 2017, **46**, 5519-5535.
20. G. Ashkenasy, T. M. Hermans, S. Otto and A. F. Taylor, *Chem. Soc. Rev.*, 2017, **46**, 2543-2554.
21. E. Mattia and S. Otto, *Nat. Nanotechol.*, 2015, **10**, 111.
22. B. A. Grzybowski and W. T. Huck, *Nat. Nanotechol.*, 2016, **11**, 585.
23. R. F. Ludlow and S. Otto, *Chem. Soc. Rev.*, 2008, **37**, 101-108.
24. F. della Sala, S. Neri, S. Maiti, J. L. Chen and L. J. Prins, *Curr. Opin. Biotechnol.*, 2017, **46**, 27-33.
25. A. Pross, *Pure Appl. Chem.*, 2005, **77**, 1905-1921.
26. R. Astumian, *Faraday Discuss.*, 2017, **195**, 583-597.
27. R. Pascal and A. Pross, *J. Syst. Chem.*, 2014, **5**, 3.
28. R. Pascal, A. Pross and J. D. Sutherland, *Open Biol.*, 2013, **3**, 130156.
29. A. Pross, *J. Syst. Chem.*, 2011, **2**, 1.
30. B. Houchmandzadeh and M. Vallade, *Phys. Rev. E*, 1996, **53**, 6320.
31. E. M. Mandelkow and E. Mandelkow, *Cytoskeleton*, 1992, **22**, 235-244.
32. O. Valiron, N. Caudron and D. J. Job, *Cell. Mol. Life Sci.*, 2001, **58**, 2069-2084.

33. B. Alberts, A. Johnson, J. Lewis, D. Morgan, M. Raff, K. Roberts and P. Walter, *Molecular biology of the cell*, Garland Science, New York, Sixth edition edn., 2014.
34. D. Kondepudi and I. Prigogine, *Modern thermodynamics: from heat engines to dissipative structures*, John Wiley & Sons, 2014.
35. F. Tantakitti, J. Boekhoven, X. Wang, R. V. Kazantsev, T. Yu, J. Li, E. Zhuang, R. Zandi, J. H. Ortony and C. J. Newcomb, *Nat. Mater.*, 2016, **15**, 469.
36. P. A. Korevaar, S. J. George, A. J. Markvoort, M. M. Smulders, P. A. Hilbers, A. P. Schenning, T. F. De Greef and E. Meijer, *Nature*, 2012, **481**, 492.
37. G. Ragazzon and L. Prins, *Nat. Nanotechol.*, 2018, **13**, 882–889.
38. B. Belousov, *Medgiz, Moscow*, 1958, **145**.
39. A. M. Zhabotinsky, *Proc. Acad. Sci. USSR*, 1964, **157**, 392-395.
40. R. D. Astumian, *Nat. Commun.*, 2019, **10**, 3837
41. R. D. Astumian, *Nat. Nanotechol.*, 2012, **7**, 684.
42. R. D. Astumian, *Annu. Rev. Biophys. Bioeng.*, 2011, **40**, 289-313.
43. R. D. Astumian and M. Bier, *Biophys. J.*, 1996, **70**, 637-653.
44. R. D. Astumian, *Phys. Chem. Chem. Phys.*, 2007, **9**, 5067-5083.
45. M. Alvarez-Pérez, S. M. Goldup, D. A. Leigh and A. M. Slawin, *J. Am. Chem. Soc.*, 2008, **130**, 1836-1838.
46. J. Boekhoven, W. E. Hendriksen, G. J. M. Koper, R. Eelkema and J. H. van Esch, *Science*, 2015, **349**, 1075-1079.
47. J. Boekhoven, A. M. Brizard, K. N. K. Kowlgi, G. J. M. Koper, R. Eelkema and J. H. van Esch, *Angew. Chem. Int. Ed.*, 2010, **122**, 4935-4938.
48. A. Arango-Restrepo, J. M. Rubi and D. Barragan, *J. Phys. Chem. B*, 2018, **122**, 4937-4945.
49. A. Arango-Restrepo, J. M. Rubi and D. Barragán, *J. Phys. Chem. B*, 2019, **123**, 5902–5908.
50. S. B. Nicholson, R. A. Bone and J. R. Green, *J. Phys. Chem. B*, 2019, **123**, 4792–4802.
51. M. Tena-Solsona, B. Rieß, R. K. Grötsch, F. C. Löhrer, C. Wanzke, B. Käsdorf, A. R. Bausch, P. Müller-Buschbaum, O. Lieleg and J. Boekhoven, *Nat. Commun.*, 2017, **8**, 15895.
52. M. Tena-Solsona, C. Wanzke, B. Riess, A. R. Bausch and J. Boekhoven, *Nat. Commun.*, 2018, **9**, 2044.
53. L. S. Kariyawasam and C. S. Hartley, *J. Am. Chem. Soc.*, 2017, **139**, 11949–11955.
54. B. Zhang, I. M. Jayalath, J. Ke, J. L. Sparks, C. S. Hartley and D. J. C. c. Konkolewicz, *Chem. Commun.*, 2019, **55**, 2086-2089.
55. S. Bal, K. Das, S. Ahmed and D. Das, *Angew. Chem. Int. Ed.*, 2019, **58**, 244-247.
56. P. Solís Muñana, G. Ragazzon, J. Dupont, C. Z. J. Ren, L. J. Prins and J. L. Y. Chen, *Angew. Chem. Int. Ed.*, 2018, **57**, 16469-16474.
57. S. Debnath, S. Roy and R. V. Ulijn, *J. Am. Chem. Soc.*, 2013, **135**, 16789-16792.
58. C. G. Pappas, I. R. Sasselli and R. V. Ulijn, *Angew. Chem. Int. Ed.*, 2015, **54**, 8119-8123.
59. M. Kumar, N. L. Ing, V. Narang, N. K. Wijerathne, A. I. Hochbaum and R. V. Ulijn, *Nat. Chem.*, 2018, **10**, 696.
60. A. Sorrenti, J. Leira-Iglesias, A. Sato and T. M. Hermans, *Nat. Commun.*, 2017, **8**, 15899.
61. J. Leira-Iglesias, A. Tassoni, T. Adachi, M. Stich and T. M. Hermans, *Nat. Nanotechol.*, 2018, **13**, 1021.
62. J. Leira-Iglesias, A. Sorrenti, A. Sato, P. A. Dunne and T. M. Hermans, *Chem. Commun.*, 2016, **52**, 9009-9012.
63. K. Jalani, S. Dhiman, A. Jain and S. George, *Chem. Sci.*, 2017, **8**, 6030-6036.
64. S. Dhiman, A. Jain and S. J. George, *Angew. Chem. Int. Ed.*, 2017, **129**, 1349-1353.
65. S. Dhiman, A. Jain, M. Kumar and S. George, *J. Am. Chem. Soc.*, 2017, **139**, 16568-16575.
66. A. Mishra, D. B. Korlepara, M. Kumar, A. Jain, N. Jonnalagadda, K. K. Bejagam, S. Balasubramanian and S. George, *Nat. Commun.*, 2018, **9**, 1295.
67. T. Heuser, E. Weyandt and A. Walther, *Angew. Chem. Int. Ed.*, 2015, **54**, 13258-13262.
68. E. Jee, T. Bánsági, A. F. Taylor and J. A. Pojman, *Angew. Chem. Int. Ed.*, 2016, **55**, 2127-2131.
69. G. Hu, J. A. Pojman, S. K. Scott, M. M. Wrobel and A. F. Taylor, *J. Phys. Chem. B*, 2010, **114**, 14059-14063.
70. L. Heinen and A. Walther, *Chem. Sci.*, 2017, **8**, 4100-4107.
71. L. Heinen, T. Heuser, A. Steinschulte and A. Walther, *Nano Lett.*, 2017, **17**, 4989-4995.
72. T. Heuser, R. Merindol, S. Loescher, A. Klaus and A. Walther, *Adv. Mater.*, 2017, **29**, 1606842.
73. C. A. Angulo-Pachón and J. F. Miravet, *Chem. Commun.*, 2016, **52**, 5398-5401.
74. D. Spitzer, L. L. Rodrigues, D. Straßburger, M. Mezger and P. Besenius, *Angew. Chem. Int. Ed.*, 2017, **56**, 15461-15465.
75. R. Otter, C. M. Berac, S. Seiffert and P. Besenius, *Eur. Polym. J.*, 2019, **110**, 90-96.
76. K. Hu and S. Sheiko, *Chem. Commun.*, 2018, **54**, 5899-5902.
77. D. Go, D. Rommel, L. Chen, F. Shi, J. Sprakel and A. J. Kuehne, *Langmuir*, 2017, **33**, 2011-2016.
78. D. Go, D. Rommel, Y. Liao, T. Haraszti, J. Sprakel and A. J. Kuehne, *Soft matter*, 2018, **14**, 910-915.
79. Y. Liu, L. Liu, E. Zhu, M. Yue, C. Gao, X. Wu, G. Che and H. Liu, *ChemPlusChem*, 2018, **83**, 1109-1118.

80. G. Wang, Y. Liu, N. Xia, W. Zhou, Q. Gao and S. Liu, *Colloids Surf. A Physicochem. Eng. Asp.*, 2017, **529**, 808-814.
81. S. Panja, C. Patterson and D. J. Adams, *Macromol. Rapid Commun.*, 2019, **40**, 1900251.
82. A. Méndez-Ardoy, J. R. Granja and J. Montenegro, *Nanoscale Horiz.*, 2018, **3**, 391-396.
83. M. Araujo and B. Escuder, *ChemistrySelect*, 2017, **2**, 854-862.
84. J. L. England, *Nat. Nanotechol.*, 2015, **10**, 919.
85. E. Te Brinke, J. Groen, A. Herrmann, H. A. Heus, G. Rivas, E. Spruijt and W. T. Huck, *Nat. Nanotechol.*, 2018, **13**, 849.
86. S. Agarwal and E. Franco, *J. Am. Chem. Soc.*, 2019, **141**, 7831–7841.
87. G. Wang, J. Sun, L. An and S. Liu, *Biomacromolecules*, 2018, **19**, 2542-2548.
88. G. Wang, B. Tang, Y. Liu, Q. Gao, Z. Wang and X. Zhang, *Chem. Sci.*, 2016, **7**, 1151-1155.
89. H. Wang, Y. Wang, B. Shen, X. Liu and M. Lee, *J. Am. Chem. Soc.*, 2019, **141**, 4182–4185.
90. F. Trausel, C. Maity, J. M. Poolman, D. Kouwenberg, F. Versluis, J. H. van Esch and R. Eelkema, *Nat. Commun.*, 2017, **8**, 879.
91. C. Maity, F. Trausel and R. Eelkema, *Chem. Sci.*, 2018, **9**, 5999-6005.

ORGANOCATALYTIC CONTROL OVER A TRANSIENT ESTERIFICATION NETWORK

CHAPTER 4

Signal transduction in living systems is the conversion of information into a chemical change, and is the principal process by which cells communicate. In nature, these functions are encoded in non-equilibrium (bio)chemical reaction networks (CRNs) controlled by enzymes. However, man-made catalytically controlled networks are rare. We incorporated catalysis into an artificial fuel-driven out-of-equilibrium CRN, where the forward (ester formation) and backward (ester hydrolysis) reactions are controlled by varying the ratio of two organocatalysts: pyridine and imidazole. This catalytic regulation enables full control over ester yield and lifetime. This fuel-driven strategy was expanded to a responsive polymer system, where transient polymer conformation and aggregation are controlled through fuel and catalyst levels. Altogether, we show that organocatalysis can be used to control a man-made fuel-driven system and induce a change in a macromolecular superstructure, as in natural non-equilibrium systems.

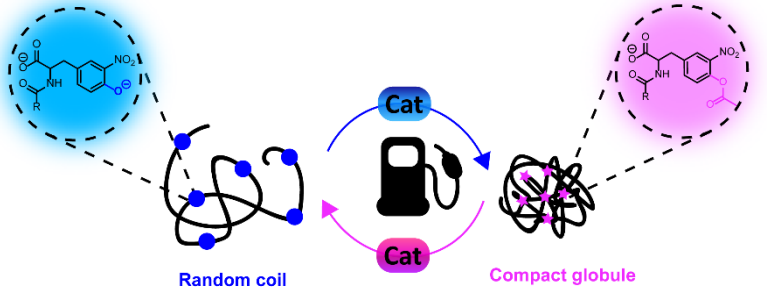

This chapter is published as:
M.P. van der Helm, C.-L. Wang, B. Fan, M. Macchione, E. Mendes R. Eelkema,
Angew. Chem. Int. Ed., 2020, **59**, 20604-20611.

4.1 INTRODUCTION

Signal transduction in living systems is the conversion of information into a chemical change and the primary process by which living cells are able to communicate over micrometre distances. Cells harbour very specific and sensitive signal-transducing mechanisms, which are regulated by membrane-bound protein receptors that respond to external signals such as antigens, light, hormones, pathogens, hypoxia, pheromones, amongst others.[1] This rudimentary communication enables functions such as time keeping and signal-amplification, which are encoded in non-equilibrium (bio)chemical reaction networks (CRNs) regulated by enzymes.[2-4] As such, out-of-equilibrium systems are an integral part of biological pathways and most complex living systems need the constant input of a chemical fuel to sustain themselves. The fuel is typically a high-energy bond molecule, e.g. adenosine triphosphate (ATP), guanosine triphosphate (GTP) or acyl-coenzyme A (acyl-CoA). For example, the latter fuel together with two enzymes plays a key role in histone (de)acetylation, which regulates gene activity and is recognized as a very important process in epigenetics.[5-7] Overall, catalysis is crucial in non-equilibrium biological CRNs and can turn ON and OFF the complete process. Inspired by catalytically controlled natural processes, we set out to design a man-made catalytically controlled out-of-equilibrium network. Successful fuel-driven CRNs have been designed before with direct (fuel integration in the building block) and indirect (fuel consumption without structure integration) chemical fuels, providing spatiotemporal control over material formation and exhibiting non-linear behaviour, such as stochastic collapse or oscillations.[8-23] Yet, the incorporation of catalysis as a control switch to regulate formation and degradation rates of a transient product in a non-equilibrium CRN has only been investigated to a limited extent. Examples using enzyme catalysis in fuel-driven CRNs exist[4, 14, 19, 23] and some recent examples of cooperative catalysis have been reported, yet those typically involve the building blocks as catalysts[24, 25]. In the current work however, we use two external catalysts in parallel to control the reaction kinetics of the CRN. Instead of enzymatic or metal-based catalysis we turned to organocatalysis. Compared to enzymes and metal-based catalysts, organocatalysts are frequently less active, but also simple, often less toxic, easily accessible, less substrate specific and deemed particularly useful to enhance the efficiency of chemical reaction networks[26, 27]. For applications in soft materials or otherwise crowded environments, organocatalysts also have a higher diffusive mobility and higher environmental tolerance than enzymes. Small molecule organocatalysts are used for a myriad of synthesis reactions and can be used in aqueous environment (chapter 2)[27]. Here, we show how two organocatalysts can be used together to control the yield and lifetime of a transiently stable product in a fuel-driven esterification CRN. First, we explain the system design and characteristics. Then, we show the performance of the system with a small molecule model CRN and investigate the reaction kinetics.

Finally, we apply the same organocatalysed fuel-driven strategy to control the shape of an amino acid functionalized polymer system by transient (de)acetylation, showing temporal regulation over polymer chain conformation and aggregation behaviour.

4.2 RESULTS AND DISCUSSION

4.2.1 Choice of fuel-driven CRN and reaction conditions

We designed a CRN, where the forward reaction (ester formation) can be accelerated by pyridine and the backward reaction by imidazole (ester hydrolysis) (Scheme 4.1). Acetic anhydride **2** is used as a direct chemical fuel, which reacts with the starting material (*p*-nitrophenol(ate) **1**) generating the product for the transient state (*p*-nitrophenyl ester **3**) and acetic acid as waste **4** (Scheme 4.1).

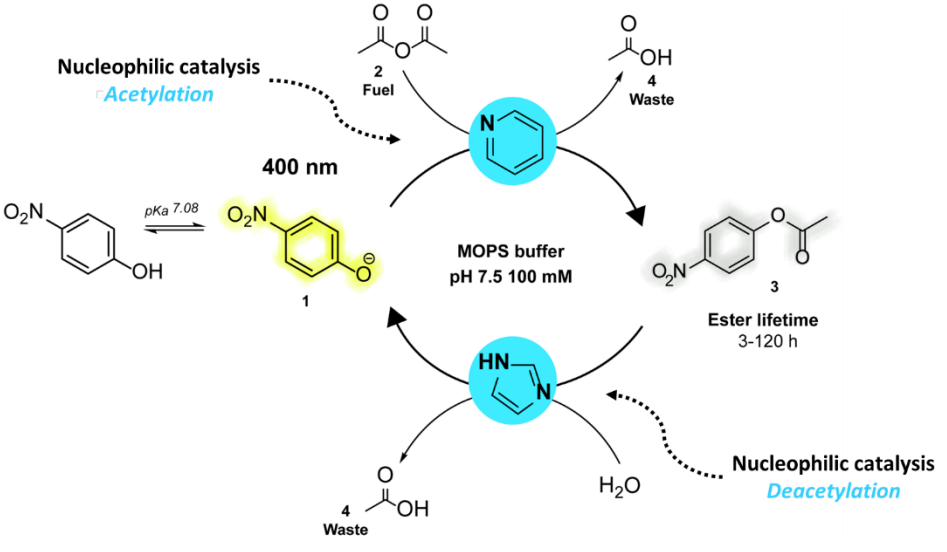

Scheme 4.1: Fuel-driven out-of-equilibrium esterification CRN, where the formation and degradation pathways can be controlled by different nucleophilic catalysts: the rate of ester formation is accelerated by pyridine and the backward ester hydrolysis reaction by imidazole.

Pyridine is a versatile tertiary amine organocatalyst, used in a plethora of everyday synthesis reactions. In particular, *O*-acetylation is typically carried out with DMAP or pyridine as organocatalyst.[28] Here, pyridine acts as nucleophilic catalyst (Lewis base – with nucleophilicity index of *N* 11.05 in water[29]), creating a reactive intermediate with acetic anhydride **2**: the acetyl-pyridinium species. The pK_a of pyridine is 5.2 meaning that at neutral pH the free base species is dominant.[30] In contrast, imidazole is known as an effective catalyst for the hydrolysis of activated esters such as *p*-nitrophenyl acetate.[31-33] The imidazole catalytic cycle proceeds through an acetyl-imidazole reactive

intermediate and the catalytic mechanism of imidazole depends on the leaving group strength of imidazole versus the –OR group.[34] Esters with weak leaving groups are subject to general base catalysis, whereas for activated esters with better leaving groups (here: nitro-phenolates) the imidazole catalysis exhibits a nucleophilic substitution mechanism.[31, 33] Additionally, the nucleophilic catalysis of imidazole (pK_a 6.9) is pH-dependent and favours higher pH, since more free base is present.[35, 36] Imidazole has a higher basicity than pyridine, yet the nucleophilicity is lower (*N* 9.63 in water [37]). Overall, imidazole has a preference for less reactive acylation agents (activated esters) compared to pyridine, which is a better catalyst for highly reactive acylation agents (anhydrides).[38, 39] The latter is exploited in this fuel-driven CRN to control the temporal acetylation of *p*-nitrophenol(ate) **1**. Experiments are performed at near neutral pH 7.5 in a strongly buffered system to take care of the acid waste. At pH 7.5 the phenolate is dominant over the phenol form, and the uncatalysed ester and anhydride hydrolysis are less prevalent than at more acidic or basic conditions.

4.2.2 Organocatalysed fuel-driven esterification CRN

In this CRN, *p*-nitrophenol(ate) **1** is acetylated with acetic anhydride **2** to generate ester **3**, which is hydrolytically unstable and over time the phenol(ate) **1** is regenerated along with forming acetic acid waste product **4**. Pyridine and imidazole are used as organocatalysts to accelerate the ester formation and hydrolysis. We varied the organocatalysts and fuel concentrations to achieve yield and lifetime variations in the transient *p*-nitrophenyl ester **3** (Figure 4.1 – shows the conversion of **1** monitored by UV-VIS at 400 nm). While a blank reaction without organocatalysts resulted in ester lifetimes of ~68 h and a max. yield of 55% after 25 min (Supplementary Figure S4.7), increasing the pyridine concentration accelerated the forward reaction (Figure 4.1A - zoomed-in region of the first 3 min) and augmented the overall ester yield (Figure 4.1A). Supply of more pyridine than anhydride **2** (0.5 mM) however did not give any effect in yield and only a very minor increase in the forward reaction by reaching the plateau-level a few seconds earlier as shown in Figure 4.1A. This observation supports the nucleophilic catalytic mechanism for pyridine, reacting directly with the anhydride and forming the reactive acetyl-pyridinium intermediate. Similarly, the ester degradation could be very precisely controlled with imidazole (Figure 4.1B). When imidazole is absent, the ester is stable for over 120 h (with a yield close to 100% after 25 min), whereas increasing the imidazole concentration leads to lower ester yields and shorter lifetimes, varying from 3 to 120 h. The amount of fuel provides another way to control the ester formation and lifetime. Logically, addition of more fuel results in higher ester yields and lifetimes as shown in Figure 4.1C. On top of that, multiple fuel cycles could be performed sequentially (Figure 4.1D). Fresh fuel was added for three consecutive times and the reaction cycle was completely repeatable and robust.

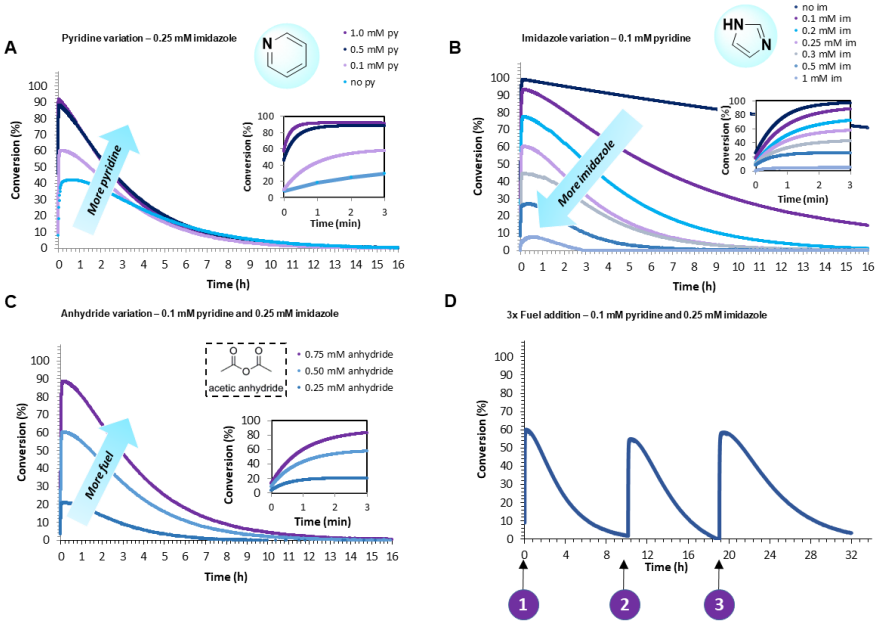

Figure 4.1: Fuel-driven esterification network controlled by organocatalysts pyridine and imidazole in MOPS buffer (100 mM, pH 7.5) with 5% acetonitrile. The conversion of *p*-nitrophenol(ate) **1** is monitored by UV-VIS, following the absorbance at 400 nm over time. A zoomed-in region of the first 3 min (0.05 h) of the reaction is shown for the pyridine, imidazole and anhydride variation plots. **(A).** Pyridine variation: 0.1 mM *p*-nitrophenol **1**, 0.5 mM acetic anhydride **2**, 0.25 mM imidazole and varying 0-1.0 mM pyridine. **(B)**. Imidazole variation: 0.1 mM *p*-nitrophenol **1**, 0.5 mM acetic anhydride **2**, 0.1 mM pyridine and varying 0-1.0 mM imidazole. **(C)**. Acetic anhydride **2** variation: 0.1 mM *p*-nitrophenol **1**, varying 0.25-0.75 mM acetic anhydride **2**, 0.25 mM imidazole and 0.1 mM pyridine. **(D)**. Three consecutive fuel cycles: 0.1 mM *p*-nitrophenol **1**, 0.5 mM acetic anhydride **2**, 0.25 mM imidazole and 0.1 mM pyridine. The second and third cycles were initiated by addition of a new batch of fuel **2**.

HPLC-MS data confirmed the formation and degradation of **3** in the fuel cycle (Supplementary Figures S4.8-12). Additionally, monitoring the colour change of the fuel cycle over time (Supplementary Figure S4.13) proves the successful formation (yellow to colourless solution) and subsequent degradation of the ester (colourless to yellow solution), while the pH is stable (Supplementary Figure S4.14). Nonetheless, the drawbacks of this system are the rapid hydrolysis of the acetic anhydride **2** fuel in water (hydrolysis rate constant 0.1575 min^{-1} [40]), resulting that after 30 min only the backward reaction remains. Also, the generation of twice as much acetic acid as waste limits the amount or number of fuel additions and calls for a strongly buffered system. Therefore, other activated carboxylic acids (i.e. vinyl acetate, isopropenyl acetate) were also tested. Yet, they were not efficient (> 500 fuel equivalents were required) and besides did not dissolve well in the water phase (Supplementary Figure S4.15 and Table S4.1).

In order to understand the underlying reaction mechanisms and the role of the catalysts in the rate accelerations, a kinetic model was developed and numerically solved with MATLAB software (see Supplementary information for full explanation, reaction equations and mechanism). In this simplified model it was assumed that both pyridine and imidazole catalyse the ester formation, hydrolysis and anhydride hydrolysis (Figure 4.2A). The preference for imidazole for ester hydrolysis and pyridine for ester formation is expressed in the value of the rate constants. The imidazole catalysed ester hydrolysis rate constant was determined experimentally and all other constants were taken from the literature (both used as initial guesses) or optimized by the kinetic model with experimental data input. In Figure 4.2 (and Supplementary Figures S4.20-22) the experimental data are compared with the modelled data. The model predicts the experimental data accurately for varying fuel (Figure 4.2B) and organocatalyst concentrations (Figure 4.2C). Also, in extreme situations where only one of the catalysts is present, the model prediction with the simplified CRN matches with the experiments (Figure 4.2D). Only for high imidazole concentrations the model starts to deviate from the experimental data (Figure 4.2C and Supplementary Figure S4.21F). We expect that this deviation is due to the presence of the acetyl-imidazole species, which is not consumed immediately, and hence the experimental data show a more gradual decay than the model. In this simplified model, it was assumed that the reactive intermediates are unstable and hence were not taken into account.

Furthermore, when comparing the reaction rates for ester **3** formation and degradation (Supplementary Figures S4.23-24) it becomes clear that the formation reaction vanishes quickly (Supplementary Figure S4.24 - after 10-20 min), around the time when most of the fuel **2** is consumed, while the backward reaction is active for hours. Imidazole is responsible for an increase in the backward reaction rate (Supplementary Figures S4.23A,B and S4.24A,B), while in the presence of pyridine the forward reaction rate is increased (Supplementary Figure S4.24A,C – steeper slopes) and anhydride **2** is consumed faster. Within the limits of the model, transient nitrophenol acetylation is accurately described by the model, corroborating the proposed simplified catalytic CRN. Also, it allows prediction of ester yield and lifetime based on the catalyst input.

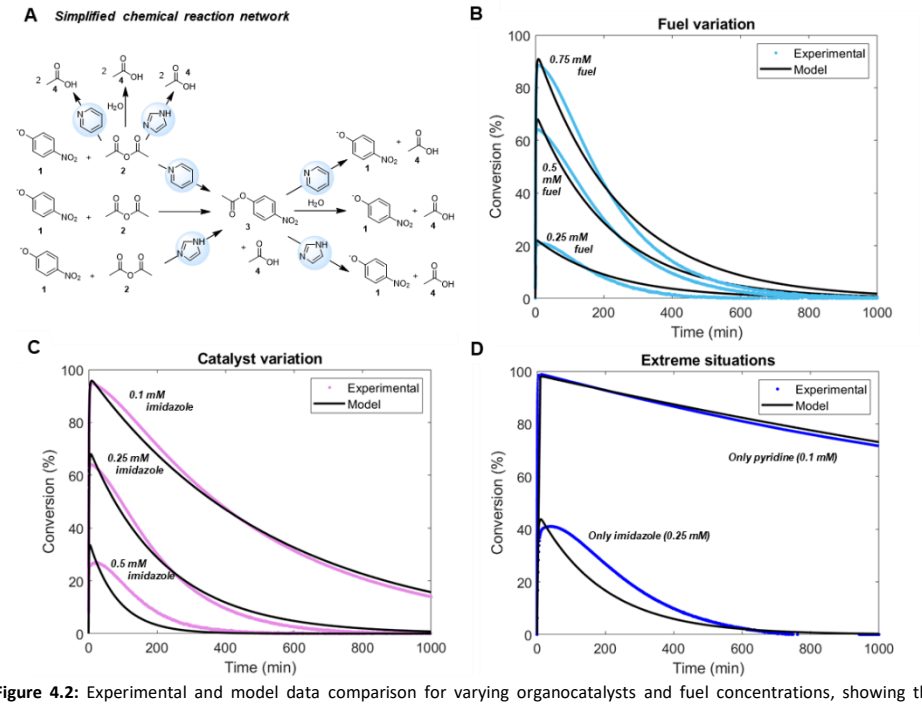

Figure 4.2: Experimental and model data comparison for varying organocatalysts and fuel concentrations, showing the conversion of p-nitrophenol(ate) **1** (start: 0.1 mM) in MOPS buffer (100 mM, pH 7.5) with 5% acetonitrile: **(A)**. Simplified chemical reaction network with pyridine and imidazole catalysing ester formation, hydrolysis and anhydride hydrolysis and blank reactions. **(B)**. Fuel variation: 0.25/ 0.5/ 0.75 mM acetic anhydride **2**, 0.25 mM imidazole and 0.1 mM pyridine. **(C)**. Catalyst variation: 0.5 mM acetic anhydride **2**, 0.1/ 0.25/ 0.5 mM imidazole and 0.1 mM pyridine. **(D)**. Extreme situations: 0.5 mM acetic anhydride **2**, 0/ 0.25 mM imidazole and 0/ 0.1 mM pyridine. The presented experimental data are equal to Figure 4.1. Details of the kinetic model are provided in the Supplementary information.

4.2.3 Fuel-driven responsive polymer system

Having established a CRN in which the formation and degradation pathways can be controlled by two organocatalysts, we then applied this CRN to a macromolecular system. The importance of catalytic control in fuel-driven macromolecular systems is also witnessed in chromatin condensation, a process that regulates the accessibility of DNA for transcription. The DNA (un)binding to histone proteins due to fuel-driven transient (de)acetylation of lysines in the amino-terminal tails of histone proteins is regulated by two enzymes and changes the nucleosome superstructure.[5-7] In analogy, with catalytically controlled fuel-driven acetylation of a polymer, we aim to control transient charge density and in that way polymer chain conformations, such as shape and hydrodynamic radius (Figure 4.3A). In our system, a nitrophenol amino acid analogue, 3-nitro-L-tyrosine (NY), was grafted onto a 130 kDa poly(acrylic acid) (PAA) backbone via peptide coupling, giving PAANY (poly(acrylic acid) 3-nitro-L-tyrosine) with 25% NY coverage (see Supplementary information for synthetic details and

characterization). PAA of relatively high molecular weight is known to have a shape transition from random coil to compact globule upon pH change due to (de)protonation of the acetate groups.[41] Based on previous reports on transient polymer assembly[42, 43], we hypothesized that such coil to globule shape transitions can be induced by transient acylation leading to a decrease of charge and reduced repulsion, and an increase in hydrophobic surface.

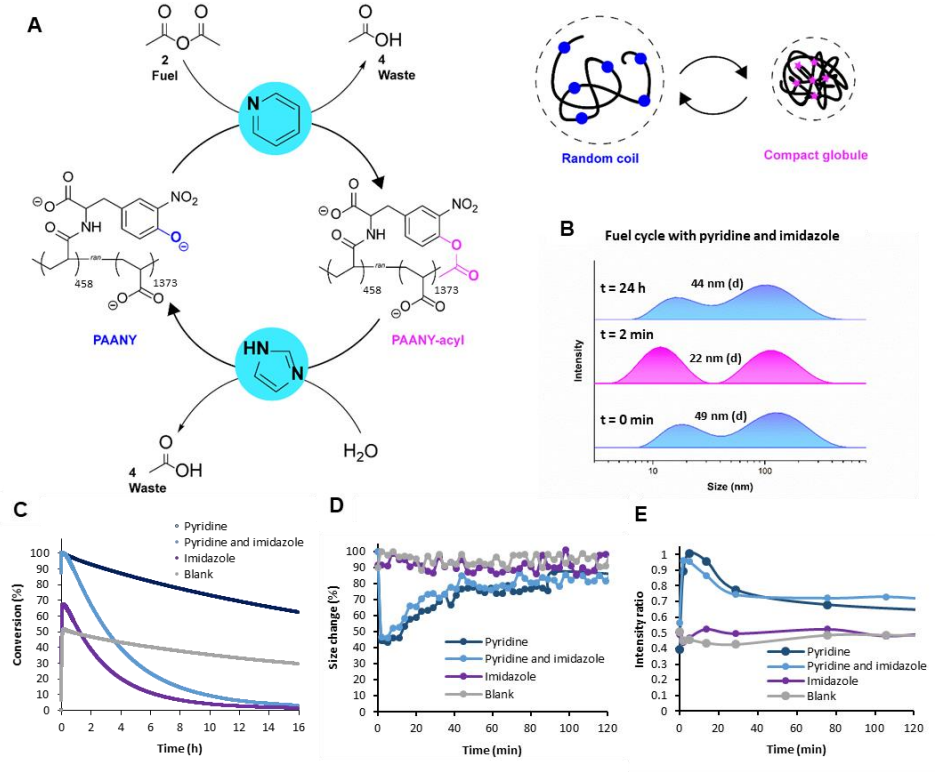

Figure 4.3: Fuel-driven responsive polymer system controlled by organocatalysts pyridine and imidazole in borate buffer (200 mM, pH 8.0). **(A)**. Schematic overview of transient acetylation of PAANY (poly(acrylic acid) 3-nitro-L-tyrosine) to PAANY-acyl by acetic anhydride (left) and the random coil to compact globule transition (top right). **(B)**. DLS size distributions by intensity over time for 0.30 mM PAANY (0.24 mg/mL), 6 mM acetic anhydride **2**, 0.75 mM imidazole and 0.30 mM pyridine. **(C)**. The conversion of PAANY is monitored by UV-VIS, following the absorbance at 420 nm over time. Conditions: 0.15 mM PAANY (0.12 mg/mL), 3 mM acetic anhydride **2**, 0-0.375 mM imidazole and 0-0.15 mM pyridine. **(D)**. Polymer size change monitored over time based on z-average size (nm) measured with DLS. **(E)**. Intensity ratio of single polymer chain vs aggregate as a function of time calculated from the peak areas of the unimer and the aggregate. Conditions: 0.30 mM PAANY (0.24 mg/mL), 6 mM acetic anhydride **2**, 0-0.75 mM imidazole and 0-0.30 mM pyridine. See Supplementary Figures S4.28-29 for corresponding DLS size distributions.

Successful fuel cycles of the PAANY polymer with pyridine and imidazole catalysis were confirmed by UV-VIS experiments by following the absorbance of 3-nitro-L-tyrosine at 420 nm in borate buffer (200 mM, pH 8.0) (Figure 4.3C). Borate buffer at pH 8.0 was

chosen because of its good solvation properties for the functionalized polymer. At pH 8.0 a larger proportion of negatively charged phenolates (89%) is present compared to pH 7.5 (72%), potentially facilitating a larger effect on polymer conformation upon acetylation. Next, the polymer size transition in a fuel cycle was investigated with dynamic light scattering (DLS) (Figure 4.3B,D). The size change in z-average diameter was monitored, which includes both single chain polymers (~10 nm) and polymer aggregates (~100 nm) (Figure 4.3B and Supplementary Figure S4.28-29). The aggregate formation is most likely caused by borate interacting with carboxylate groups on the PAA backbone and carboxylate and phenolate anions on the NY functionalities. Boric acid or borate anions are known to form polymer hybrid structures due to hydrogen bonding. At neutral pH boric acid can even react with carboxylate groups to form a boric anhydride crosslink. [44-46] The aggregate formation in borate is not specific to functionalized PAA, because it is also observed for unmodified PAA in borate buffer (Supplementary Figure S4.30).

With pyridine present, upon addition of fuel **2** the hydrodynamic radius quickly reduces by more than 50% after which it slowly comes back to almost the original size (Figure 4.3D and Supplementary Figures S4.28-29). We expect that the radius does not fully come back to the original value due to a slight drop in pH (from 8.0 to 7.7). In detail, the z-average diameter starts at 49 nm, goes to 22 nm (at t = 2 min) and back to 44 nm after 2 h, while the number average goes from 8.6 ± 2.6 nm to 5.9 ± 1.6 nm (at t = 2 min) back to 7.4 ± 2.0 nm. Concomitantly, the ratio between the two peaks (peak area) in the DLS size intensity distribution changes (Figure 4.3B and Supplementary Figures S4.28A,B). At the start the aggregate peak around 100 nm is more prevalent than the single polymer chain (unimer) peak around 10 nm, whereas after fuel addition (at t = 2 min) the unimer peak has a larger contribution, which changes again at the end of the fuel cycle. Based on this finding, it becomes clear that the fuel-driven acetylation changes the portion of polymers present as single chains (unimers) and in an aggregated form. The unimer to aggregate ratio as a function of time based on the peak areas is depicted in Figure 4.3E. Similar to the change in the z-average diameter over time, we can identify a transient shift towards the unimer upon fuel addition and acetylation in the presence of pyridine. Hence, the transient acetylation shifts the unimer/aggregate equilibrium and after 2 h the equilibrium is restored again. This equilibrium shift could indicate that the non-equilibrium compact polymer structure (when acetylated) has a preference for the unimer over the aggregate, whereas the equilibrium random coil structure is rather in the aggregated form. However, when only imidazole or no catalysts (blank reaction) are present, no significant size change and no aggregate to unimer shift is observed (Figure 4.3D, E and Supplementary Figures S4.28-29C,D). By comparing the DLS size data with the UV-Vis conversion (Figure 4.3C) for the measurements with imidazole and the blank

it becomes clear that the compact polymer structure expands to a coil after 2 h, with about 70% of conversion as a threshold value, meaning about 60% of phenolate (negative charge) needs to be acetylated to induce a polymer conformational change. Based on this threshold criterion and by looking at the UV-VIS conversion result (Figure 4.3C), the polymer sample with only pyridine should collapse after 16 h, but in Figure 4.3D, we observe a faster decay. We hypothesize the behaviour of the polymer chain in solution is more complex and the conversion kinetics and the polymer shape transition have a non-linear relationship. Similar to the small molecule CRN, consecutive fuel cycles could be performed with PAANY by addition of a new batch of fuel (Figure 4.4).

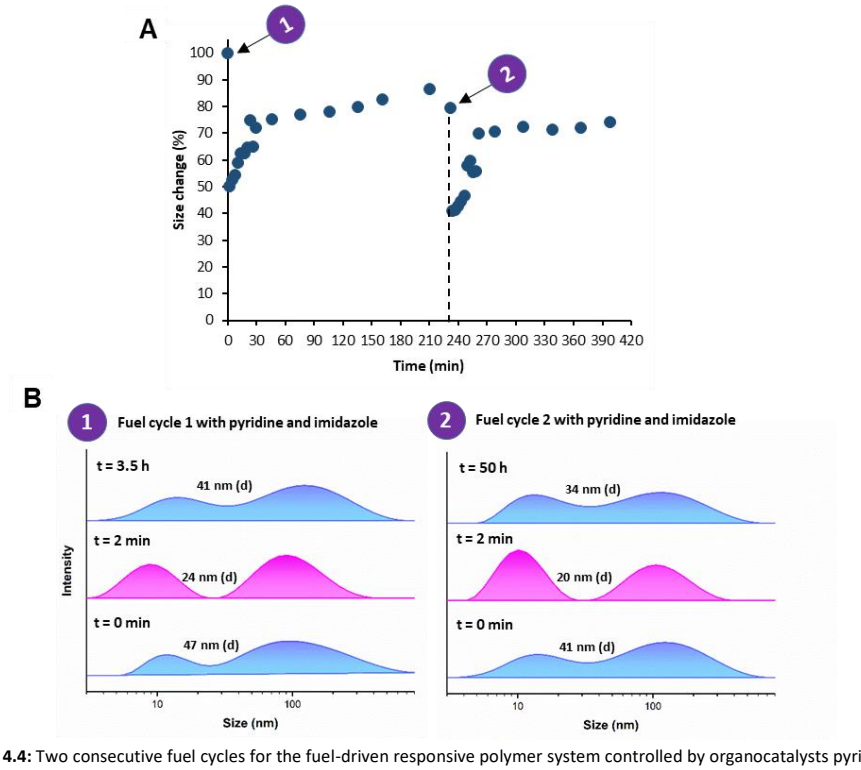

Figure 4.4: Two consecutive fuel cycles for the fuel-driven responsive polymer system controlled by organocatalysts pyridine and imidazole in borate buffer (300 mM, pH 8.0): **(A)**. Polymer size change monitored over time based on z-average size (nm) measured with DLS. **(B)**. DLS size distributions by intensity over time. Conditions: 0.30 mM PAANY (0.24 mg/mL), 6/ 12 mM acetic anhydride **2**, 0 0.75 mM imidazole and 0-0.30 mM pyridine. The second cycle was initiated by addition of fresh fuel **2**.

The z-average diameter change (Figure 4.4A) and the size distributions (Figure 4.4B) show similar trends as with the single fuel cycle, having a sharp size change directly after fuel addition and shift in the intensity distribution to ~10 nm. Because of the addition of more anhydride and hence more acid waste production, the pH drops from 8.0 to 7.5, even though a buffer of 300 mM was used to mitigate this pH drop. Hence, the final size

of the polymer is 34 nm and does not come back to the original value (47 nm). Moreover, the true hydrodynamic radius of the single polymer chain was confirmed by DOSY NMR diffusion coefficient measurements[47] using the Stokes Einstein relation, giving similar sizes in the nanometre range (~8 nm) as with DLS (Supplementary Figure S4.32) and in good agreement with earlier literature examples on PAA polymers[48-50]. The polymer in borate buffer was also imaged with cryo-EM, revealing globular structures with an average diameter of 9.7 ± 1.6 nm along with larger clusters with an average largest dimension of 23.9 ± 7.1 nm (Figure 4.5 and Supplementary Figure S4.33). The 10 nm structures are in line with the DLS and DOSY single polymer diameter, yet the diameter of the polymer aggregates in cryo-EM appears somewhat lower than the 100 nm observed with DLS. There, it might be that the polymer aggregate diameter from DLS is overestimated, as DLS measures fractal dimensions.

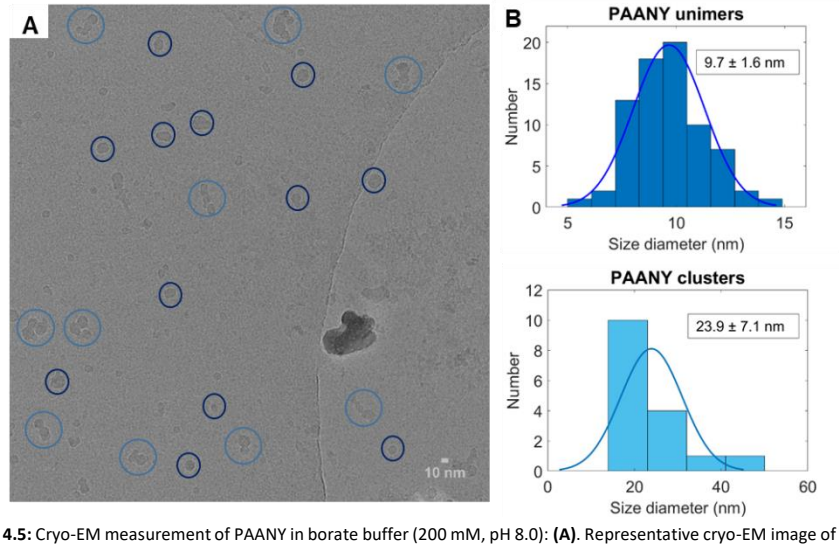

Figure 4.5: Cryo-EM measurement of PAANY in borate buffer (200 mM, pH 8.0): **(A)**. Representative cryo-EM image of PAANY, where the dark blue circles represent spherical polymer structures and the light blue circles the polymer clusters. **(B)**. Histograms of PAANY unimers (top) with average diameter of 9.7 ± 1.6 nm and PAANY aggregates (bottom) with average diameter of 23.9 ± 7.1 nm, both calculated from multiple cryo-EM images.

Because of the conformational change from coil to compact globule for PAANY upon acetylation by chemical fuel **2** we would expect to observe a viscosity change during the cycle. Despite the noisy data typical of dilute solutions in a rheology measurement, time sweep measurements (Supplementary Figure S4.34) showed a lowered viscosity immediately after acetylation of PAANY. On a timescale of hours, the viscosity of acetylated PAANY changes to larger values (Supplementary Figure S4.34B), which is in line with the DLS results. Control experiments on buffer, PAANY or where fuel was added to buffer, do not show any significant viscosity change (Supplementary Figure

S4.34A,C,D). Furthermore, with additional flow step measurements we did not observe a change in the behaviour of the polymer solution (acetylated or not) compared to the buffer and observe a shear-thinning behaviour for all samples (Supplementary Figure S4.35). In contrast to the time sweep measurements, the flow step measurements probe the behaviour of the bulk solvent, which is similar for all.

Altogether, transient polymer conformational and aggregation changes of PAANY were achieved with this fuel-driven esterification CRN for which the presence of the pyridine catalyst turned out to be critical. Yet, the exact behaviour of the functionalized polyelectrolyte in response to organocatalytic action is more complex than anticipated.

4.3 CONCLUSION

In this work, we have shown how two organocatalysts can be incorporated in a fuel-driven esterification CRN and individually regulate product yield and lifetime. In this CRN, *p*-nitrophenol(ate) is acetylated with acetic anhydride as a chemical fuel, and pyridine and imidazole are used as organocatalysts to accelerate the forward and backward reaction, respectively. Variation of the chemical fuel and organocatalysts concentrations enabled full control over ester yield and lifetime. A kinetic model was developed, which corroborated the experimental results. As a proof of principle, the same organocatalytic control was applied on an amino acid functionalized polymer system, leading to control over polymer chain conformation in time. Overall, we have demonstrated that organocatalysis is a powerful tool to regulate reaction kinetics of a non-equilibrium CRN and with that temporally control material properties by inducing a change in a macromolecular superstructure, reminiscent of living systems.

4.4 REFERENCES

1. D. L. Nelson, M. M. Cox and A. L. Lehninger, *Lehninger principles of biochemistry*, W.H. Freeman, New York, 2013.
2. B. N. Kholodenko, *Nat. Rev. Mol.*, 2006, **7**, 165.
3. J. E. Ferrell Jr., T. Y. C. Tsai and Q. Yang, *Cell*, 2011, **144**, 874-885.
4. S. N. Semenov, A. S. Y. Wong, R. M. van der Made, S. G. J. Postma, J. Groen, H. W. H. van Roekel, T. F. A. de Greef and W. T. S. Huck, *Nat. Chem.*, 2015, **7**, 160.
5. E. Verdin and M. Ott, *Nat. Rev. Mol.*, 2015, **16**, 258.
6. G. E. Zentner and S. Henikoff, *Nat. Struct. Mol. Biol.*, 2013, **20**, 259.
7. M. Grunstein, *Nature*, 1997, **389**, 349.
8. J. Boekhoven, A. M. Brizard, K. N. K. Kowlgi, G. J. M. Koper, R. Eelkema and J. H. van Esch, *Angew. Chem. Int. Ed.*, 2010, **122**, 4935-4938.
9. J. Boekhoven, W. E. Hendriksen, G. J. M. Koper, R. Eelkema and J. H. van Esch, *Science*, 2015, **349**, 1075-1079.
10. L. S. Kariyawasam and C. S. Hartley, *J. Am. Chem. Soc.*, 2017, **139**, 11949–11955.
11. M. Tena-Solsona, B. Rieß, R. K. Grötsch, F. C. Löhrer, C. Wanzke, B. Käsdorf, A. R. Bausch, P. Müller-Buschbaum, O. Lieleg and J. Boekhoven, *Nat. Commun.*, 2017, **8**, 15895.
12. J. Leira-Iglesias, A. Tassoni, T. Adachi, M. Stich and T. M. Hermans, *Nat. Nanotechol.*, 2018, **13**, 1021.
13. A. Sorrenti, J. Leira-Iglesias, A. J. Markvoort, T. F. de Greef and T. M. Hermans, *Chem. Soc. Rev.*, 2017, **46**, 5476-5490.
14. A. Sorrenti, J. Leira-Iglesias, A. Sato and T. M. Hermans, *Nat. Commun.*, 2017, **8**, 15899.

15. S. A. P. van Rossum, M. Tena-Solsona, J. H. van Esch, R. Eelkema and J. Boekhoven, *Chem. Soc. Rev.*, 2017, **46**, 5519-5535.
16. F. Della Sala, S. Maiti, A. Bonanni, P. Scrimin and L. J. Prins, *Angew. Chem. Int. Ed.*, 2018, **130**, 1627-1631.
17. F. della Sala, S. Neri, S. Maiti, J. L. Chen and L. J. Prins, *Curr. Opin. Biotechnol.*, 2017, **46**, 27-33.
18. G. Ragazzon and L. Prins, *Nat. Nanotechol.*, 2018, **13**, 882–889.
19. S. Dhiman, A. Jain and S. J. George, *Angew. Chem. Int. Ed.*, 2017, **129**, 1349-1353.
20. A. Jain, S. Dhiman, A. Dhayani, P. K. Vemula and S. George, *Nat. Commun.*, 2019, **10**, 450.
21. T. Heuser, E. Weyandt and A. Walther, *Angew. Chem. Int. Ed.*, 2015, **54**, 13258-13262.
22. L. Heinen, T. Heuser, A. Steinschulte and A. Walther, *Nano Lett.*, 2017, **17**, 4989-4995.
23. S. Debnath, S. Roy and R. V. Ulijn, *J. Am. Chem. Soc.*, 2013, **135**, 16789-16792.
24. P. Solís Muñana, G. Ragazzon, J. Dupont, C. Z. J. Ren, L. J. Prins and J. L. Y. Chen, *Angew. Chem. Int. Ed.*, 2018, **57**, 16469-16474.
25. S. Bal, K. Das, S. Ahmed and D. Das, *Angew. Chem. Int. Ed.*, 2019, **58**, 244-247.
26. P. Tremmel, H. Griesser, U. E. Steiner and C. Richert, *Angew. Chem. Int. Ed.*, 2019, **58**, 13087-13092.
27. M. P. van der Helm, B. Klemm and R. Eelkema, *Nat. Rev. Chem.*, 2019, **3**, 491-508.
28. B. Neises and W. Steglich, *Angew. Chem. Int. Ed.*, 1978, **17**, 522-524.
29. F. Brotzel, B. Kempf, T. Singer, H. Zipse and H. Mayr, *Chem. Eur. J.*, 2007, **13**, 336-345.
30. D. Ripin and D. Evans, *Heterocycles*, 2005, **462**, 1-6.
31. T. C. Bruice and G. L. Schmir, *J. Am. Chem. Soc.*, 1957, **79**, 1663-1667.
32. W. P. Jencks and J. Carriuolo, *J. Biol. Chem.*, 1959, **234**, 1280-1285.
33. J. F. Kirsch and W. P. Jencks, *J. Am. Chem. Soc.*, 1964, **86**, 837-846.
34. F. Schneider, *Angew. Chem. Int. Ed.*, 1978, **17**, 583-592.
35. P. Nieri, S. Carpi, S. Fogli, B. Polini, M. C. Breschi and A. Podestà, *Sci. Rep.*, 2017, **8**, 45760.
36. A. Kirby and A. Neuberger, *Biochem. J*, 1938, **32**, 1146.
37. M. Baidya, F. Brotzel and H. Mayr, *Org. Biomol. Chem.*, 2010, **8**, 1929-1935.
38. A. R. Fersht and W. P. Jencks, *J. Am. Chem. Soc.*, 1970, **92**, 5432-5442.
39. M. L. Bender and B. W. Turnquest, *J. Am. Chem. Soc.*, 1957, **79**, 1656-1662.
40. V. Gold, *J. Chem. Soc. Faraday Trans*, 1948, **44**, 506-518.
41. T. Swift, L. Swanson, M. Geoghegan and S. Rimmer, *Soft Matter*, 2016, **12**, 2542-2549.
42. G. Wang, B. Tang, Y. Liu, Q. Gao, Z. Wang and X. Zhang, *Chem. Sci.*, 2016, **7**, 1151-1155.
43. T. Heuser, A.-K. Steppert, C. Molano Lopez, B. Zhu and A. Walther, *Nano Lett.*, 2015, **15**, 2213-2219.
44. B. Wicklein, D. Kocjan, F. Carosio, G. Camino and L. Bergström, *Chem. Mater.*, 2016, **28**, 1985-1989.
45. E. L. Simion, G. Stîngă, A. Băran, L. Aricov, I. C. Gîfu and D. F. Anghel, *Colloid. Polym. Sci.*, 2016, **294**, 927-939.
46. H. Lundberg, F. Tinnis, N. Selander and H. Adolfsson, *Chem. Soc. Rev.*, 2014, **43**, 2714-2742.
47. A. Chen, D. Wu and C. S. Johnson Jr, *J. Am. Chem. Soc.*, 1995, **117**, 7965-7970.
48. Z. Adamczyk, A. Bratek, B. Jachimska, T. Jasiński and P. Warszyński, *J. Phys. Chem. B*, 2006, **110**, 22426-22435.
49. M. S. Sulatha and U. Natarajan, *Ind. Eng. Chem. Res.*, 2011, **50**, 11785-11796.
50. D. Reith, B. Müller, F. Müller-Plathe and S. Wiegand, *J. Chem. Phys.*, 2002, **116**, 9100-9106.

4.5 SUPPLEMENTARY INFORMATION

4.5.1 Experimental details

General materials and methods

Chemicals were purchased in the highest available purity and used without further purification unless reported otherwise. *p*-Nitrophenol **1**, acetic anhydride **2**, pyridine anhydrous, imidazole, isopropenyl acetate, vinyl acetate, poly(acrylic acid) (PAA ~130 kDa), N,N-dimethyl formamide (DMF) anhydrous, dimethyl sulfoxide (DMSO), N-(3-Dimethylaminopropyl)-N'-ethylcarbodiimide hydrochloride (EDC), acetonitrile, N,N-diisopropylethylamine (DIPEA), were purchased from Sigma-Aldrich. *p*-Nitrophenyl acetate **3** was from TCI Europe. 3-nitro-L-tyrosine ethyl ester (NY-ethyl ester) was from Chem Impex International. 1-Hydroxybenzotriazole hydrate (HOBt) was from Acros Organics. Solid salts were used for the preparation of aqueous buffers: sodium tetraborate decahydrate (Borax), boric acid, sodium hydroxide were from Sigma Aldrich and 3-(N-Morpholino)propanesulfonic acid (MOPS) from Alfa Aesar. Unless stated otherwise, all preparations and analyses were performed at room temperature (RT) (~21 °C) and atmospheric pressure. Nuclear Magnetic Resonance (NMR) experiments were performed using Agilent-400 MR DD2 (400 MHz for ^{1}H and 100.5 MHz for ^{13}C) at 25 °C using residual deuterated solvent signals as internal standard. To suppress the water peak, PRESAT configuration (suppress one highest peak) was used. Prior to every diffusion-ordered spectroscopy (DOSY) NMR measurement, scouting experiments were performed to obtain the longest t1 relaxation and get an optimal diffusion gradient and delay. DOSY spectra were analysed with MestReNova software. UV-Vis spectroscopic experiments were carried out using Analytik Jena Specord 250 spectrophotometer; quartz cuvette with a 1 cm path length, volume of 3 mL, at RT. Liquid Chromatography–Mass Spectrometry (LC-MS) was performed on a Shimadzu Liquid Chromatograph Mass Spectrometer 2010, LC-8A pump with a diode array detector SPD-M20. Negative and/or positive mode Electro Spray Ionization Mass Spectrometry (ESI-MS) was used for the peak assignment. Fourier Transform Infrared Spectroscopy (FTIR) spectroscopy was performed with NicoletTM 6700 FT-IR Spectrometer from Thermo Electron Corporation equipped with OMNIC Software using the ATR method. Spectra were recorded at wavenumber range 4000-400 cm^{-1} with 4 cm^{-1} resolution. Prior to each experiment a background of the ZnSe crystal was measured. Dynamic light scattering (DLS) measurements were recorded with a Malvern Zetasizer Nano equipped with a 633 nm laser, collecting the optical data with a 90° scattering angle; quartz cuvette with 1 cm path length, volume of 3 mL, at 20 °C. Cryo-EM (Cryogenic electron microscopy) images were obtained with a JEOL JEM3200-FSC, operated at 300kV with Gatan camera K2-Summit operated in counting mode with 10s exposure time, dose fractionated 0.2s aligned by SerialEM. Zero-Loss filtered with a 20eV slit. Samples were prepared with a

Leica plunger EM GP, 21 °C, 98% RH, 8 seconds blotting time. The final images were analysed with ImageJ software. Polymer viscosity change was measured using a rheometer (AR G2, TA instruments) equipped with a steel plate-and-plate geometry of 40 mm in diameter, using a with hexadecane filled water trap.

Polymer functionalization: 3-nitro-L-tyrosine on poly(acrylic acid) PAANY

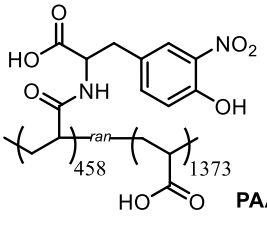

PAANY

Poly(acrylic acid) PAA (M_n 130-230 kDa (reported by Sigma-Aldrich), Đ = 2.3 (GPC in water)) was functionalized with 3-nitro-L-tyrosine (NY)-ethyl ester via peptide coupling with EDC/HOBt and DIPEA in DMF. For 25% coverage: PAA (50 mg) was mixed with NY-ethyl ester (50 mg, 0.25 molar eq.), EDC (50 mg, 0.5 molar eq.), HOBt (102.3 mg, 0.625 molar eq.) and DIPEA (138 µL, 1.125 molar eq.) in DMF (15 mL). The reaction mixture was stirred for 24 h at RT. Afterwards, the mixture was concentrated under reduced pressure and the final product precipitated in a DMSO/ water mixture, giving PAANY-ethyl ester (yield: 79%). To obtain the hydrolysed polymer PAANY, stock solutions were left overnight in the respective buffer solution and the hydrolysis was confirmed by ^{1}H NMR (Figure S4.27). **^{1}H NMR** (400 MHz, DMF): δ = 12.61 (s, 1H, -OH), 10.93 (s, 1H, -COOH), 7.88 (s, 1H, -ArH-), 7.57 (s, 1H, -ArH-), 7.17 (s, 1H, -ArH), 4.64 (s, 1H, -CHα-), 4.11 (s, 2H, -CH_2-), 3.12 (s, 2H, -CHβ-), 2.00-1.50 (PAA backbone), 1.17 (s, 3H, -CH_3) . N.B. the multiplicity of 3-nitro-L-tyrosine in the NMR spectrum is lost because the peaks are too broad on the polymer (appearance as broad singlets). After hydrolysis the peaks of the ethyl ester at 4.11 and 1.17 ppm have disappeared. **FTIR** (ATR, cm^{-1}): ν 1730 (C=O stretch ester), 1700 (C=O stretch acid backbone), 1680 (C=O stretch amide), 1350 (OH-bend phenol), 1050 (C-O-C stretch ester).

UV-Vis assay

Stock solutions were prepared in MOPS buffer (pH 7.5, 100 mM), borate buffer (pH 8.0, 200 mM) or acetonitrile (for acetic anhydride **2** only – to avoid significant hydrolysis in the stock solution). Unless stated otherwise, the fuel cycle was performed with 0.1 mM *p*-nitrophenol **1**, 0.5 mM acetic anhydride **2**, 0-1 mM of pyridine, and 0-1 mM of imidazole in MOPs buffer (pH 7.5, 100 mM), in quartz cuvettes, path length of 1 cm (total reaction volume of 3 mL) at RT. The stock solutions of the reactants were always added in the following order: *p*-nitrophenol **1**, pyridine, imidazole and acetic anhydride **2**. Teflon caps were used to close the cuvette. The cuvette was turned upside down to mix the solution. The reactant peak was followed using slow time scan, measuring wavelength 400 nm. The pH was measured before and after the reaction (or followed during the reaction; see SI: pH monitoring of fuel-driven esterification network). The

conversion was calculated with the extinction coefficients (see Calibration lines) and Lambert-Beer law:

$$A = \varepsilon l C$$

, where *A* is the absorbance, ε the extinction coefficient, *l* the path length of the cuvette and *C* the concentration. The experiments with PAANY were performed similarly, only following the decrease/ increase at 420 nm from NY. Because we anticipated problems with concentrated sulfonate buffers with macromolecules (such as precipitation), we used borate buffer (pH 8.0, 200 mM). Experiments were performed at pH 8.0 to have a higher percentage of phenolate (negative charge) compared to phenol and co-solvent was avoided, since it could affect the polyelectrolyte behaviour in solution.

DLS measurements

Stock solutions were prepared in borate buffer (pH 8.0, 200 mM) and filtered with syringe filters (0.2 µm) before use. Unless stated otherwise, the fuel cycle was performed with 0.30 mM PAANY (0.24 mg/mL), 6 mM acetic anhydride **2**, 0-0.30 mM of pyridine, and 0-0.75 mM of imidazole in borate buffer (pH 8.0, 200 mM), in quartz cuvettes, 1 cm path length (3 mL reaction volume) at 20 °C. The stock solutions of the reactants were always added in the following order: PAANY, pyridine, imidazole and acetic anhydride **2**. Cuvettes were closed with Teflon caps and turned upside down to mix the solution. A fuel cycle was measured in continuous mode with 1000 measurements consisting of 11 runs each 3 min. An equilibration time of 2 min was applied for each measurement. Calculated size changes (%) are based on z-average diameters (nm). A DLS size calibration was performed to find the polymer concentration with minimal size fluctuation (see DLS size calibration). The pH was always measured before and after the reaction.

Viscosity rheology measurements

For the blank experiments, 0.7 mL of the sample (PAANY (0.3 mM) in borate buffer (200 mM pH 8.0), borate buffer (200 mM pH 8.0) alone or borate buffer with 6 mM acetic anhydride fuel **2**) was directly positioned on the rheometer plate. For the PAANY acetylation experiment, the stock solutions of the reactants were added into a glass vial in the following order: PAANY, imidazole, pyridine and acetic anhydride **2**. The vial was turned upside down to mix the solution. Then, the 0.7 mL sample (0.3 mM PAANY, 0.75 mM imidazole, 0.3 mM pyridine, 6 mM acetic anhydride **2**) was positioned on the rheometer plate. Time sweep measurements were performed at fixed strain (γ = 0.05 %) and frequency (ω =6.28 rad/s = 1 Hz). Flow step measurements were performed after time sweep measurements on the same sample.

Kinetic modelling

A kinetic model for the esterification CRN was written in MATLAB 2018b. The rate constant of imidazole catalysed ester hydrolysis was determined by varying the concentration of imidazole in the hydrolysis of *p*-nitrophenyl acetate **3** with UV-VIS, following the appearance of the hydrolysis product **1** at 400 nm. The other rate constants were taken from the literature or obtained from the MATLAB model fitting (see Kinetic model for fuel-driven esterification CRN).

4.5.2 UV-VIS spectroscopy

Calibration lines

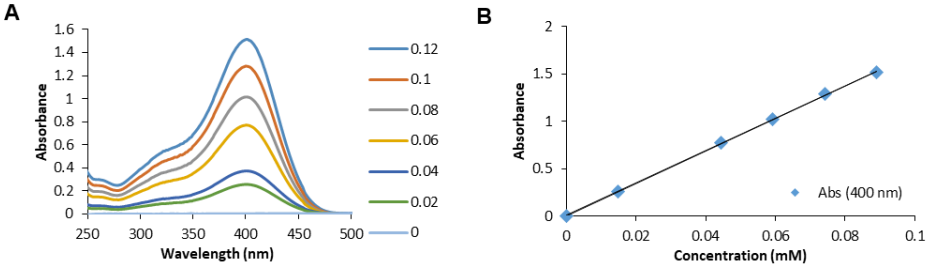

Figure S4.1: Extinction coefficient for *p*-nitrophenol **1** in MOPs buffer (100 mM, pH 7.5) at 400 nm: 16.74 $mM^{-1}cm^{-1}$. **(A)**. UV-Vis absorbance spectra of *p*-nitrophenol **1** at different concentrations. **(B)**. Absorbance at 400 nm of *p*-nitrophenol **1** at different concentrations.

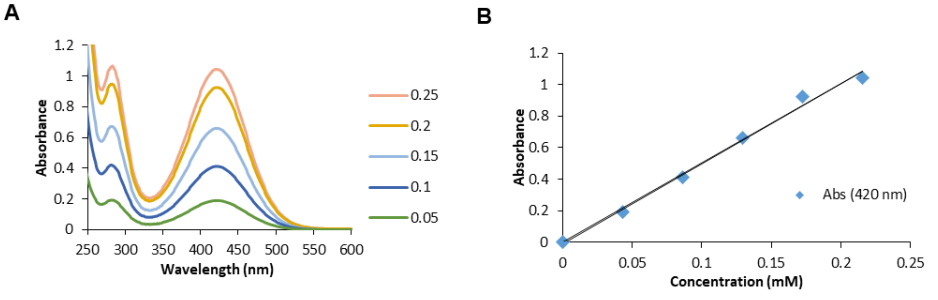

Figure S4.2: Extinction coefficient for 3-nitro-L-tyrosine (NY) in Borate buffer (200 mM, pH 8.0) at 420 nm: 5.03 $mM^{-1}cm^{-1}$. **(A)**. UV-Vis absorbance spectra of 3-nitro-L-tyrosine (NY) at different concentrations. **(B)**. Absorbance at 420 nm of 3-nitro-L-tyrosine (NY) at different concentrations.

Absorbance plots

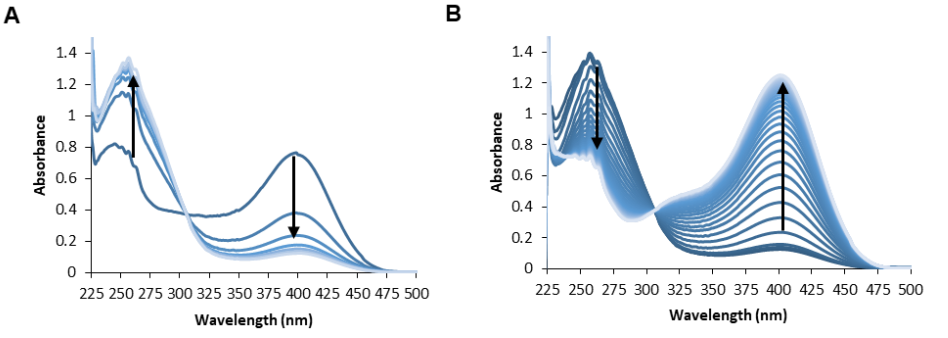

Figure S4.3: Absorbance vs wavelength for fuel-driven esterification network controlled by organocatalysts pyridine and imidazole in MOPS buffer (100 mM, pH 7.5) with 5% acetonitrile. Monitoring the conversion of *p*-nitrophenol(ate): 0.1 mM *p*-nitrophenol **1**, 0.5 mM acetic anhydride **2** (stock in acetonitrile), 0.25 mM imidazole and 0.1 mM pyridine. **(A)**. First 10 min of reaction, showing the decrease in 400 nm and increase for 270 nm – from dark to light blue (N.B. the first sample was measured after 10-30 s, hence part of the phenolate was already consumed). **(B)**. From 10 min to 16.5 h, showing the increase in 400 nm and decrease for 270 nm - from dark to light blue. The isosbestic point for this reaction is located at 305 nm. N.B Acetyl-imidazole disappearance is shown at 245 nm and acetyl-pyridinium at 272 nm [1, 2].

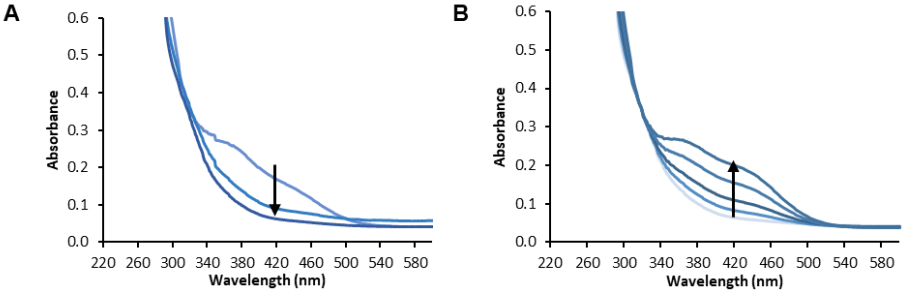

Figure S4.4: Absorbance vs wavelength for fuel-driven responsive polymer system controlled by organocatalysts pyridine and imidazole in borate buffer (200 mM, pH 8.0). Monitoring the conversion of PAANY by UV-VIS: 0.15 mM PAANY (0.12 mg/mL), 1.5 mM acetic anhydride **2**, 0.375 mM imidazole and 0.15 mM pyridine. **(A)**. First 5 min of reaction, showing the decrease in 420 nm (N.B. the first sample was measured after 10-30 s, hence part of the phenolate was already consumed). **(B)**. From 5 min to 3 h, showing the increase in 420 nm.

Fuel cycle error analysis

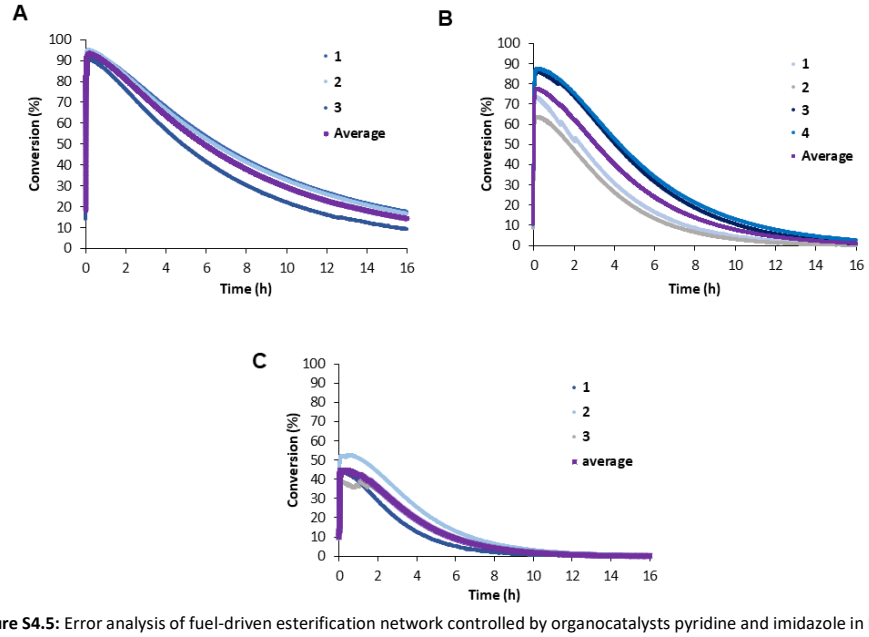

Figure S4.5: Error analysis of fuel-driven esterification network controlled by organocatalysts pyridine and imidazole in MOPS buffer (100 mM, pH 7.5) with 5% acetonitrile: **(A)**. Monitoring the conversion of *p*-nitrophenol(ate): 0.1 mM *p*-nitrophenol **1**, 0.5 mM acetic anhydride **2** (stock in acetonitrile), 0.1 mM pyridine and 0.1 mM imidazole, given in triplicate with average and the average standard deviation is 2.8% (n=3). **(B)**. Monitoring the conversion of *p*-nitrophenol(ate): 0.1 mM *p*-nitrophenol **1**, 0.5 mM acetic anhydride **2** (stock in acetonitrile), 0.1 mM pyridine and 0.2 mM imidazole, given in quadruplicate with average and the average standard deviation is 10.5% (n=4). **(C)**. Monitoring the conversion of *p*-nitrophenol(ate): 0.1 mM *p*-nitrophenol **1**, 0.5 mM acetic anhydride **2** (stock in acetonitrile), 0.1 mM pyridine and 0.3 mM imidazole, given in triplicate with average and the average standard deviation is 6.5% (n=3).

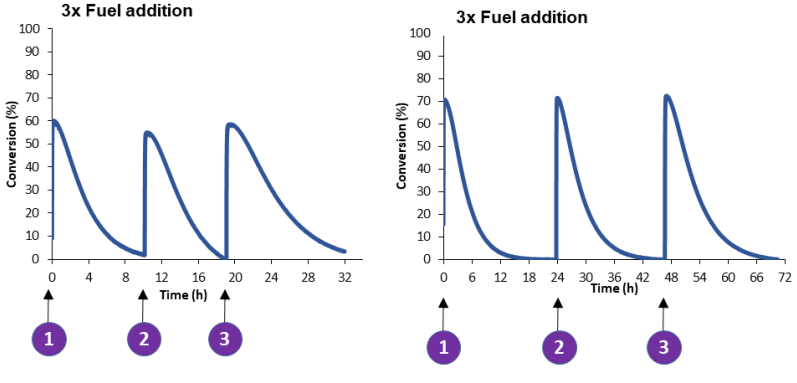

Figure S4.6: Three consecutive fuel cycles: 0.1 mM *p*-nitrophenol **1**, 0.5 mM acetic anhydride **2** (stock in acetonitrile), 0.25 mM imidazole and 0.1 mM pyridine. The second and third cycles were initiated by addition of a new batch of fuel **2**. The discrepancy between the first and second graph is most likely caused by a faster hydrolysis of the anhydride fuel **2** in the stock solution for the left graph before addition to the reaction mixture. In Figure S4.5 the same discrepancies are observed, inherent to this system where the fuel consumption is very fast.

Blank reaction without catalysts

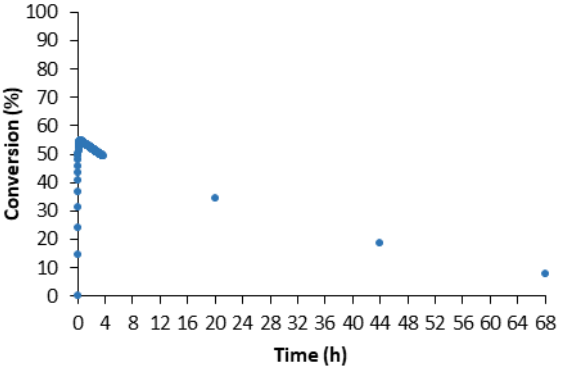

Figure S4.7: Blank reaction for fuel-driven esterification network in MOPS buffer (100 mM, pH 7.5) with 5% acetonitrile. Monitoring the conversion of *p*-nitrophenol(ate): 0.1 mM *p*-nitrophenol **1** with 0.5 mM acetic anhydride **2** (stock in acetonitrile).

4.5.3 HPLC-MS analysis

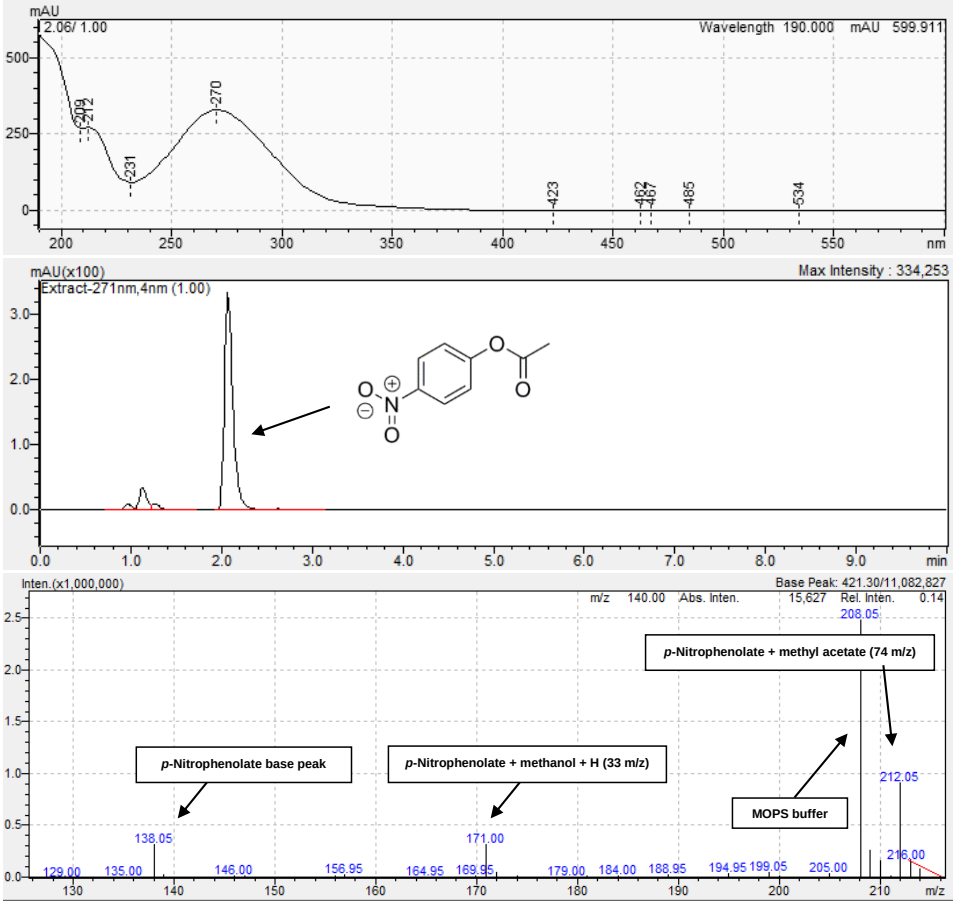

Figure S4.8: HPLC-MS: Fuel-driven esterification network controlled by organocatalysts pyridine and imidazole in MOPS buffer (100 mM, pH 7.5) with 5% acetonitrile. Conditions: 0.1 mM *p*-nitrophenol **1**, 0.5 mM acetic anhydride **2** (stock in acetonitrile), 0.1 mM imidazole and 0.1 mM pyridine. Sample was measured 10 min after addition of all compounds. *p*-Nitrophenylacetate **3** elutes at ~2.05 min, shows an absorbance maximum ~270 nm and 138 as m/z value (*p*-nitrophenyl esters give base peaks of the corresponding phenolate[3, 4]).

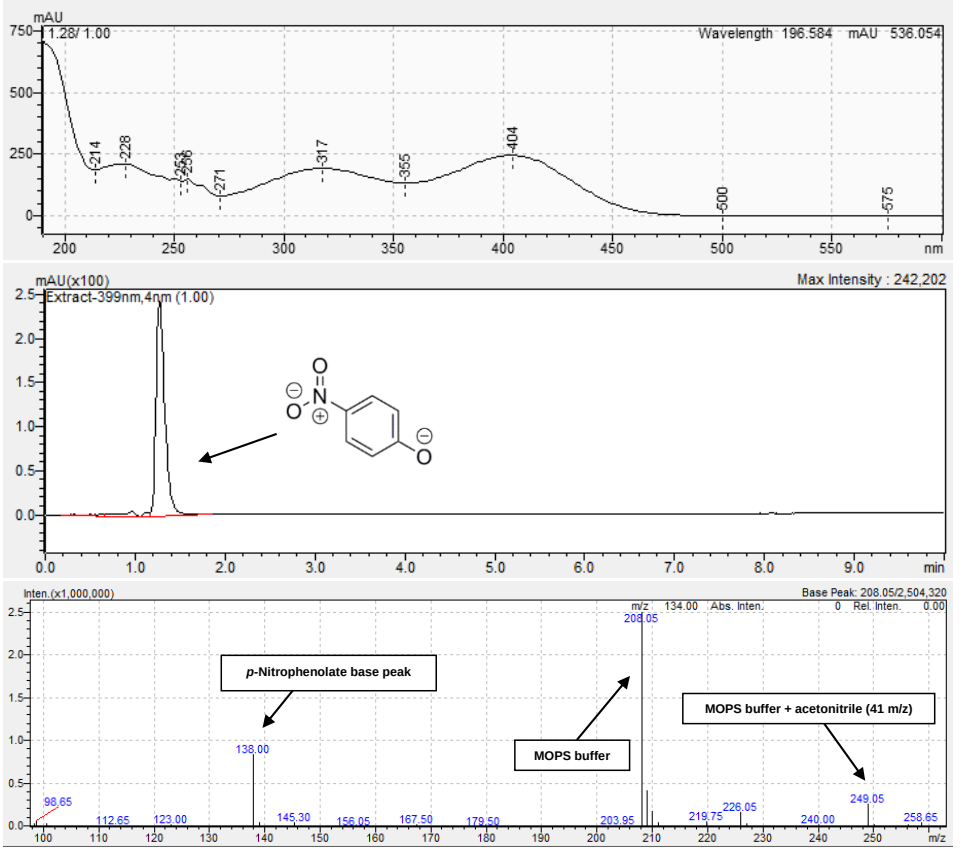

Figure S4.9: HPLC-MS: Fuel-driven esterification network controlled by organocatalysts pyridine and imidazole in MOPS buffer (100 mM, pH 7.5) with 5% acetonitrile. Conditions: 0.1 mM *p*-nitrophenol **1**, 0.5 mM acetic anhydride **2** (stock in acetonitrile), 0.1 mM imidazole and 0.1 mM pyridine. Sample was measured 18h after addition of all compounds. *p*-Nitrophenol(ate) **1** elutes at ~1.3 min, shows an absorbance maximum ~400 nm and 138 as m/z value.

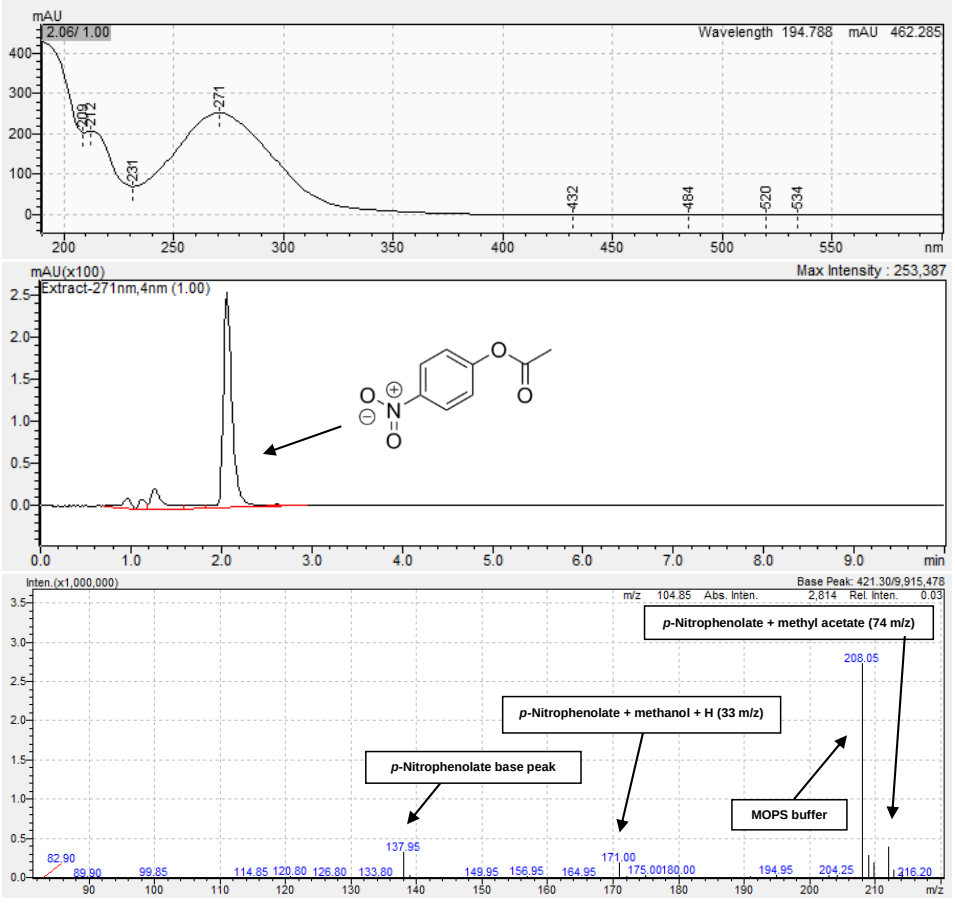

Figure S4.10: HPLC-MS: Blank reaction for fuel-driven esterification network in MOPS buffer (100 mM, pH 7.5) with 5% acetonitrile. Conditions: 0.1 mM *p*-nitrophenol **1** and 0.5 mM acetic anhydride **2** (stock in acetonitrile). Sample was measured 25 min after addition of all compounds. *p*-Nitrophenylacetate **3** elutes at ~2.05 min, shows an absorbance maximum ~270 nm and 138 as m/z value (*p*-nitrophenyl esters give base peaks of the corresponding phenolate[3, 4]).

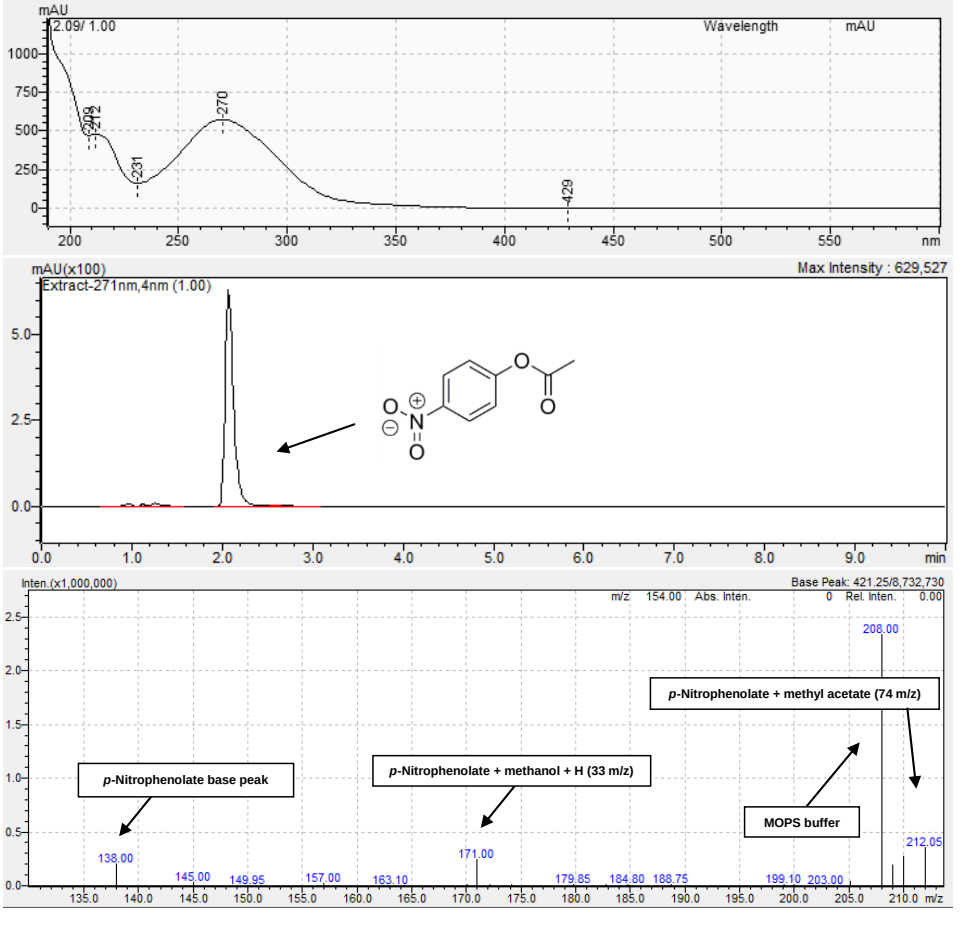

Figure S4.11: HPLC-MS: *p*-Nitrophenylacetate **3** reference compound in MOPS buffer (100 mM, pH 7.5) with 5% acetonitrile elutes at ~2.05 min, shows an absorbance maximum ~270 nm and 138 as m/z value (*p*-nitrophenyl esters give base peaks of the corresponding phenolate[3, 4]).

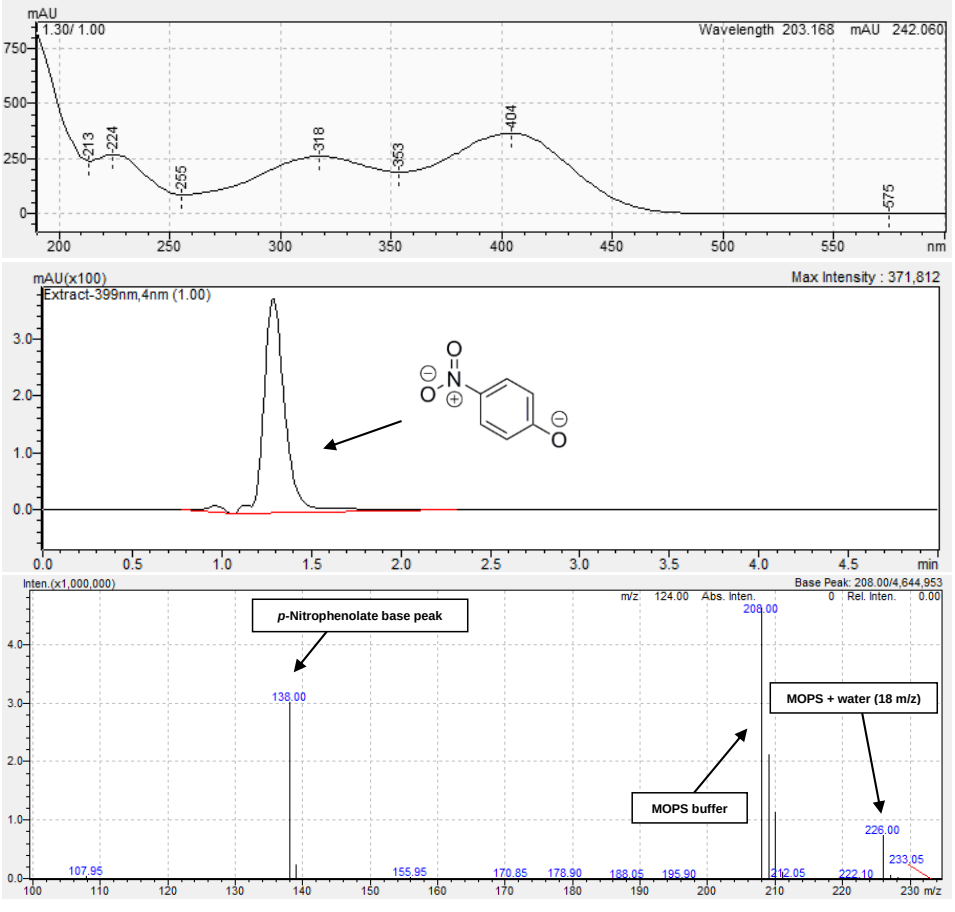

Figure S4.12: HPLC-MS: *p*-Nitrophenol(ate) **1** reference compound in MOPS buffer (100 mM, pH 7.5) elutes at ~1.3 min, shows an absorbance maximum ~400 nm and 138 as m/z value.

4.5.4 Monitoring esterification network by colour progress

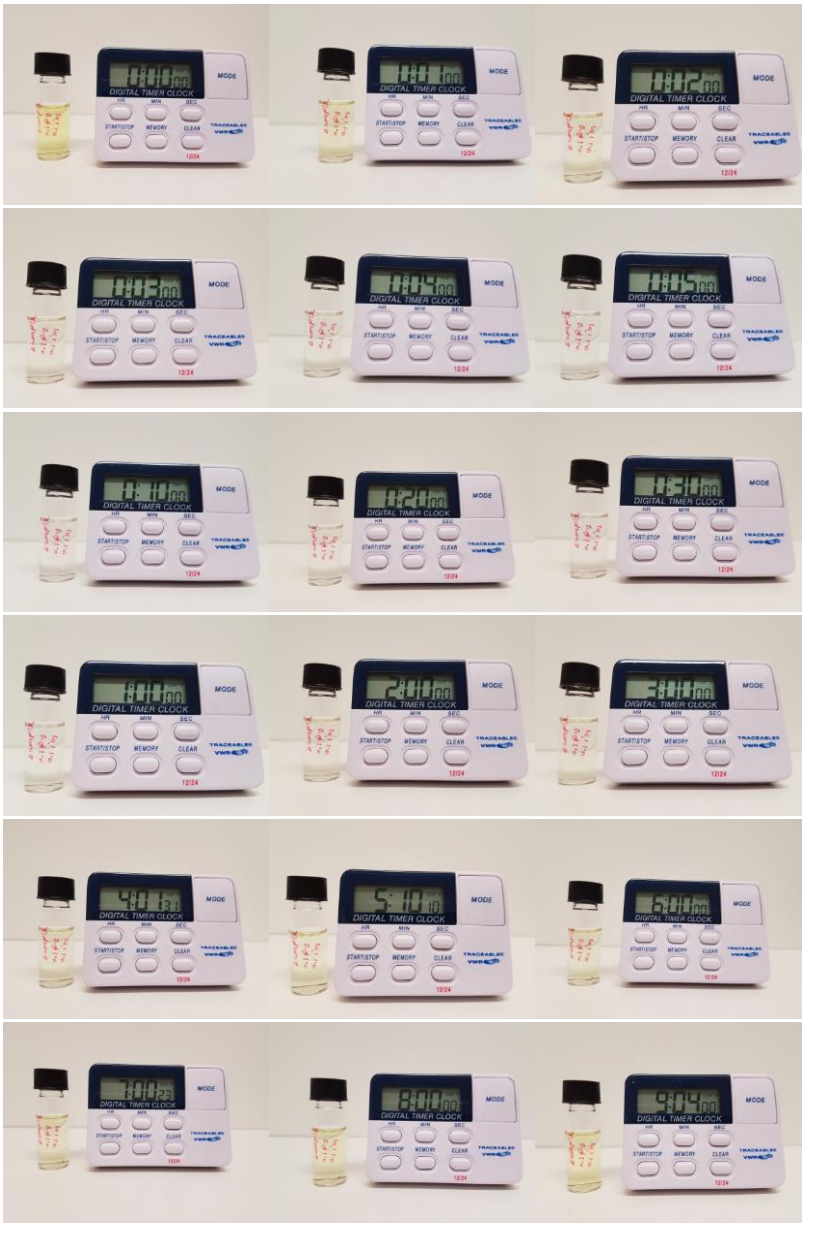

Figure S4.13: Fuel-driven esterification network controlled by organocatalysts pyridine and imidazole in MOPS buffer (100 mM, pH 7.5) with 5% acetonitrile, monitoring reaction by colour progress; yellow to transparent and back to yellow again (Conditions: 0.1 mM *p*-nitrophenol **1**, 0.5 mM acetic anhydride **2** (stock in acetonitrile), 0.1 mM imidazole and 0.1 mM pyridine).

4.5.5 pH monitoring of fuel-driven esterification network

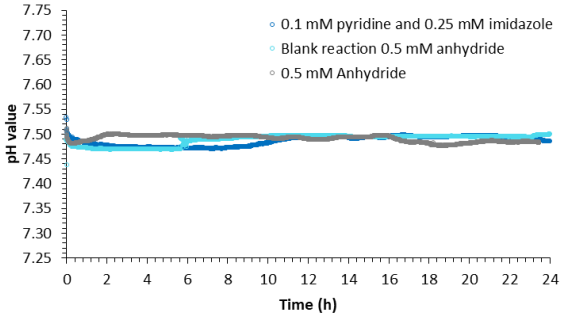

Figure S4.14: pH monitoring of reaction with organocatalysts, blank reaction and anhydride stock in MOPS buffer (pH 7.5 100 mM).

4.5.6 Different acyl donors

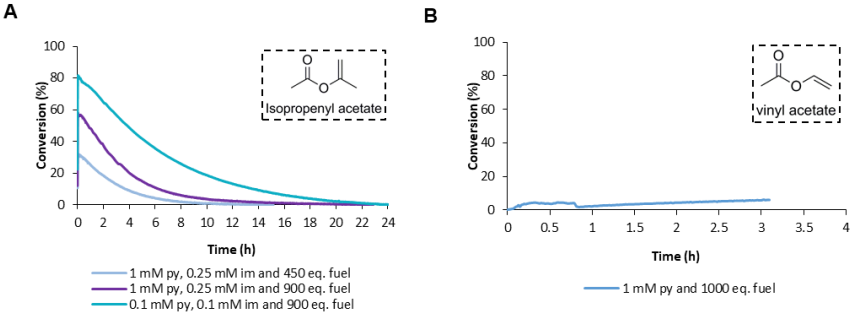

Figure S4.15: Fuel-driven esterification network with varying concentration of organocatalysts, monitoring the conversion of *p*-nitrophenol(ate) **1**: **(A)**. 450-900 molar eq. isopropenyl acetate. **(B)**. 1000 molar eq. vinyl acetate. Conditions: 0.1 mM *p*-nitrophenol **1** in MOPS buffer (pH 7.5, 100 mM), pyridine (0.1-1 mM) and imidazole (0.1-0.25 mM).

Table S4.1: Overview of tested acyl donors as fuels for esterification of *p*-nitrophenol(ate) **1**.

Fuel	Structure	Waste product(s)	UV-VIS	Remarks
Acetic anhydride	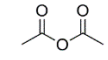 acetic anhydride		5 molar eq. of fuel to drive the esterification	Acetic anhydride completely hydrolysed after 30 minutes. Then only backward reactions remain.
Isopropenyl acetate	 Isopropenyl acetate	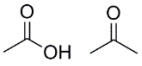	450-900 molar eq. of fuel (45-90 mM) needed to drive the reaction	- Heterogeneous mixture (fuel hardly dissolves in water and creates little bubbles). - Due to high concentration of fuel pH drops to 7.46 at the end of the reaction.
Vinyl acetate	 vinyl acetate	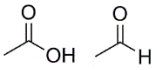	1000 molar eq. of fuel (100 mM) not sufficient	

4.5.7 Kinetic model for fuel-driven esterification CRN

In this section the development of the numerical model for the reaction kinetics of the esterification CRN written in MATLAB 2018b is discussed. First, we deal with the kinetics of the blank reaction (uncatalysed), then the pyridine catalysis, followed by imidazole catalysis and eventually all individual reaction schemes are combined to model the entire fuel cycle (Scheme S4.1) with varying catalysts and fuel concentrations. In all cases, first an overview of the reaction pathway is given, followed by the rate equations (system of ODEs) and the experimental data fitting, showing the concentration profiles of the different species over time for the modelled and experimental data. We end with a note on how the model was optimized for the various experimental conditions.

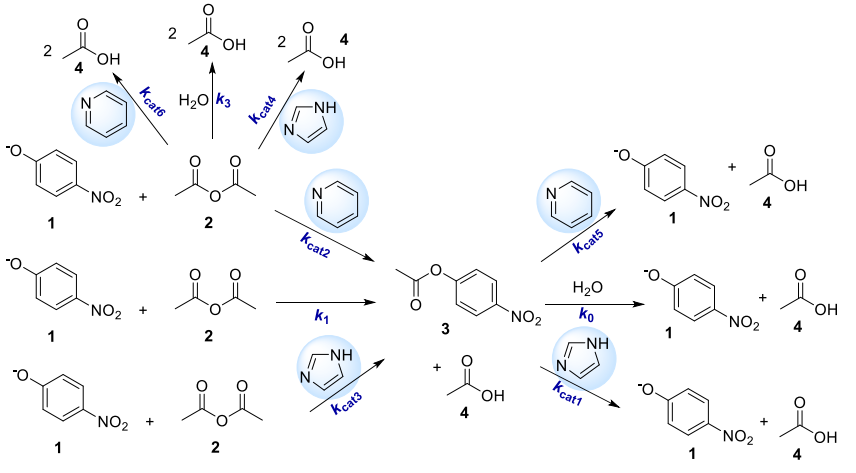

Scheme S4.1: Full reaction pathway overview, including organocatalysed and blank (uncatalysed) reactions. Both pyridine and imidazole catalyse the ester formation, hydrolysis and anhydride hydrolysis.

Blank reaction rate equations

When only the blank reaction takes place, the following equations apply:

Formation and degradation of the ester (**3**)

$$\frac{d[\mathbf{3}]}{dt} = k_1[\mathbf{1}][\mathbf{2}] - k_0[\mathbf{3}]$$

Formation of the acid (**4**)

$$\frac{d[\mathbf{4}]}{dt} = k_1[\mathbf{1}][\mathbf{2}] + 2k_3[\mathbf{2}] + k_0[\mathbf{3}]$$

Formation and degradation of the phenolate (**1**)

$$-\frac{d[\mathbf{1}]}{dt} = k_1[\mathbf{1}][\mathbf{2}] - k_0[\mathbf{3}]$$

Degradation of the anhydride (**2**)

$$-\frac{d[\mathbf{2}]}{dt} = k_1[\mathbf{1}][\mathbf{2}] + k_3[\mathbf{2}]$$

Experimental data fitting

Using k_0 0.0001 min^{-1} (blank hydrolysis – determined experimentally), the literature value for k_3 0.1575 min^{-1} for the hydrolysis of acetic anhydride **2** [5] and k_1 0.25 mM^{-1}min^{-1} as initial guesses. k_1 was determined by fitting the data of the blank reaction, giving k_1 0.3750 mM^{-1}min^{-1}, k_3 0.2219 min^{-1} and k_0 0.0001 min^{-1}.

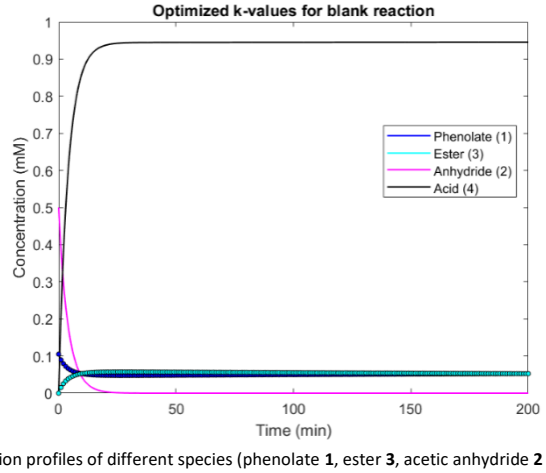

Figure S4.16: Concentration profiles of different species (phenolate **1**, ester **3**, acetic anhydride **2** and acetic acid **4**) over time for the blank reaction (uncatalysed): experimental data (dots) and model (lines) with new *k*-values k_1 0.375 mM^{-1}min^{-1}, k_3 0.2219 min^{-1} and k_0 0.0001 min^{-1}.

Pyridine catalysis and blank reaction rate equations

Next, with only the blank reaction and pyridine catalysis, the following equations apply:

Formation and degradation of the ester (**3**)

$$\frac{d[\mathbf{3}]}{dt} = k_1[\mathbf{1}][\mathbf{2}] + k_{cat2}[\boldsymbol{Py}][\mathbf{1}][\mathbf{2}] - k_0[\mathbf{3}] - k_{cat5}[\boldsymbol{Py}][\mathbf{3}]$$

Formation of the acid (**4**)

$$\frac{d[\mathbf{4}]}{dt} = k_1[\mathbf{1}][\mathbf{2}] + k_{cat2}[\boldsymbol{Py}][\mathbf{1}][\mathbf{2}] + 2k_3[\mathbf{2}] + k_0[\mathbf{3}] + k_{cat5}[\boldsymbol{Py}][\mathbf{3}] + 2\,k_{cat6}[\boldsymbol{Py}][\mathbf{2}]$$

Formation and degradation of the phenolate (**1**)

$$-\frac{d[\mathbf{1}]}{dt} = k_1[\mathbf{1}][\mathbf{2}] + k_{cat2}[\boldsymbol{Py}][\mathbf{1}][\mathbf{2}] - k_0[\mathbf{3}] - k_{cat5}[\boldsymbol{Py}][\mathbf{3}]$$

Degradation of the anhydride (**2**)

$$-\frac{d[\mathbf{2}]}{dt} = k_1[\mathbf{1}][\mathbf{2}] + k_{cat2}[\boldsymbol{Py}][\mathbf{2}] + k_3[\mathbf{2}] + k_{cat6}[\boldsymbol{Py}][\mathbf{2}]$$

Experimental data fitting

The previous k-values from the blank reaction were again used to determine k_{cat2} 35.0 $mM^{-2}min^{-1}$, k_{cat5} 0.002 $mM^{-1}min^{-1}$ and k_{cat6} 1.525 $mM^{-1}min^{-1}$.

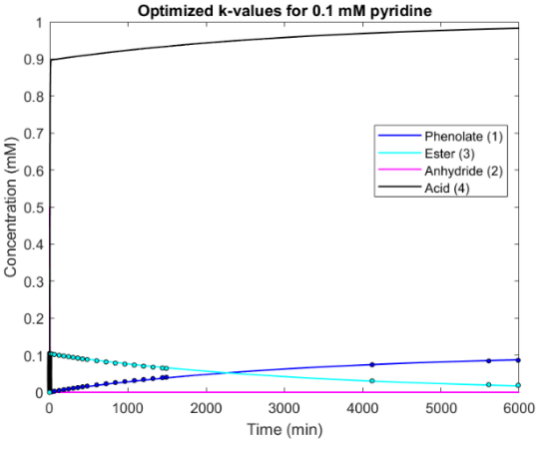

Figure S 4.17: Concentration profiles of different species (phenolate **1**, ester **3**, acetic anhydride **2** and acetic acid **4**) over time for the pyridine (0.1 mM) catalysed ester formation: Experimental data (dots) and model (line) with new *k*-values k_{cat2} 35.0 $mM^{-2}min^{-1}$, k_{cat5} 0.002 $mM^{-1}min^{-1}$ and k_{cat6} 1.525 $mM^{-1}min^{-1}$.

Imidazole catalysis and blank reaction rate equations

With only the blank reaction and the imidazole catalysis, the following equations apply:

Formation and degradation of the ester (**3**)

$$\frac{d[\mathbf{3}]}{dt} = k_1[\mathbf{1}][\mathbf{2}] + k_{cat3}[\boldsymbol{Im}][\mathbf{1}][\mathbf{2}] - k_0[\mathbf{3}] - k_{cat1}[\boldsymbol{Im}][\mathbf{3}]$$

Formation of the acid (**4**)

$$\frac{d[\mathbf{4}]}{dt} = k_1[\mathbf{1}][\mathbf{2}] + k_{cat3}[\boldsymbol{Im}][\mathbf{1}][\mathbf{2}] + 2k_3[\mathbf{2}] + k_0[\mathbf{3}] + k_{cat1}[\boldsymbol{Im}][\mathbf{3}] + 2\,k_{cat4}[\boldsymbol{Im}][\mathbf{2}]$$

Formation and degradation of the phenolate (**1**)

$$-\frac{d[\mathbf{1}]}{dt} = k_1[\mathbf{1}][\mathbf{2}] + k_{cat3}[\boldsymbol{Im}][\mathbf{1}][\mathbf{2}] - k_0[\mathbf{3}] - k_{cat1}[\boldsymbol{Im}][\mathbf{3}]$$

Degradation of the anhydride (**2**)

$$-\frac{d[\mathbf{2}]}{dt} = k_1[\mathbf{1}][\mathbf{2}] + k_{cat3}[\boldsymbol{Im}][\mathbf{1}][\mathbf{2}] + k_3[\mathbf{2}] + k_{cat4}[\boldsymbol{Im}][\mathbf{2}]$$

Experimental data fitting

k_{cat1} and k_0 were determined experimentally (k_{cat1} 0.475 $M^{-1}s^{-1}$ and k_0 $-4.0\cdot10^{-5}$ s^{-1}) (Table S4.2 comparison with literature). Yet, the k-values were optimized with MATLAB to fit the experimental data better (N.B. data for 5 mM imidazole were used as experimental values). Lower and upper bounds for the k-values were opposed with the fmincon constrained optimization function using a least squared cost function. The new k-values are: k_{cat} 0.0254 $mM^{-1}min^{-1}$ (0.423 $M^{-1}s^{-1}$) and k_0 0.0001 min^{-1} ($1.67\cdot10^{-6}$ s^{-1}).

Table S4.2: Rate constants comparison against literature values.

	This work	Bruice[6]	Bruice[6]	Lombardo[7]
k_{cat1} ($M^{-1}s^{-1}$)	0.475 ± 0.0034	0.211 ± 0.0035	0.328 ± 0.0152	0.130
k_0 (s^{-1})	$-4.0\cdot10^{-5}$	$9.0\cdot10^{-6}$	$7.33\cdot10^{-5}$	$4.35\cdot10^{-5}$
Buffer	MOPS pH 7.5 100 mM	Phosphate pH 7.9-8.0 5.4 mM	Phosphate pH 7.9-8.0 200 mM	Imidazole in 0.1 M KCl
Temperature	21 °C (294 K)	25 °C (298 K)	30 °C (298 K)	25 °C (298 K)
Method	Abs 400 nm	Abs 400 nm	Abs 400 nm	Abs 400 nm
Remarks	Corrected for imidazole free base species	Corrected for imidazole free base species	Corrected for imidazole free base species	Pure imidazole buffers used

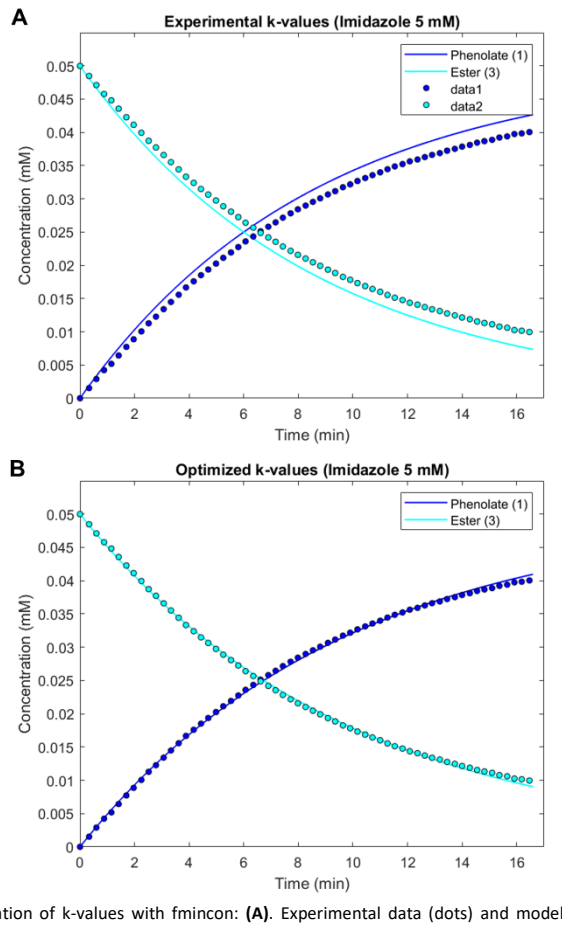

Figure S4.18: Optimization of k-values with fmincon: **(A)**. Experimental data (dots) and model (line) with experimentally obtained k-values (k_{cat1} 0.475 $M^{-1}s^{-1}$ and k_0 $-4.0 \cdot 10^{-5}$ s^{-1}). **(B)**. Experimental data (dots) and model (line) with new k-values k_{cat1} 0.0254 $mM^{-1}min^{-1}$ and k_0 0.00010 min^{-1}.

Then, the previous k-values were again used to determine k_{cat3} 0.124 $mM^{-2}min^{-1}$ and k_{cat4} 0.0565 $mM^{-1}min^{-1}$.

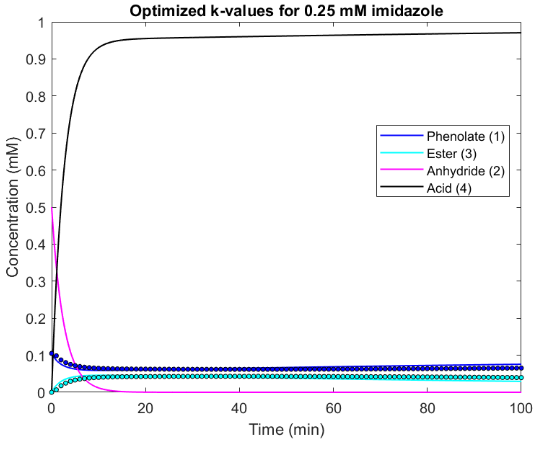

Figure S 4.19: Concentration profiles of different species (phenolate **1**, ester **3**, acetic anhydride **2** and acetic acid **4**) over time for the imidazole (0.25 mM) catalysed ester formation: Experimental data (dots) and model (line) with new k-values k_{cat3} 0.124 $mM^{-2}min^{-1}$ and k_{cat4} 0.0565 $mM^{-1}min^{-1}$.

Pyridine and imidazole catalysed reaction cycle rate equations

When the blank reaction, pyridine and imidazole catalysis take place the following equations apply:

Formation and degradation of the ester (**3**)

$$\frac{d[\mathbf{3}]}{dt} = k_1[\mathbf{1}][\mathbf{2}] + k_{cat2}[\boldsymbol{Py}][\mathbf{1}][\mathbf{2}] - k_0[\mathbf{3}] - k_{cat5}[\boldsymbol{Py}][\mathbf{3}] + k_{cat3}[\boldsymbol{Im}][\mathbf{1}][\mathbf{2}] - k_{cat1}[\boldsymbol{Im}][\mathbf{3}]$$

Formation of the acid (**4**)

$$\frac{d[\mathbf{4}]}{dt} = k_1[\mathbf{1}][\mathbf{2}] + k_{cat2}[\boldsymbol{Py}][\mathbf{1}][\mathbf{2}] + 2k_3[\mathbf{2}] + k_0[\mathbf{3}] + k_{cat5}[\boldsymbol{Py}][\mathbf{3}] + 2\,k_{cat6}[\boldsymbol{Py}][\mathbf{2}] + k_{cat1}[\boldsymbol{Im}][\mathbf{3}] + k_{cat3}[\boldsymbol{Im}][\mathbf{1}][\mathbf{2}] + 2\,k_{cat4}[\boldsymbol{Im}][\mathbf{2}]$$

Formation and degradation of the phenolate (**1**)

$$-\frac{d[\mathbf{1}]}{dt} = k_1[\mathbf{1}][\mathbf{2}] + k_{cat2}[\boldsymbol{Py}][\mathbf{1}][\mathbf{2}] - k_0[\mathbf{3}] - k_{cat5}[\boldsymbol{Py}][\mathbf{3}] + k_{cat3}[\boldsymbol{Im}][\mathbf{1}][\mathbf{2}] - k_{cat1}[\boldsymbol{Im}][\mathbf{3}]$$

Degradation of the anhydride (**2**)

$$-\frac{d[\mathbf{2}]}{dt} = k_1[\mathbf{1}][\mathbf{2}] + k_{cat2}[\boldsymbol{Py}][\mathbf{1}][\mathbf{2}] + k_3[\mathbf{2}] + k_{cat6}[\boldsymbol{Py}][\mathbf{2}] + k_{cat3}[\boldsymbol{Im}][\mathbf{1}][\mathbf{2}] + k_{cat4}[\boldsymbol{Im}][\mathbf{2}]$$

Explanation for model optimization and deviations

The k-values were allowed to be optimised by MATLAB using the constrained optimization function (fmincon) with a least squared cost function (opposing lower and upper bounds for the k-values: k_{min}=0.5·k_0 and k_{max}=2·k_0). Yet even with the optimization, these k-values show some deviation (Table S4.3):

Table S4.3: Final reaction rate constants as determined from experimental data and subsequent MATLAB fitting.

k-value	Units	Reaction	Average	St. Dev.	Final
k_0	($\cdot 10^{-4}$) min^{-1}	Ester hydrolysis uncatalysed	1.23	0.44	1.23 ± 0.44
k_1	($\cdot 10^{-1}$) $mM^{-1}min^{-1}$	Ester formation uncatalysed	3.57	2.03	3.57 ± 2.03
k_3	($\cdot 10^{-1}$) min^{-1}	Anhydride hydrolysis uncatalysed	3.00	1.33	3.00 ± 1.33
k_{cat1}	($\cdot 10^{-2}$) $mM^{-1}min^{-1}$	Ester hydrolysis imidazole catalysed	2.23	1.06	2.23 ± 1.06
k_{cat2}	($\cdot 10^{1}$) $mM^{-2}min^{-1}$	Ester formation pyridine catalysed	1.88	1.04	1.88 ± 1.04
k_{cat3}	($\cdot 10^{-2}$) $mM^{-2}min^{-1}$	Ester formation imidazole catalysed	6.41	4.15	6.41 ± 4.15
k_{cat4}	($\cdot 10^{-1}$) $mM^{-1}min^{-1}$	Anhydride hydrolysis imidazole catalysed	1.66	0.76	1.66 ± 0.76
k_{cat5}	($\cdot 10^{-3}$) $mM^{-1}min^{-1}$	Ester hydrolysis pyridine catalysed	2.68	1.64	2.68 ± 1.64
k_{cat6}	$mM^{-1}min^{-1}$	Anhydride hydrolysis pyridine catalysed	4.03	1.68	4.03 ± 1.68

The k-values with most variation are related to the anhydride species and a deviation is anticipated, since the acetic anhydride hydrolysis is very rapid[5] and already occurs before the first sample has been measured. Besides, the mechanism for imidazole and pyridine catalysis is in fact more complicated than was assumed in this simplified model and deals with a pre-equilibrium of reactive intermediate formation (acetyl-pyridinium and acetyl-imidazole), acetate ion inhibition and contributions from nucleophilic and general acid/ base catalysis.[2, 8] Finally, the reactive intermediates for imidazole and pyridine catalysis can also be interconverted, complicating the model.

Pyridine variation: experimental data versus model

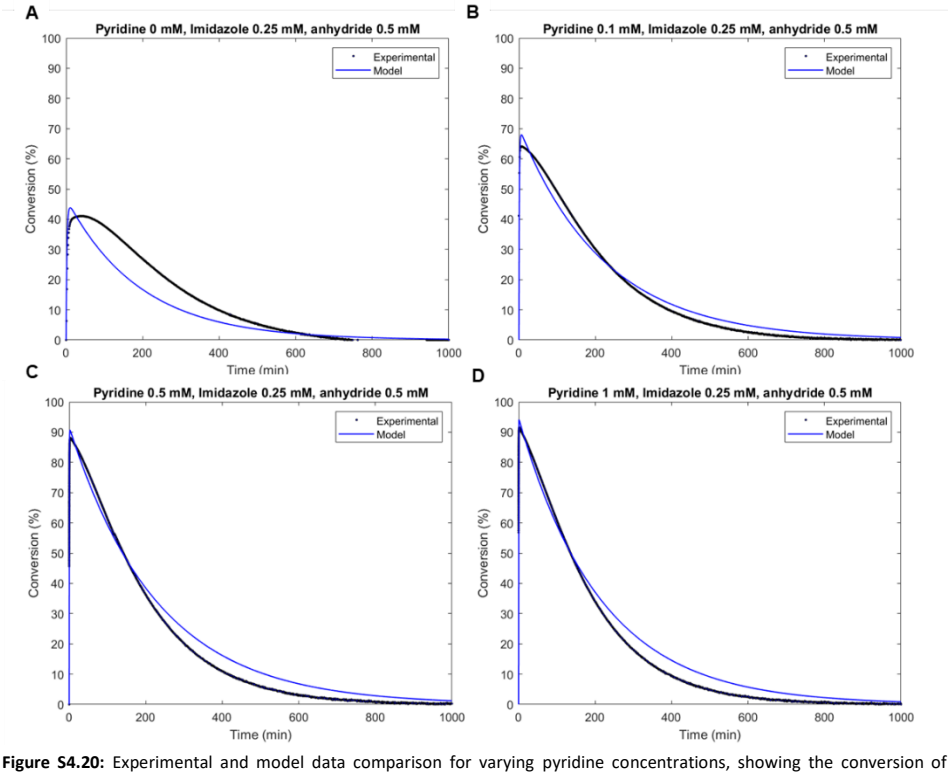

Figure S4.20: Experimental and model data comparison for varying pyridine concentrations, showing the conversion of *p*-nitrophenol(ate) **1** (start: 0.1 mM) in MOPS buffer (100 mM, pH 7.5) with 5% acetonitrile: **(A)**. 0.5 mM acetic anhydride **2**, 0.25 mM imidazole and 0 mM pyridine. **(B)**. 0.5 mM acetic anhydride **2**, 0.25 mM imidazole and 0.1 mM pyridine. **(C)**. 0.5 mM acetic anhydride **2**, 0.25 mM imidazole and 0.5 mM pyridine. **(D)**. 0.5 mM acetic anhydride **2**, 0.25 mM imidazole and 1 mM pyridine. The presented experimental data are equal to Figure 4.1A.

Imidazole variation: experimental data versus model

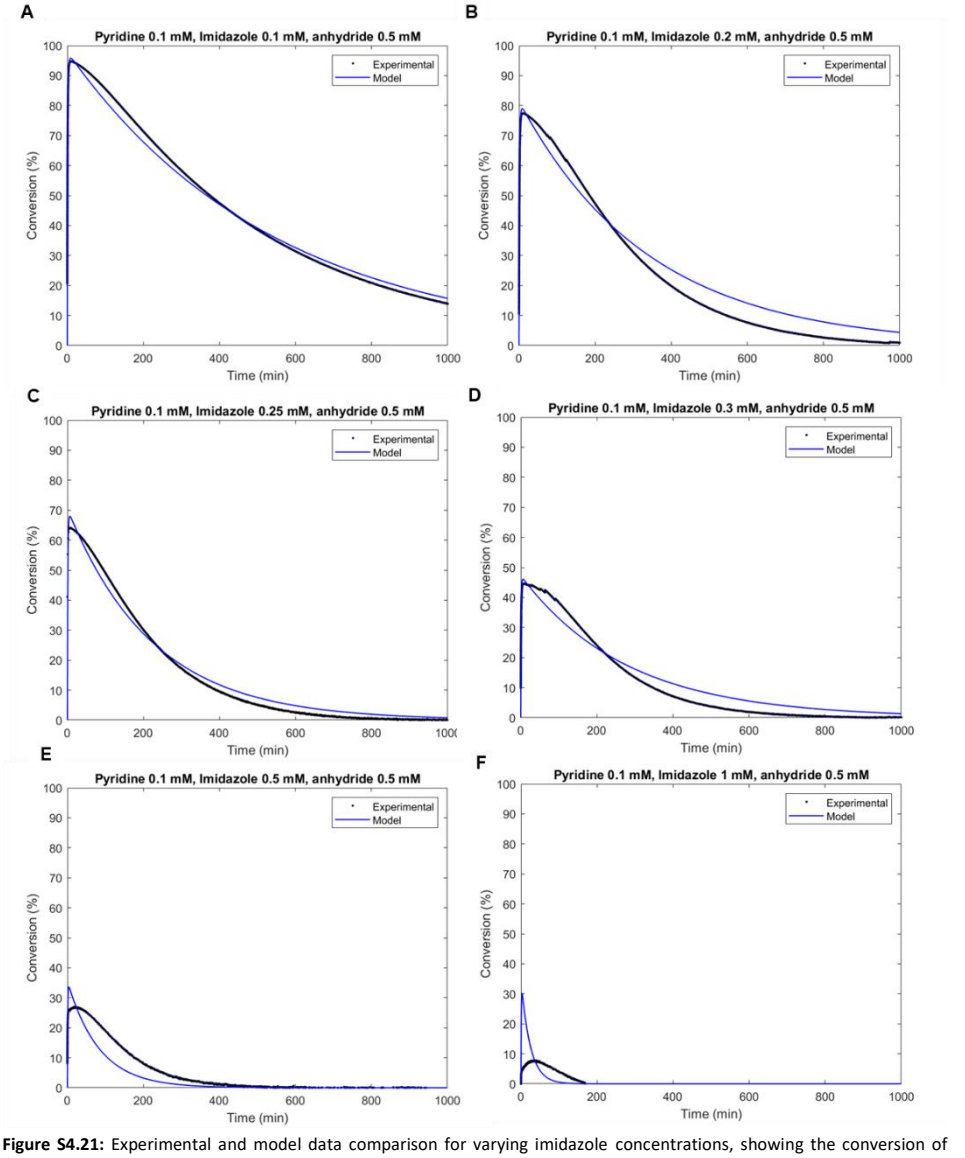

Figure S4.21: Experimental and model data comparison for varying imidazole concentrations, showing the conversion of *p*-nitrophenol(ate) **1** (start: 0.1 mM) in MOPS buffer (100 mM, pH 7.5) with 5% acetonitrile: **(A)**. 0.5 mM acetic anhydride **2**, 0.1 mM imidazole and 0.1 mM pyridine. **(B)**. 0.5 mM acetic anhydride **2**, 0.2 mM imidazole and 0.1 mM pyridine. **(C)**. 0.5 mM acetic anhydride **2**, 0.25 mM imidazole and 0.1 mM pyridine. **(D)**. 0.5 mM acetic anhydride **2**, 0.3 mM imidazole and 0.1 mM pyridine. **(E)**. 0.5 mM acetic anhydride **2**, 0.5 mM imidazole and 0.1 mM pyridine. **(F)**. 0.5 mM acetic anhydride **2**, 1 mM imidazole and 0.1 mM pyridine. The presented experimental data are equal to Figure 4.1B.

Acetic anhydride variation: experimental data versus model

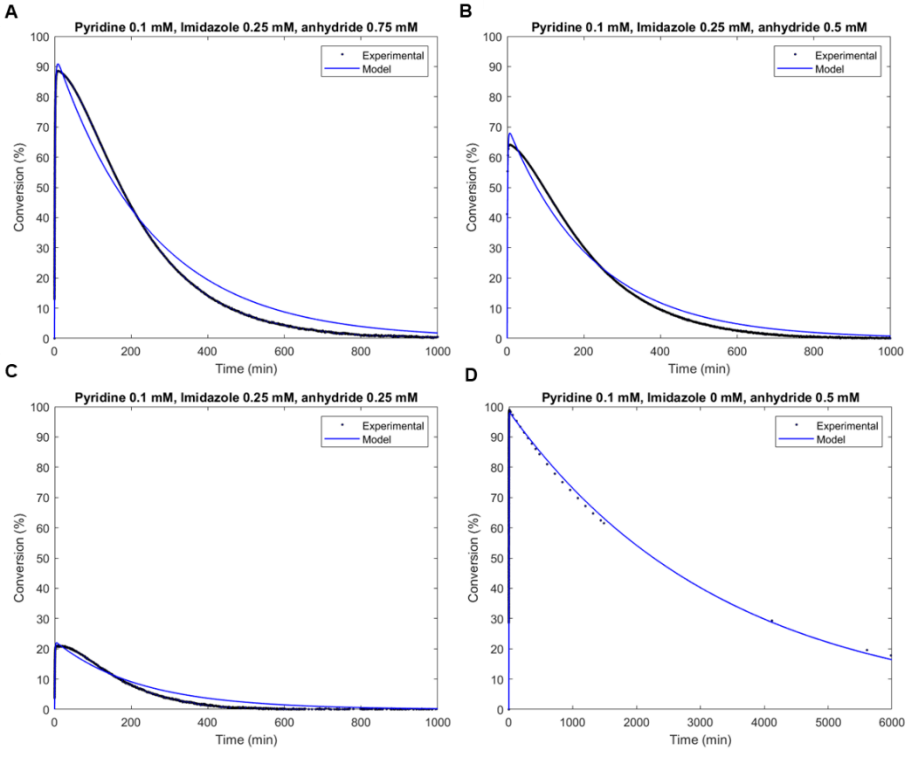

Figure S4.22: Experimental and model data comparison for varying acetic anhydride **2** concentrations and imidazole, showing the conversion of *p*-nitrophenol(ate) **1** (start: 0.1 mM) in MOPS buffer (100 mM, pH 7.5) with 5% acetonitrile: **(A)**. 0.75 mM acetic anhydride **2**, 0.25 mM imidazole and 0.1 mM pyridine. **(B)**. 0.5 mM acetic anhydride **2**, 0.25 mM imidazole and 0.1 mM pyridine. **(C)**. 0.25 mM acetic anhydride **2**, 0.25 mM imidazole and 0.1 mM pyridine. **(D)**. 0.5 mM acetic anhydride **2**, 0 mM imidazole and 0.1 mM pyridine. The presented experimental data are equal to Figure 4.1C.

Ester forward and backward reaction rate comparison

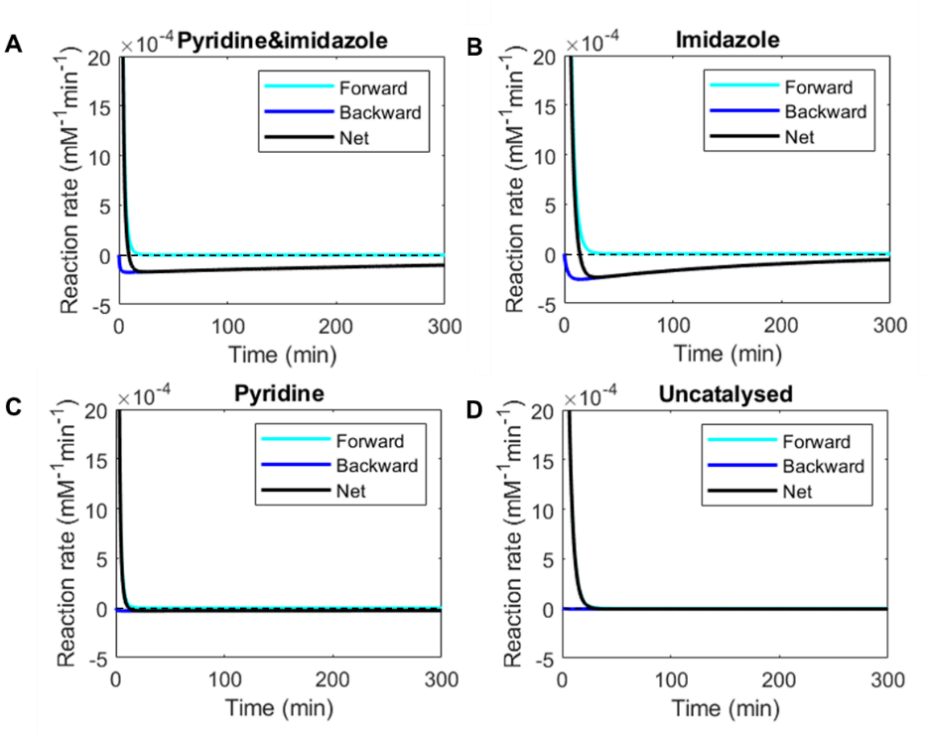

Figure S4.23: Rate of ester **3** formation (Forward - cyan line), degradation (Backward - blue line) and net formation (Net - black line) based on the rate equations of the kinetic model for various catalytic conditions from 0-300 min: **(A)**. Pyridine and imidazole catalysis: 0.5 mM acetic anhydride **2**, 0.1 mM imidazole and 0.1 mM pyridine. **(B)**. Imidazole catalysis: 0.5 mM acetic anhydride **2**, 0.25 mM imidazole and no pyridine. **(C)**. Pyridine catalysis: 0.5 mM acetic anhydride **2**, 0.1 mM pyridine and no imidazole. **(D)**. Uncatalysed blank reaction: 0.5 mM acetic anhydride **2**. N.B. for panel **(D)** the forward reaction rate coincides with the net rate and is therefore obscured.

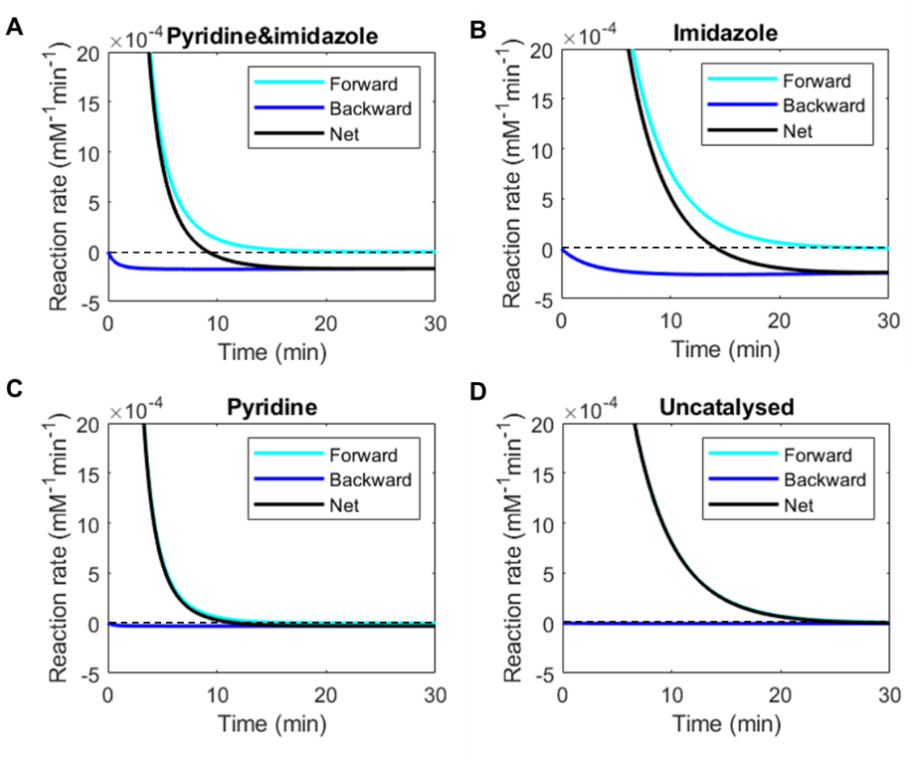

Figure S4.24: Rate of ester **3** formation (Forward - cyan line), degradation (Backward - blue line) and net formation (Net - black line) based on the rate equations of the kinetic model for various catalytic conditions from 0-30 min: **(A)**. Pyridine and imidazole catalysis: 0.5 mM acetic anhydride **2**, 0.1 mM imidazole and 0.1 mM pyridine. **(B)**. Imidazole catalysis: 0.5 mM acetic anhydride **2**, 0.25 mM imidazole and no pyridine. **(C)**. Pyridine catalysis: 0.5 mM acetic anhydride **2**, 0.1 mM pyridine and no imidazole. **(D)**. Uncatalysed blank reaction: 0.5 mM acetic anhydride **2**. N.B. for panel **(D)** the forward reaction rate coincides with the net rate and is therefore obscured.

4.5.8 FTIR PAANY

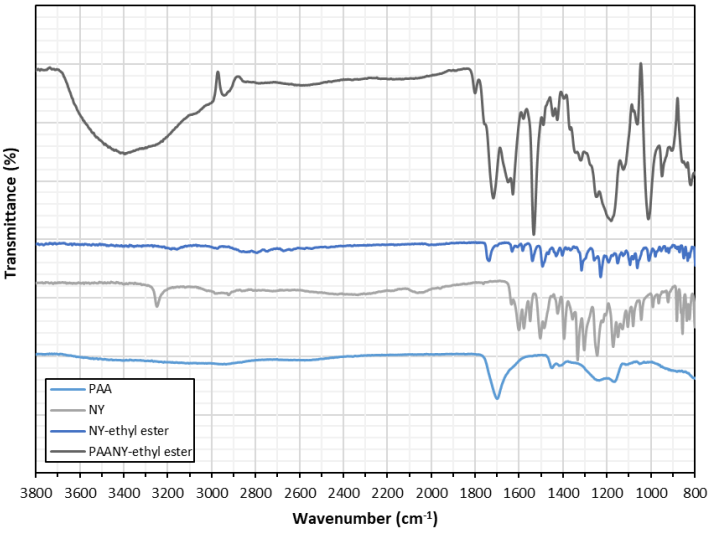

Figure S4.25: FTIR spectra comparison between PAANY-ethyl ester, PAA, NY-ethyl ester and NY. The following peaks can be identified: C=O stretching mode 1730 cm^{-1} from the ester (in PAANY-ethyl ester and NY-ethyl ester), C=O stretching mode 1700 cm^{-1} from the acid backbone (in PAANY-ethyl ester and PAA), C=O stretching mode 1680 cm^{-1} from the amide bond (in PAANY-ethyl ester, NY-ethyl ester and NY), O-H bending mode 1350 cm^{-1} from the phenol (in PAANY-ethyl ester, NY-ethyl ester and NY) and the C-O-C stretching mode 1050 cm^{-1} from the ester (in PAANY-ethyl ester and NY-ethyl ester).

4.5.9 ^{1}H NMR PAANY

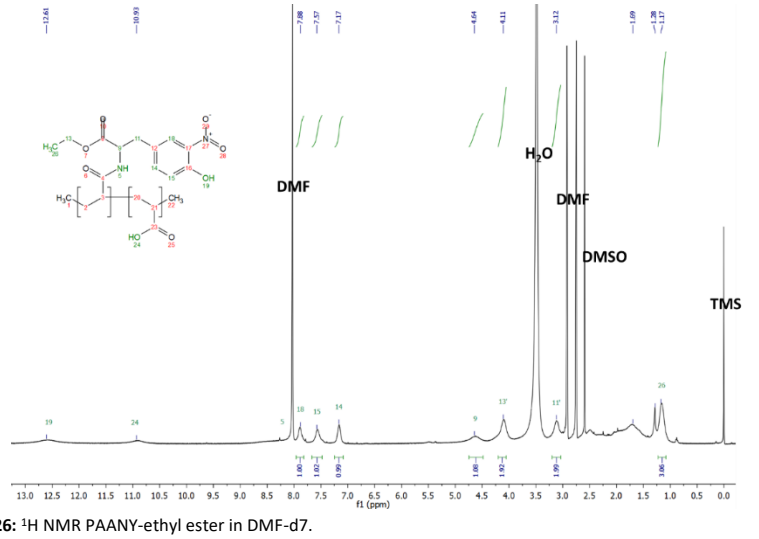

Figure S4.26: ^{1}H NMR PAANY-ethyl ester in DMF-d7.

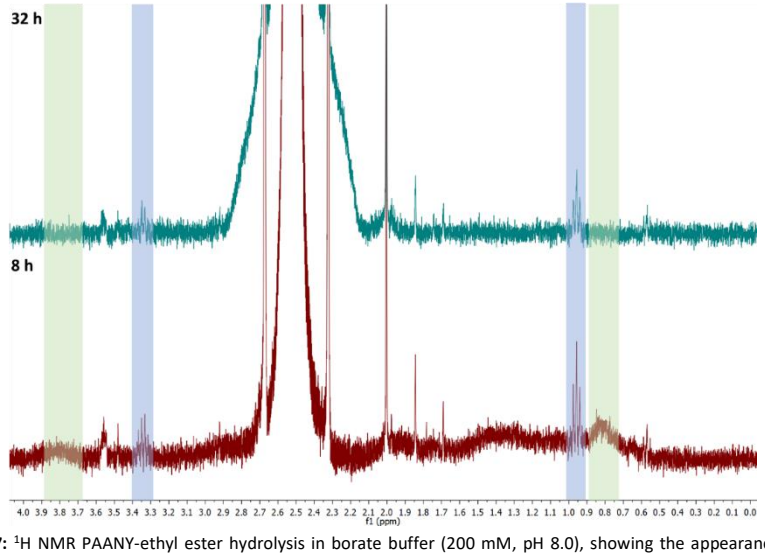

Figure S4.27: ^{1}H NMR PAANY-ethyl ester hydrolysis in borate buffer (200 mM, pH 8.0), showing the appearance of sharp ethanol peaks around 0.95 ppm (triplet) and 3.35 ppm (quartet) highlighted in the blue frames and the disappearance of the broader polymer ethyl ester peaks (0.8 ppm and 3.8 ppm) highlighted in the green frames.

4.5.10 DLS size distributions

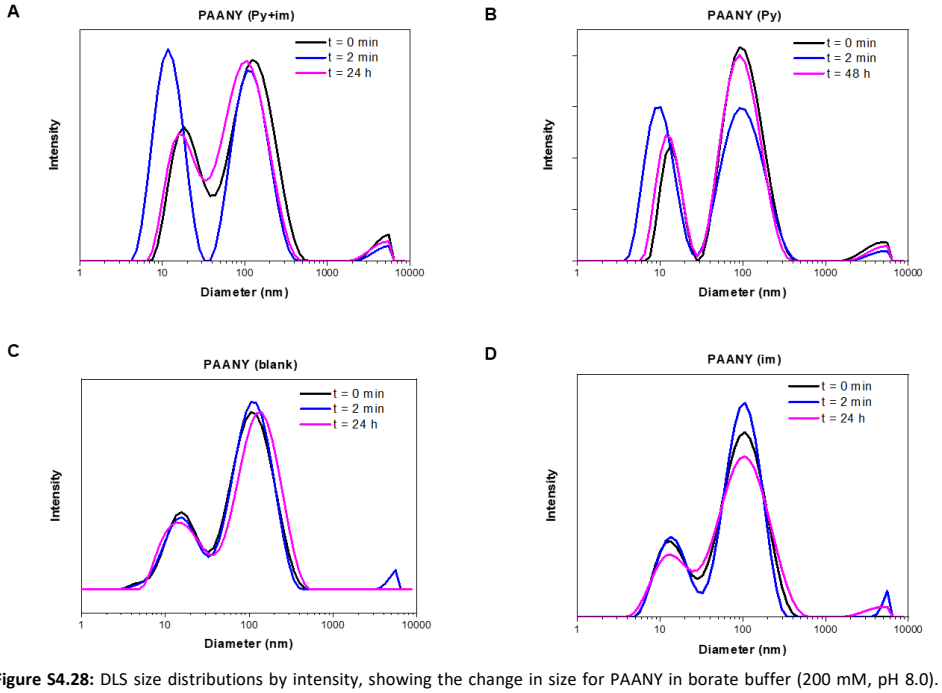

Figure S4.28: DLS size distributions by intensity, showing the change in size for PAANY in borate buffer (200 mM, pH 8.0). **(A)**. 0.30 mM PAANY (0.24 mg/mL), 6 mM acetic anhydride **2**, 0.75 mM imidazole and 0.30 mM pyridine. **(B)**. 0.30 mM PAANY (0.24 mg/mL), 6 mM acetic anhydride **2** and 0.30 mM pyridine. **(C)**. 0.30 mM PAANY (0.24 mg/mL) and 6 mM acetic anhydride **2**. **(D)**. 0.30 mM PAANY (0.24 mg/mL), 6 mM acetic anhydride **2** and 0.75 mM imidazole.

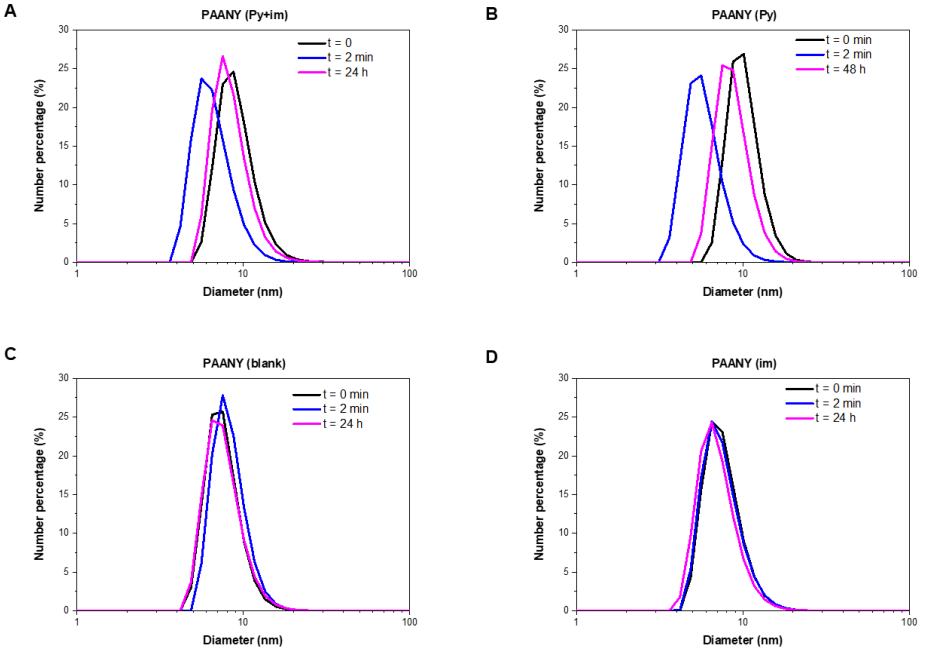

Figure S4.29: DLS size distributions by number, showing the change in size for PAANY (~10 nm) in borate buffer (200 mM, pH 8.0). **(A)**. 0.30 mM PAANY (0.24 mg/mL), 6 mM acetic anhydride **2**, 0.75 mM imidazole and 0.30 mM pyridine. **(B)**. 0.30 mM PAANY (0.24 mg/mL), 6 mM acetic anhydride **2** and 0.30 mM pyridine. **(C)**. 0.30 mM PAANY (0.24 mg/mL) and 6 mM acetic anhydride **2**. **(D)**. 0.30 mM PAANY (0.24 mg/mL), 6 mM acetic anhydride **2** and 0.75 mM imidazole.

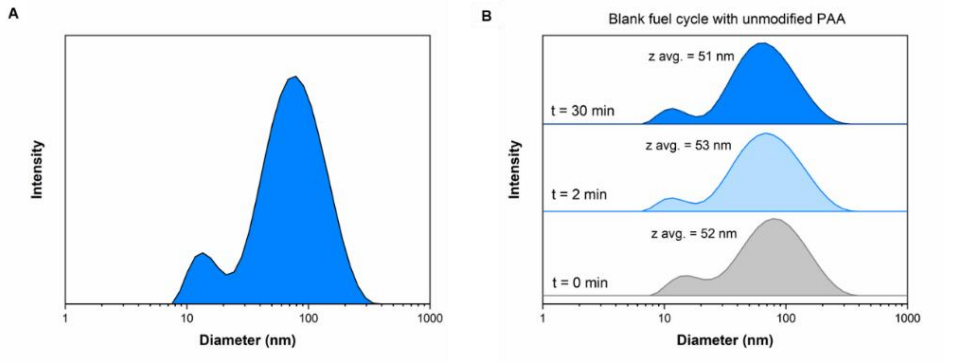

Figure S4.30: (A). DLS size distribution by intensity of unmodified PAA (0.24 mg/mL) in borate buffer (200 mM, pH 8.0), showing two peaks: a small unimer and larger aggregate peak. **(B)**. DLS size distribution by intensity of blank reaction with unmodified PAA in borate buffer (200 mM, pH 8.0), showing no size change over time. Conditions: PAA (0.24 mg/mL), 6 mM acetic anhydride **2**, 0.75 mM imidazole and 0.30 mM pyridine.

4.5.11 DLS size calibration

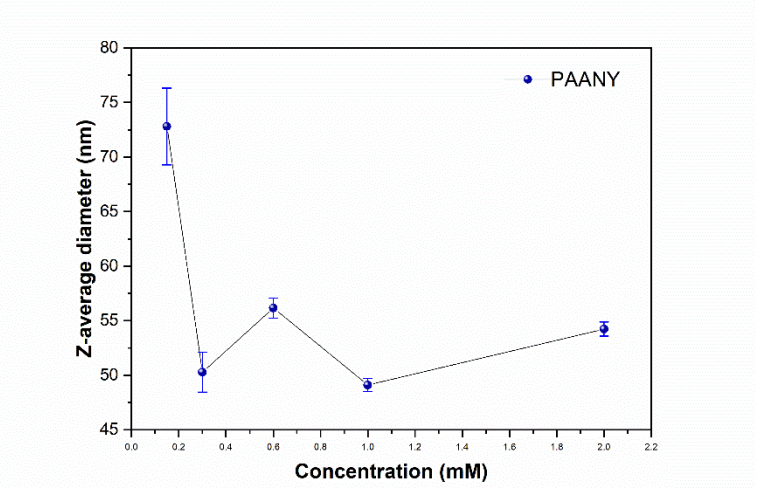

Figure S4.31: DLS size calibration for various PAANY concentrations in borate buffer (200 mM, pH 8.0). With higher polymer concentrations the size fluctuations become smaller. The reported diameter is the z-average diameter, which takes into account PAANY unimers (~10 nm) and buffer/ polymer aggregates (~100 nm).

4.5.12 DOSY diffusion coefficient and size calculation

By measuring the DOSY spectrum of the polymer with NMR and extracting the diffusion coefficient, we can confirm the particle size via the Stokes-Einstein equation:

$$D = \frac{k_B T}{3\pi\mu d}$$

, where D is the diffusion coefficient, K_B the Boltzmann constant, T the temperature, μ the viscosity of the bulk medium and d the solute diameter (polymer).

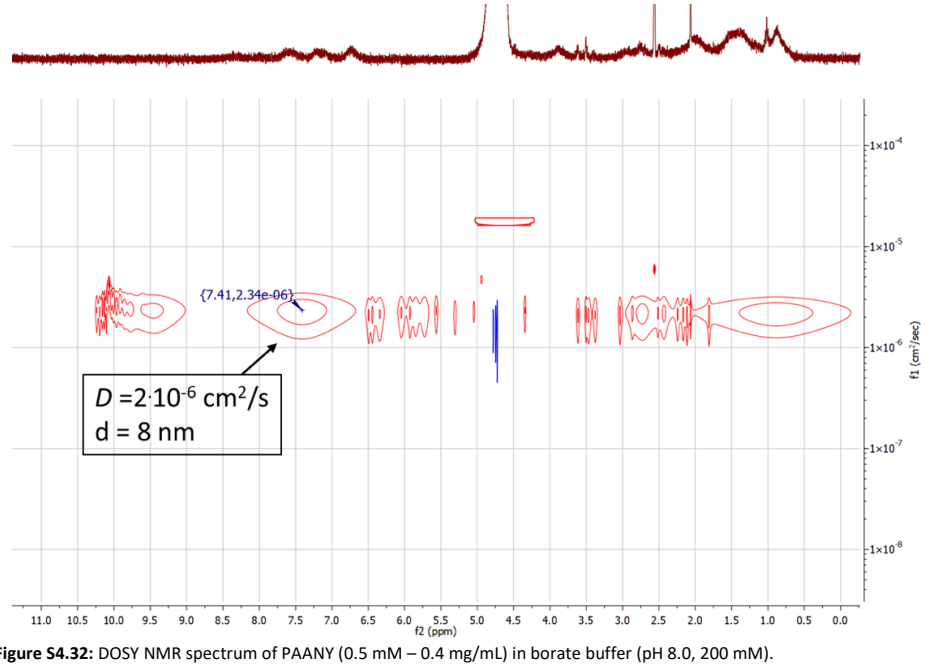

Figure S4.32: DOSY NMR spectrum of PAANY (0.5 mM – 0.4 mg/mL) in borate buffer (pH 8.0, 200 mM).

4.5.13 Cryo-EM imaging of PAANY

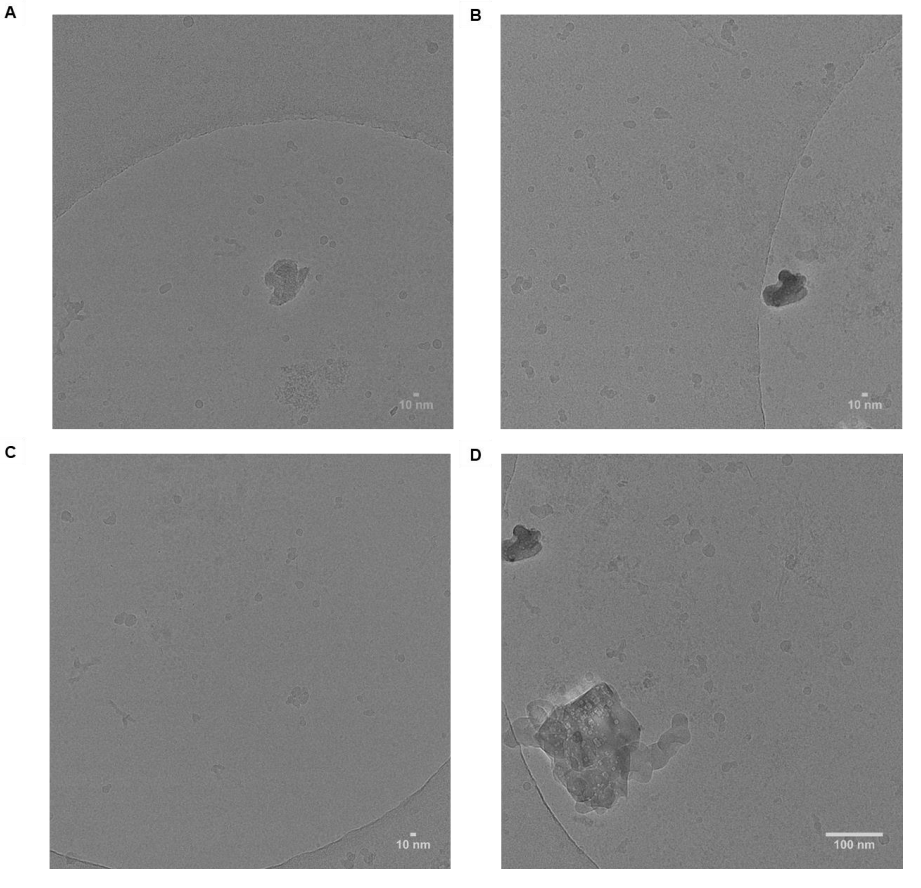

Figure S4.33: Representative Cryo-EM images of PAANY in borate buffer (200 mM, pH 8.0) at different magnifications. Small spherical structures can be identified with an average diameter of 10 nm along with larger clusters with an average diameter of 24 nm.

4.5.14 Viscosity measurements of PAANY

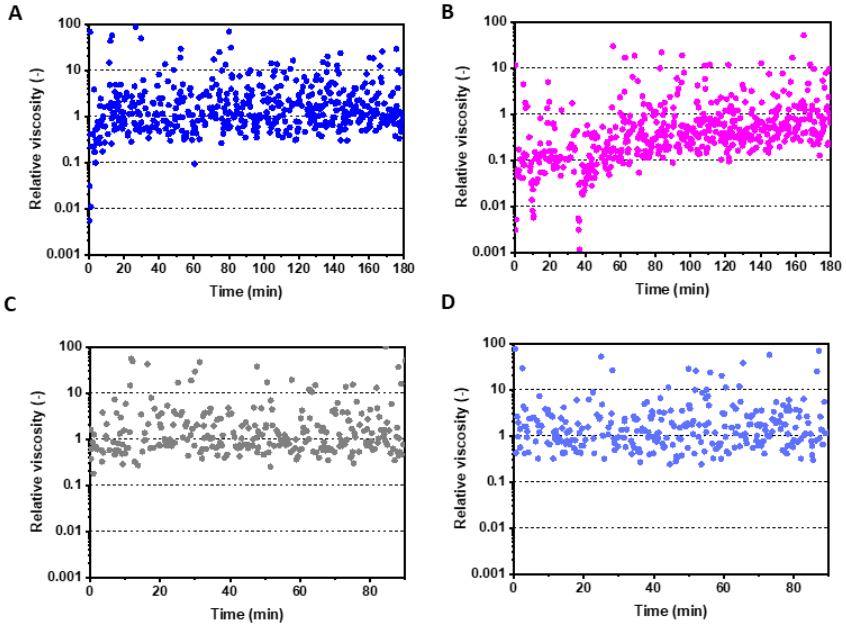

Figure S4.34: Relative viscosity under time sweep measurements of the following samples: **(A)**. Only PAANY (0.3 mM) in borate buffer (200 mM, pH 8.0). **(B)**. Acetylated PAANY (0.3 mM) with 0.75 mM imidazole, 0.3 mM pyridine, 6 mM acetic anhydride **2** in borate buffer (200 mM, pH 8.0). **(C)**. Only borate buffer (200 mM, pH 8.0). **(D)**. 6 mM acetic anhydride **2** in borate buffer (200 mM, pH 8.0). The relative viscosity for each sample was determined by normalisation with the viscosity value at the end of the time sweep measurement. (γ = 0.05%, ω = 1 Hz, 25 °C)

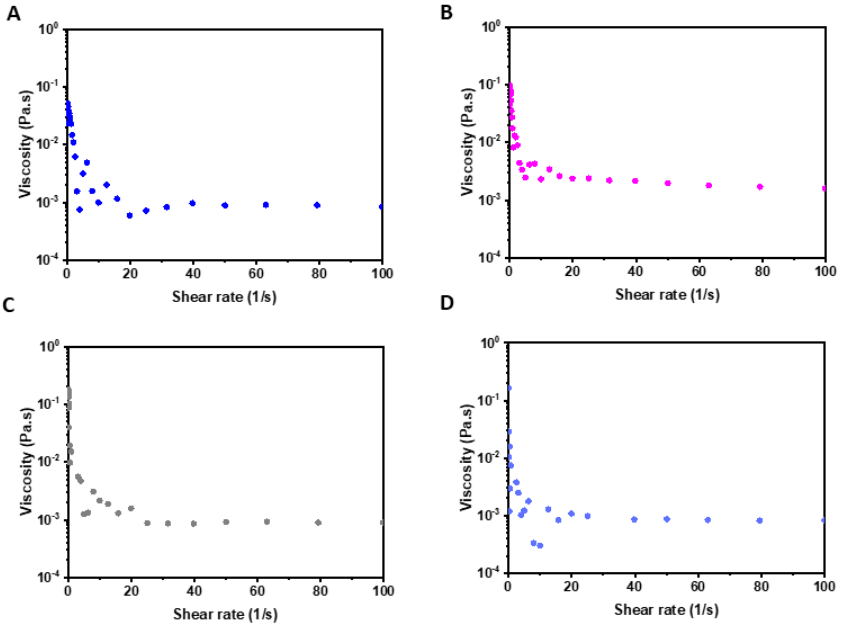

Figure S4.35: Viscosity under flow step measurements of the following samples: **(A)**. Only PAANY (0.3 mM) in borate buffer (200 mM, pH 8.0). **(B)**. Acetylated PAANY (0.3 mM) with 0.75 mM imidazole, 0.3 mM pyridine, 6 mM acetic anhydride **2** in borate buffer (200 mM, pH 8.0). **(C)**. Only borate buffer (200 mM, pH 8.0). **(D)**. 6 mM acetic anhydride **2** in borate buffer (200 mM, pH 8.0).

4.5.15 Supplementary references

1. J. F. Kirsch and W. P. Jencks, *J. Am. Chem. Soc.*, 1964, **86**, 837-846.
2. A. R. Fersht and W. P. Jencks, *J. Am. Chem. Soc.*, 1970, **92**, 5432-5442.
3. J. Bowie and B. Nussey, *J. Mass Spectrom.*, 1972, **6**, 429-442.
4. J. H. Bowie and B. J. Stapleton, *Aust. J. Chem.*, 1975, **28**, 1011-1015.
5. V. Gold, *J. Chem. Soc. Faraday Trans*, 1948, **44**, 506-518.
6. T. C. Bruice and G. L. Schmir, *J. Am. Chem. Soc.*, 1957, **79**, 1663-1667.
7. A. Lombardo, *J. Chem. Educ.*, 1982, **59**, 887.
8. J. F. Kirsch and W. P. Jencks, *J. Am. Chem. Soc.*, 1964, **86**, 833-837.

TRANSIENT COLLOID ASSEMBLY BY FUEL-DRIVEN MODULATION OF DEPLETION INTERACTIONS

CHAPTER 5

In biology, energy stored in chemical fuels is used to drive processes energetically uphill, enabling the highly dynamic behaviour of living organisms. The out-of-equilibrium behaviour can propagate from molecular reaction networks to the micro- and macroscopic scale. These natural phenomena have sparked the design of man-made out-of-equilibrium chemical reaction networks (CRNs) and dissipative assembly systems with hydrogels, (supra)polymers, vesicles/micelles and colloids. In colloidal systems, the assembly process is typically controlled by balancing the interaction forces. Here, we use a polymeric depletant integrated in a fuel-driven esterification CRN to induce transient colloidal assembly. The polymer undergoes a temporal coil-globule transition upon acetylation by the chemical fuel. In the random coil conformation, it acts as depletant agent for the silica colloids, promoting colloidal aggregation. As compact globule, the polymer loses its depletant characteristics. During the fuel cycle the polymer cyclically transitions from one form to the other, directly influencing colloidal aggregation and redispersion. Thus, a fuel-driven CRN on the molecular scale results in a microscopic response with a transient colloidal depletion cycle. Overall, the time-dependent propagation of out-of-equilibrium activity across length scales presented here, offers opportunities to design responsive materials with life-like properties.

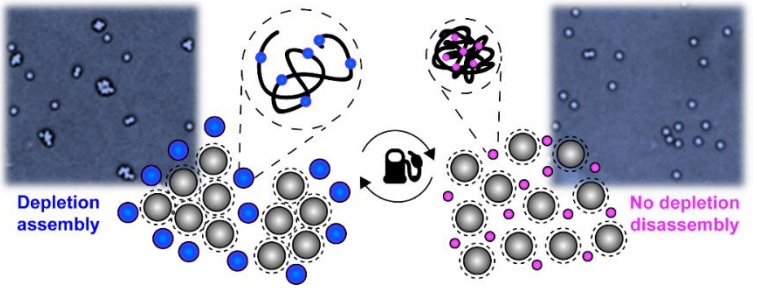

This chapter will be published as:
M.P. van der Helm, C.-L. Wang, R.W. Lewis, S. Schyck, L. Rossi, R. Eelkema, *manuscript submitted*.

5.1 INTRODUCTION

Living systems use energy in the form of chemical fuels to drive thermodynamically unfavourable processes, which gives them the ability to sense, replicate, proliferate, self-heal and amplify signals. These biological out-of-equilibrium systems have a molecular origin, yet can give rise to micro- or even macroscopic responses.[1-3] Prime examples from biology are microtubules and actin filaments that play key roles in cellular motility. Their underlying CRNs are based on the consumption of a chemical fuel (i.e. GTP or ATP) to drive the assembly of transiently stable supramolecular polymers from individual activated tubulin or actin building blocks.[4] Inspired by these natural systems, many dissipative assembly processes have been designed,[5-13] including fuel-driven colloidal assembly[14-20]. The majority of these colloidal systems decorate the colloids' surface with functional groups that can then participate in a specific fuel-driven CRN. That way the interaction potential of the colloids can be altered during the fuel cycle, leading to a transient assembly response. In general, colloidal stability and assembly are governed by an interplay between different interaction forces.[21, 22] On top of that, nanoscale polymeric particles and surfactant assemblies can also promote colloidal assembly via depletion.[23] Depletion is an attractive force of entropic origin which arises when colloids are dispersed in a solution containing non-adsorbing polymers.[24-26] In this scenario colloids are surrounded by a so-called exclusion zone, a volume depleted of polymers which thickness corresponds to the radius of gyration of the polymers. When two colloids approach each other so that the corresponding exclusion zones overlap (i.e. polymers cannot fit between the colloids anymore), colloids become attractive due to an osmotic pressure imbalance. The size, orientation and hydrophilicity of the depletants can be controlled by external factors, such as pH, temperature and ionic interactions for reversible regulation of depletion interactions.[27-33] In the current work, however, we aim to control colloidal interactions with a polymeric depletant that is integrated in a fuel-driven CRN. The fuel cycle integration provides autonomous control over the time domain and does not require any external temperature or pH changes. Previously (chapter 4), we developed a fuel-driven transient polymer acetylation CRN with acetic anhydride as chemical fuel to regulate product yield and lifetime.[34] We were able to control polymer conformation and aggregation with two organocatalysts (pyridine and imidazole) and by varying fuel levels. The polymer we developed consisted of a poly(acrylic acid) (PAA) backbone with 25% coverage of 3-nitro-L-tyrosine (NY), which could undergo transient acetylation causing a temporal coil to globule transition. Now, we exploit this fuel-driven polymer coil-globule transition to dynamically control its depletion ability, leading to transient colloidal assembly (Figure 5.1). PAANY with negatively charged NY groups has a random coil conformation (diameter 8.6 nm). Upon addition of the chemical fuel (acetic anhydride) the NY moieties get acetylated, generating PAANY-acyl, which adopts a compact globule

conformation (diameter ~5.9 nm) due to a decreased charged density and increased hydrophobic surface. We hypothesize that native PAANY in the random coil conformation is a polymeric depletant for silica colloids (diameter = 1 µm), making the colloids assemble. PAANY-acyl, as a smaller compact globule, loses the depletion capacity, leading to disassembly of the colloids. Over time, PAANY-acyl will revert back to native PAANY through hydrolysis, leading to a conformational change and a concomitant increase in depletion ability. Hence, a full fuel cycle initiated by the addition of chemical fuel on the molecular scale causes a transient colloidal assembly-disassembly-assembly cycle on the microscopic level.

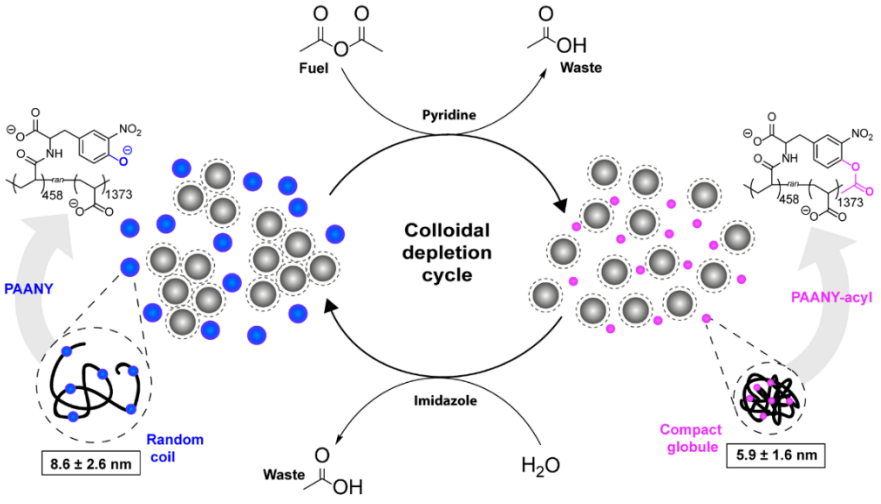

Figure 5.1: Colloidal depletion cycle regulated by a fuel-driven esterification network with a polymer random coil (large size - depletant) to compact globule transition (small size – no depletant) due to transient acetylation of 3-nitro-L-tyrosine functionalized (poly)acrylic acid (PAANY).

5.2 RESULTS AND DISCUSSION

At first, the depletion capability of PAANY was investigated. To this end, different concentrations of PAANY in borate buffer (pH 9.0, 200 mM) were added to a solution of silica microspheres ($1.15 \cdot 10^8$ # colloids/mL) to construct an aggregation calibration curve (Figure S5.1). From this curve, it becomes clear that at least 0.5 mM PAANY should be used to have a significant depletion effect. In contrast to our previous work (chapter 4)[34], for these colloidal experiments borate buffer of pH 9.0 was used as colloidal silica was found to stick to the glass wall of the capillary at lower pH. In the absence of the anhydride fuel the colloids form a stable dispersion with PAANY acting as a depletant. Subsequently, different concentrations of PAANY (0.5/0.6/0.7 mM) were used in fuel cycles with acetic anhydride (chemical fuel), pyridine (catalyst forward reaction) and imidazole (catalyst backward reaction) (Figure 5.2 and Figure S5.3-4).

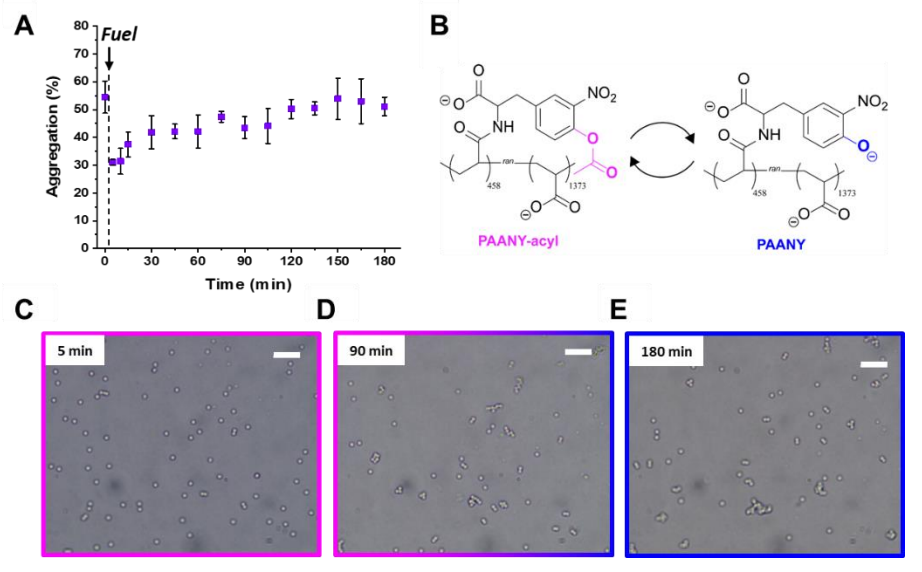

Figure 5.2: (A). Colloid aggregation as a function time for a fuel cycle. **(B)**. Upon fuel (acetic anhydride) addition PAANY is acetylated to PAANY-acyl. **(C)**. The acetylation induces colloidal disassembly (30% aggregation at 5 min). **(D-E)**. Over time PAANY-acyl is deacetylated giving rise to the reappearance of colloidal clusters (40% aggregation at 90 min and 50% aggregation at 180 min). Conditions: PAANY 0.7 mM, pyridine 1.75 mM, imidazole 1.75 mM, acetic anhydride 14 mM in borate buffer (pH 9.0 200 mM) with silica microspheres (diameter = 1 µm). The standard deviation between two samples is shown (n=2). The point measured at t=0 min is a different sample without fuel addition, but all other conditions the same. The scale bar in all images is 10 µm. The aggregation (%) was determined by using MATLAB.

With lower pyridine concentration (0.7 mM) only 50% of PAANY is acetylated at its maximum (Figure S5.3A – UV-VIS conversion) and the colloid (dis)assembly response is less strong (Figure S5.4A,B,C) compared to the optimized conditions (Figure 5.2A and Figure S5.4D). With more pyridine present (1.75 mM) almost 90% of the NY groups on the polymer are acetylated (Figure S5.3B – UV-VIS conversion) and the colloidal assembly cycle is more pronounced (Figure 5.2A and Figure S5.4D). In Figure 5.2A the colloid aggregation (%) as a function of time is shown for the optimized conditions (0.7 mM PAANY with 2.5 equivalents of pyridine and imidazole). Initially, the colloids are 55% aggregated due to effective depletion interactions with PAANY. After addition of 20 equivalents of the anhydride fuel, the colloid clusters immediately disassemble and an aggregation of only 30% can be observed with mostly dimer structures present (Figure 5.2C – microscopy image 5 min). Hence, the polymer in its globule state is not able to deplete the colloids anymore at this concentration and the large clusters disassemble. During the fuel cycle the colloidal aggregation increases again and microscopy images after 90 min and 180 min show the reappearance of the larger colloidal clusters (Figure 5.2D,E). This can be attributed to an increase in the depletion interactions as the polymer is deacetylated back and in its random coil conformation again. The colloidal

clusters from the reference microscopy images of the starting sample can be viewed in Figure S5.5 (high and low magnification), overall corresponding to an average aggregation percentage of 54.5 ± 5.78%. Microscopy images of colloidal assembly over the course of a full fuel cycle are presented in Figures S5.6-7 (high and low magnification).

Next to the overall aggregation over time, the distribution over the various cluster sizes was evaluated (Figure 5.3). As apparent from Figure 5.3, the percentage of dimer structures (Figure 5.3A) remains fairly constant over the course of the fuel cycle. On the contrary, the contribution of trimers (Figure 5.3B) and especially larger clusters (> 3 particles) (Figure 5.3C) changes over time and follows the trend of the overall aggregation. Larger clusters are present from the start and disappear completely upon fuel addition, while over time they slowly reassemble.

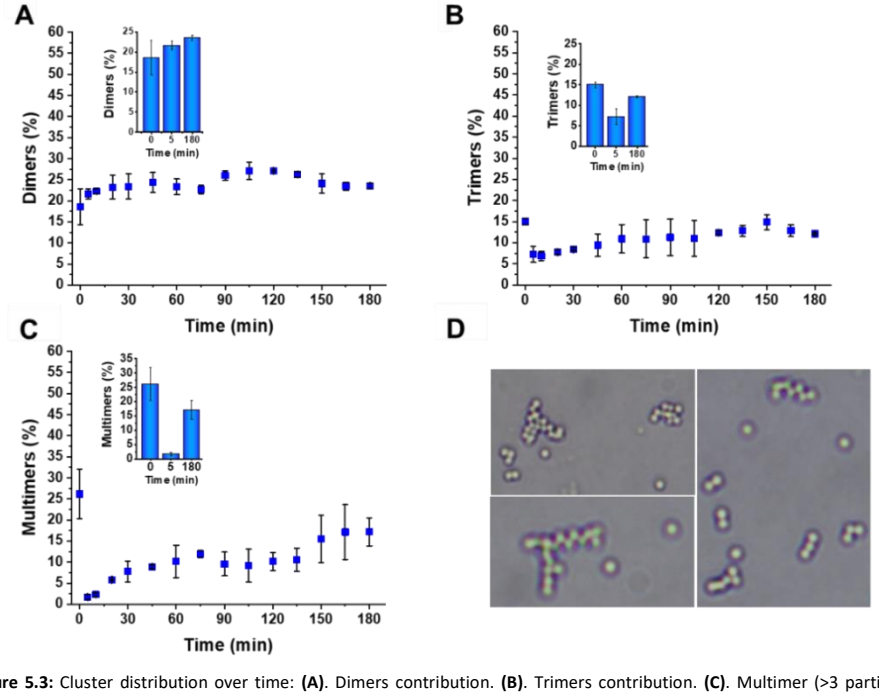

Figure 5.3: Cluster distribution over time: **(A)**. Dimers contribution. **(B)**. Trimers contribution. **(C)**. Multimer (>3 particles) contribution. **(D)**. Representative image of multimer fractal structures. Conditions: PAANY 0.7 mM, pyridine 1.75 mM, imidazole 1.75 mM, acetic anhydride 14 mM in borate buffer (pH 9.0 200 mM) with silica microspheres (diameter = 1 µm). The standard deviation between two samples is shown (n=2). The point measured at t=0 min is a different sample without fuel addition, but all other conditions the same. The bar charts inside the plots highlight the starting point (0 min), the start of fuel addition (5 min) and the endpoint (180 min).

The cluster structures that we observe for all samples are not entirely crystalline, but show a fractal-like open structure (Figure 5.3D). We hypothesize that this is due to the existence of a secondary minimum in the interaction potential. The formation of the fractal structures is most likely caused by an increased depletion attraction force and hence reduced probability of escape for a particle in a cluster. This phenomenon has also been observed in other research with PAA polymers used for depletion-flocculation studies of polystyrene latex particles[35, 36] and silica surfaces[37]. The secondary minimum is also quite shallow, as corroborated by the presence of single particles alongside the larger clusters (Figure 5.3D). Another reason for the presence of open structures can be polymer adsorption onto the colloid surface. However, adsorption here can be ruled out since it usually happens for PAA polymers having protonated carboxylates at low pH.[35, 37] Furthermore, the mobility of the particles is not influenced by the fuel cycle. We confirmed this by calculating the mean squared displacement (MSD) as a function of time (see SI section Mean squared displacement from particle tracking).

5.3 CONCLUSION

In this work, we have shown how polymer conformational changes regulated by a fuel-driven esterification CRN can induce transient colloidal depletion aggregation. Upon acetylation by a chemical fuel, the polymer undergoes a temporal transition from a random coil to a compact globule. In the random coil conformation, it acts as a polymeric depletant for silica colloids, while in its globular form it is too small to act as depletant for this system. Later in the fuel cycle the polymer is deacetylated again, reobtaining its depletion capacity. The concept was visualized using optical microscopy. The colloidal clusters are fractal-like structures due to the existence of a secondary minimum and the colloids remain dynamic over the course of the fuel cycle. Overall, a fuel cycle initiated by the addition of chemical fuel on the molecular scale results in a microscopic response with a transient colloidal depletion cycle and thus provides a temporary way out of thermodynamic equilibrium on large length scales. Understanding the propagation from a molecular reaction network to the microscopic or even macroscopic world is important for further research in this field and can support the design of responsive materials with life-like properties.

5.4 REFERENCES

1. W. Bialek, *Biophysics: searching for principles*, Princeton University Press, 2012.
2. E. Branscomb, T. Biancalani, N. Goldenfeld and M. Russell, *Phys. Rep.*, 2017, **677**, 1-60.
3. F. Gnesotto, F. Mura, J. Gladrow and C. P. Broedersz, *Rep. Prog. Phys.*, 2018, **81**, 066601.
4. B. Alberts, A. Johnson, J. Lewis, D. Morgan, M. Raff, K. Roberts and P. Walter, *Molecular biology of the cell*, Garland Science, New York, Sixth edition edn., 2014.
5. S. A. P. van Rossum, M. Tena-Solsona, J. H. van Esch, R. Eelkema and J. Boekhoven, *Chem. Soc. Rev.*, 2017, **46**, 5519-5535.
6. N. Singh, G. J. Formon, S. De Piccoli and T. M. Hermans, *Adv. Mater.*, 2020, **32**, 1906834.
7. J. Boekhoven, W. E. Hendriksen, G. J. M. Koper, R. Eelkema and J. H. van Esch, *Science*, 2015, **349**, 1075-1079.
8. J. Leira-Iglesias, A. Tassoni, T. Adachi, M. Stich and T. M. Hermans, *Nat. Nanotechol.*, 2018, **13**, 1021.
9. G. Ragazzon and L. Prins, *Nat. Nanotechol.*, 2018, **13**, 882–889.
10. T. Heuser, E. Weyandt and A. Walther, *Angew. Chem. Int. Ed.*, 2015, **54**, 13258-13262.
11. S. Dhiman, A. Jain, M. Kumar and S. George, *J. Am. Chem. Soc.*, 2017, **139**, 16568-16575.
12. S. Debnath, S. Roy and R. V. Ulijn, *J. Am. Chem. Soc.*, 2013, **135**, 16789-16792.
13. A. Sorrenti, J. Leira-Iglesias, A. Sato and T. M. Hermans, *Nat. Commun.*, 2017, **8**, 15899.
14. B. G. van Ravensteijn, I. K. Voets, W. K. Kegel and R. Eelkema, *Langmuir*, 2020, **36**, 10639−10656.
15. B. G. van Ravensteijn, W. E. Hendriksen, R. Eelkema, J. H. van Esch and W. K. Kegel, *J. Am. Chem. Soc.*, 2017, **139**, 9763-9766.
16. R. K. Grötsch, A. Angı, Y. G. Mideksa, C. Wanzke, M. Tena-Solsona, M. J. Feige, B. Rieger and J. Boekhoven, *Angew. Chem. Int. Ed.*, 2018, **57**, 14608-14612.
17. R. K. Grötsch, C. Wanzke, M. Speckbacher, A. Angı, B. Rieger and J. Boekhoven, *J. Am. Chem. Soc.*, 2019, **141**, 9872-9878.
18. T. Heuser, A.-K. Steppert, C. Molano Lopez, B. Zhu and A. Walther, *Nano Lett.*, 2015, **15**, 2213-2219.
19. H. Dehne, A. Reitenbach and A. Bausch, *Sci. Rep.*, 2019, **9**, 1-9.
20. B. Rieß, C. Wanzke, M. Tena-Solsona, R. K. Grötsch, C. Maity and J. Boekhoven, *Soft Matter*, 2018, **14**, 4852-4859.
21. W. B. Russel, W. Russel, D. A. Saville and W. R. Schowalter, *Colloidal dispersions*, Cambridge university press, 1991.
22. D. F. Evans and H. Wennerström, *The colloidal domain: where physics, chemistry, biology, and technology meet*, 1999.
23. R. Tuinier and H. N. Lekkerkerker, *Colloids and the Depletion Interaction*, Springer Netherlands, 2011.
24. S. Asakura and F. Oosawa, *J. Polym. Sci.*, 1958, **33**, 183-192.
25. S. Asakura and F. Oosawa, *J. Chem. Phys.*, 1954, **22**, 1255-1256.
26. Y. Mao, M. Cates and H. Lekkerkerker, *Physica A*, 1995, **222**, 10-24.
27. S. Buzzaccaro, J. Colombo, A. Parola and R. Piazza, *Phys. Rev. Lett.*, 2010, **105**, 198301.
28. R. Piazza, S. Buzzaccaro, A. Parola and J. Colombo, *J. Phys.: Condens. Matter*, 2011, **23**, 194114.
29. Z. Liu and Z.-w. Niu, *Chin. J. Polym. Sci.*, 2014, **32**, 1271-1275.
30. B. J. Lele and R. D. Tilton, *J. Colloid Interface Sci.*, 2019, **553**, 436-450.
31. X. Xing, Z. Li and T. Ngai, *Macromolecules*, 2009, **42**, 7271-7274.
32. M. D. Gratale, T. Still, C. Matyas, Z. S. Davidson, S. Lobel, P. J. Collings and A. Yodh, *Phys. Rev. E*, 2016, **93**, 050601.
33. L. Feng, B. Laderman, S. Sacanna and P. Chaikin, *Nat. Mater.*, 2015, **14**, 61-65.
34. M. P. van der Helm, C.-L. Wang, B. Fan, M. Macchione, E. Mendes and R. Eelkema, *Angew. Chem. Int. Ed.*, 2020, **59**, 20604-20611.
35. J. L. Burns, G. J. Jameson and S. Biggs, *Colloids Surf. A Physicochem. Eng. Asp.*, 2000, **162**, 265-277.
36. W. Liang, T. F. Tadros and P. Luckham, *Langmuir*, 1994, **10**, 441-446.
37. A. J. Milling and B. Vincent, *J. Chem. Soc., Faraday Trans.*, 1997, **93**, 3179-3183.

5.5 SUPPLEMENTARY INFORMATION

5.5.1 Experimental details

General materials and methods

Unless stated otherwise, all preparations and analyses were performed at room temperature (RT) (~21 °C) and atmospheric pressure. Chemicals were purchased in the highest available purity and used without any further purification unless mentioned otherwise. 3-nitro-L-tyrosine (NY), acetic anhydride, pyridine anhydrous, imidazole, poly(acrylic acid) (PAA ~130 kDa), N,N-dimethyl formamide (DMF) anhydrous, dimethyl sulfoxide (DMSO), N-(3-Dimethylaminopropyl)-N'-ethylcarbodiimide hydrochloride (EDC) and N,N-diisopropylethylamine (DIPEA) were from Sigma-Aldrich. 3-nitro-L-tyrosine ethyl ester (NY-ethyl ester) was purchased from Chem Impex International and 1-Hydroxybenzotriazole hydrate (HOBt) from Acros Organics. The functionalization of the PAA polymer with 3-nitro-L-tyrosine via EDC/HOBt peptide coupling was performed according to our previous reported procedure (chapter 4).[1] Sodium tetraborate decahydrate (Borax) and boric acid were used as solid salts to prepare borate buffer and were from Sigma Aldrich. Silica microspheres (Si-OH surface functional groups; diameter = 1.21± 0.144 µm; density 2 g/ml; $5.745 \cdot 10^{10}$ #colloids/ml; surface area $2.490 \cdot 10^{12}$ $\mu m^2/g$) were purchased from Bangs laboratory. Capillary tubes (rectangle boro tubing: 0.10 x 2.00 mm and 50 mm in length) were purchased from VitroCom. UV-Vis spectroscopic experiments were carried out using Analytik Jena Specord 250 spectrophotometer with a quartz cuvette with a 1 cm path length, volume of 3 mL, at RT. Microscopy images of the capillary tubes were recorded with a Nikon Eclipse E600POL equipped with a U-III Film Camera System. The captured photographs were processed with NIS-elements AR3.0 software.

Microscopy measurements

Silica microspheres (diameter = 1 µm) suspended in aqueous solution were sonicated and centrifuged (1000 rpm, 1 min, rotor F45-24-11 eppendorf), whereupon the water supernatant was removed and equal amounts of borate buffer (pH 9.0, 200 mM) were added to make the stock solution. The sample with colloid solution (500x dilution; final concentration $1.15 \cdot 10^8$ #colloids/ml) was then transferred to a capillary tube (0.10 x 2.00 mm and 50 mm in length) by dipping the empty capillary vertically into the solution for 5 sec. The capillary tube was placed on a glass slide and sealed with wax on both ends. Subsequently, the silica microspheres were observed through the capillary under the microscope. All stock solutions were filtered with a syringe filter (0.2 µm) before use. Except for the acetic anhydride, all other reagents were mixed beforehand with silica microspheres (500x diluted; final concentration $1.15 \cdot 10^8$ #colloids/ml) in a 4 ml vial. In order to start the fuel cycle acetic anhydride was added to the vial and subsequently the

capillary was dipped into this solution. Images of the colloids during the fuel cycle were taken at different magnifications and varying time intervals. Additionally, movies were taken at a speed of 0.8-1.3 fr/sec for 15-25 sec during the fuel cycle. The pH was measured before and after the reaction from the solution left in the 4 ml vial. For the analysis, the aggregation percentage of the colloids was calculated from the recorded microscopy images according to the following equation:

$$Aggregation\ (\%) = \frac{Particles\ in\ aggregate}{Total\ particles} * 100\%$$

, where the *particles in aggregate* represents the sum of particles present as dimers, trimers and larger clusters. The *total particles* is the sum of the aggregated particles and the single particles. The aggregation percentage was calculated with a MATLAB script (see MATLAB particle counting).

UV-Vis assay

Stock solutions were prepared in borate buffer (pH 9.0, 200 mM). The fuel cycle was performed with 0.15 mM PAANY, 3 mM acetic anhydride, 0.15 or 0.375 mM of pyridine and 0.375 mM of imidazole in borate buffer (pH 9.0, 200 mM), in quartz cuvettes, path length of 1 cm (total reaction volume of 3 mL) at RT. The stock solutions of the reactants were always added in the following order: PAANY, pyridine, imidazole and acetic anhydride. Teflon caps were used to close the cuvette. The cuvette was turned upside down to mix the solution. The reactant peak was followed using slow time scan, measuring wavelength at 420 nm. The pH was measured before and after the reaction. The conversion was calculated with the extinction coefficient (see calibration line 3-nitro-L-tyrosine in UV-VIS section) and the Lambert-Beer law:

$$A = \varepsilon l C$$

, where A is the absorbance, ε the extinction coefficient, l the path length of the cuvette and C the concentration.

5.5.2 Aggregation calibration

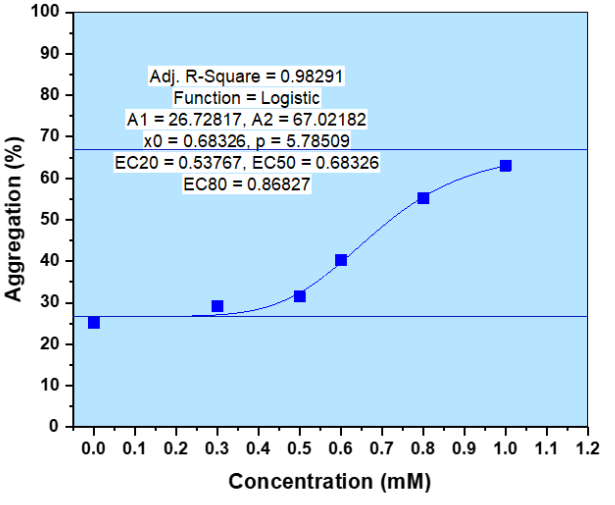

Figure S5.1: Colloidal aggregation calibration curve of PAANY (depletant) with silica microspheres (d = 1 µm). Different concentrations of PAANY were used, following a sigmoidal trend line (fitted with Origin).

5.5.3 UV-VIS spectroscopy

Calibration line

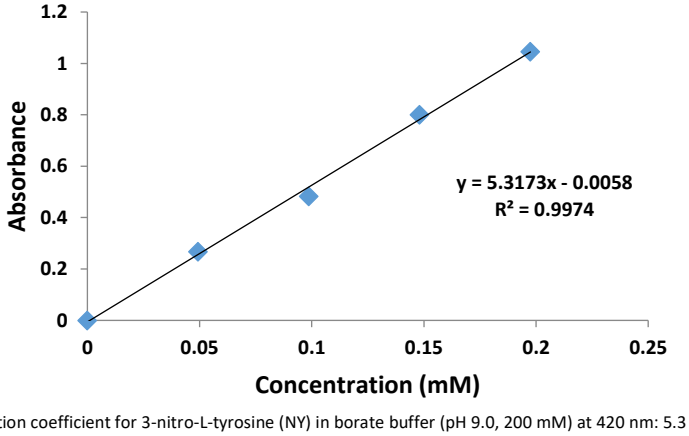

Figure S5.2: Extinction coefficient for 3-nitro-L-tyrosine (NY) in borate buffer (pH 9.0, 200 mM) at 420 nm: 5.3 $mM^{-1}cm^{-1}$. The absorbance at 420 nm of 3-nitro-L-tyrosine (NY) at different concentrations is shown.

Conversion plots

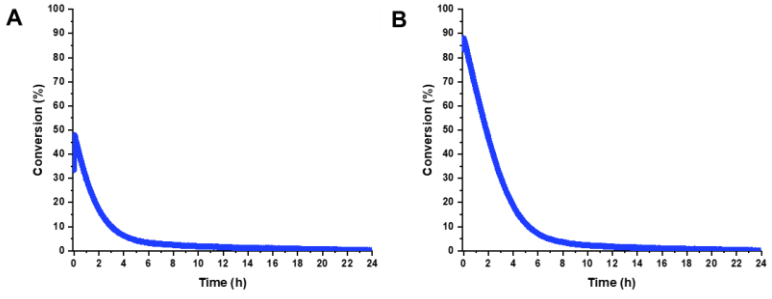

Figure S5.3: Conversion of PAANY upon acetylation to PAANY-acyl and subsequent hydrolysis. The absorbance of the 3-nitro-L-tyrosine moiety at 420 nm is monitored over time during a fuel cycle. **(A)**. PAANY 0.15 mM, pyridine 0.15 mM, imidazole 0.375 mM, acetic anhydride 3 mM in borate buffer (pH 9.0, 200 mM). **(B)**. PAANY 0.15 mM, pyridine 0.375 mM, imidazole 0.375 mM, acetic anhydride 3 mM in borate buffer (pH 9.0, 200 mM).

5.5.4 Aggregation as a function of time

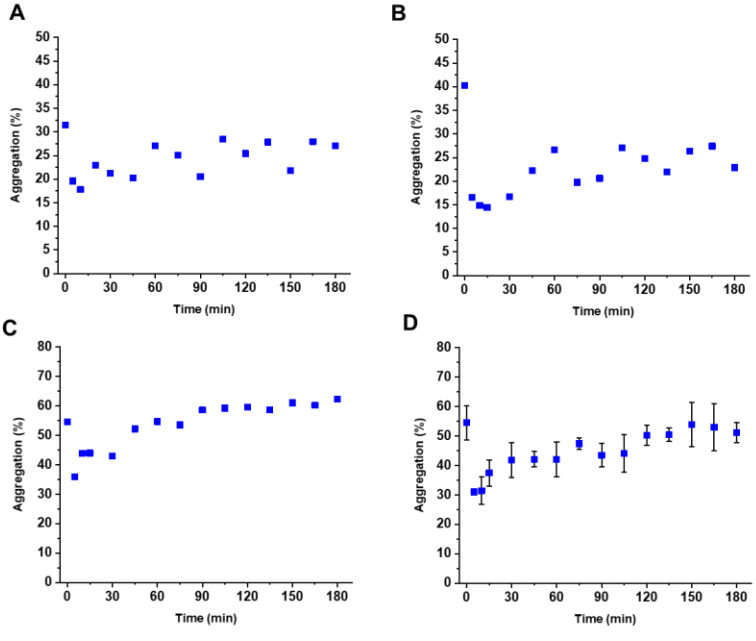

Figure S5.4: Colloid aggregation as a function time for fuel cycles under different conditions. Upon fuel (acetic anhydride) addition PAANY is acetylated to PAANY-acyl inducing colloidal disassembly (decreased aggregation %), while over time PAANY-acyl is deacetylated again giving rise to the reappearance of colloidal clusters (increased aggregation %). **(A)**. PAANY 0.5 mM, pyridine 0.5 mM, imidazole 1.25 mM, acetic anhydride 10 mM in borate buffer (pH 9.0, 200 mM). **(B)**. PAANY 0.6 mM, pyridine 0.6 mM, imidazole 1.5 mM, acetic anhydride 12 mM in borate buffer (pH 9.0, 200 mM). **(C)**. PAANY 0.7 mM, pyridine 0.7 mM, imidazole 1.75 mM, acetic anhydride 14 mM in borate buffer (pH 9.0, 200 mM). **(D)**. PAANY 0.7 mM, pyridine 1.75 mM, imidazole 1.75 mM, acetic anhydride 14 mM in borate buffer (pH, 9.0 200 mM). The standard deviation between two samples is shown (n=2). Silica microspheres (diameter = 1 µm) were used for all samples. The point measured at t=0 min is a different sample without fuel addition, but all other conditions the same.

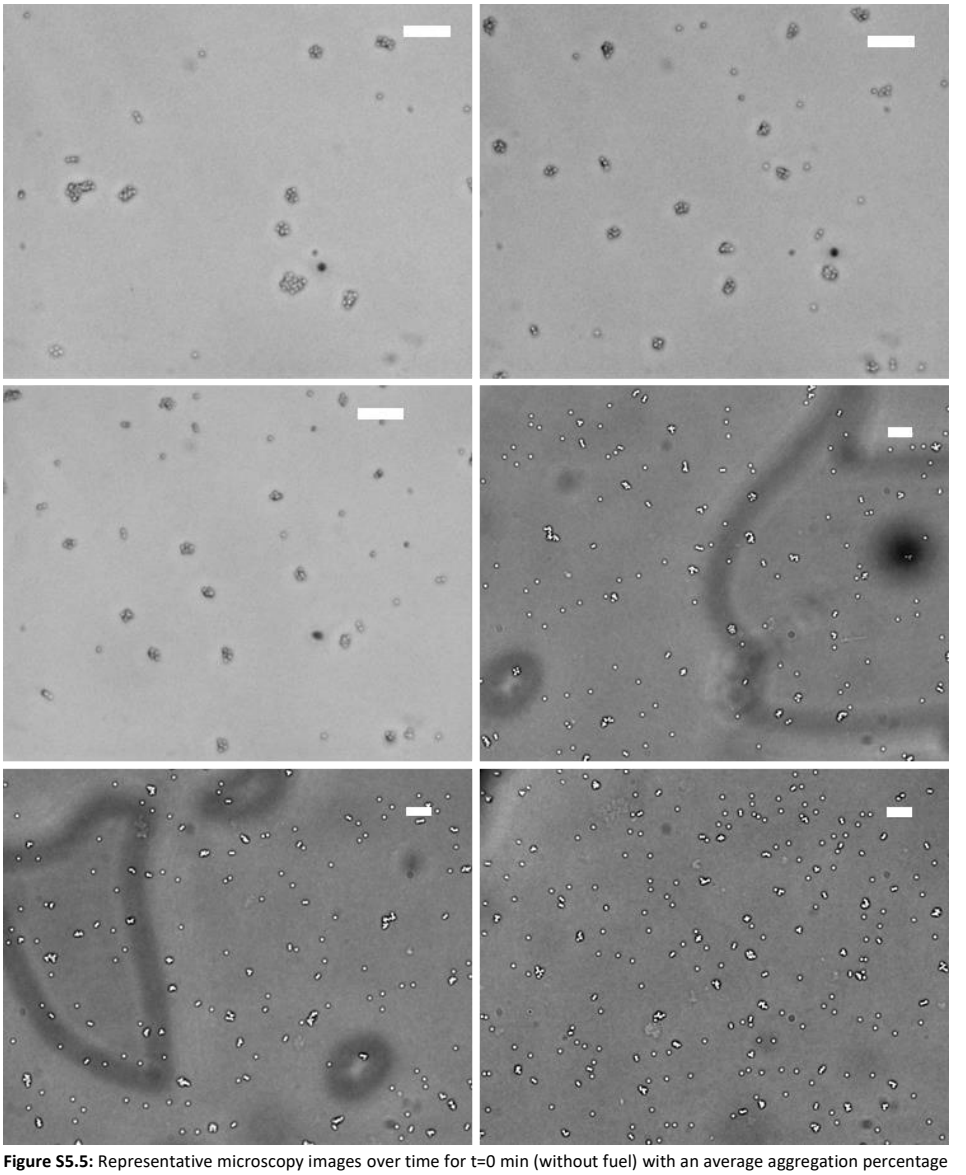

Figure S5.5: Representative microscopy images over time for t=0 min (without fuel) with an average aggregation percentage of 54.5 ± 5.78 (MATLAB counting) corresponding to the conditions in Figure S5.4D: PAANY 0.7 mM, pyridine 1.75 mM, imidazole 1.75 mM in borate buffer (pH 9.0, 200 mM). The first three pictures are at higher magnification (100/0.7) and the last three at lower magnification (50/0.45). The scale bar in all images is 10 µm.

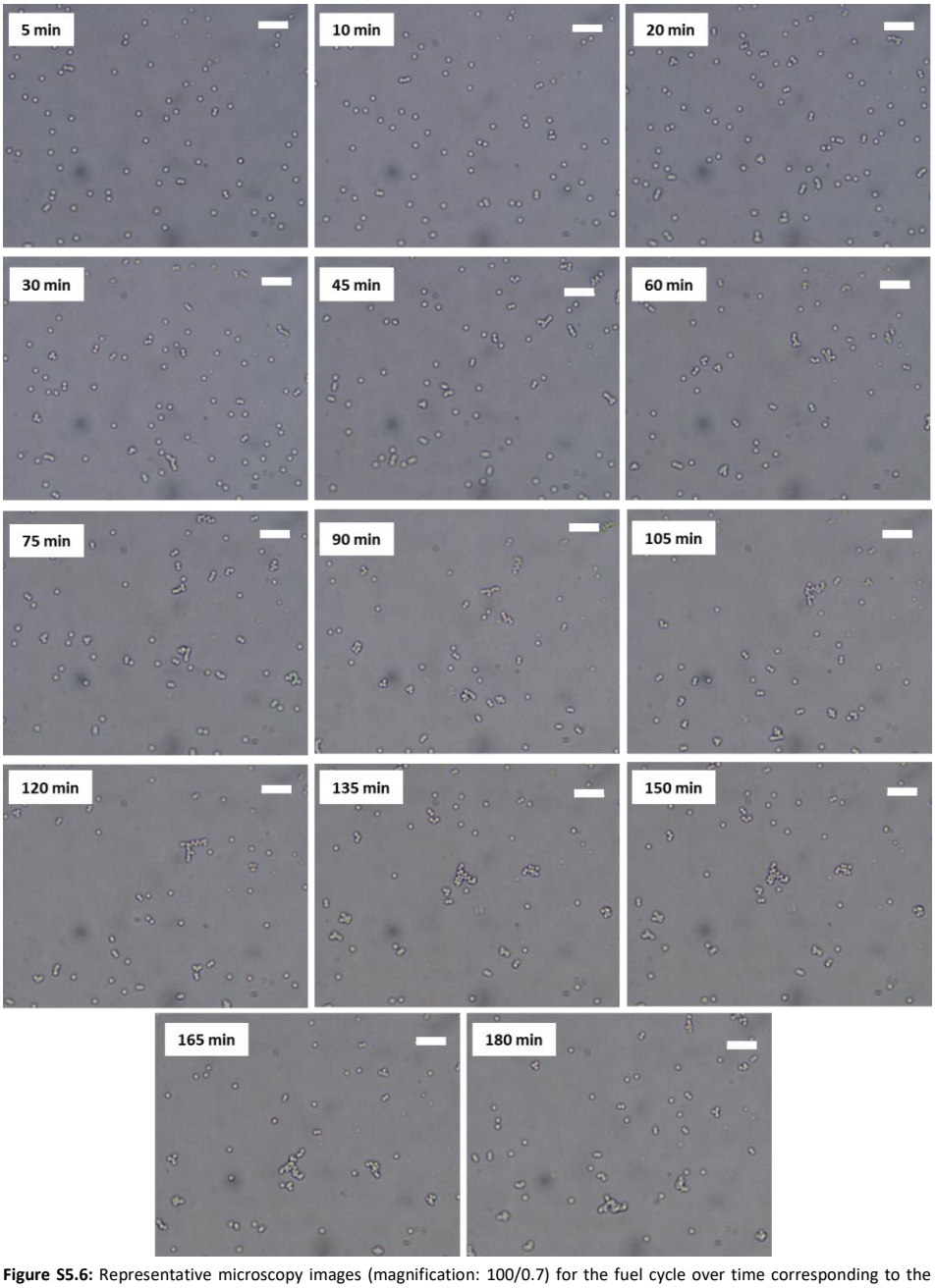

Figure S5.6: Representative microscopy images (magnification: 100/0.7) for the fuel cycle over time corresponding to the conditions in Figure S5.4D: PAANY 0.7 mM, pyridine 1.75 mM, imidazole 1.75 mM, acetic anhydride 14 mM in borate buffer (pH 9.0, 200 mM). The scale bar is 10 µm in all images.

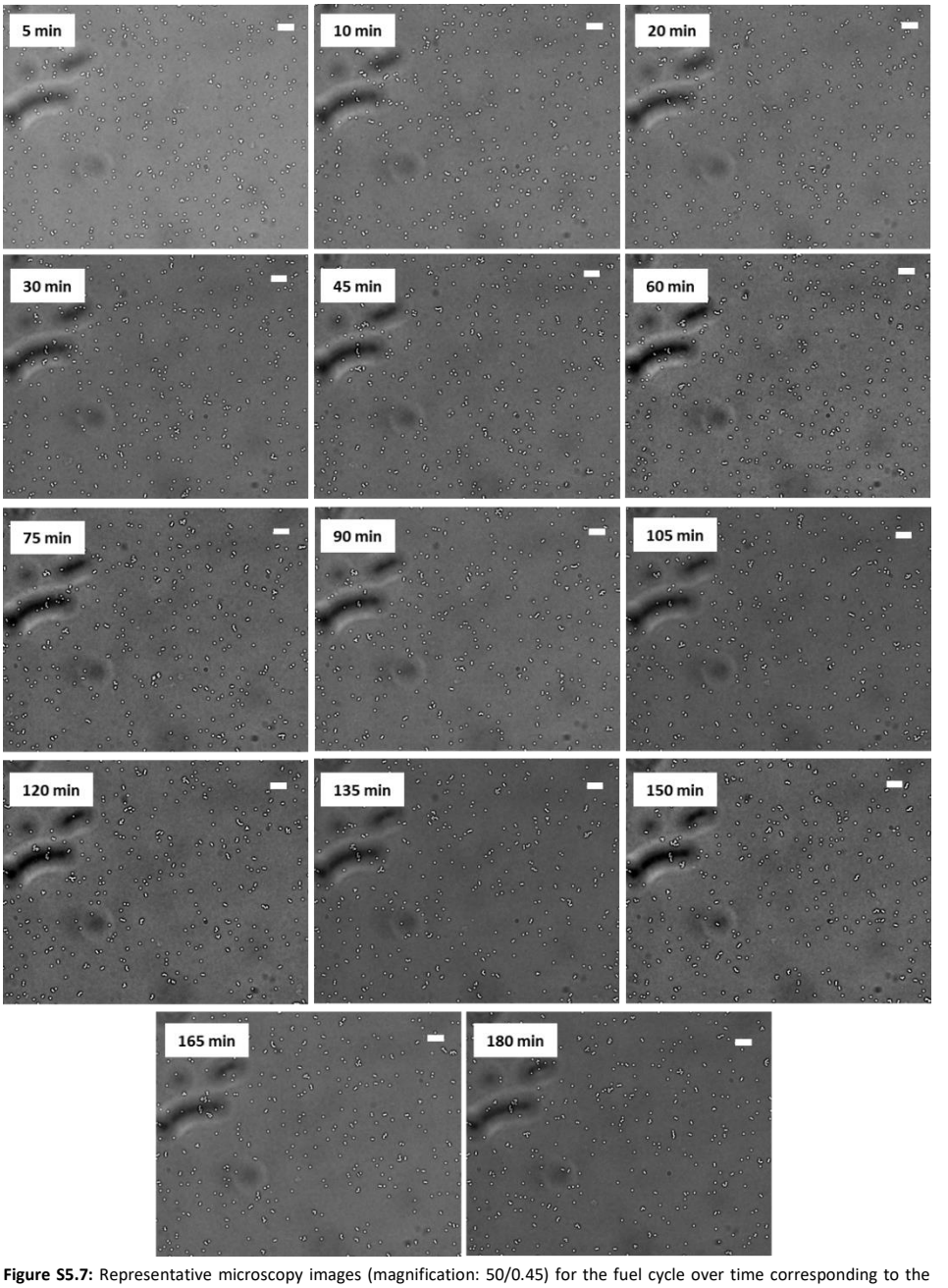

Figure S5.7: Representative microscopy images (magnification: 50/0.45) for the fuel cycle over time corresponding to the conditions in Figure S5.4D: PAANY 0.7 mM, pyridine 1.75 mM, imidazole 1.75 mM, acetic anhydride 14 mM in borate buffer (pH 9.0, 200 mM). The scale bar is 10 µm in all figures.

5.5.5 MATLAB particle counting

The microscopy images were calculated with a MATLAB particle counting script. For the latter, the image file obtained with the microscope is loaded into MATLAB. Subsequently, the code searches for the single, dimer, trimer and larger clusters. Examples of typical MATLAB output files for the fuel cycle microscopy images at 5 min and 3 h are shown below.

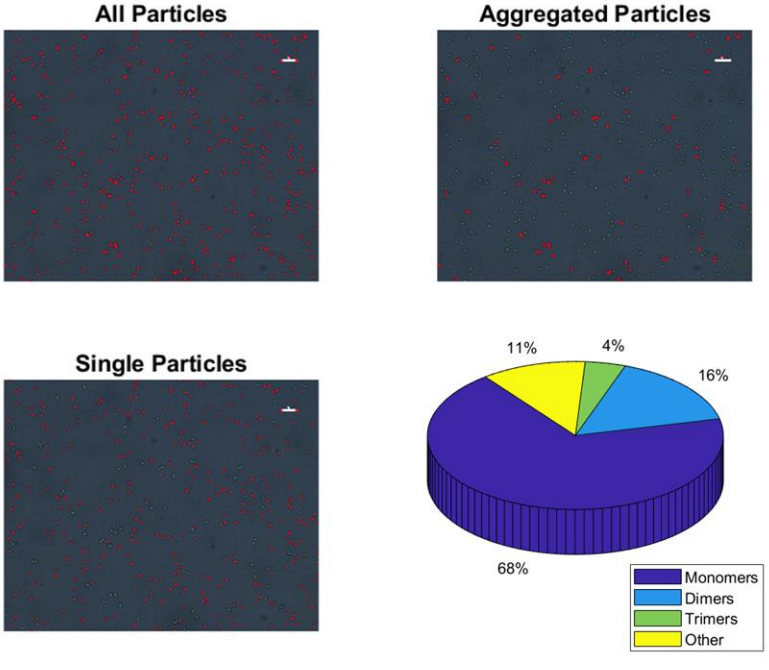

Figure S5.8: Representative MATLAB particle counting output. First all particles are identified, whereupon a distinction is made between aggregated and single particles. The aggregated particles are further divided into dimers, trimers and other (multimers; >3 particles). Conditions: PAANY 0.7 mM, pyridine 1.75 mM, imidazole 1.75 mM, acetic anhydride 14 mM in borate buffer (pH 9.0, 200 mM), image recorded at 5 min.

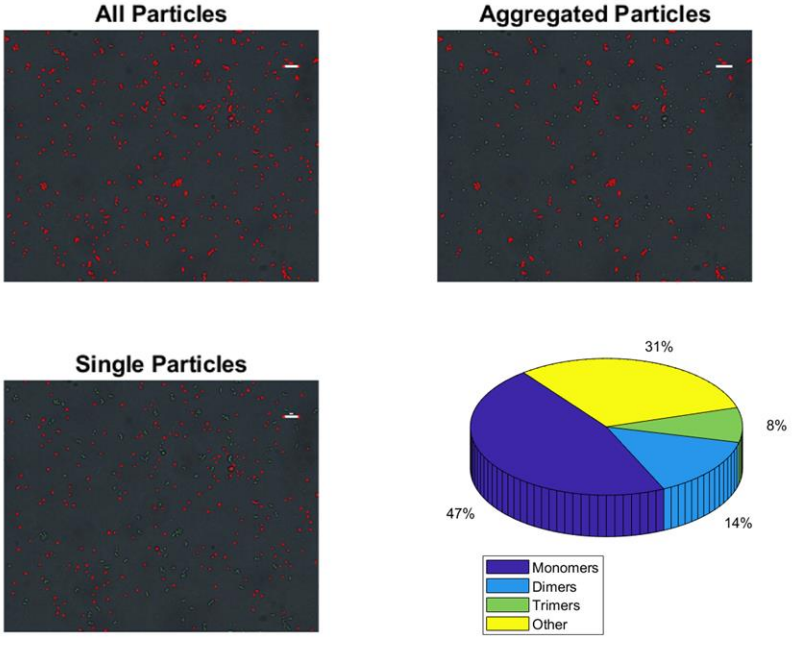

Figure S5.9: Representative MATLAB particle counting output. First all particles are identified, whereupon a distinction is made between aggregated and single particles. The aggregated particles are further divided into dimers, trimers and other (multimers; >3 particles). Conditions: PAANY 0.7 mM, pyridine 1.75 mM, imidazole 1.75 mM, acetic anhydride 14 mM in borate buffer (pH 9.0, 200 mM), image recorded at 3 h.

For a careful examination of the distribution over the various clusters, microscopy video files were also evaluated with the MATLAB model. The final calculated distribution is then the average over 20 frames. An example of a MATLAB output file for a video frame is shown on the next page.

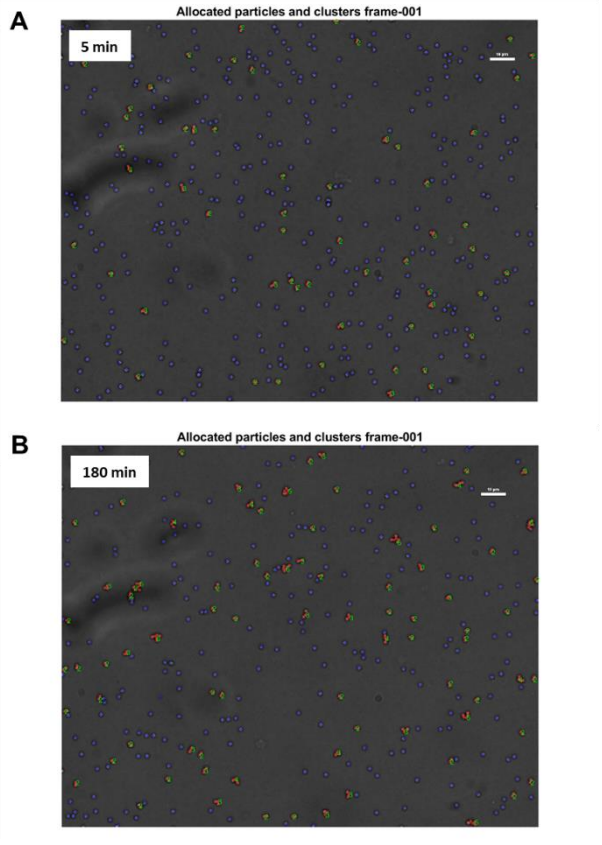

Figure S5.10: Representative MATLAB particle processed video frame images. For all videos frames the particles are counted and the clusters identified as dimers, trimers and multimers. Conditions: PAANY 0.7 mM, pyridine 1.75 mM, imidazole 1.75 mM, acetic anhydride 14 mM in borate buffer (pH 9.0, 200 mM), image recorded at 5 min **(A)** and 3 h **(B)**.

5.5.6 Mean squared displacement from particle tracking

To examine the mobility of the colloid particles during the course of the fuel cycle, the mean squared displacement (MSD) was calculated based on multiple recorded videos from the microscope as a function of time. The MSD is defined according to the following equation:

$$MSD \equiv \frac{1}{N}\sum_{i=1}^{N} |x^{(i)}(t) - x^{(i)}(0)|^2$$

, where *N* is the number of particles (i.e. silica colloids), $x^{(i)}(0)$ the reference position and $x^{(i)}(t)$ the position of the *i-th* particle at time *t*. The reference position and the new positions were calculated with a MATLAB particle tracking model for every particle for each frame of the video. A typical video consisted of 20 individual image frames with each having about 450 particles in total. The MSD was calculated with single particles and particles in clusters together (Figure S5.11) and with only single particles (Figure S5.12).

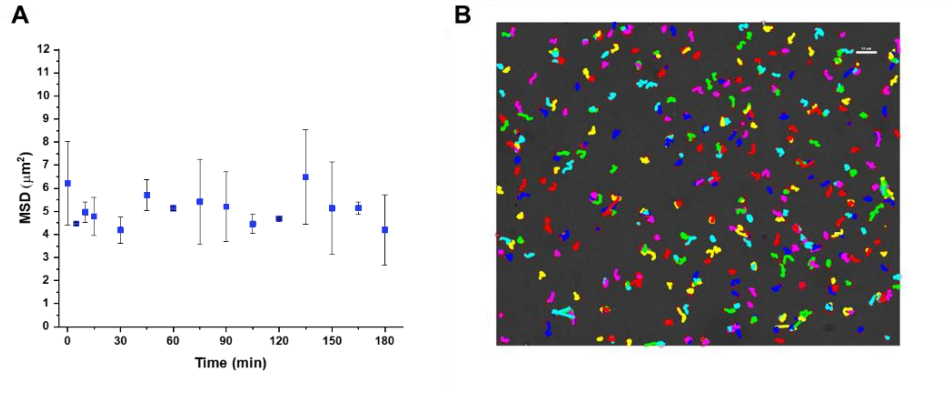

Figure S5.11: (A). MSD as a function of time for single particles and particles in clusters together. The standard deviation from two samples is shown (n=2). **(B).** Example image of particle (single and in clusters) trajectories calculated by the MATLAB tracking model. The scale bar is 10 µm. Sample conditions: PAANY 0.7 mM, pyridine 1.75 mM, imidazole 1.75 mM, acetic anhydride 14 mM in borate buffer (pH 9.0, 200 mM).

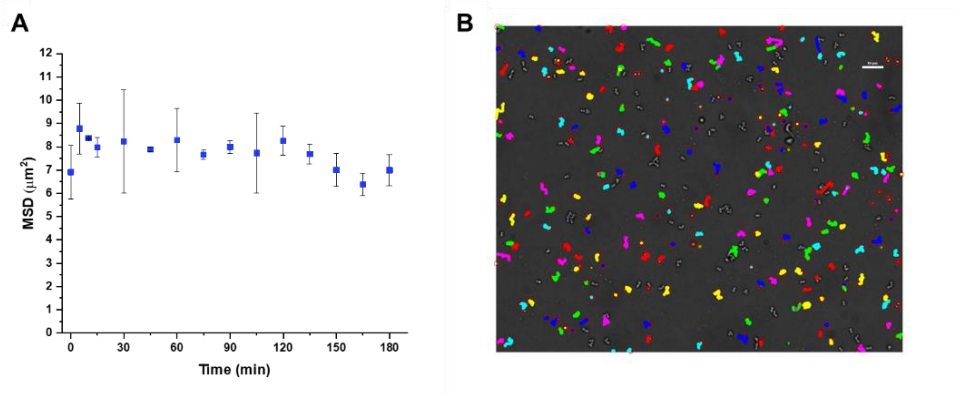

Figure S5.12: (A). MSD as a function of time for only single particles. The standard deviation between two samples is shown (n=2). **(B).** Example image of particle (only single) trajectories calculated by the MATLAB tracking model. The scale bar is 10 µm. Sample conditions: PAANY 0.7 mM, pyridine 1.75 mM, imidazole 1.75 mM, acetic anhydride 14 mM in borate buffer (pH 9.0, 200 mM).

5.5.7 Supplementary references

1. M. P. van der Helm, C.-L. Wang, B. Fan, M. Macchione, E. Mendes and R. Eelkema, *Angew. Chem. Int. Ed.*, 2020, **59**, 20604-20611.

ON THE USE OF CATALYSIS TO BIAS REACTION PATHWAYS IN OUT-OF-EQUILIBRIUM SYSTEMS

CHAPTER 6

Catalysis is an essential function in living systems and provides a way to control complex reaction networks. In natural out-of-equilibrium chemical reaction networks (CRNs) driven by the consumption of chemical fuels, enzymes provide catalytic control over pathway kinetics, giving rise to complex functions. Catalytic regulation of man-made fuel-driven systems is far less common and mostly deals with enzyme catalysis instead of synthetic catalysts. Here, we show via simulations, illustrated by literature examples, how any catalyst can be incorporated in a non-equilibrium CRN and what their effect is on the behaviour of the system. Alteration of the catalysts' concentrations in batch and flow gives rise to responses in product yield, lifetime and steady states. *In-situ* up or downregulation of catalysts' levels temporarily changes the product steady state, whereas feedback elements can give unusual concentration profiles as a function of time and self-regulation in a CRN. We show that simulations can be highly effective in predicting CRN behaviour and mapping parameter space, for complex processes that can proceed counterintuitively. In the future, shifting the focus from enzyme catalysis towards small molecule and metal catalysis in out-of-equilibrium systems can provide us with new reaction networks and enhance their application potential in synthetic materials, overall advancing the design of man-made responsive and interactive systems.

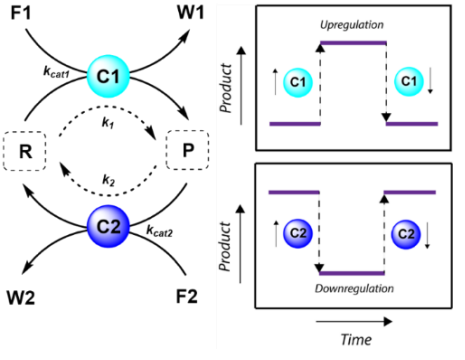

This chapter will be published as:
M.P. van der Helm, T. de Beun, R. Eelkema, *manuscript submitted.*

6.1 INTRODUCTION

Regulation of chemical processes by catalytic activity is crucial to life. Metabolic pathways rely heavily on enzymes to catalyse individual reaction steps and control complex reaction networks. In contrast, deregulation of enzymes in signal transduction pathways can have severe consequences for cells and their organisms by generation of oncogenic signals and the onset of cancer, e.g. for tyrosine kinase in acute myeloid leukemia.[1, 2] Much of the complex functions in living systems are encoded in out-of-equilibrium (bio)chemical reaction networks (CRNs) and require an input of chemical fuel, which is often a high-energy bond molecule, like the phosphoanhydride bond in ATP (Adenosine triphosphate) and GTP (Guanosine triphosphate).[3-7] Examples of such fuel-driven systems in biology include the actin and microtubule protein filament assembly which make up the cytoskeleton, histone acetylation to regulate gene transcription and ribosomal protein biosynthesis with aminoacyl-tRNA synthetases.[8] All these biological examples combine a fuel-driven system with catalysis to achieve highly dynamic behaviour and control vital cellular processes.

At the basis of the above systems are out-of-equilibrium CRNs, reaction networks consisting of at least two competing reactions (product formation and degradation). Essential properties of such systems are dictated by reaction kinetics rather than thermodynamic stability and the products can only be sustained in the presence of enough chemical fuel. The transient state of the system will start to disintegrate when the chemical fuel is depleted, whereupon it converts back to the thermodynamic equilibrium state of the starting building blocks. As in the biological examples above, the reaction kinetics of the forward and backward reaction can be regulated by catalysis, which in turn can have a large impact on the behaviour of the system. To illustrate this, in this chapter, we show the kinetic modelling of a generalized fuel-driven system, where catalysts are introduced to alter reaction kinetics, allowing pathway biasing in an out-of-equilibrium system and shifting between out-of-equilibrium steady states. Both batch and flow systems are investigated, as well as feedback mechanisms. The modelling results are illustrated using relevant literature examples of catalytic out-of-equilibrium systems. Furthermore, we conclude this chapter with directions for future research in this field. Noteworthy, we focus on the impact of catalysis on reaction pathways governing these fuel-driven reaction networks and less on the behaviour, function or application of the transient product. For the latter we refer to a comprehensive review from our group with the Boekhoven group[6], two other reviews on application and design from the Boekhoven group[9, 10], a review from the Klajn group[11], a perspective from the Prins group[12] and a recent review from the Hermans group[13].

6.2 CATALYTIC NETWORK REGULATION IN FUEL-DRIVEN BATCH AND FLOW SYSTEMS

The majority of man-made fuel-driven systems makes use of batch-wise fuel additions. A key control factor in these systems is the supply of fuel. The amount of fuel added typically changes the yield and lifetime of the transient product. With lifetime it is understood here the duration that the transient product is present in significant amounts, in other words the time it takes to bring the system back to the thermodynamic equilibrium state. This lifetime is directly affected by the presence of fuel. Although batch-wise additions have been mostly studied so far, studying continuous supply of fuel can be very interesting. Continuous chemical fuel supply can give rise to unusual features, like oscillations, bistable switching or chaotic behaviour.[6, 14] Besides the fuel, introducing catalysts in an out-of-equilibrium CRN to alter the reaction kinetics of the forward or backward reaction can provide additional control elements. In the current work, we established two kinetic models based on a minimalistic reaction network (Scheme 6.1), to be able to compare the influence of catalysis in batch and flow fuel-driven systems. In this CRN, Reactant (R) is converted into product (P) by supplying chemical fuel (F1) and concomitantly generating waste (W1). This formation reaction is catalysed by catalyst C1 with rate constant k_{cat1} and an uncatalysed background reaction with constant k_1. P is unstable and only transiently formed and degrades again with reagent (F2), generating back reactant R together with waste (W2). The degradation reaction is catalysed by catalyst C2 with rate constant k_{cat2} and an uncatalysed background reaction with constant k_2. We assume that the reactions are first order in catalyst C1 and C2 and not take into account any intermediate reaction steps, so only use the essential rate determining steps (k_{cat}).

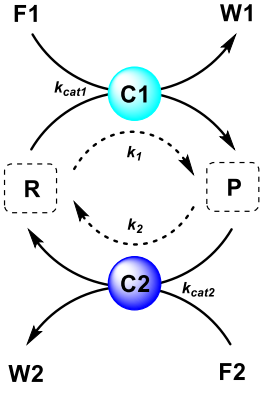

System of differential equations

$$\frac{d[P]}{dt} = (k_{cat1}[\boldsymbol{C1}]+k_1)[\boldsymbol{F1}][\boldsymbol{R}] - (k_{cat2}[\boldsymbol{C2}] + k_2)[\boldsymbol{F2}][\boldsymbol{P}]$$

$$\frac{d[R]}{dt} = -(k_{cat1}[\boldsymbol{C1}] + k_1)[\boldsymbol{F1}][\boldsymbol{R}] + (k_{cat2}[\boldsymbol{C2}] + k_2)[\boldsymbol{F2}][\boldsymbol{P}]$$

$$\frac{d[F1]}{dt} = -(k_{cat1}[\boldsymbol{C1}] + k_1)[\boldsymbol{F1}][\boldsymbol{R}]$$

$$\frac{d[F2]}{dt} = -(k_{cat2}[\boldsymbol{C2}] + k_2)[\boldsymbol{F2}][\boldsymbol{P}]$$

$$\frac{d[W1]}{dt} = (k_{cat1}[\boldsymbol{C1}] + k_1)[\boldsymbol{F1}][\boldsymbol{R}]$$

$$\frac{d[W2]}{dt} = (k_{cat2}[\boldsymbol{C2}] + k_2)[\boldsymbol{F2}][\boldsymbol{P}]$$

Scheme 6.1: Generic fuel-driven CRN, where both formation and degradation pathways are catalysed. Reactant (R) is converted into product (P) by supplying fuel (F1) and concomitantly generating waste (W1), catalysed by C1. P is unstable and only transiently formed and degrades again with reagent (F2), generating R and waste (W2), catalysed by C2.

6.2.1 Batch and CSTR non-equilibrium systems

Numerically solving this CRN in batch-mode gives rise to concentration profiles over time of all species. Figure 6.1A-D shows the concentration profiles as a function of time, when the concentrations of C1 and C2 are kept equal. In the batch-mode the fuel supply is finite and hence the non-equilibrium state is of temporary nature, resulting in a transient profile of product P and reactant R (Figure 6.1B). Fuel (F1) and waste (W1) are quickly interconverted into each other (Figure 6.1C), whereas reagent (F2) and waste (W2) interconversion is slightly delayed (Figure 6.1D), because the backward reaction only kicks in from the moment product P is formed. Corresponding reaction rates and conversion plots are given in Figure 6.1E,F. At the start of the fuel cycle the forward reaction dominates over the backward reaction resulting in the net formation of product P (Figure 6.1E). The backward reaction reaches its maximum rate when the concentration of product P is at its maximum. But as product P is consumed again the backward reaction also quickly slows down.

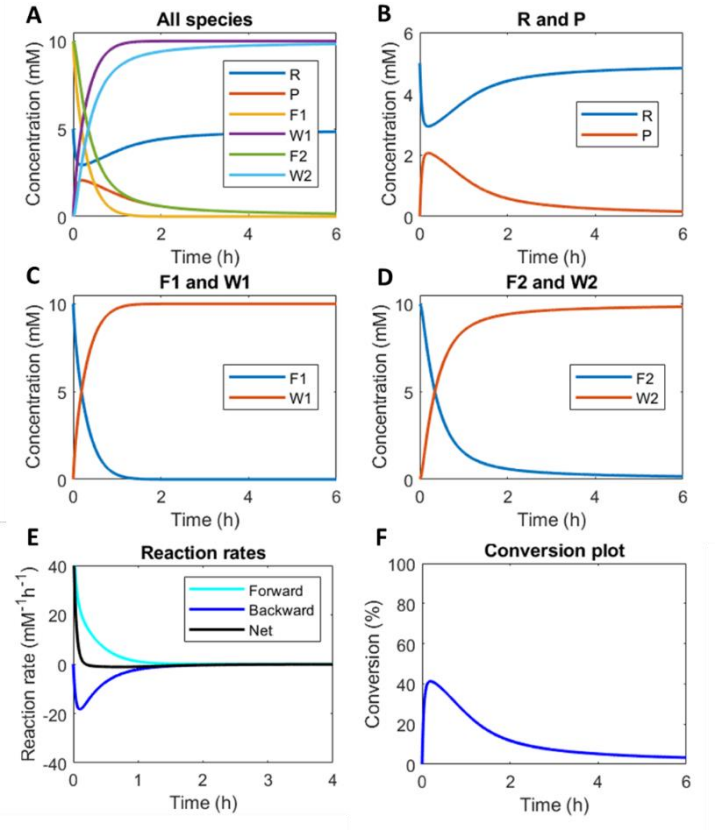

Figure 6.1: Numerical modelling output in batch-mode: **(A)**. Concentration of all species as a function of time. **(B)**. Concentration of reactant R and product P as a function of time. **(C)**. Concentration of fuel F1 and waste W1 as a function

of time. **(D)**. Concentration of reagent F2 and waste W2 as a function of time. **(E)**. Reaction rates for product P formation and degradation as a function of time. **(F)**. Conversion plot of reactant R. Initial conditions: [F1]=10 mM, [W1]=0 mM, [F2]=10 mM, [W2]=0 mM, [R]=5 mM, [P]=0 mM, [C1]=0.1 mM, [C2]=0.1 mM and rate constants k_{cat1}=10 $mM^{-2}h^{-1}$, k_1=0.1 $mM^{-1}h^{-1}$, k_{cat2}=10 $mM^{-2}h^{-1}$, k_2=0.1 $mM^{-1}h^{-1}$. N.B. In multiple out-of-equilibrium CRNs reagent F2 is the solvent (e.g. water). Then, the rate equation becomes independent of the F2 concentration.

Changing the concentrations of C1 and C2 gives rise to varying yields and lifetime of transient product P, as is apparent from Figure 6.2 (for individual plots at different catalytic conditions see SI Figure S6.1-6). Increasing the C1 concentration leads to an increase in the maximum conversion of P, whereas the opposite holds true for C2 and a decrease in the maximum conversion is observed. Bringing one of the catalyst concentrations to zero results in prolonged lifetime of P (with no C2) (SI Figure S6.5) or hardly any generation of P (with no C1) (SI Figure S6.6).

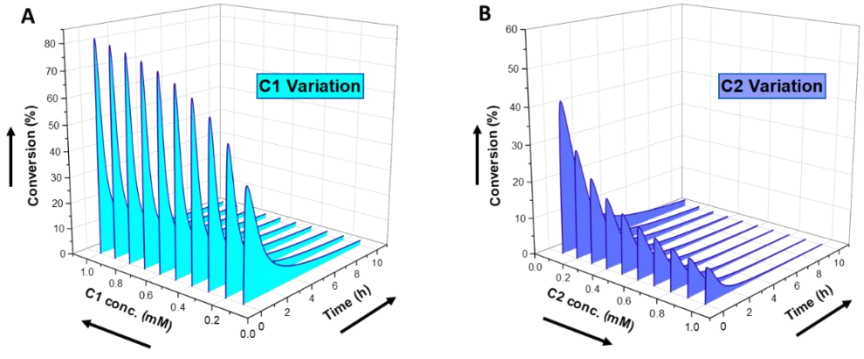

Figure 6.2: Numerical modelling output in batch-mode: **(A)**. Variation of catalyst C1 concentration from 0.1-1 mM. **(B)**. Variation of catalyst C2 concentration from 0.1-1 mM. Conditions: [F1]=10 mM, [W1]=0 mM, [F2]=10 mM, [W2]=0 mM, [R]=5 mM, [P]=0 mM, [C1]=0-1 mM, [C2]=0-1 mM and rate constants k_{cat1}=10 $mM^{-2}h^{-1}$, k_1=0.1 $mM^{-1}h^{-1}$, k_{cat2}=10 $mM^{-2}h^{-1}$, k_2=0.1 $mM^{-1}h^{-1}$.

Several experimental systems with behaviour that is broadly described by this batch model, have been reported in the literature. This catalytic regulation to alter lifetimes and yields of transient products has mostly been realized using enzyme catalysis. For instance, Ulijn and co-workers already introduced in 2013 a non-equilibrium CRN where α-chymotrypsin catalyses both the formation and degradation of a transient hydrogel.[15] The backward reaction was very sensitive to the protease concentration, while the forward reaction showed little change upon changing the catalyst concentration. Only the maximum gelator conversion was slightly changed by using a lower catalyst concentration. Hence, using just one catalyst for both formation and degradation seems to come at the cost of limited control over individual reaction pathways. Next to proteases and esterases[16], (de)phosphorylating enzymes are popular catalysts in out-of-equilibrium systems[17-22]. Using different enzymes for each path, for instance a kinase and phosphatase couple, increases the level of control. Yet, using enzymes as catalysts still faces major bottlenecks, such as limited long-term stability under

operational conditions and inhibition by generated waste products. It is worth discussing that in contrast to the reaction systems described above with two catalysts and two significant background reactions, enzyme catalysed CRNs often have little to no background reaction and the enzymes are essential to make and break the transient product. In such a scenario, with near zero rate background reactions, the simulated scenario would still give similar concentration profiles for equal amounts of catalysts C1 and C2 (Figure S6.7). However, when also the level of catalyst C2 is brought to zero the backward reaction no longer takes place and the conversion of reactant R into product P is the final equilibrium state (Figure S6.8). In zero-rate background reaction scenarios, the catalysts have complete control over the behaviour of the system.

Compared to using biocatalysis, up to date only a few examples of metal catalysis, organocatalysis (chapter 4) and acid/base catalysis have been reported.[23-25] As an illustrative example, Das and co-workers introduced a catalytic histidine moiety in a self-supporting hydrogel, exhibiting fuel-driven transient stability and cooperative catalysis.[26] The transient hydrogel was generated by esterification of the carboxylic end group of lipid functionalized histidine amphiphile precursors using a water-soluble carbodiimide as chemical fuel in combination with a *p*-nitrophenol nucleophile. A cooperative catalytic effect was realized by the proximity of the imidazole group of histidine, boosting the ester hydrolysis rate in the assembled state and consequently the disassembly of the gel state. Overall, this approach shows much resemblance with the enhanced GTPase activity of microtubules in living systems. The analogy to microtubules is also exemplified in follow-up works where the system shows designed negative feedback from the assembled structure, even harnessing temporal regulation of cross-β amyloid network electronic properties.[27, 28] Although this example from Das relies on organocatalysis, it is distinctly different from the simulation described here, because the catalyst (i.e. the histidine moiety) is integrated in the transient product. In that way, precise and predictable control over the yield of the transient product with the catalyst concentration is not straightforward, although it does show fascinating feedback control (vide infra).

Thus, with (two) catalysts participating in a non-equilibrium CRN it is obvious that a higher degree of control can be achieved over the product yield and lifetime than with the fuel alone. The catalytic regulation is of kinetic origin by alteration of the forward and backward reaction rates. Yet, in batch-mode when the fuel reservoir is exhausted the system reaches its equilibrium again and only the supply of new fuel can bring the system in a non-equilibrium state. Compared to these batch systems, supplying fuel in a continuous manner can give rise to a higher degree of control and for prolonged time.

Here, we demonstrate this by modelling the same reaction network (Scheme 6.1) in a continuous stirred tank reactor (CSTR). The catalyst concentrations can be varied to achieve different non-equilibrium steady states. Figure 6.3 illustrates the concentration profiles of all species, when both catalysts are supplied in equal amounts. For product P and reactant R a non-equilibrium steady state is reached at around 1h (Figure 6.3B). Steady state profiles of both fuel and reagent (F1 and F2) are reached around 1h as well, whereas the waste products (W1 and W2) reach their steady state some time later around 4h (Figure 6.3C,D). Because the fuel is supplied in a continuous fashion there is a continuous net formation of product P (Figure 6.3E), which results in a continuous conversion around 30% (Figure 6.3F).

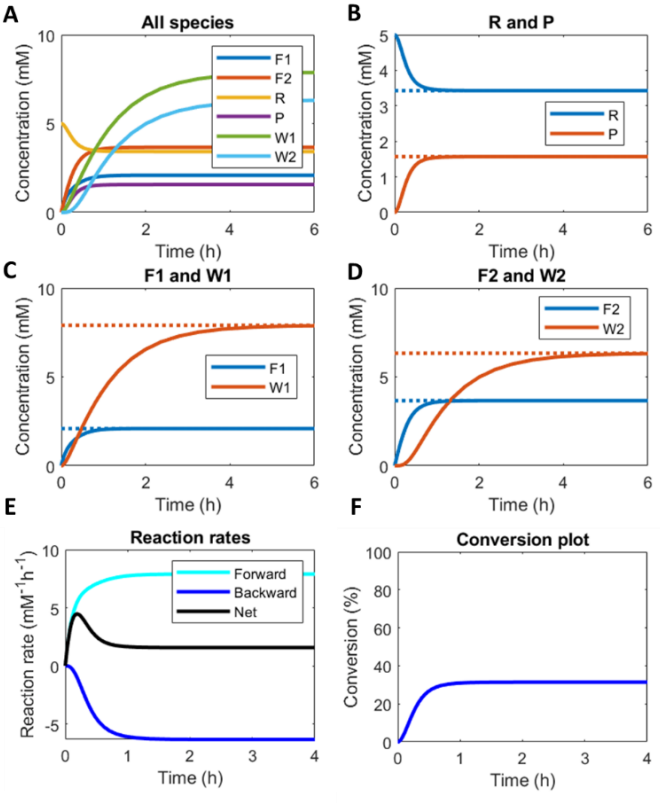

Figure 6.3: Numerical modelling output in CSTR: **(A)**. Concentration of all species as a function of time. **(B)**. Concentration of reactant R and product P as a function of time (solid lines) and their steady states (dashed lines). **(C).** Concentration of fuel F1 and waste W1 as a function of time (solid lines) and their steady states (dashed lines). **(D)**. Concentration of reagent F2 and waste W2 as a function of time (solid lines) and their steady states (dashed lines). **(E)**. Reaction rates for product P formation and degradation as a function of time. **(F)**. Conversion plot of reactant R. Inlet conditions: [F1]=10 mM, [W1]=0 mM, [F2]=10 mM, [W2]=0 mM, [R]=5 mM, [P]=0 mM, [C1]=0.1 mM, [C2]=0.1 mM, rate constants k_{cat1}=10 $mM^{-2}h^{-1}$, k_1=0.1 $mM^{-1}h^{-1}$, k_{cat2}=10 $mM^{-2}h^{-1}$, k_2=0.1 $mM^{-1}h^{-1}$ and residence time τ=1 h.

Altering the catalyst ratios for this CSTR system changes the steady states levels of the various species. Supplying high amounts (1 mM and 0.1 mM) of either catalyst results in a fast establishment of the non-equilibrium steady states (SI Figures S6.9-10), while lower catalyst concentrations (0.1 mM and 0.01 mM) extend the time to reach steady state (SI Figures S6.11-12). Increasing [C1] relative to [C2] brings the steady state conversion above 40% (SI Figure S6.9 – C1 1 mM and C2 0.1 mM) or at 60% (SI Figure S6.11– C1 0.1 mM and C2 0.01 mM. Lowering [C1] relative to [C2] brings the conversion around 12% (SI Figure S6.12 – C1 0.1 mM and C2 0.01 mM) or even below 10% (SI Figure S6.10– C1 0.1 mM and C2 1 mM).

Additionally, the catalyst concentrations can be altered *in-situ* (Figure 6.4). An increase in catalyst C1 results in an upregulation of the forward reaction and hence an increase in the steady state level of product P (red/orange line - Figure 6.4A). Conversely, increasing C2 results in a downregulation of the net formation rate and a decrease in the steady state level of P (red/orange line - Figure 6.4B). Over the course of the reaction up and downregulation of C1 or C2 can be performed sequentially to create a temporary up or downregulated steady state of P (Figure 6.4C,D). Interestingly, the sequential up and downregulation resembles the onset of a chemical signal, which terminates again when the catalyst is removed from the reaction cycle. In this way, catalytic regulation can provide a high degree of control over the system.

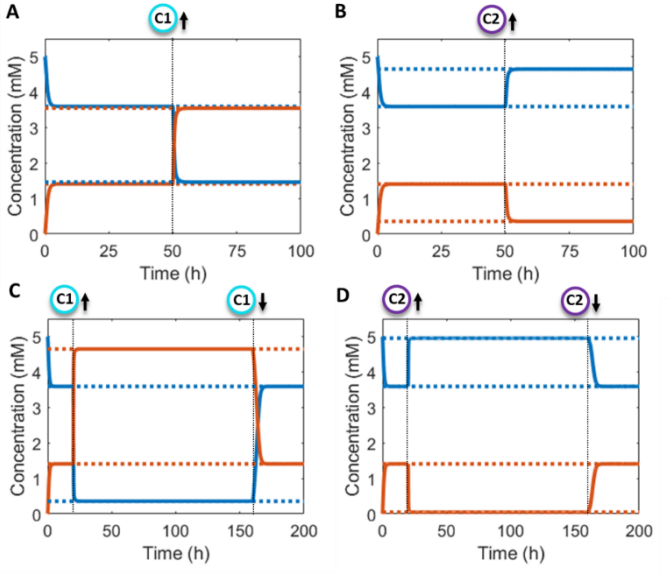

Figure 6.4: Numerical modelling output in CSTR system with *in-situ* catalyst concentration change: **(A)**. Concentration of product P (red/ orange line) and reactant R (blue line) as a function of time (solid lines) and their steady states (dashed lines). C1= 0 mM, 0.1 mM (50 h) and C2= 0 mM constant. **(B).** Concentration of product P (red/ orange line) and reactant R (blue line) as a function of time (solid lines) and their steady states (dashed lines). C1= 0 mM constant and C2= 0 mM, 0.1 mM (50 h). **(C).** Concentration of product P (red/ orange line) and reactant R (blue line) as a function of time (solid lines) and their steady

states (dashed lines). C1= 0 mM, 1 mM (20 h), 0 mM (160 h) and C2= 0 mM constant. **(D)**. Concentration of product P (red/orange line) and reactant R (blue line) as a function of time (solid lines) and their steady states (dashed lines). C1= 0 mM constant and C2= 0 mM, 1 mM (20 h), 0 mM (160 h). Inlet conditions: [F1]=10 mM, [W1]=0 mM, [F2]=10 mM, [W2]=0 mM, [R]=5 mM, [P]=0 mM, rate constants k_{cat1}=10 $mM^{-2}h^{-1}$, k_1=0.1 mM-$1h^{-1}$, k_{cat2}=10 $mM^{-2}h^{-1}$, k_2=0.1 $mM^{-1}h^{-1}$ and residence time τ=1 h.

In the literature, examples of continuous flow out-of-equilibrium systems are less common.[5] Hermans and co-workers used an enzyme catalysed approach with a fuel-driven out-of-equilibrium systems based on ATP-fuelled phosphorylation to switch between right-handed and left-handed helix conformations of a peptide-perylenediimide supramolecular polymer. [22] They could achieve various non-equilibrium steady states in a membrane reactor with a continuous flow set-up. Switching between steady states was also realized with regulation of the amount of fuel, but not with the catalysts, as fixed concentrations of enzymes were compartmentalized inside the reactor.

In continuous flow systems, in general not only the catalyst concentrations can be tuned, but also the residence time is an important design criterion. A shorter residence time decreases the time needed to reach the steady states (SI Figure S6.13), while for longer residence times the steady states are reached later (SI Figure S6.14). However, because of the non-equilibrium nature, there is an optimal residence time for reaching a maximum level of the product steady state. In Figure 6.5 the steady state concentration of product P is plotted versus the residence time. For a system without backward reaction, increasing the residence time will keep increasing the steady state concentration (blue symbols – Figure 6.5A). Yet, for a non-equilibrium system, where the product is also degraded at the same time, an optimum in residence time is observed (red/orange symbols – Figure 6.5A). The height of this optimum can be altered accordingly by changing the catalyst ratios (Figure 6.5B).

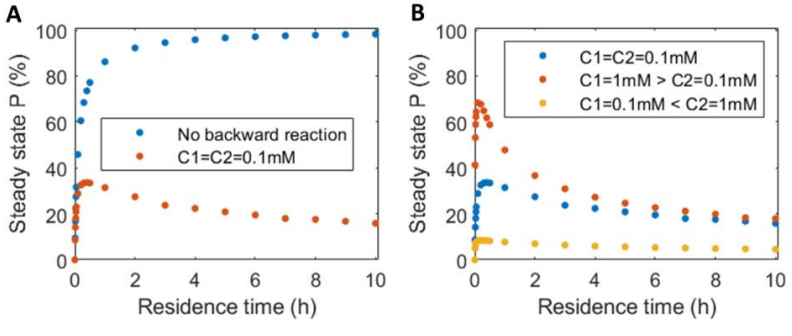

Figure 6.5: Residence time variation vs the steady state concentration of product P: **(A).** Fuel cycle with equal catalysts concentrations (red symbols) vs no backward reaction present (blue symbols). **(B)**. Fuel cycle with varying catalysts concentrations: equal catalysts concentrations C1=C2=0.1 mM (blue symbols), catalyst C1 1mM > catalyst C2 0.1 mM (red symbols) and catalyst C2 1 mM > catalyst C1 0.1 mM (yellow symbols). Inlet conditions: [F1]=10 mM, [W1]=0 mM,

[F2]=10 mM, [W2]=0 mM, [R]=5 mM, [P]=0 mM, [C1]=0.1/1 mM, [C2]=0.1/1 mM, rate constants k_{cat1}=10 $mM^{-2}h^{-1}$, k_1=0.1 $mM^{-1}h^{-1}$, k_{cat2}=10 $mM^{-2}h^{-1}$, k_2=0.1 $mM^{-1}h^{-1}$ and residence time variation from τ=0-10 h. N.B. For no backward reactions, the rate of the catalysed and uncatalysed backward reactions were set to zero.

6.2.2 Feedback regulation

Biasing of pathways in a CRN using two separate catalysts offers a high level of control under batch and flow conditions. Yet, inclusion of additional feedback elements can make the system even more adaptive. Feedback loops are a powerful strategy in cell regulation and used in, amongst others, gene transcription processes and maintenance of protein concentrations levels. A negative feedback speeds up the response to an activating input and steady state levels can be reached more quickly. This way, feedback elements are useful for the protection of cells from perturbations and make them robust towards environmental changes.[8] Incorporation of feedback elements in synthetic materials can mimic cellular homeostasis and ultimately have a huge impact on biomedical designs, such as medical implants.[29-31]

Functionalities like oscillations and bifurcations, often found in non-equilibrium systems, are in essence composed of simpler network motifs combined with positive and negative feedback loops. [7, 32] A classic example of a bistable system and the basis of some oscillatory systems is an autocatalytic reaction in a CSTR.[33, 34] Due to the inherent non-linearity the system shows hysteresis in the reactant efflux vs feed rate.[35] Illustrative examples of oscillatory CRNs with integrated feedback elements come from the hands of Semenov, Huck and Whitesides.[5, 36] Specifically, Semenov and Whitesides designed a system based on thiol chemistry, whereas Semenov and Huck used enzyme activation and inhibition to arrive at a dynamic oscillatory system. Both systems feature an autocatalytic reaction (positive feedback) and an inhibition reaction (negative feedback) in a CSTR.

Here, to illustrate how a simple feedback loop can be incorporated in this generic fuel-driven CRN, we add an additional reaction step (Scheme 6.2 –reaction in maroon colour). Instead of having both catalysts C1 and C2 from the beginning in the reaction mixture, we introduce an inactive procatalyst[37-39] for C2, which can be converted into the active catalyst C2 and a waste product (W3). This activation is catalysed by product P itself. In this way, product P is responsible for an acceleration of its own degradation, which creates an extra negative feedback element. In Figure 6.6 the concentration profiles over time are given for all the species (A), the catalyst species (B), reactant R and product P (C), fuel F1 and waste W1 (D) and reagent F2 and waste W2 (E). Catalyst C2 is generated from proC2 (Figure 6.6B) and both species reach a steady state around 2h. Because of the increase in C2 over time, product P (and reactant R), show(s) a bump in the concentration profile. At first the concentration of P increases rapidly because its degradation is limited due to a low C2 concentration. However, as more P is generated

also more C2 is generated and hence the concentration of P starts to drop again, after which it reaches a steady state. As such, a simple catalytic activation step can change the behaviour of the system significantly and introduce a catalytic negative feedback of the product on its own production.

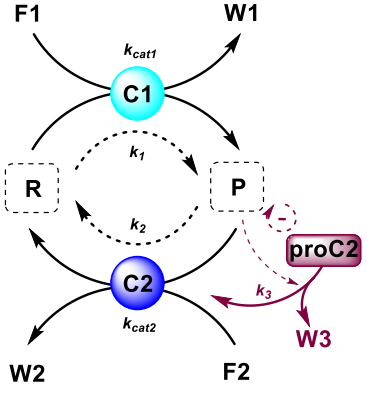

Scheme 6.2: Generic fuel-driven CRN with (un)catalysed formation and degradation reactions and an additional procatalyst activation by product P. Product P catalyses the formation of catalyst C2 and waste W3 from procatalyst proC2. Product P is thus responsible for an acceleration of its own degradation.

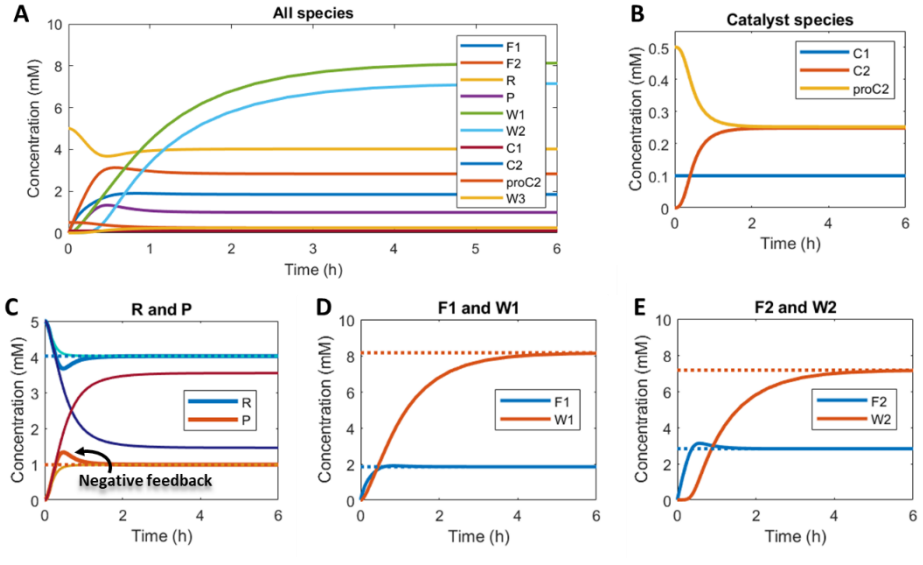

Figure 6.6: Numerical modelling output in CSTR with procatalyst activation by product P: **(A)**. Concentration of all species as a function of time. **(B)**. Concentration over time of the catalyst species: C1, C2 and proC2. **(C)**. Concentration of reactant R and product P as a function of time (red and blue solid lines) and their steady states (red and blue dashed lines). The light blue and yellow line represent the scenario without feedback (without proC2, but 0.25 mM C2 from the start), while the dark blue line and dark red line give the outcome of the scenario without feedback and without C2 (0 mM from the start). **(D)**. Concentration of fuel F1 and waste W1 as a function of time (solid lines) and their steady states (dashed lines). **(E)**. Concentration of reagent

F2 and waste W2 as a function of time (solid lines) and their steady states (dashed lines). Inlet conditions: [F1]=10 mM, [W1]=0 mM, [F2]=10 mM, [W2]=0 mM, [R]=5 mM, [P]=0 mM, [C1]=0.1 mM, [C2]=0 mM, [proC2]=0.5 mM, [W3]=0 mM rate constants k_{cat1}= 10 $mM^{-2}h^{-1}$, k_1= 0.1 $mM^{-1}h^{-1}$, k_{cat2}= 10 $mM^{-2}h^{-1}$, k_2= 0.1 $mM^{-1}h^{-1}$, k_3= 1 $mM^{-1}h^{-1}$ and residence time τ = 1 h.

6.3 PERSPECTIVE AND OUTLOOK

Catalysis is extremely important in biology processes and regulates many non-equilibrium biological CRNs. In these natural systems, catalysis is performed by enzymes. Recently, examples of man-made fuel-driven non-equilibrium CRNs have been growing in number. Incorporation of catalysis in such systems is not trivial, especially because of the high degree of complexity including many simultaneous chemical reactions and reactive chemical functionalities. Nonetheless, several examples of artificial non-equilibrium systems with enzyme, transition metal, organocatalysis (chapter 4) and acid catalysis have been developed in recent years.[15-20, 22-26, 40, 41] The majority of these examples exploit enzyme catalysis to regulate transient product yield and lifetime. Only a small number of transition metal and organocatalytically regulated out-of-equilibrium systems is reported to date. Expanding nature's toolbox by using artificial catalysts, such as transition metals, simpler small molecule organocatalysts or even acid/ base catalysis could significantly boost the application potential of this field. Especially organocatalysts can be easily modified and applied in soft materials or bulk polymer materials[42, 43], although they do often suffer from low activity and high background reactivity. Transition metal catalysts generally outperform organocatalysts when it comes to activity and on/off-ratios. Incorporation of catalysis in materials could open up a new type of matter with a more dynamic character. As a proof of principle, we showed here, using a kinetic model, how two general catalysts can influence the behaviour of a fuel-driven non-equilibrium CRN. Altering catalysts' levels in a batch system results in varying transient product yield and lifetime. Alternatively, the same system in a CSTR can switch between different non-equilibrium steady states depending on the catalysts' ratios. *In-situ* up and downregulation of catalysts' concentrations gives a temporary rise in the product steady state. Additionally, the system can be designed with a negative feedback element, altering the concentration over time profile. In this way simulations can effectively predict the behaviour of CRNs and determine the parameter space of the system.

Having demonstrated that catalytic regulation in a fuel-driven non-equilibrium CRN provides a high degree of control in the simulated system, the next step would be to find chemical reactivity, especially catalysts, that can be used for the design of catalytic non-equilibrium CRNs. Moreover, coupling catalysis to a dissipative CRN containing assembling products could give rise to unusual assembly behaviour and feedback.[26-28] Here, instead of using enzymes, with limited operational stability and high specificity, it would be recommended to start exploring small molecules and metal catalysts. This way

organocatalysis in combination with metal catalysis in non-natural systems can play similar roles as enzymes in nature and provide new systems with a high degree of control and an adaptive character. Ultimately, a better understanding of such systems and the associated chemistry can bring us closer to the design of man-made signal responsive and interactive materials.[29-31, 44]

6.4 REFERENCES

1. P. Blume-Jensen and T. Hunter, *Nature*, 2001, **411**, 355-365.
2. S. Fernandez, V. Desplat, A. Villacreces, A. V. Guitart, N. Milpied, A. Pigneux, I. Vigon, J.-M. Pasquet and P.-Y. Dumas, *Int. J. Mol. Sci.*, 2019, **20**, 3429.
3. B. N. Kholodenko, *Nat. Rev. Mol.*, 2006, **7**, 165.
4. J. E. Ferrell Jr., T. Y. C. Tsai and Q. Yang, *Cell*, 2011, **144**, 874-885.
5. S. N. Semenov, A. S. Y. Wong, R. M. van der Made, S. G. J. Postma, J. Groen, H. W. H. van Roekel, T. F. A. de Greef and W. T. S. Huck, *Nat. Chem.*, 2015, **7**, 160.
6. S. A. P. van Rossum, M. Tena-Solsona, J. H. van Esch, R. Eelkema and J. Boekhoven, *Chem. Soc. Rev.*, 2017, **46**, 5519-5535.
7. A. S. Wong and W. T. Huck, *Beilstein J. Org. Chem.*, 2017, **13**, 1486-1497.
8. B. Alberts, A. Johnson, J. Lewis, D. Morgan, M. Raff, K. Roberts and P. Walter, *Molecular biology of the cell*, Garland Science, New York, Sixth edition edn., 2014.
9. B. Rieß and J. Boekhoven, *ChemNanoMat*, 2018, **4**, 710-719.
10. B. Rieß, R. K. Grötsch and J. Boekhoven, *Chem*, 2020, **6**, 552-578.
11. S. De and R. Klajn, *Adv. Mater.*, 2018, **30**, 1706750.
12. G. Ragazzon and L. Prins, *Nat. Nanotechol.*, 2018, **13**, 882–889.
13. N. Singh, G. J. Formon, S. De Piccoli and T. M. Hermans, *Adv. Mater.*, 2020, **32**, 1906834.
14. G. Lebon, D. Jou and J. Casas-Vázquez, *Understanding non-equilibrium thermodynamics*, Springer, 2008.
15. S. Debnath, S. Roy and R. V. Ulijn, *J. Am. Chem. Soc.*, 2013, **135**, 16789-16792.
16. L. Heinen, T. Heuser, A. Steinschulte and A. Walther, *Nano Lett.*, 2017, **17**, 4989-4995.
17. S. Maiti, I. Fortunati, C. Ferrante, P. Scrimin and L. J. Prins, *Nat. Chem.*, 2016, **8**, 725.
18. C. Pezzato and L. J. Prins, *Nat. Commun.*, 2015, **6**, 7790.
19. S. Dhiman, A. Jain and S. J. George, *Angew. Chem. Int. Ed.*, 2017, **129**, 1349-1353.
20. S. Dhiman, A. Jain, M. Kumar and S. George, *J. Am. Chem. Soc.*, 2017, **139**, 16568-16575.
21. A. Mishra, D. B. Korlepara, M. Kumar, A. Jain, N. Jonnalagadda, K. K. Bejagam, S. Balasubramanian and S. George, *Nat. Commun.*, 2018, **9**, 1295.
22. A. Sorrenti, J. Leira-Iglesias, A. Sato and T. M. Hermans, *Nat. Commun.*, 2017, **8**, 15899.
23. C. S. Wood, C. Browne, D. M. Wood and J. R. Nitschke, *ACS Cent. Sci.*, 2015, **1**, 504-509.
24. M. P. van der Helm, C.-L. Wang, B. Fan, M. Macchione, E. Mendes and R. Eelkema, *Angew. Chem. Int. Ed.*, 2020, **59**, 20604-20611.
25. N. Singh, B. Lainer, G. J. Formon, S. De Piccoli and T. M. Hermans, *J. Am. Chem. Soc.*, 2020, **142**, 4083-4087.
26. S. Bal, K. Das, S. Ahmed and D. Das, *Angew. Chem. Int. Ed.*, 2019, **58**, 244-247.
27. S. P. Afrose, S. Bal, A. Chatterjee, K. Das and D. Das, *Angew. Chem. Int. Ed.*, 2019, **131**, 15930-15934.
28. S. Bal, C. Ghosh, T. Ghosh, R. K. Vijayaraghavan and D. Das, *Angew. Chem. Int. Ed.*, 2020, **59**, 13506-13510.
29. P. A. Korevaar, C. N. Kaplan, A. Grinthal, R. M. Rust and J. Aizenberg, *Nat. Commun.*, 2020, **11**, 1-10.
30. X. He, M. Aizenberg, O. Kuksenok, L. D. Zarzar, A. Shastri, A. C. Balazs and J. Aizenberg, *Nature*, 2012, **487**, 214-218.
31. M. M. Lerch, A. Grinthal and J. Aizenberg, *Adv. Mater.*, 2020, **32**, 2070159.
32. B. Novák and J. J. Tyson, *Nat. Rev. Mol.*, 2008, **9**, 981-991.
33. A. I. Hanopolskyi, V. A. Smaliak, A. I. Novichkov and S. N. Semenov, *ChemSystemsChem*, 2020, DOI: 10.1002/syst.202000026.
34. A. J. Bissette and S. P. Fletcher, *Angew. Chem. Int. Ed.*, 2013, **52**, 12800-12826.
35. G. Koper and W. Hendriksen, in *Non-equilibrium Thermodynamics with Applications*, 2016, ch. Chapter 7 Non-equilibrium Molecular Self-assembly, pp. 134-153.
36. S. N. Semenov, L. J. Kraft, A. Ainla, M. Zhao, M. Baghbanzadeh, V. E. Campbell, K. Kang, J. M. Fox and G. M. Whitesides, *Nature*, 2016, **537**, 656-660.

37. C. Maity, F. Trausel and R. Eelkema, *Chem. Sci.*, 2018, **9**, 5999-6005.
38. F. Trausel, C. Maity, J. M. Poolman, D. Kouwenberg, F. Versluis, J. H. van Esch and R. Eelkema, *Nat. Commun.*, 2017, **8**, 879.
39. T. G. Brevé, M. Filius, C. Araman, M. P. van der Helm, P. L. Hagedoorn, C. Joo, S. I. van Kasteren and R. Eelkema, *Angew. Chem. Int. Ed.*, 2020, **59**, 9340-9344.
40. J. Deng and A. Walther, *J. Am. Chem. Soc.*, 2020, **142**, 685-689.
41. L. Heinen and A. Walther, *Sci. Adv.*, 2019, **5**, eaaw0590.
42. J. C. Worch and A. P. Dove, *ACS Macro Lett.*, 2020, **9**, 1494-1506.
43. C. Jehanno, M. M. Pérez-Madrigal, J. Demarteau, H. Sardon and A. P. Dove, *Polym. Chem.*, 2019, **10**, 172-186.
44. A. Walther, *Adv. Mater.*, 2020, **32**, 1905111.

6.5 SUPPLEMENTARY INFORMATION

6.5.1 Kinetic model design

The fuel-driven CRN consists of four reactions, two catalysed formation and degradation reactions and two uncatalysed formation and degradation reactions. A numerical model for this reaction network was written in MATLAB R2018b. Reactant (R) is interconverted into product (P) by suppling fuel (F1) and concomitantly generating waste (W1), catalysed by C1 ($kcat_1$) and uncatalysed (k_1). P is only transiently stable and degrades again with reagent (F2), generating R and waste (W2), catalysed by C2 ($kcat_2$) and uncatalysed (k_2). This results in the following system of differential equations (ODEs):

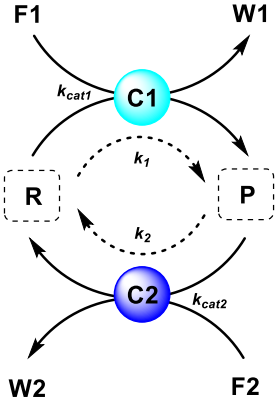

$$\frac{d[P]}{dt} = (k_{cat1}[\boldsymbol{C1}]+k_1)[\boldsymbol{F1}][\boldsymbol{R}] - (k_{cat2}[\boldsymbol{C2}] + k_2)[\boldsymbol{F2}][\boldsymbol{P}]$$

$$\frac{d[R]}{dt} = -(k_{cat1}[\boldsymbol{C1}] + k_1)[\boldsymbol{F1}][\boldsymbol{R}] + (k_{cat2}[\boldsymbol{C2}] + k_2)[\boldsymbol{F2}][\boldsymbol{P}]$$

$$\frac{d[F1]}{dt} = -(k_{cat1}[\boldsymbol{C1}] + k_1)[\boldsymbol{F1}][\boldsymbol{R}]$$

$$\frac{d[F2]}{dt} = -(k_{cat2}[\boldsymbol{C2}] + k_2)[\boldsymbol{F2}][\boldsymbol{P}]$$

$$\frac{d[W1]}{dt} = (k_{cat1}[\boldsymbol{C1}] + k_1)[\boldsymbol{F1}][\boldsymbol{R}]$$

$$\frac{d[W2]}{dt} = (k_{cat2}[\boldsymbol{C2}] + k_2)[\boldsymbol{F2}][\boldsymbol{P}]$$

The system of ODEs is solved numerically in batch and continuous flow (i.e. CSTR) for different initial/inlet conditions, which are all specified in the caption of each figure in the main text and the supplementary information.

For the CSTR system the inflow and outflow of reactants and products is taken into account, following the equation for all species:

$$\boldsymbol{Accumulation = in - out + reaction}$$

$$\frac{d[\boldsymbol{C}]}{dt} = \frac{\boldsymbol{C_{in} - C_{out}}}{\boldsymbol{\tau}} + \boldsymbol{reaction}$$

In order to calculate the steady states levels in the CSTR system the differential equations are set to zero and calculated numerically with MATLAB:

In steady state

$$\frac{d[\boldsymbol{C}]}{dt} = \frac{\boldsymbol{C_{in}} - \boldsymbol{C_{out}}}{\boldsymbol{\tau}} + \boldsymbol{reaction} = \mathbf{0}$$

For the system with an additional negative feedback element, the procatalyst activation step catalysed by product P leads to the introduction of the following extra rate equations to the system of ODEs:

System with procatalyst activation for C2 (catalysed by product P)

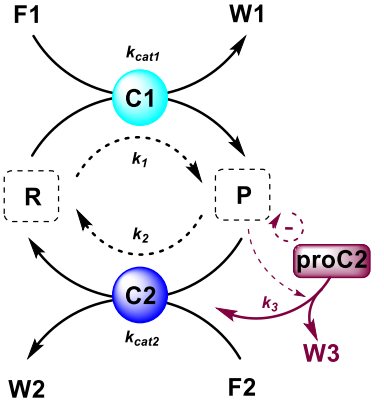

$$\frac{d[\boldsymbol{proC2}]}{dt} = -k_3[\boldsymbol{P}][\boldsymbol{proC2}]$$

$$\frac{d[\boldsymbol{C2}]}{dt} = k_3[\boldsymbol{P}][\boldsymbol{proC2}]$$

$$\frac{d[\boldsymbol{W3}]}{dt} = k_3[\boldsymbol{P}][\boldsymbol{proC2}]$$

6.5.2 Batch reaction output

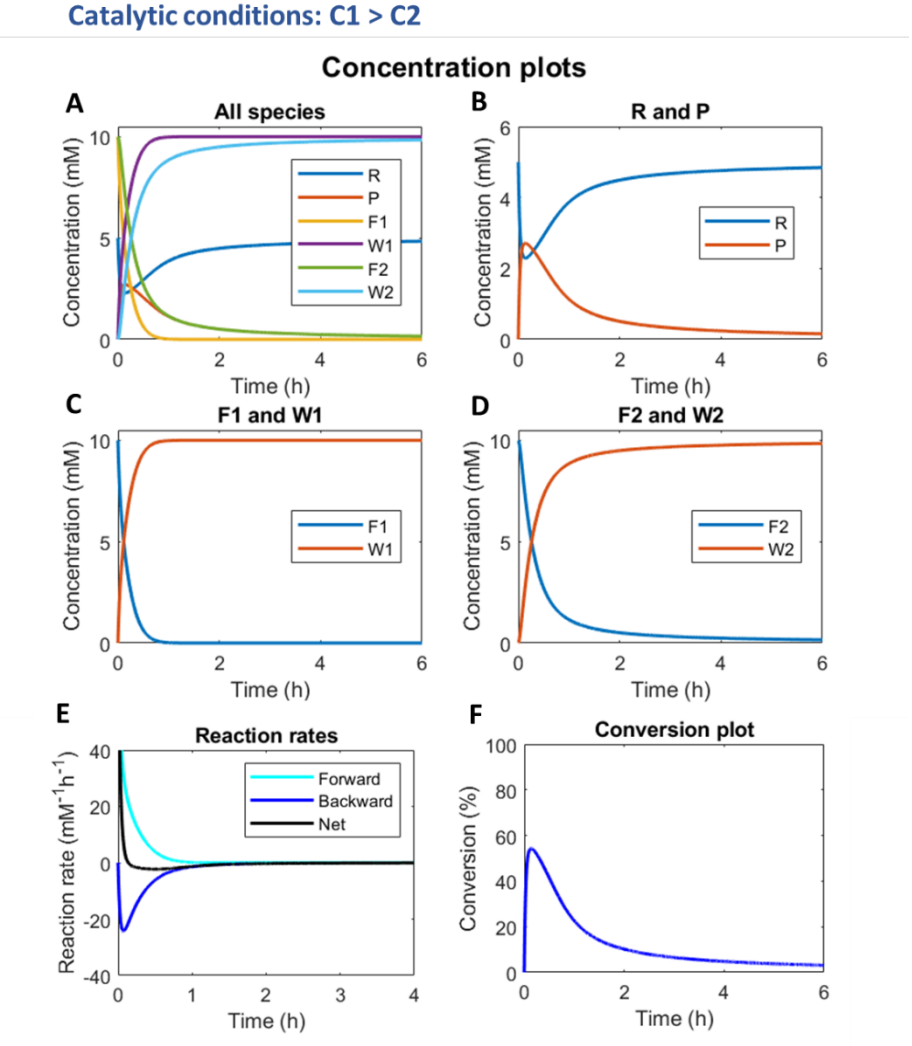

Figure S6.1: Numerical modelling output in batch-mode: **(A).** Concentration of all species as a function of time. **(B).** Concentration of reactant R and product P as a function of time. **(C).** Concentration of fuel F1 and waste W1 as a function of time. **(D).** Concentration of reagent F2 and waste W2 as a function of time. **(E).** Reaction rates for product P formation and degradation as a function of time. **(F).** Conversion plot of reactant R. Initial conditions: [F1]=10 mM, [W1]=0 mM, [F2]=10 mM, [W2]=0 mM, [R]=5 mM, [P]=0 mM, **[C1]=0.2 mM**, **[C2]=0.1 mM** and rate constants k_{cat1}= 10 $mM^{-2}h^{-1}$, k_1= 0.1 $mM^{-1}h^{-1}$, k_{cat2}= 10 $mM^{-2}h^{-1}$, k_2= 0.1 $mM^{-1}h^{-1}$.

Catalytic conditions: C1 < C2

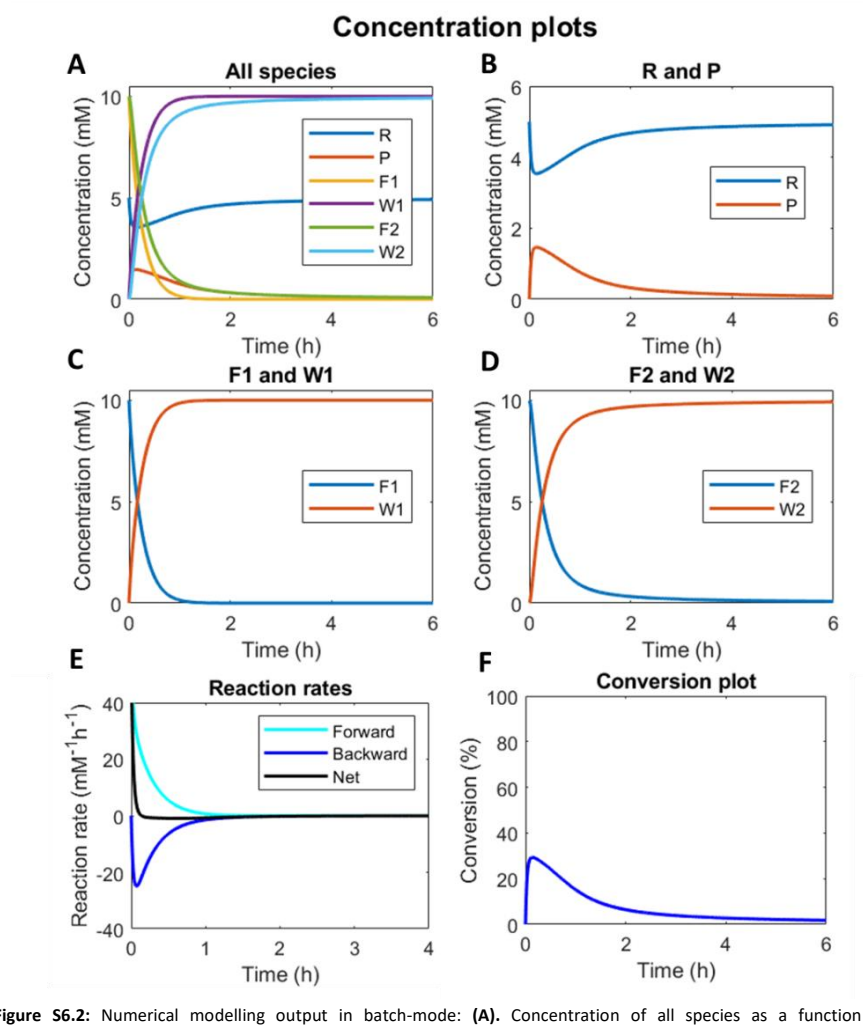

Figure S6.2: Numerical modelling output in batch-mode: **(A).** Concentration of all species as a function of time. **(B).** Concentration of reactant R and product P as a function of time. **(C).** Concentration of fuel F1 and waste W1 as a function of time. **(D).** Concentration of reagent F2 and waste W2 as a function of time. **(E).** Reaction rates for product P formation and degradation as a function of time. **(F).** Conversion plot of reactant R. Initial conditions: [F1]=10 mM, [W1]=0 mM, [F2]=10 mM, [W2]=0 mM, [R]=5 mM, [P]=0 mM, **[C1]=0.1 mM**, **[C2]=0.2 mM** and rate constants k_{cat1}= 10 $mM^{-2}h^{-1}$, k_1= 0.1 $mM^{-1}h^{-1}$, k_{cat2}= 10 $mM^{-2}h^{-1}$, k_2= 0.1 $mM^{-1}h^{-1}$.

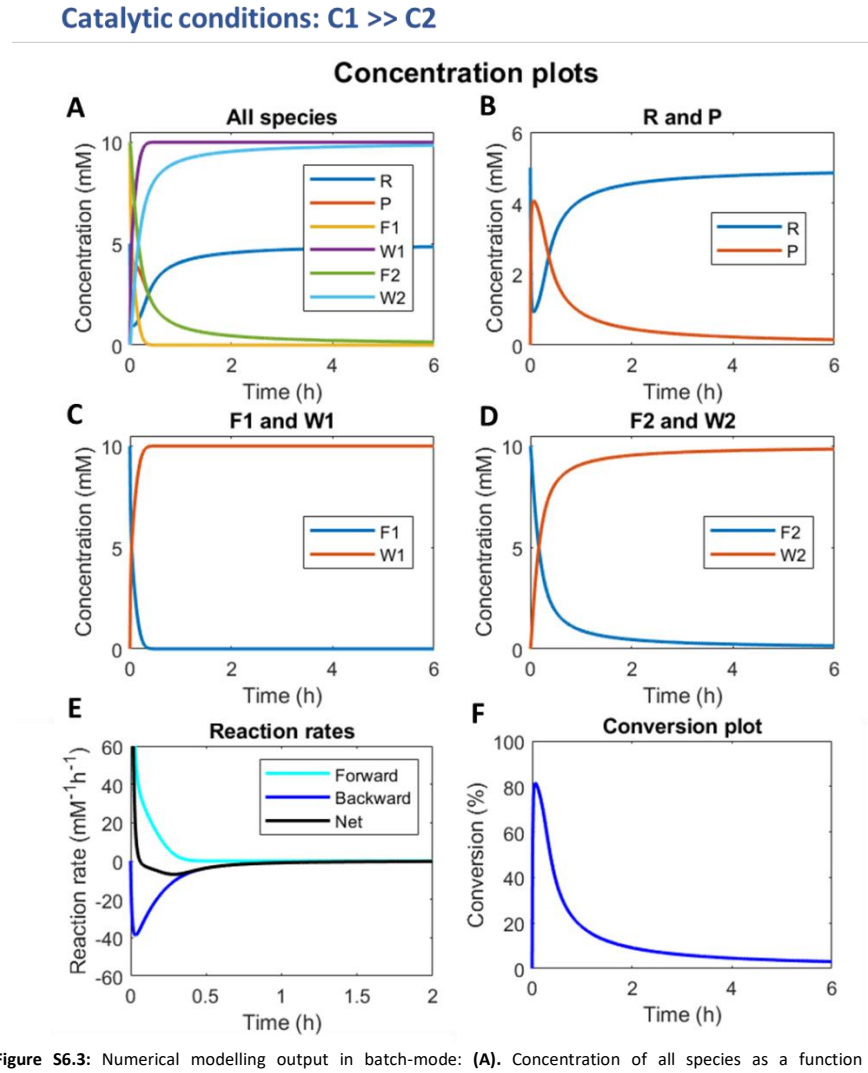

Figure S6.3: Numerical modelling output in batch-mode: **(A).** Concentration of all species as a function of time. **(B).** Concentration of reactant R and product P as a function of time. **(C).** Concentration of fuel F1 and waste W1 as a function of time. **(D).** Concentration of reagent F2 and waste W2 as a function of time. **(E).** Reaction rates for product P formation and degradation as a function of time. **(F).** Conversion plot of reactant R. Initial conditions: [F1]=10 mM, [W1]=0 mM, [F2]=10 mM, [W2]=0 mM, [R]=5 mM, [P]=0 mM, **[C1]=1 mM**, **[C2]=0.1 mM** and rate constants k_{cat1}= 10 $mM^{-2}h^{-1}$, k_1= 0.1 $mM^{-1}h^{-1}$, k_{cat2}= 10 $mM^{-2}h^{-1}$, k_2= 0.1 $mM^{-1}h^{-1}$.

Catalytic conditions: C1 << C2

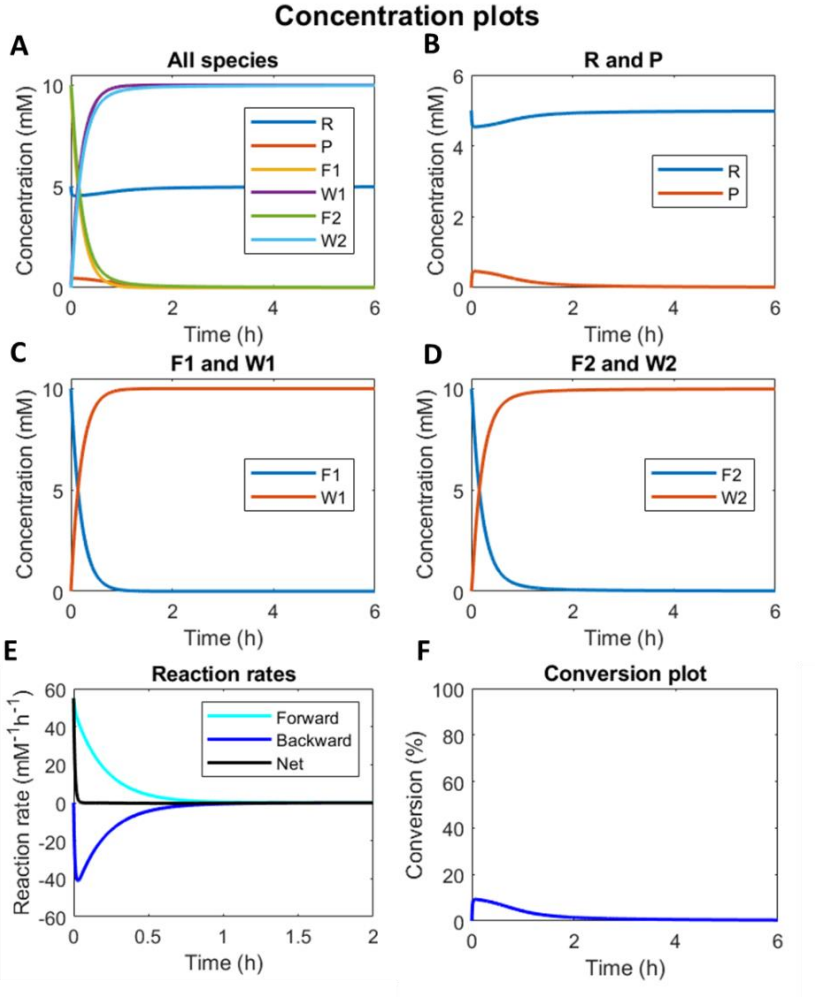

Figure S6.4: Numerical modelling output in batch-mode: **(A).** Concentration of all species as a function of time. **(B).** Concentration of reactant R and product P as a function of time. **(C).** Concentration of fuel F1 and waste W1 as a function of time. **(D).** Concentration of reagent F2 and waste W2 as a function of time. **(E).** Reaction rates for product P formation and degradation as a function of time. **(F).** Conversion plot of reactant R. Initial conditions: [F1]=10 mM, [W1]=0 mM, [F2]=10 mM, [W2]=0 mM, [R]=5 mM, [P]=0 mM, **[C1]=0.1 mM**, **[C2]=1 mM** and rate constants k_{cat1}= 10 $mM^{-2}h^{-1}$, k_1= 0.1 $mM^{-1}h^{-1}$, k_{cat2}= 10 $mM^{-2}h^{-1}$, k_2= 0.1 $mM^{-1}h^{-1}$.

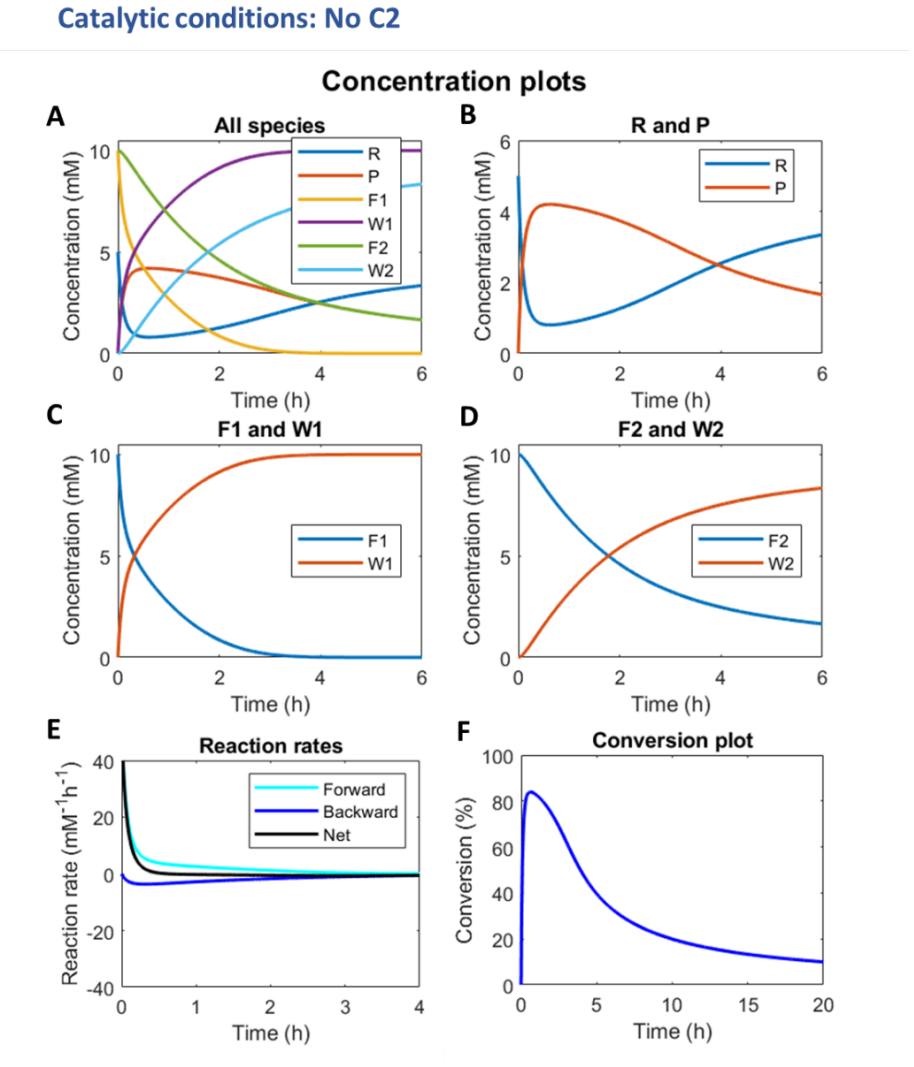

Figure S6.5: Numerical modelling output in batch-mode: **(A).** Concentration of all species as a function of time. **(B).** Concentration of reactant R and product P as a function of time. **(C).** Concentration of fuel F1 and waste W1 as a function of time. **(D).** Concentration of reagent F2 and waste W2 as a function of time. **(E).** Reaction rates for product P formation and degradation as a function of time. **(F).** Conversion plot of reactant R. Initial conditions: [F1]=10 mM, [W1]=0 mM, [F2]=10 mM, [W2]=0 mM, [R]=5 mM, [P]=0 mM, **[C1]=0.1 mM**, **[C2]=0 mM** and rate constants k_{cat1}= 10 $mM^{-2}h^{-1}$, k_1= 0.1 $mM^{-1}h^{-1}$, k_{cat2}= 10 $mM^{-2}h^{-1}$, k_2= 0.1 $mM^{-1}h^{-1}$.

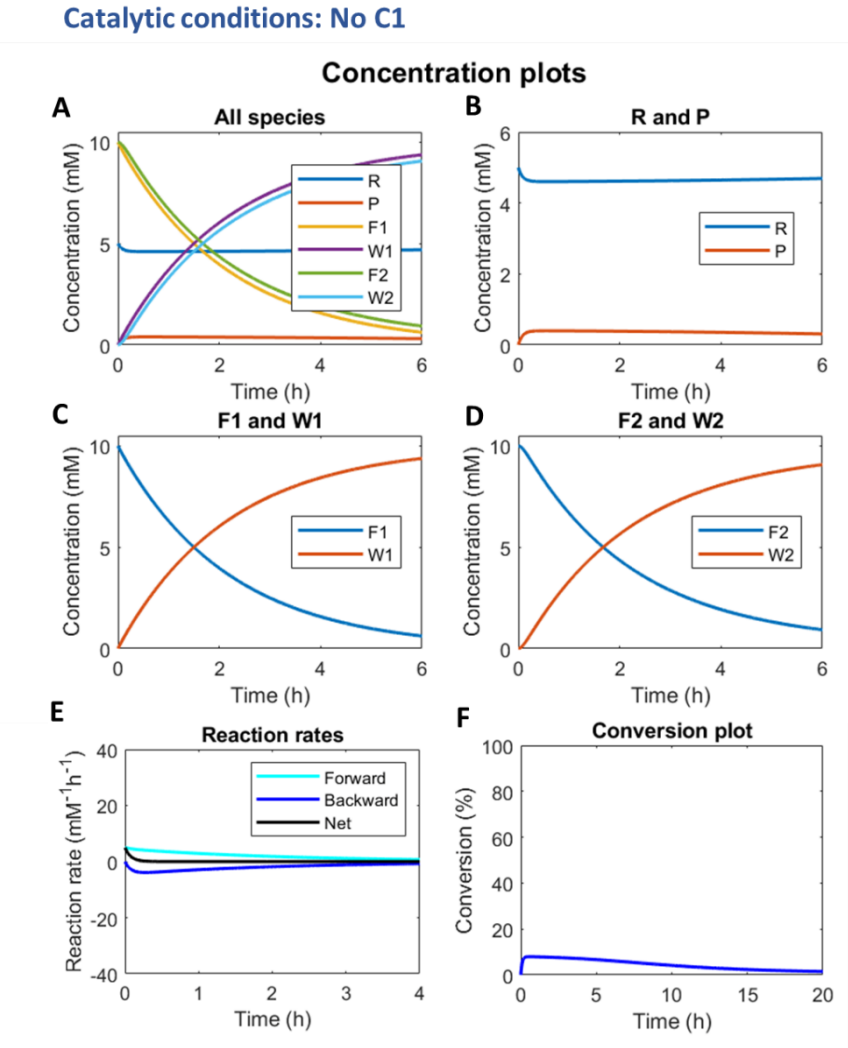

Figure S6.6: Numerical modelling output in batch-mode: **(A).** Concentration of all species as a function of time. **(B).** Concentration of reactant R and product P as a function of time. **(C).** Concentration of fuel F1 and waste W1 as a function of time. **(D).** Concentration of reagent F2 and waste W2 as a function of time. **(E).** Reaction rates for product P formation and degradation as a function of time. **(F).** Conversion plot of reactant R. Initial conditions: [F1]=10 mM, [W1]=0 mM, [F2]=10 mM, [W2]=0 mM, [R]=5 mM, [P]=0 mM, **[C1]=0 mM**, **[C2]=0.1 mM** and rate constants k_{cat1}= 10 $mM^{-2}h^{-1}$, k_1= 0.1 $mM^{-1}h^{-1}$, k_{cat2}= 10 $mM^{-2}h^{-1}$, k_2= 0.1 $mM^{-1}h^{-1}$.

Catalytic conditions: C1=C2, no background for forward and backward reaction

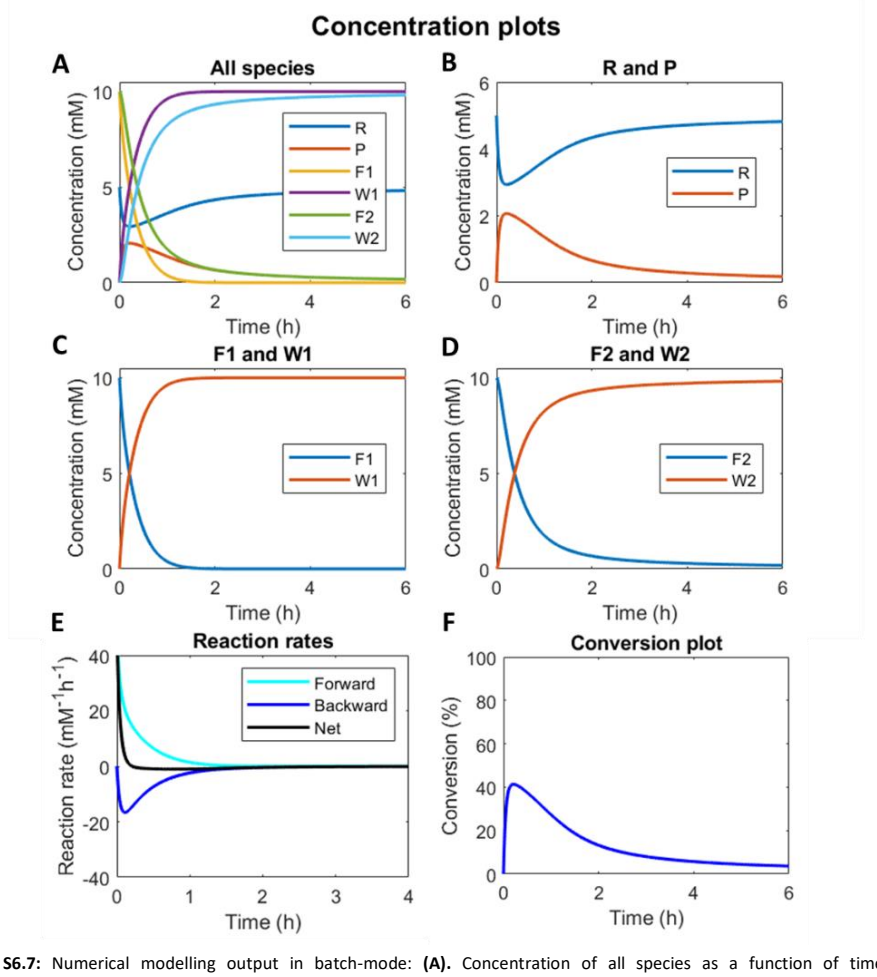

Figure S6.7: Numerical modelling output in batch-mode: **(A).** Concentration of all species as a function of time. **(B).** Concentration of reactant R and product P as a function of time. **(C).** Concentration of fuel F1 and waste W1 as a function of time. **(D).** Concentration of reagent F2 and waste W2 as a function of time. **(E).** Reaction rates for product P formation and degradation as a function of time. **(F).** Conversion plot of reactant R. Initial conditions: [F1]=10 mM, [W1]=0 mM, [F2]=10 mM, [W2]=0 mM, [R]=5 mM, [P]=0 mM, **[C1]=0.1 mM**, **[C2]=0.1 mM** and rate constants k_{cat1}= 10 $mM^{-2}h^{-1}$, $\boldsymbol{k_1}$**= 0** $\mathbf{mM^{-1}h^{-1}}$, k_{cat2}= 10 $mM^{-2}h^{-1}$, $\boldsymbol{k_2}$**= 0** $\mathbf{mM^{-1}h^{-1}}$.

Catalytic conditions: No C2 and no background for forward and backward reaction

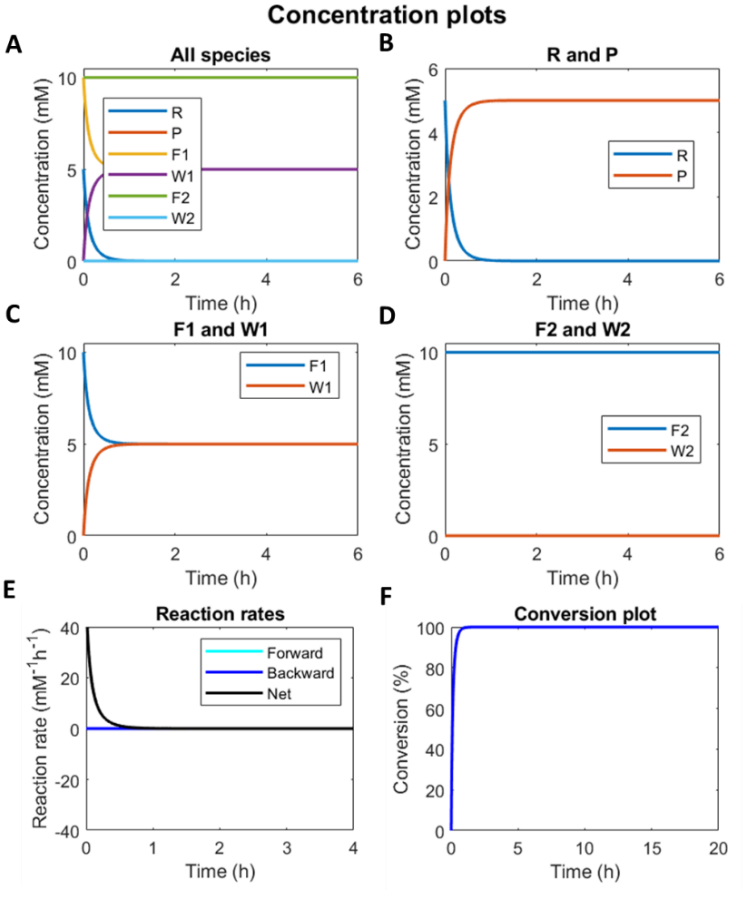

Figure S6.8: Numerical modelling output in batch-mode: **(A).** Concentration of all species as a function of time. **(B).** Concentration of reactant R and product P as a function of time. **(C).** Concentration of fuel F1 and waste W1 as a function of time. **(D).** Concentration of reagent F2 and waste W2 as a function of time. **(E).** Reaction rates for product P formation and degradation as a function of time. **(F).** Conversion plot of reactant R. Initial conditions: [F1]=10 mM, [W1]=0 mM, [F2]=10 mM, [W2]=0 mM, [R]=5 mM, [P]=0 mM, **[C1]=0.1 mM**, **[C2]=0 mM** and rate constants k_{cat1}= 10 $mM^{-2}h^{-1}$, $\boldsymbol{k_1}$**= 0** $\mathbf{mM^{-1}h^{-1}}$, k_{cat2}= 10 $mM^{-2}h^{-1}$, $\boldsymbol{k_2}$**= 0** $\mathbf{mM^{-1}h^{-1}}$.

6.5.3 CSTR reaction output

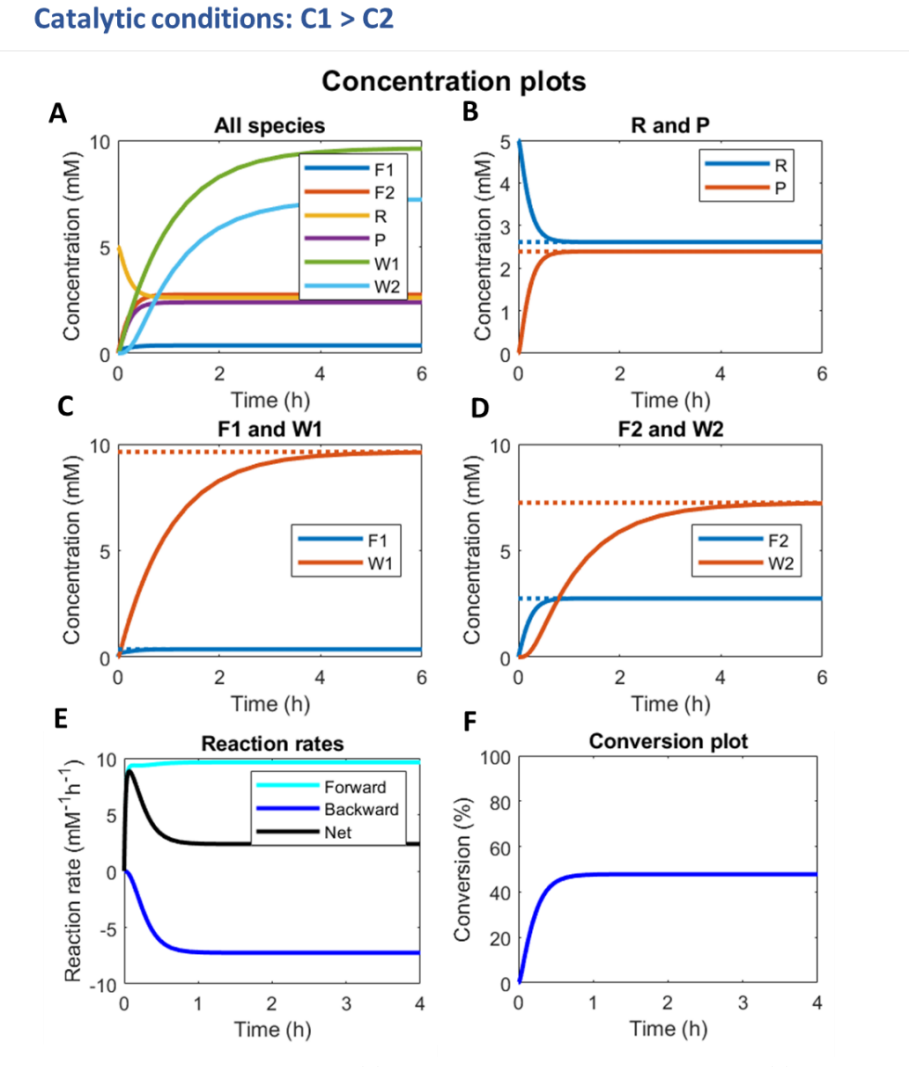

Figure S6.9: Numerical modelling output in CSTR: **(A).** Concentration of all species as a function of time. **(B).** Concentration of reactant R and product P as a function of time (solid lines) and their steady states (dashed lines). **(C).** Concentration of fuel F1 and waste W1 as a function of time (solid lines) and their steady states (dashed lines). **(D).** Concentration of reagent F2 and waste W2 as a function of time (solid lines) and their steady states (dashed lines). **(E).** Reaction rates for product P formation and degradation as a function of time. **(F).** Conversion plot of reactant R. Inlet conditions: [F1]=10 mM, [W1]=0 mM, [F2]=10 mM, [W2]=0 mM, [R]=5 mM, [P]=0 mM, **[C1]=1 mM, [C2]=0.1 mM**, rate constants k_{cat1}= 10 $mM^{-2}h^{-1}$, k_1= 0.1 $mM^{-1}h^{-1}$, k_{cat2}=10 $mM^{-2}h^{-1}$, k_2= 0.1 $mM^{-1}h^{-1}$ and **residence time τ = 1 h**.

Catalytic conditions: C1 < C2

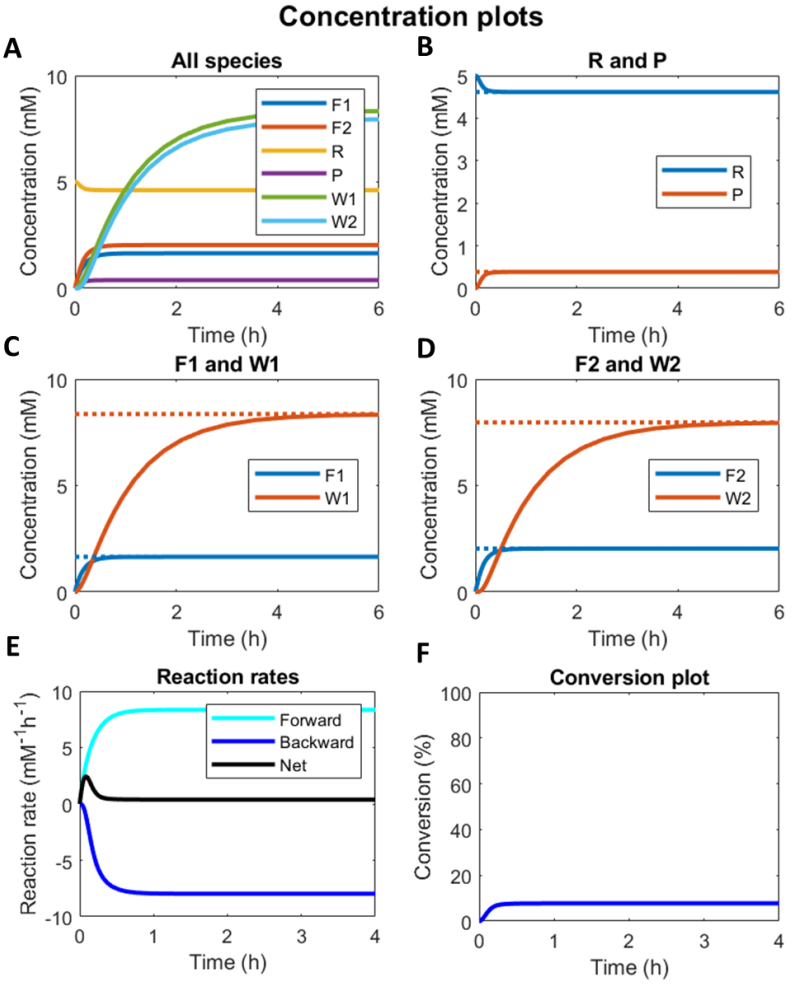

Figure S6.10: Numerical modelling output in CSTR: **(A).** Concentration of all species as a function of time. **(B).** Concentration of reactant R and product P as a function of time (solid lines) and their steady states (dashed lines). **(C).** Concentration of fuel F1 and waste W1 as a function of time (solid lines) and their steady states (dashed lines). **(D).** Concentration of reagent F2 and waste W2 as a function of time (solid lines) and their steady states (dashed lines). **(E).** Reaction rates for product P formation and degradation as a function of time. **(F).** Conversion plot of reactant R. Inlet conditions: [F1]=10 mM, [W1]=0 mM, [F2]=10 mM, [W2]=0 mM, [R]=5 mM, [P]=0 mM, **[C1]=0.1 mM, [C2]=1 mM**, rate constants k_{cat1}= 10 $mM^{-2}h^{-1}$, k_1= 0.1 $mM^{-1}h^{-1}$, k_{cat2}=10 $mM^{-2}h^{-1}$, k_2= 0.1 $mM^{-1}h^{-1}$ and **residence time τ = 1 h**.

Catalytic conditions: C1 > C2

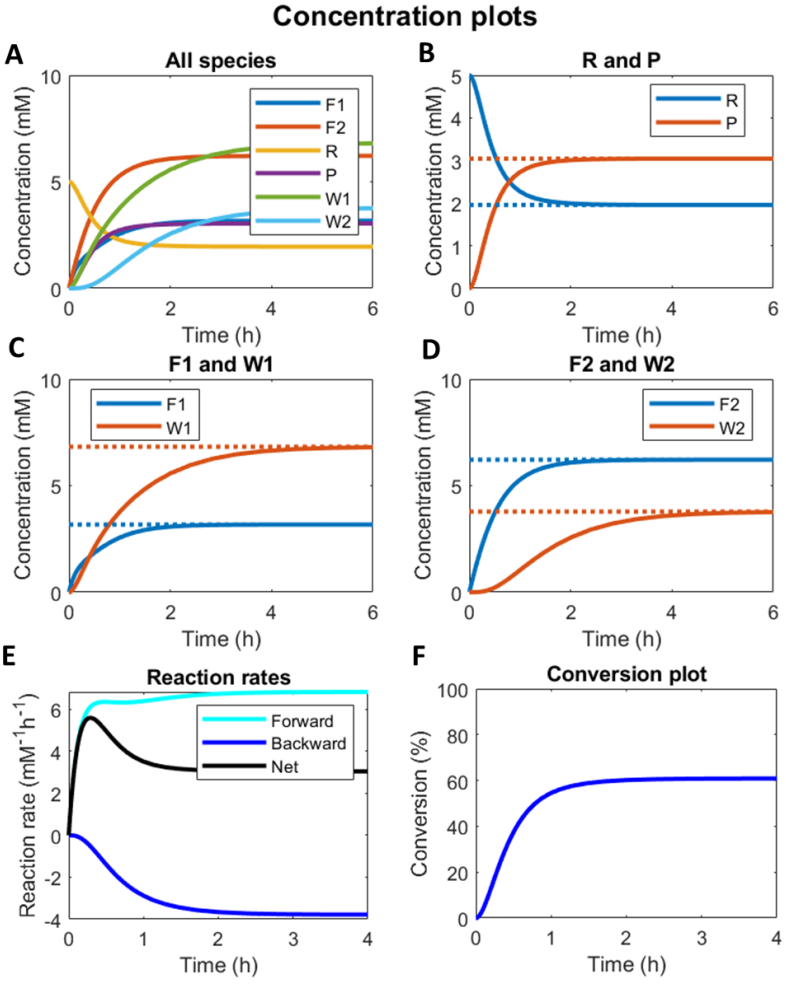

Figure S6.11: Numerical modelling output in CSTR: **(A).** Concentration of all species as a function of time. **(B).** Concentration of reactant R and product P as a function of time (solid lines) and their steady states (dashed lines). **(C).** Concentration of fuel F1 and waste W1 as a function of time (solid lines) and their steady states (dashed lines). **(D).** Concentration of reagent F2 and waste W2 as a function of time (solid lines) and their steady states (dashed lines). **(E).** Reaction rates for product P formation and degradation as a function of time. **(F).** Conversion plot of reactant R. Inlet conditions: [F1]=10 mM, [W1]=0 mM, [F2]=10 mM, [W2]=0 mM, [R]=5 mM, [P]=0 mM, **[C1]=0.1 mM, [C2]=0.01 mM**, rate constants k_{cat1}= 10 $mM^{-2}h^{-1}$, k_1= 0.1 $mM^{-1}h^{-1}$, k_{cat2}=10 $mM^{-2}h^{-1}$, k_2= 0.1 $mM^{-1}h^{-1}$ and **residence time τ = 1 h**.

Catalytic conditions: C1 < C2

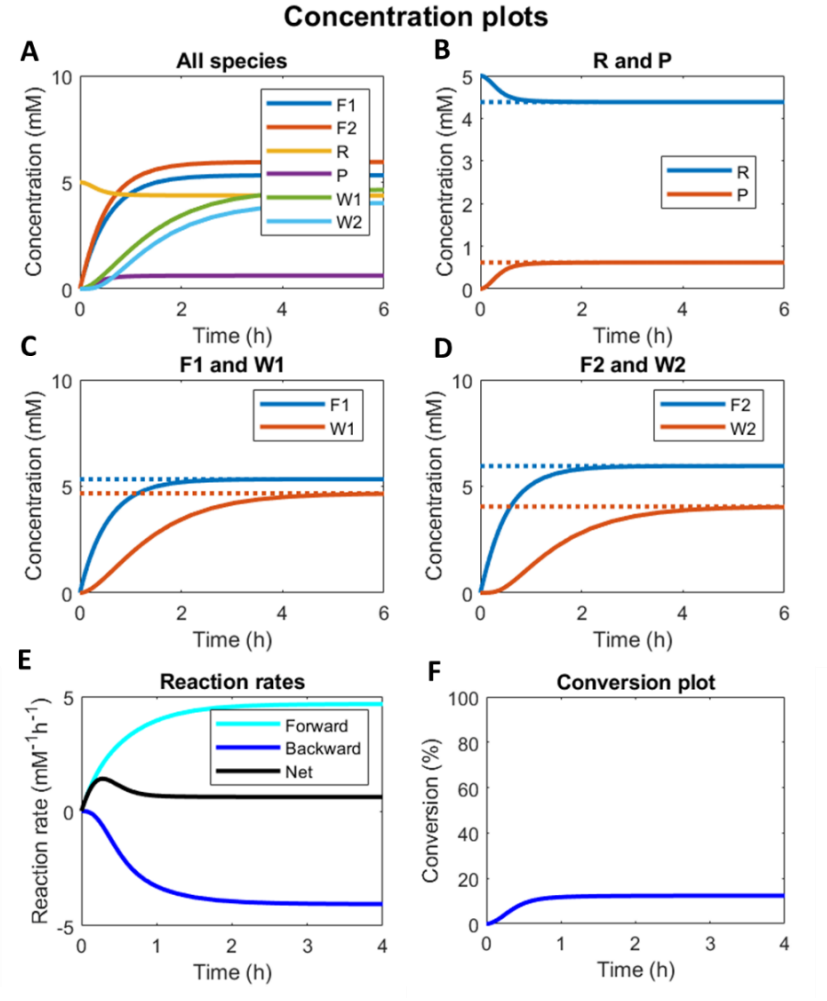

Figure S6.12: Numerical modelling output in CSTR: **(A).** Concentration of all species as a function of time. **(B).** Concentration of reactant R and product P as a function of time (solid lines) and their steady states (dashed lines). **(C).** Concentration of fuel F1 and waste W1 as a function of time (solid lines) and their steady states (dashed lines). **(D).** Concentration of reagent F2 and waste W2 as a function of time (solid lines) and their steady states (dashed lines). **(E).** Reaction rates for product P formation and degradation as a function of time. **(F).** Conversion plot of reactant R. Inlet conditions: [F1]=10 mM, [W1]=0 mM, [F2]=10 mM, [W2]=0 mM, [R]=5 mM, [P]=0 mM, **[C1]=0.01 mM, [C2]=0.1 mM**, rate constants k_{cat1}= 10 $mM^{-2}h^{-1}$, k_1= 0.1 $mM^{-1}h^{-1}$, k_{cat2}=10 $mM^{-2}h^{-1}$, k_2= 0.1 $mM^{-1}h^{-1}$ and **residence time τ = 1 h**.

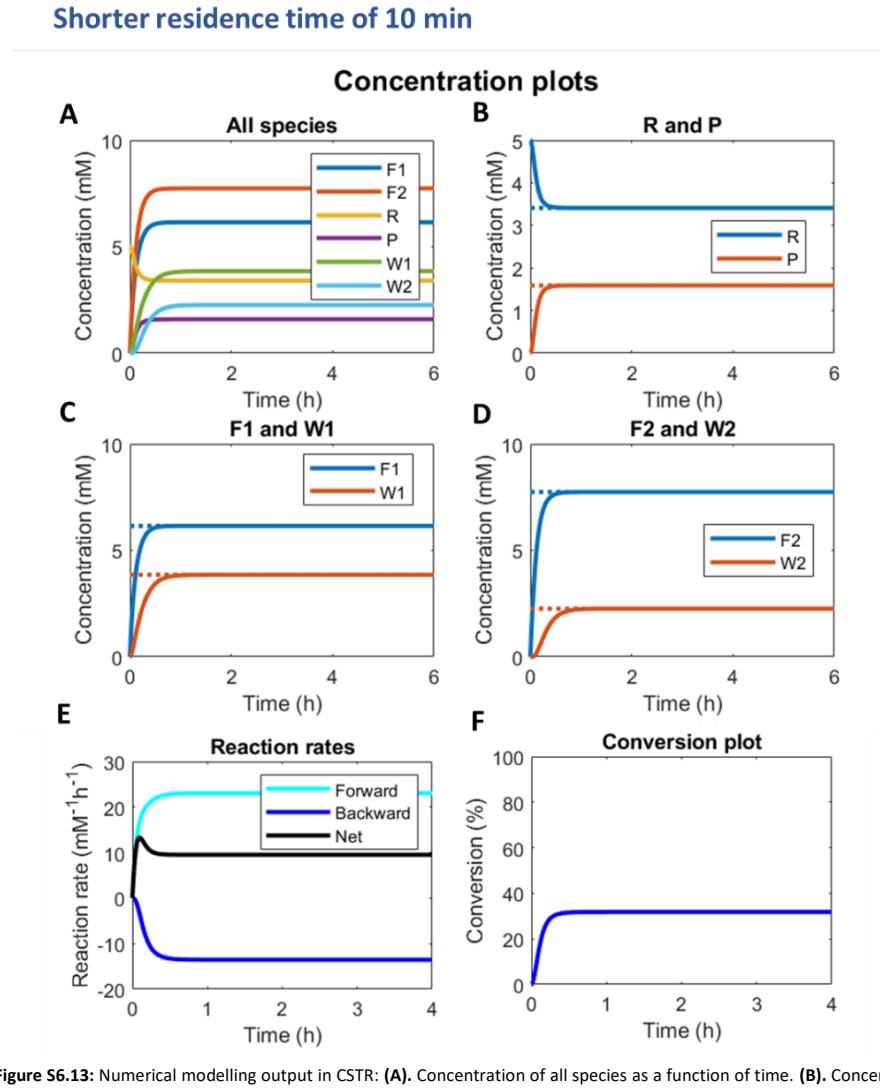

Figure S6.13: Numerical modelling output in CSTR: **(A).** Concentration of all species as a function of time. **(B).** Concentration of reactant R and product P as a function of time (solid lines) and their steady states (dashed lines). **(C).** Concentration of fuel F1 and waste W1 as a function of time (solid lines) and their steady states (dashed lines). **(D).** Concentration of reagent F2 and waste W2 as a function of time (solid lines) and their steady states (dashed lines). **(E).** Reaction rates for product P formation and degradation as a function of time. **(F).** Conversion plot of reactant R. Inlet conditions: [F1]=10 mM, [W1]=0 mM, [F2]=10 mM, [W2]=0 mM, [R]=5 mM, [P]=0 mM, **[C1]=0.1 mM, [C2]=0.1 mM**, rate constants k_{cat1}= 10 $mM^{-2}h^{-1}$, k_1= 0.1 $mM^{-1}h^{-1}$, k_{cat2}=10 $mM^{-2}h^{-1}$, k_2= 0.1 $mM^{-1}h^{-1}$ and **residence time τ = 10 min (0.167 h)**.

Longer residence time of 1.5 h

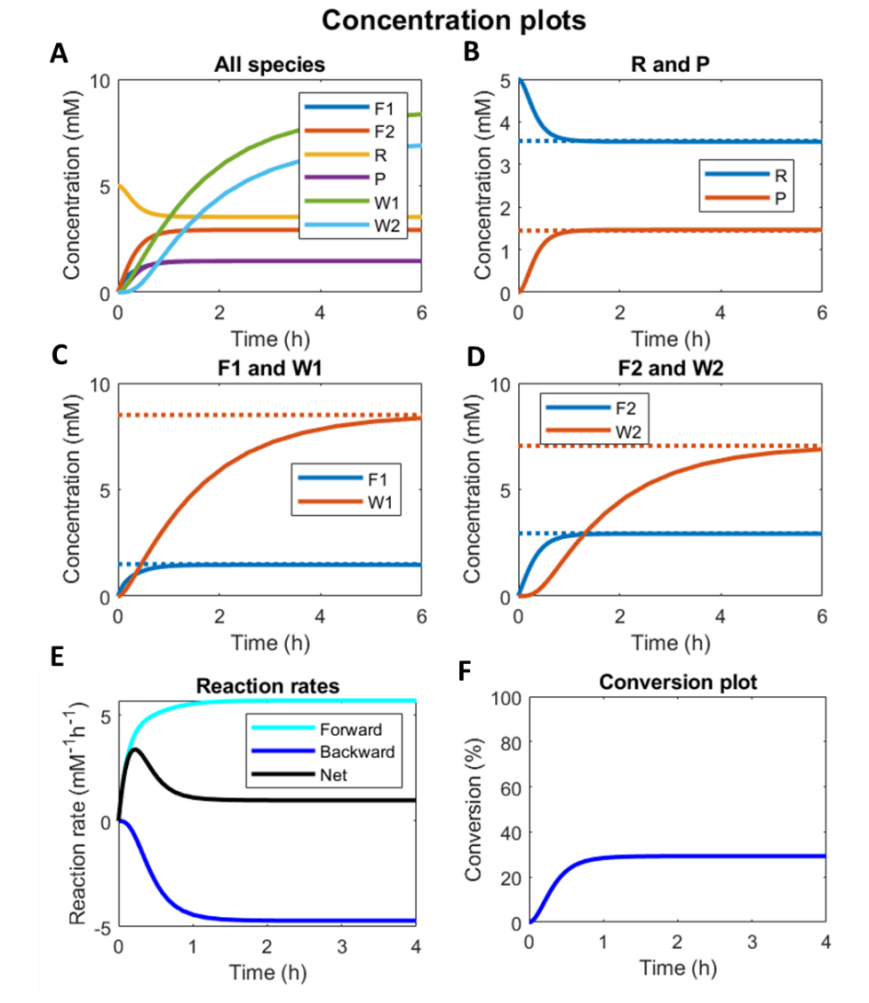

Figure S6.14: Numerical modelling output in CSTR: **(A).** Concentration of all species as a function of time. **(B).** Concentration of reactant R and product P as a function of time (solid lines) and their steady states (dashed lines). **(C).** Concentration of fuel F1 and waste W1 as a function of time (solid lines) and their steady states (dashed lines). **(D).** Concentration of reagent F2 and waste W2 as a function of time (solid lines) and their steady states (dashed lines). **(E).** Reaction rates for product P formation and degradation as a function of time. **(F).** Conversion plot of reactant R. Inlet conditions: [F1]=10 mM, [W1]=0 mM, [F2]=10 mM, [W2]=0 mM, [R]=5 mM, [P]=0 mM, **[C1]=0.1 mM, [C2]=0.1 mM**, rate constants k_{cat1}= 10 $mM^{-2}h^{-1}$, k_1= 0.1 $mM^{-1}h^{-1}$, k_{cat2}= 10 $mM^{-2}h^{-1}$, k_2= 0.1 $mM^{-1}h^{-1}$ and **residence time τ = 1.5 h**.

TRANSIENT HOST-GUEST COMPLEXATION TO CONTROL CATALYTIC ACTIVITY

CHAPTER 7

Signal transduction mechanisms are key to living systems. Cells respond to signals by changing catalytic activity of enzymes. This signal responsive catalysis is crucial in the regulation of (bio)chemical reaction networks (CRNs). Inspired by these networks, we report an artificial signal responsive system based on catalytic (de)activation. We combine a fuel-driven CRN with supramolecular chemistry, establishing transient host-guest complexes to control catalytic activity. Esters with favourable binding towards cucurbit[7]uril (CB[7]) supramolecular host are used as chemical fuels to form a transient complex with CB[7]. The esters are hydrolytically unstable, generating acid and alcohol, which do not bind to CB[7]. Dye release experiments demonstrated the feasibility of the concept. The same fuel-driven system was used to control the reaction rate of aniline catalysed hydrazone formation. Varying the ester structure and concentration gave access to different catalyst liberation times and free catalyst concentrations, regulating the overall reaction rate. Thus, with fuel-driven transient complex formation we can control the kinetics of a second chemical reaction, in which the fuel does not participate. This system shows promise for building more complex non-biological networks and ultimately arrive at signal transduction in organic materials.

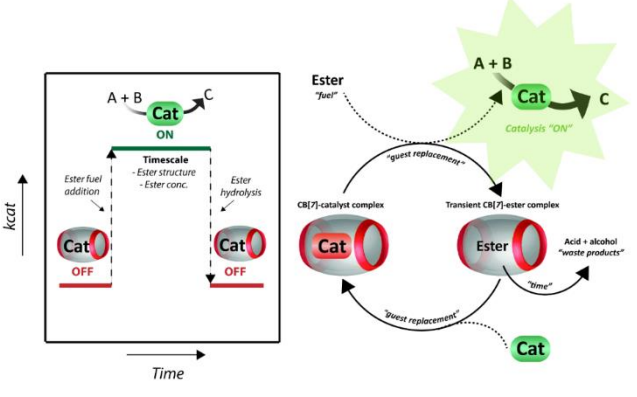

This chapter will be published as:
M.P. van der Helm, M. Hartono, R. Eelkema, *manuscript in preparation*.

7.1 INTRODUCTION

Nature is full of elegant and complex signal transduction mechanisms to control key cellular processes. Cells respond to external and internal signals by altering enzyme's activity via covalent chemistry involving phosphorylation[1] or non-covalently by allosteric activation or inhibition[2, 3]. Yet, artificial chemical reaction networks (CRNs) with the same complexity and control as found in living systems remain out of reach. Only few examples of minimal signal integration exist.[4-7] Incorporation of signal responsive catalysis in such systems is key to the regulation of artificial complex CRNs, reminiscent of the natural analogues. Here, we design a man-made signal responsive system based on catalytic (de)activation. Specifically, we use a combination of fuel-driven chemical reaction networks (CRN) and host-guest chemistry to exert control over catalytic activity. The last decade witnessed a steep rise in the design of fuel-driven non-equilibrium systems.[8] Here, a high-energy bond molecule is used as a sacrificial reagent to drive an otherwise unfavourable chemical reaction, giving rise to non-equilibrium product distributions, transiently stable structures and unusual system behaviours (i.e. oscillations, instabilities or chaotic behaviour).[8-12] Non-covalent interactions are frequently exploited to access non-equilibrium structures, such as in the ATP systems from Prins[13-16] and in the multitude of transient supramolecular polymer systems assembled from (non)-biological building blocks[9, 17-21]. At the same time, host-guest chemistry has proven a powerful tool to regulate reactivity of guest molecules, for example to control dissipative catalysis[22] or fuel-driven transient crystallization[23]. Here, in continuation to our previous works we use cucurbit[7]uril (CB[7]) as a supramolecular host to encapsulate guest molecules in aqueous environment.[24, 25] CB[7] has a high binding affinity for hydrophobic and positively charged molecules.[26] We exploit this property to establish a CRN via transient complex formation. Inspired by the fuel-driven systems from the Walther group[27], we use various hydrolytically unstable esters as chemical fuels to form a transient complex with CB[7]. The esters compete for CB[7] binding with the catalyst of the second chemical reaction, in this case aniline catalysed hydrazone formation, and their hydrolysis controls the liberation of the catalyst from CB[7] and hence the catalytic activity and the overall reaction rate (Figure 7.1). First, we explain the design of this fuel-driven CRN and the choice of the chemical fuel. Next, we demonstrate the proof-of-concept by controlling a dye replacement study. Finally, we show precise control over the rate of the organocatalytic chemical reaction supported by a kinetic model.

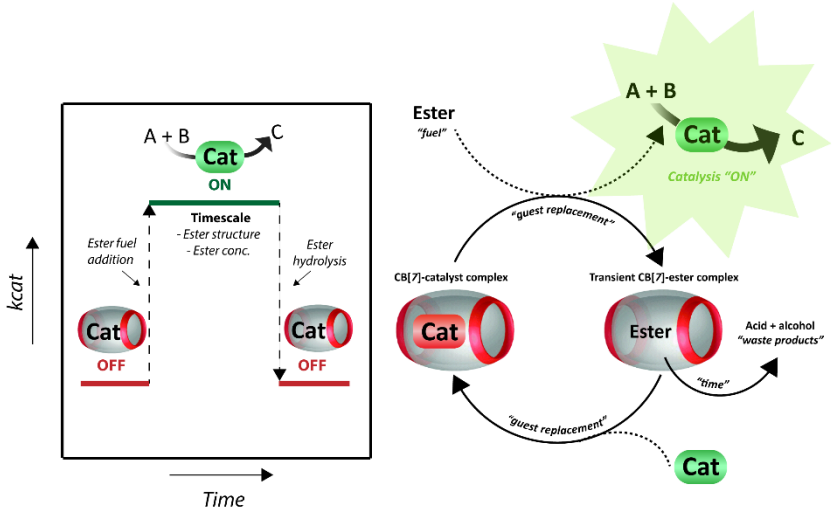

Figure 7.1: Fuel-driven transient complex formation of hydrolysable esters with CB[7] to control the rate of a chemical reaction by catalyst capture and release. *kcat* (represents the catalytic rate constant) versus time is shown, responding to ester addition and ester hydrolysis. Cat = catalyst

7.2 RESULTS AND DISCUSSION

7.2.1 Design of fuel-driven ester-CB[7] network

For the design of this fuel-driven ester CB[7] CRN, the first requirement for the ester chemical fuels is a moderate to high binding affinity with CB[7]. Secondly, they should be hydrolysable within the timescale of a catalytic chemical reaction. Thirdly, the generated carboxylic acid and alcohol should have no binding affinity towards CB[7]. Hence, we considered glycine betaine esters as the ideal candidates and three different varieties were synthesized: methyl **1**, ethyl **2** and isopropyl **3** (see SI for synthesis procedures). The positive charge from the ammonium gives favourable binding properties towards CB[7][26], resulting in binding constants (K_a in M^{-1}) of order 10^4-10^5 (Table S7.1). Their binding inside CB[7] was also confirmed by NMR studies (SI Figures S7.3-5). Amino acid esters are activated towards hydrolysis due to the neighbouring α-amino group. Additionally, the positively charged betaine increases the hydrolysis rate compared to uncharged amino acid esters.[28] Furthermore, the acid and alcohol hydrolysis products of the esters show no binding towards CB[7] (Table S7.1). The hydrolysis rates of the esters were measured at different pH and in the presence of CB[7] (SI Figures S7.6-7). Due to the electron donating effect and the generation of an unfavourable point charge, the hydrolysis rate displays the following order: methyl (fast) > ethyl > isopropyl (slow). Logically, a higher pH increases the ester hydrolysis rate and the presence of CB[7] slows down the hydrolysis. In the presence of CB[7] the hydrolysis of the isopropyl ester is even almost entirely switched off (SI Figure S7.7C,D)

7.2.2 Fuel-driven ester-CB[7] network: Dye replacement study

We tested the system with a fluorescent dye replacement study as a proof-of-concept (Figure 7.2). We use acridine orange (AO) **5**, which has a pK_a of 9.8 and is predominantly present in the protonated form at pH 7.5. The fluorescence intensity of the AO dye **5** is known to increase in the presence of CB[7].[29-31] Initially, the fluorescence intensity of AO and CB[7] at 525 nm (maximum in emission spectrum) is about 0.5 (Start in Figure 7.2 shown as green column).

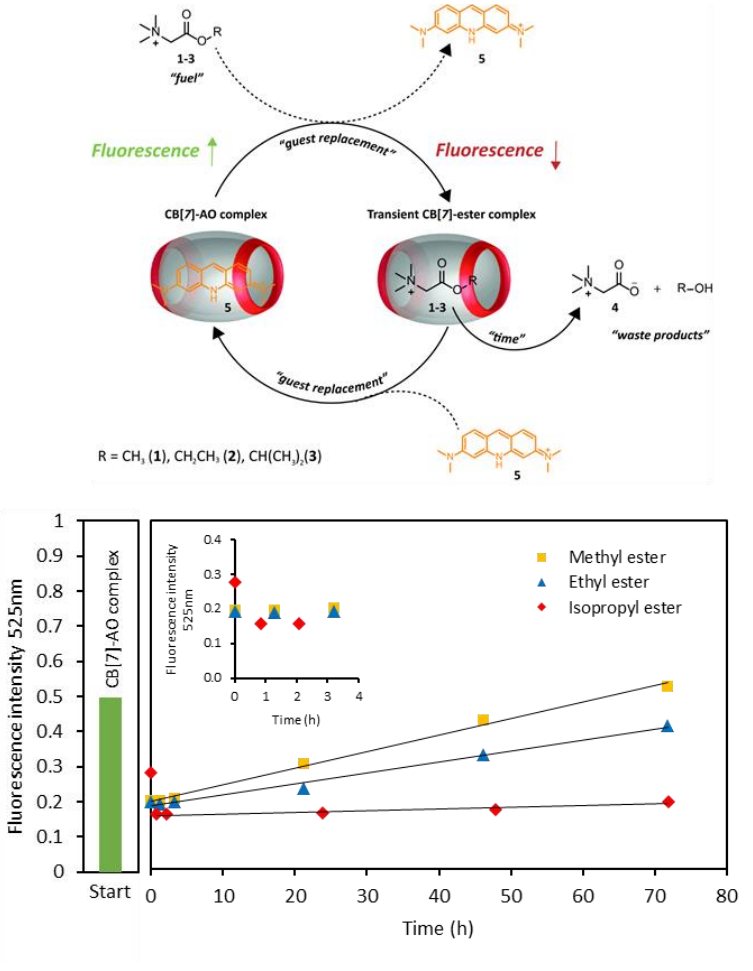

Figure 7.2: Fluorescence intensity of acridine orange (AO) **5** in and outside CB[7] over time at 525 nm (maximum in emission spectrum) with addition of different esters. The fluorescence intensity for **5** increases inside CB[7] (Start – green column). When the esters replace the dye inside CB[7] the fluorescence intensity decreases. The fluorescence intensity increases again when the esters hydrolyse over time and the dye is captured inside CB[7]. Conditions: esters (2.68 mM methyl **1**, 0.67 mM ethyl **2** or 0.13 mM isopropyl **3**) with 0.054 mM CB[7] and 0.027 mM AO **5** in sodium phosphate buffer (100 mM, pH 7.5) at RT. Samples were excited at wavelength 465 nm.

As is apparent from Figure 7.2, when the esters are added the fluorescence intensity decreases, which indicates that the esters replace the dye inside CB[*7*]. The decrease in fluorescence intensity happens instantly for the methyl **1** and ethyl ester **2** (Figure 7.2 yellow and blue symbols, and S7.11A,B emission spectra). However, for the isopropyl ester **3**, where because of the higher binding constant only a low concentration is needed to reach the same percentage of transient ester⊂CB[7] complex, the decrease is more gradually (Figure 7.2 red symbols in inset and S7.11C emission spectrum). Over time the esters hydrolyse, generating glycine betaine **4** and an alcohol as waste products. Due to the negative charge on **4** the binding affinity for CB[7] is lost and the dye is slowly captured inside CB[7] again. This is witnessed by the increase in fluorescence over time in Figure 7.2. In accordance to the height of the hydrolysis rate constants for the different esters (SI Figures S7.6-7), the fluorescence intensity increases more rapidly for the methyl ester **1**, followed by the ethyl ester **2** and finally the isopropyl ester **3**. Thus, the chemical structure of the ester fuel has a direct and strong effect on the replacement rate. Overall, with this dye replacement experiment we illustrate that we can control the rate of a second process (i.e. dye capture and release) by fuel-driven transient complex formation.

7.2.3 Fuel-driven ester-CB[7] network: Regulation of catalytic activity

Taking this one step further, we use the same fuel-driven transient complex formation strategy to control the rate of a catalytic reaction. In our previous work we showed that CB[7] can be used to control aniline **6** catalysed hydrazone formation in a buffered system.[25] Here, we exploit the same reaction between aldehyde **7** and hydrazide **8** to form hydrazone **9** in combination with the hydrolysable esters to achieve transient control over the reaction rate (Scheme 7.1). In order to measure the reaction rate and determine the rate constant, the yield of hydrazone product **9** is determined with UV-Vis by following the absorbance at 287 nm (see SI Hydrazone UV-VIS absorbance and reaction kinetics). As we confirmed previously, aniline **6** binds moderately strong to CB[7] with a K_a of $2.78 \cdot 10^4$ M^{-1} and the reactants and product do not bind to CB[7] (SI Figure S7.1 and Table S7.1). To illustrate the change in reaction rate we calculated the reaction rate constant over time for the various conditions and different time intervals: with only catalyst; catalyst with CB[7] and catalyst with varying concentrations of ester fuels **1**-**3** (Figures 7.3A-F and see SI Figures S7.13-14 for the yield of hydrazone **9** and the slopes for the determination of the rate constants).

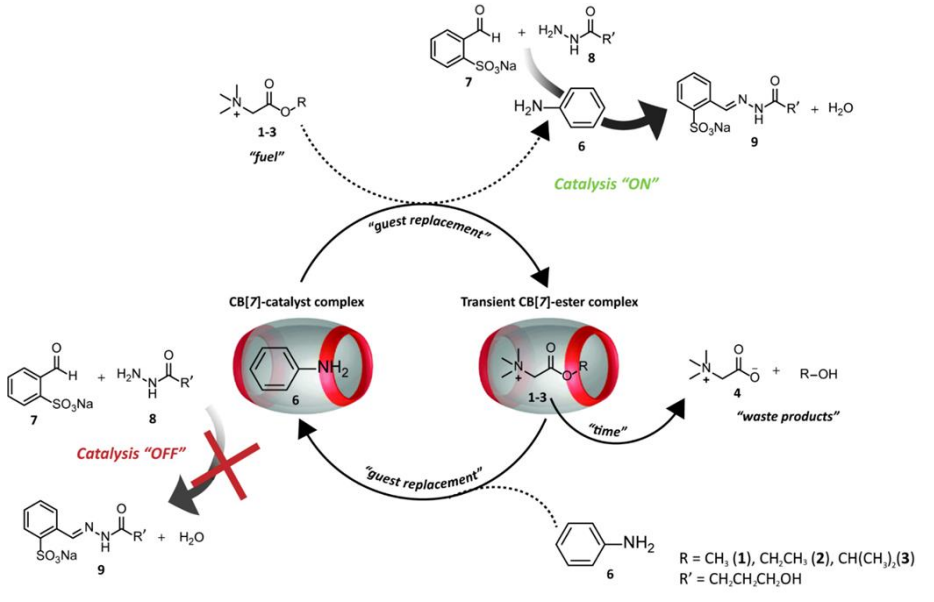

Scheme 7.1: Fuel-driven transient complex formation of hydrolysable esters with CB[*7*] to control the rate of hydrazone formation by aniline catalyst **6** capture and release.

With 0.2 mM catalyst **6** hydrazone formation is accelerated with a rate constant of 0.081 $mM^{-1}h^{-1}$, whereas by addition of 0.6 mM CB[7] a rate decrease is observed with a rate constant of 0.025 $mM^{-1}h^{-1}$. The reaction is not completely switched off due to a background reaction with constant 0.014 $mM^{-1}h^{-1}$ (SI Figure S7.18) and with 0.6 mM CB[7] only 92% of catalyst is complexed with CB[7], together giving the rate constant of 0.025 $mM^{-1}h^{-1}$. Upon addition of the ester fuels a guest replacement takes place. The esters replace the catalyst inside CB[7], liberating the catalyst, which in turn starts to accelerate the hydrazone formation. However, over time the esters hydrolyse and the catalyst is gradually captured inside CB[7] again. This behaviour is illustrated by a decrease in the reaction rate constant (Figures 7.3A-F orange lines). For the ester experiments we calculated the reaction rate constant for various time intervals based on the changing slopes (SI Figures S7.13-15). Because of small deviations in the UV data the time intervals had to remain large (SI Figures S7.13-15). Especially at the end of the measurement time the deviations become larger and hence larger time intervals were used (SI Figure S7.15).

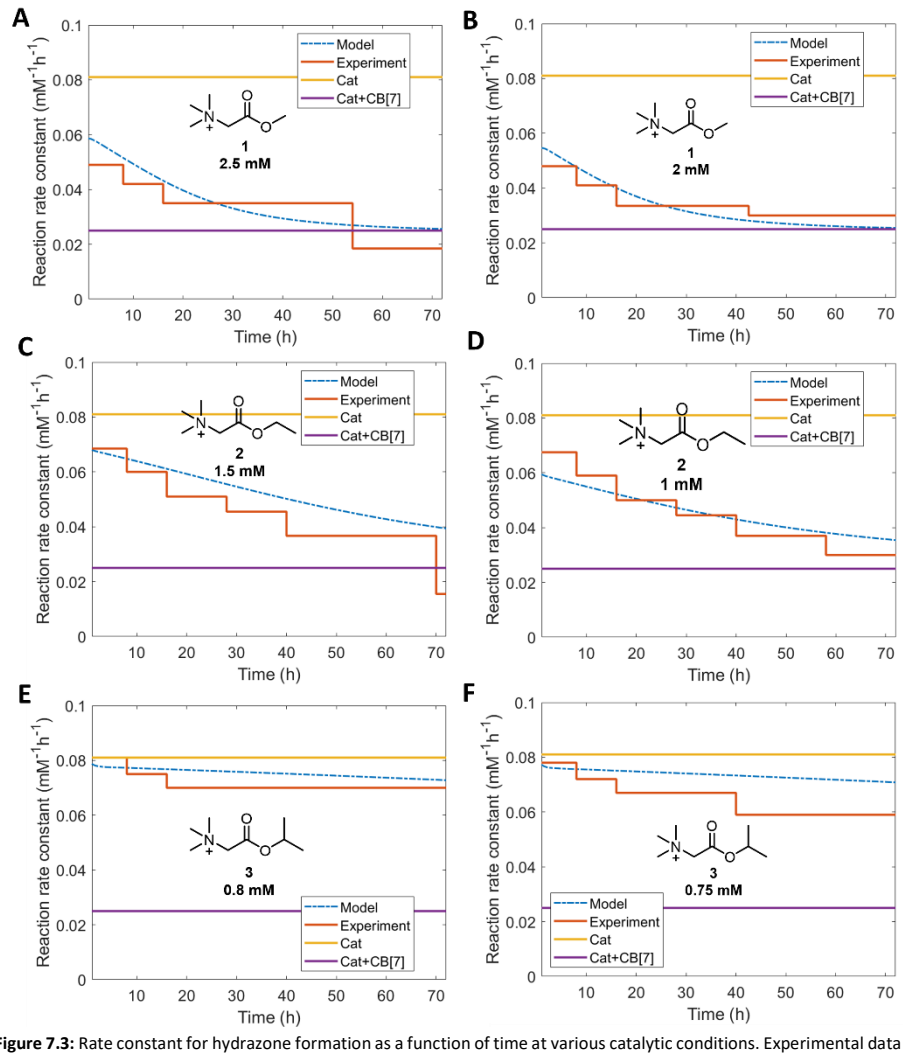

Figure 7.3: Rate constant for hydrazone formation as a function of time at various catalytic conditions. Experimental data with ester fuels (orange lines) are compared with the model (blue dashed line): **(A)**. Methyl ester **1** 2.5 mM, **(B)**. Methyl ester **1** 2 mM, **(C)**. Ethyl ester **2** 1.5 mM, **(D)**. Ethyl ester **2** 1 mM, **(E)**. Isopropyl ester **3** 0.8 mM, and **(F)**. Isopropyl ester **3** 0.75 mM. Conditions: 0.2 mM aldehyde **7**, 0.02 mM hydrazide **8**, 0.2 mM catalyst **6** and 0.6 mM CB[7].

Overall, the ester structure and concentration control the decrease in reaction rate and the final hydrazone **9** product yield. With 2.5 mM methyl ester **1** the catalysis is switched off after about 50 h (Figure 7.3A orange line) with 61% yield of hydrazone **9** after 168 h (SI Figure S7.13A), whereas with 2 mM the switch off time reduces to 40 h (Figure 7.3B orange line) with 65% hydrazone **9** yield after 168 h (SI Figure S7.14A). For 1.5 mM ethyl ester **2** the switch off time is about 70 h (Figure 7.3C orange line) showing 67% yield of hydrazone **9** after 168 h (SI Figure S7.13C) and for 1 mM of **2** about 60 h (Figure 7.3D

orange line) with 69% yield of **9** after 168 h (SI Figure S7.14C). However, the isopropyl ester **3** almost resembles a permanent guest, as with both 0.8 and 0.75 mM the reaction rate hardly reduces over time (Figure 7.3E and 7.3F orange lines), both concentrations of **3** give 90% yield of hydrazone **9** after 168 h (SI Figure S7.13E, S7.14E). The rate constant of the reaction is changing over time due to a changing free catalyst concentration in solution as a consequence of the ester fuel hydrolysis. Using the equilibrium relations of esters and catalyst with CB[7] and the previously determined ester hydrolysis rate constants in and outside CB[7], we designed a kinetic model to determine the concentration of all the species over time (see SI Kinetic model and Figures S7.16-17). Based on the free catalyst concentration as a function of time we calculate the changing rate constant for hydrazone formation over time and compare it with the experimental data. As is apparent from Figures 7.3A-F (blue dashed lines) the modelled rate constant predicts the experimental data accurately for varying ester concentrations. Only for the experiments with the methyl ester **1** the model rate constant starts off higher than for the measured data, this is most likely due to minor ester hydrolysis already taking place before the UV measurement is started.

Instead of adding the esters from the start, an *in-situ* catalyst activation experiment was also performed (Figure 7.4). At the start the rate of all experiments is similar to the catalyst⊂CB[7] experiment. Yet, when the ester fuels are added after 8 h, they effectively replace the catalyst inside CB[7]. Hence, in Figure 7.4B, C, D after ester addition a rate increase is observed, indicating that catalyst **6** is liberated and accelerating the hydrazone formation. Next, upon ester hydrolysis a gradual decay in rate is observed (Figure 7.4B, C, D orange lines). The decrease in rate constant and the final yield of hydrazone **9** follows a similar trend as in Figure 7.3 with the methyl ester **1** hydrolysing the fastest (lowest yield of **9** in Figure 7.4A) and the isopropyl ester **3** the slowest (highest yield of **9** in Figure 7.4A). Also, for the *in-situ* catalyst activation, the numerical model predicts the decrease in rate constant accurately for the different esters (Figure 7.4B, C, D blue dashed lines). Only for the methyl ester **1** the model rate prediction is higher from the start, possibly due to some ester hydrolysis already occurring. In all, by transient complex formation with unstable ester fuels inside a supramolecular host we have control over and can numerically predict the rate of a second chemical reaction by tuning the catalyst liberation time and hence the free catalyst concentration in solution.

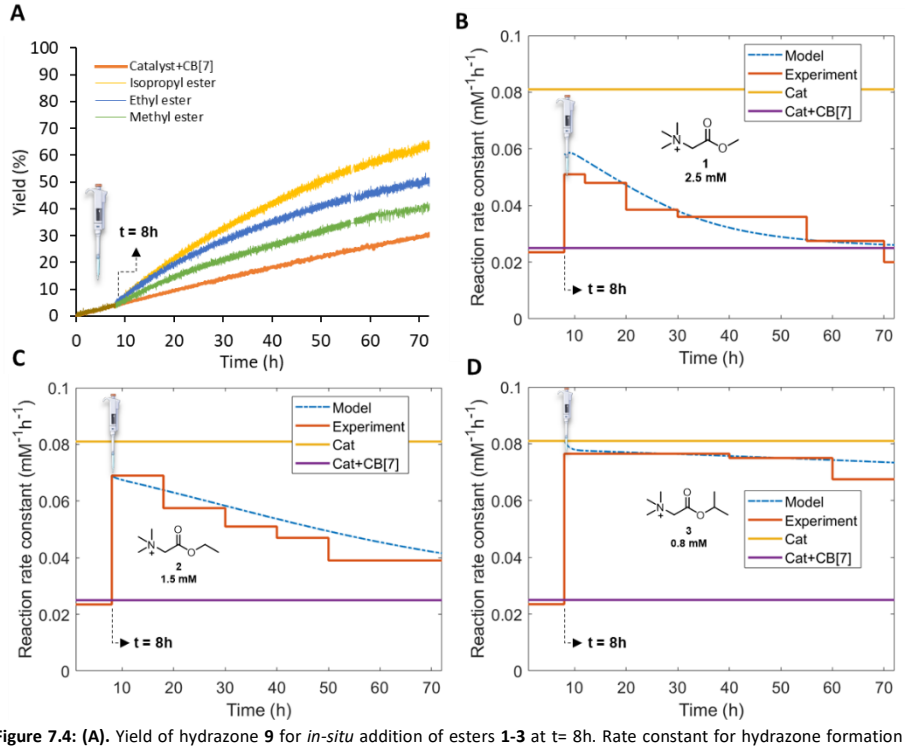

Figure 7.4: (A). Yield of hydrazone **9** for *in-situ* addition of esters **1-3** at t= 8h. Rate constant for hydrazone formation as a function of time at various catalytic conditions. Experimental data with ester fuels (orange lines) are compared with the model (blue dashed line): **(B)**. Methyl ester **1** 2.5 mM, **(C)**. Ethyl ester **2** 1.5 mM and **(D)**. Isopropyl ester **3** 0.8 mM. Conditions: 0.2 mM aldehyde **7**, 0.02 mM hydrazide **8**, 0.2 mM catalyst **6** and 0.6 mM CB[7].

7.3 CONCLUSION

In this work, we designed a fuel-driven transient complex formation CRN to control capture and release of guest molecules from a supramolecular host. Specifically, we used glycine betaine esters, with favourable binding towards CB[7]. Since the esters are unstable under aqueous conditions, hydrolysis takes place and acid and alcohol are formed, which do not bind to CB[7]. With the transient ester CB[7] complexes, we controlled a dye release experiment, showing the feasibility of the concept. Next, we made the network more complicated and introduced a second chemical reaction. We used the fuel-driven transient complex formation to control the reaction rate of aniline catalysed hydrazone formation. Tuning the ester structure and concentration gave different catalyst liberation times and changed the concentration of free catalyst and the overall reaction rate. The ester fuels were effectively used for *in-situ* activation of the organocatalyst. The experimental data were supported by a kinetic model. With fuel-driven transient complex formation we are able to control the kinetics of a second process, in which the fuel itself does not take part (i.e. dye capture or chemical product

formation). This generic non-equilibrium CRN, based on ester hydrolysis and supramolecular encapsulation, shows promise for building more complex non-biological networks. The non-covalent (de)activation of catalysis could be applied to soft materials, similar to the covalent (de)activation[4]. Altogether, this work is a first step forward towards incorporation of signal transduction in man-made systems.

7.4 REFERENCES

1. G. Burnett and E. P. Kennedy, *J. Biol. Chem.*, 1954, **211**, 969-980.
2. J.-P. C. a. F. J. Jacques Monod, *J ..Mol. Biol.*, 1963, **6**, 306-329.
3. A. Cornish-Bowden, *FEBS J.*, 2014, **281**, 621–632.
4. F. Trausel, C. Maity, J. M. Poolman, D. Kouwenberg, F. Versluis, J. H. van Esch and R. Eelkema, *Nat. Commun.*, 2017, **8**, 879.
5. C. Maity, F. Trausel and R. Eelkema, *Chem. Sci.*, 2018, **9**, 5999-6005.
6. B. S. Pilgrim, D. A. Roberts, T. G. Lohr, T. K. Ronson and J. R. Nitschke, *Nat. Chem.*, 2017, **9**, 1276.
7. P. A. Korevaar, C. N. Kaplan, A. Grinthal, R. M. Rust and J. Aizenberg, *Nat. Commun.*, 2020, **11**, 1-10.
8. S. A. P. van Rossum, M. Tena-Solsona, J. H. van Esch, R. Eelkema and J. Boekhoven, *Chem. Soc. Rev.*, 2017, **46**, 5519-5535.
9. J. Boekhoven, W. E. Hendriksen, G. J. M. Koper, R. Eelkema and J. H. van Esch, *Science*, 2015, **349**, 1075-1079.
10. J. Leira-Iglesias, A. Tassoni, T. Adachi, M. Stich and T. M. Hermans, *Nat. Nanotechol.*, 2018, **13**, 1021.
11. M. Tena-Solsona, B. Rieß, R. K. Grötsch, F. C. Löhrer, C. Wanzke, B. Käsdorf, A. R. Bausch, P. Müller-Buschbaum, O. Lieleg and J. Boekhoven, *Nat. Commun.*, 2017, **8**, 15895.
12. J. Boekhoven, A. M. Brizard, K. N. K. Kowlgi, G. J. M. Koper, R. Eelkema and J. H. van Esch, *Angew. Chem. Int. Ed.*, 2010, **122**, 4935-4938.
13. C. Pezzato and L. J. Prins, *Nat. Commun.*, 2015, **6**, 7790.
14. P. Solís Muñana, G. Ragazzon, J. Dupont, C. Z. J. Ren, L. J. Prins and J. L. Y. Chen, *Angew. Chem. Int. Ed.*, 2018, **57**, 16469-16474.
15. S. Chandrabhas, M. Olivo and L. J. Prins, *ChemSystemsChem*, 2020, **2**, e1900063.
16. L. J. Prins and M. A. Cardona, *Chem. Sci.*, 2020, **11**, 1518-1522.
17. S. Debnath, S. Roy and R. V. Ulijn, *J. Am. Chem. Soc.*, 2013, **135**, 16789-16792.
18. A. Sorrenti, J. Leira-Iglesias, A. Sato and T. M. Hermans, *Nat. Commun.*, 2017, **8**, 15899.
19. S. Dhiman, A. Jain and S. J. George, *Angew. Chem. Int. Ed.*, 2017, **129**, 1349-1353.
20. D. Spitzer, L. L. Rodrigues, D. Straßburger, M. Mezger and P. Besenius, *Angew. Chem. Int. Ed.*, 2017, **56**, 15461-15465.
21. R. Otter, C. M. Berac, S. Seiffert and P. Besenius, *Eur. Polym. J.*, 2019, **110**, 90-96.
22. C. Biagini, S. D. Fielden, D. A. Leigh, F. Schaufelberger, S. Di Stefano and D. Thomas, *Angew. Chem.*, 2019, **131**, 9981-9985.
23. S. Choi, R. D. Mukhopadhyay, Y. Kim, I. C. Hwang, W. Hwang, S. K. Ghosh, K. Baek and K. Kim, *Angew. Chem.*, 2019, **131**, 17006-17009.
24. T. G. Brevé, M. Filius, C. Araman, M. P. van der Helm, P. L. Hagedoorn, C. Joo, S. I. van Kasteren and R. Eelkema, *Angew. Chem. Int. Ed.*, 2020, **59**, 9340-9344.
25. G. L. Li, F. Trausel, M. P. van der Helm, B. Klemm, T. G. Brevé, S. A. P. van Rossum , M. Hartono, H. H. P. J. Gerlings, M. Lovrak, J. H. van Esch and R. Eelkema, *manuscript in preparation*, 2020.
26. S. J. Barrow, S. Kasera, M. J. Rowland, J. del Barrio and O. A. Scherman, *Chem. Rev*, 2015, **115**, 12320-12406.
27. L. Heinen, T. Heuser, A. Steinschulte and A. Walther, *Nano Lett.*, 2017, **17**, 4989-4995.
28. R. Hay, L. Porter and P. Morris, *Aust. J. Chem.*, 1966, **19**, 1197-1205.
29. M. Shaikh, J. Mohanty, P. K. Singh, W. M. Nau and H. Pal, *Photochem. Photobiol. Sci.*, 2008, **7**, 408-414.
30. J. Liu, N. Jiang, J. Ma and X. Du, *Eur. J. Org. Chem.*, 2009, **2009**, 4931-4938.
31. R. N. Dsouza, U. Pischel and W. M. Nau, *Chem. Rev.*, 2011, **111**, 7941-7980.

7.5 SUPPLEMENTARY INFORMATION

7.5.1 Experimental details

General materials and methods

Chemicals were purchased in the highest purity and used without further purification unless reported otherwise. Tetrahydrofuran (THF), methanol and diethyl ether (DE) of technical grades were purchased from VWR International. Acridine orange **5** (AO) hydrochloride solution (10 mg/mL) and aniline catalyst **6** (99.5%) of ACS reagent grade were purchased from Sigma Aldrich. CB[7] hydrate (99%) was purchased from Strem Chemicals Inc. *o*-Sulfobenzaldehyde **7** was purchased from Honeywell Fluka Fischer Scientific and *p*-hydroxybutiric acid hydrazide **8** (98%) from Alfa Aesar. Methyl bromoacetate (99%), ethyl bromoacetate (98%), isopropyl bromoacetate (99%) and trimethylamine solution (31-35 wt% ethanol) were purchased from Sigma Aldrich. Solid salts were used for the preparation of aqueous buffers. Sodium phosphate monobasic monohydrate (98%) was purchased from Sigma Aldrich, while sodium phosphate dibasic (+99%, analysis grade) was from Acros Organics. Unless stated otherwise, all preparations and analyses were performed at room temperature (RT) (~21 °C) and atmospheric pressure. Nuclear Magnetic Resonance (NMR) experiments were performed using Agilent-400 MR DD2 (400 MHz for ^{1}H and 100.5 MHz for ^{13}C) at 25 °C using residual deuterated solvent signals as internal standard. To suppress the water peak, PRESAT configuration (suppress one highest peak) was used. UV-Vis spectroscopic experiments were carried out using Analytik Jena Specord 250 spectrophotometer; quartz cuvette with a 1 cm path length, volume of 3 mL, at a controlled temperature of 25 °C. Fluorescence spectra were recorded on a JASCO J-815 CD spectrometer (sensitivity 450 Volts, data pitch 1 nm, band width 5 nm, excitation wavelength of 465 nm for AO **5**); black quartz cuvette with a 1 cm path length, volume of 200 µL, at RT. Isothermal titration calorimetry (ITC) experiments were performed using a MicroCal VP-ITC. Liquid Chromatography–Mass Spectrometry (LC-MS) was performed on a Shimadzu Liquid Chromatograph Mass Spectrometer 2010, LC-8A pump with a diode array detector SPD-M20. Negative and/ or positive mode Electro Spray Ionization Mass Spectrometry (ESI-MS) was used for the peak assignment.

Glycine betaine esters (methyl 1, ethyl 2 and isopropyl 3) synthesis

Following the literature[1], for methyl ester **1**, trimethylamine (1.5 equivalents; 33 wt % in EtOH) was added to a solution of methyl bromoacetate (1 equivalent) in THF (50 mL/g). The reaction mixture was stirred for 24h at RT, during this time the product precipitated as a white solid. The resulting suspension was cooled with ice, filtered, washed with ice-cold Et_2O and dried in the vacuum oven at 40 °C overnight to yield the ammonium salt with bromine counter ion as white solid. For the ethyl and isopropyl

esters (**2-3**) the same procedure was followed with ethyl bromoacetate or isopropyl bromoacetate, respectively.

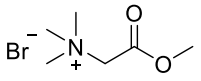

1

Methyl ester **1** (yield 95%, 1.5 g, 7.1 mmol): **^{1}H NMR** (400 MHz, D_2O): δ = 4.37 (s, 2H, -CH_2-), 3.87 (s, 3H, -CH_3), 3.36 (s, 9H, -CH_3). **^{13}C NMR** (100.5 MHz, D_2O): 165.7, 63.4, 54.0, 53.2. **MS** (ESI, positive) m/z: 132 [$(M)^+$] (expected m/z = 132.10).

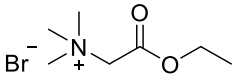

2

Ethyl ester **2** (yield 97%, 1.5 g, 6.6 mmol): **^{1}H NMR** (400 MHz, D_2O): δ = 4.29 (s, 2H, -CH_2-), 4.32-4.26 (q, 2H, -CH_2-, *J* = 7 Hz), 3.31 (s, 9H, -CH_3), 1.29-1.26 (t, 3H, -CH_3, *J* = 7 Hz). **^{13}C NMR** (100.5 MHz, D_2O): 165.2, 63.6, 63.3, 54.0, 13.1. **MS** (ESI, positive) m/z: 146 [$(M)^+$] (expected m/z = 146.12).

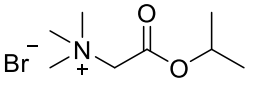

3

Isopropyl ester **3** (yield 99.5%, 1.2 g, 5.0 mmol): **^{1}H NMR** (400 MHz, D_2O): δ = 5.21-5.15 (m, 1H, -CH-), 4.31 (s, 2H, -CH_2-), 3.35 (s, 9H, -CH_3), 1.34-1.32 (d, 6H, -CH_3, *J* = 7 Hz). **^{13}C NMR** (100.5 MHz, D_2O): 164.6, 72.2, 63.8, 54.0, 20.6. **MS** (ESI, positive) m/z: 160 [$(M)^+$] (expected m/z = 160.13).

7

Hydrazone product 9 synthesis

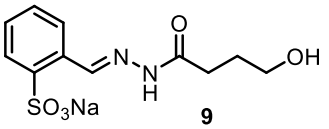

9

The synthesis was performed according to our previous reported procedure[2]. The purity of the product was confirmed by NMR and MS: N.B. Extra splitting of the peaks in the NMR spectrum is due to *cis* and *trans* isomers. **^{1}H NMR** (400 MHz, D_2O): δ = 8.96 (s, 1H, -CH=N-), 8.15-8.13 (d, 2H, Ar-H, *J* = 7 Hz), 7.96-7.94 (d, 2H, Ar-H, *J* = 7 Hz), 7.68-7.59 (m, 2H, Ar-H), 3.71-3.65 (t, 2H, -CH_2-, *J* = 7 Hz), 2.49-2.45 (t, 2H, -CH_2-, *J* = 7 Hz), 1.97-1.90 (m, 2H, -CH_2-). **^{13}C NMR** (100.5 MHz, D_2O): 173.0, 147.5, 141.4, 131.7, 130.7, 130.1, 127.3, 126.9, 60.7, 30.6, 27.4. **MS** (ESI, negative) m/z: 285 [$(M\text{-}Na^+)^-$] (expected m/z = 285.05). **Extinction coefficient** in sodium phosphate buffer (100 mM, pH 7.5) at 287 nm: 19.2 $mM^{-1}cm^{-1}$.

ITC binding constant measurement

A solution of the guest molecule ($3x10^{-5}$ mol from 10 mM stock) was titrated to CB[7] (0.5 mM) solution at 25 °C. Unless stated differently, the solutions were prepared in sodium phosphate buffer (100 mM, pH 7.5). The first titration point out of 28 injection points was discarded. Binding constants were fitted with Microcal LLC ITC Origin 7 software.

Fluorescence assay of acridine orange 5 and CB[7]

Fluorescence measurements were performed in sodium phosphate buffer (100 mM, pH 7.5) with 0.027 mM AO **5**, 0.054 mM CB[7] and esters (2.68 mM methyl **1**, 0.67 mM ethyl **2** or 0.13 mM isopropyl **3**) in black quartz cuvettes, path length of 1 cm (total reaction volume of 200 µL) at RT. Based on these concentrations, 96% of the methyl ester **1** will bind to CB[7], 96% of ethyl ester **2** and 97% of isopropyl ester **3**. The stock solutions were added in the following order: phosphate buffer, dye **5** and CB[7] (premixed for 1 h) and ester **1-3** solution. Teflon caps were used to close the cuvette. The cuvette was turned upside down to mix the solution. Samples were excited at wavelength 465 nm. N.B. AO **5** has a pK_a of 9.8 and is predominantly present in the protonated form at pH 7.5.[3]

UV-Vis assay to follow the hydrazone formation reaction

Unless stated otherwise, the hydrazone reaction was performed in sodium phosphate buffer (100 mM, pH 7.5), containing 0.2 mM aldehyde **7**, 0.02 mM hydrazide **8**, 0.2 mM aniline **6**, and 0.6 mM CB[7] in quartz cuvettes, path length of 1 cm (total reaction volume of 3 mL) at 25 °C. The stock solutions of the reactants were added in the following order: catalyst **6** solution and CB[*7*] (premixed for 1 h), aldehyde **7** solution, phosphate buffer and hydrazide **8** solution. Teflon caps were used to close the cuvette. The cuvette was turned upside down five times to mix the solution. The product peak was followed (at 287 nm) using a 6-sample holder (configuration: slow time scan, measuring wavelength 350 nm, scan every 20 s). The pH was measured before and after the reaction. Experiments with esters **1-3** (2.5/ 2 mM methyl **1**, 1.5/ 1 mM ethyl **2** and 0.8/ 0.75 mM isopropyl **3**) were performed similarly, with the ester **1-3** stock solution being added at the last moment. Based on these concentrations, 95%/ 94% of the methyl ester **1** will bind to CB[7], 97%/ 95% of ethyl ester **2** and 99%/ 99% of isopropyl ester **3**. The concentration of hydrazone product **9** was calculated with the extinction coefficient and Lambert-Beer law.

7.5.2 ITC binding constants with CB[7]

Catalyst, product and reactants

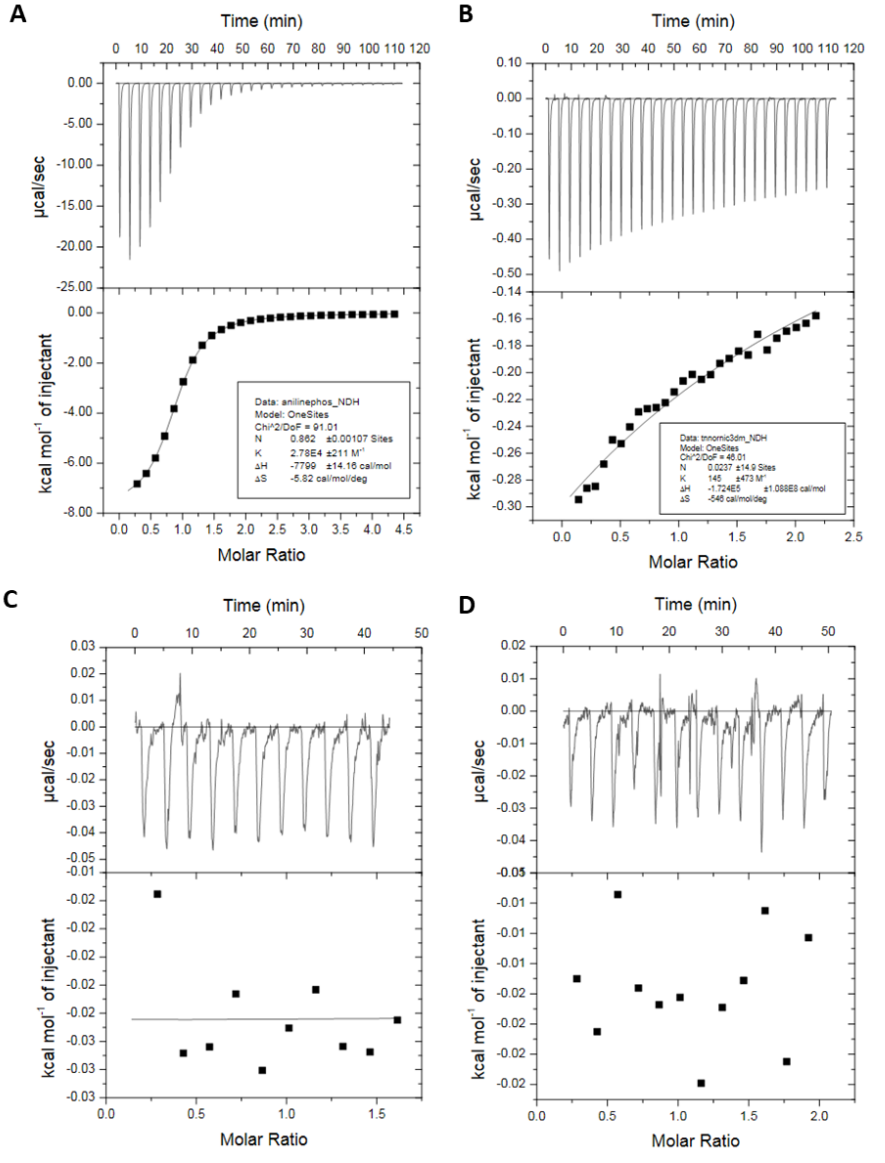

Figure S7.1: Binding constant measurement using ITC, guest (10 mM) and CB[7] (0.5 mM) in sodium phosphate buffer (pH 7.4, 100 mM) at RT. **(A)**. Aniline catalyst **6**, **(B)**. Hydrazone **9**, **(C)**. Aldehyde **7** and **(D)**. Hydrazide **8**.

Ester fuels and acid waste

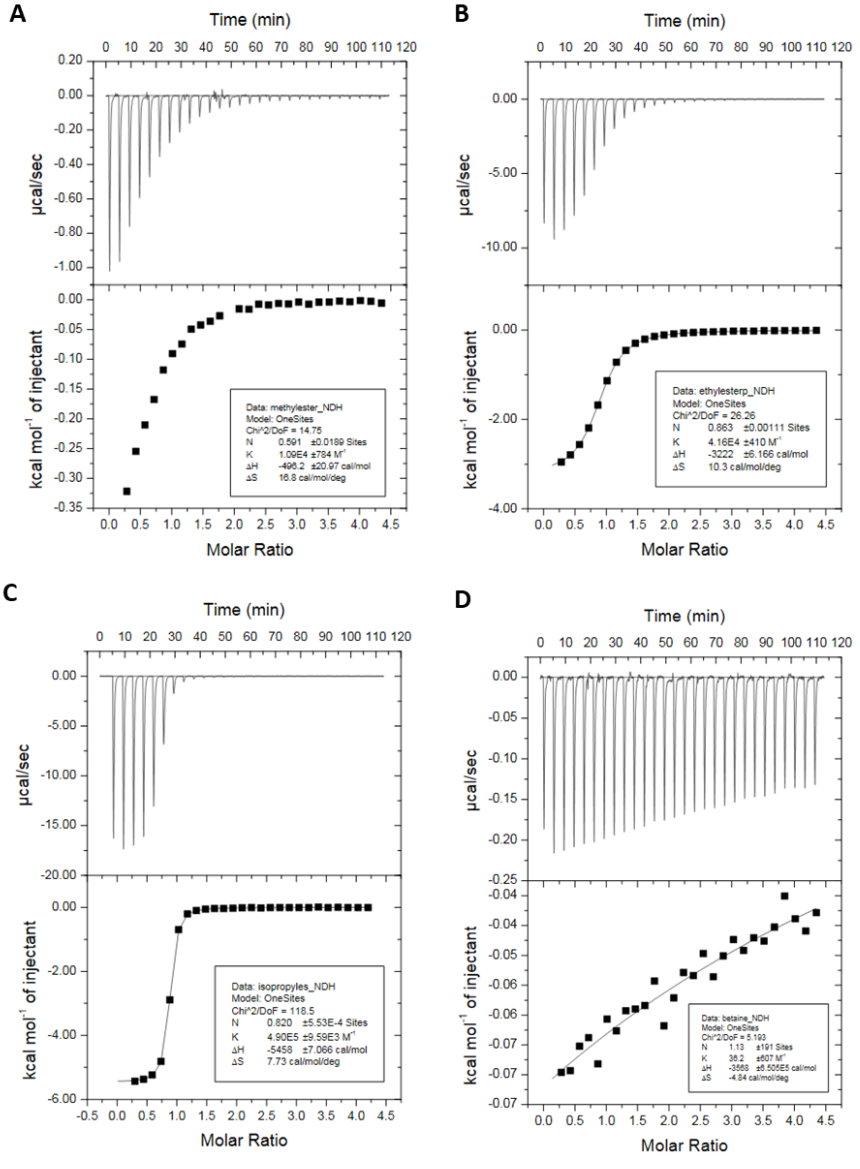

Figure S7.2: Binding constant measurement using ITC, esters or acid (10 mM) and CB[7] (0.5 mM) in sodium phosphate buffer (pH 7.5, 100 mM) at RT. **(A)**. Methyl ester **1**, **(B)**. Ethyl ester **2**, **(C)**. Isopropyl ester **3** and **(D)**. Betaine **4**.

Overview of CB[7] binding constants from ITC

Table S7.1: Binding constants (K_a) and thermodynamic binding values (ΔH and TΔS) for ester fuels **1-3**, their hydrolysis products, acridine orange (AO) **5**, aniline catalyst **6**, aldehyde **7**, hydrazide **8** and hydrazone **9** as determined by Isothermal titration calorimetry (ITC) or from the literature. A negative ΔH value indicates an enthalpic gain, while a positive TΔS indicates an entropic gain. Not measurable means that the binding constant cannot be measured, because it is under the detection limit of the ITC. * The binding constant for AO **5** was taken from the literature obtained with fluorescence titration.[4]

Molecular structure	Name	K_a, M^{-1}	ΔH, kcal mol^{-1}	TΔS, kcal mol^{-1}
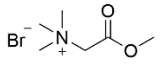 **1**	Glycine betaine methyl ester **1** (fuel)	$(1.09 \pm 0.08) \times 10^4$	-0.496 ± 0.02	5.01
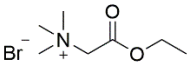 **2**	Glycine betaine ethyl ester **2** (fuel)	$(4.16 \pm 0.04) \times 10^4$	-3.22 ± 0.06	3.07
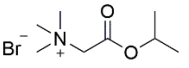 **3**	Glycine betaine isopropyl ester **3** (fuel)	$(4.90 \pm 0.01) \times 10^5$	-5.46 ± 0.007	2.30
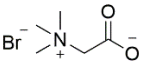 **4**	Glycine betaine **4**: Hydrolysis product of **1-3**	Not measurable	Not measurable	Not measurable
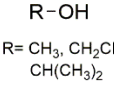	Methanol/ ethanol/ isopropanol: Hydrolysis products of **1-3**	Not measurable	Not measurable	Not measurable
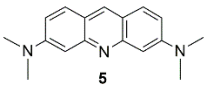 **5**	Acridine orange (AO) dye **5**	5.6×10^5 (pH 7.5 phosphate buffer saline)*	Not reported	Not reported
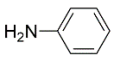 **6**	Aniline **6** (hydrazone formation catalyst)	$(2.78 \pm 0.20) \times 10^4$	-7.8 ± 0.018	1.7
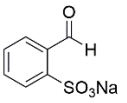 **7**	Aldehyde **7**	Not measurable	Not measurable	Not measurable
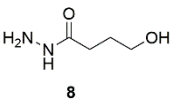 **8**	Hydrazide **8**	Not measurable	Not measurable	Not measurable
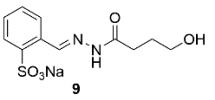 **9**	Hydrazone product **9**	Not measurable	Not measurable	Not measurable

7.5.3 Ester-CB[7] binding ^{1}H NMR spectra

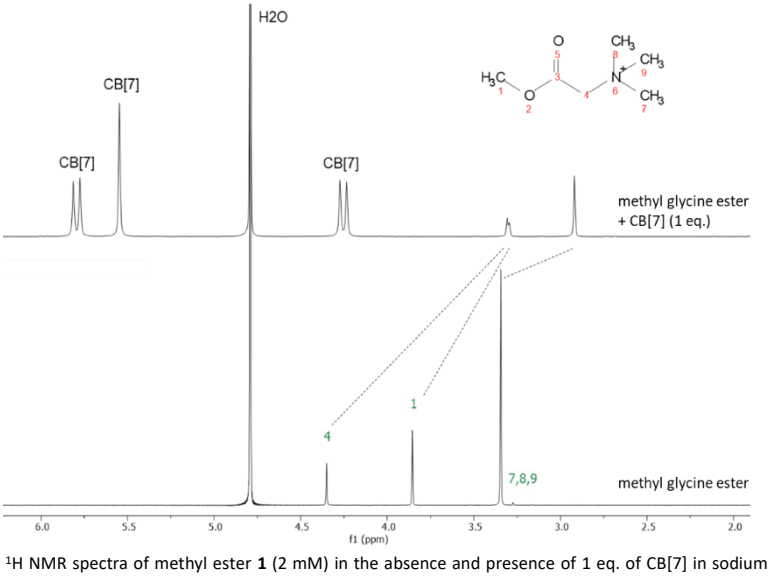

Figure S7.3: ^{1}H NMR spectra of methyl ester **1** (2 mM) in the absence and presence of 1 eq. of CB[7] in sodium phosphate buffer (100 mM, pH 7.5) at RT (NMR solvent D_2O).

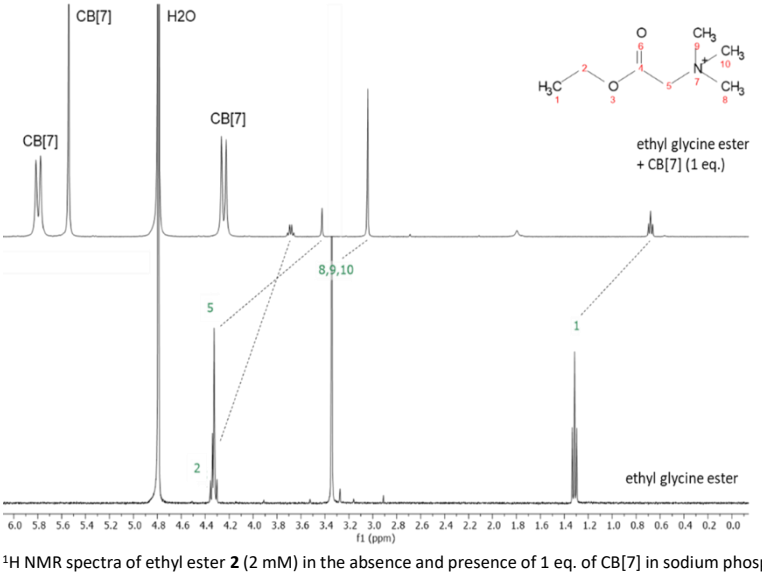

Figure S7.4: ^{1}H NMR spectra of ethyl ester **2** (2 mM) in the absence and presence of 1 eq. of CB[7] in sodium phosphate buffer (100 mM, pH 7.5) at RT (NMR solvent D_2O).

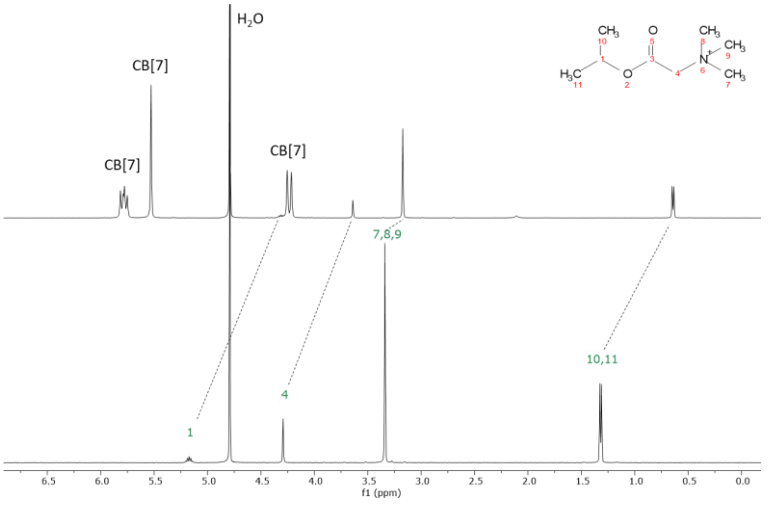

Figure S7.5: ^{1}H NMR spectra of isopropyl ester **3** (2 mM) in the absence and presence of 1 eq. of CB[7] in sodium phosphate buffer (100 mM, pH 7.5) at RT (NMR solvent D_2O).

7.5.4 Ester hydrolysis profiles

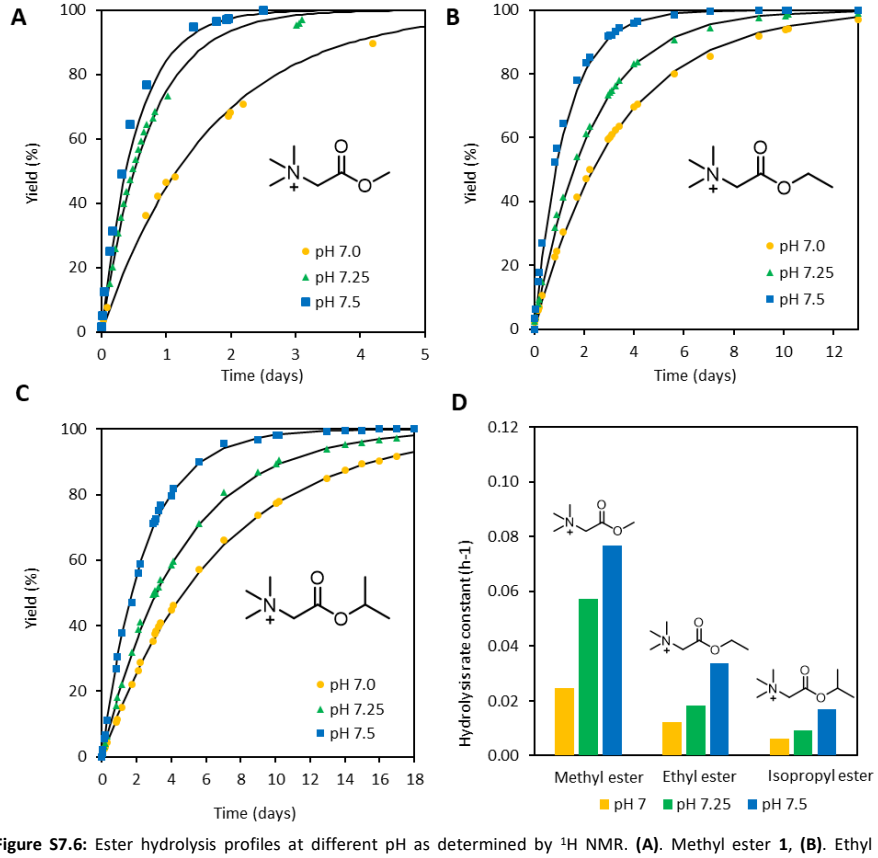

Figure S7.6: Ester hydrolysis profiles at different pH as determined by ^{1}H NMR. **(A)**. Methyl ester **1**, **(B)**. Ethyl ester **2**, **(C)**. Isopropyl ester **3** and **(D)**. A summary of the corresponding hydrolysis rate constants. Conditions: ester (2 mM) in sodium phosphate buffer (100 mM, (pH 7.0, 7.25 or 7.5)) at RT. The blue, green and yellow symbols are the experimental data points as determined by ^{1}H NMR. The black line shows a first-order reaction rate model based on the reaction rate constants shown in panel **(D)**.

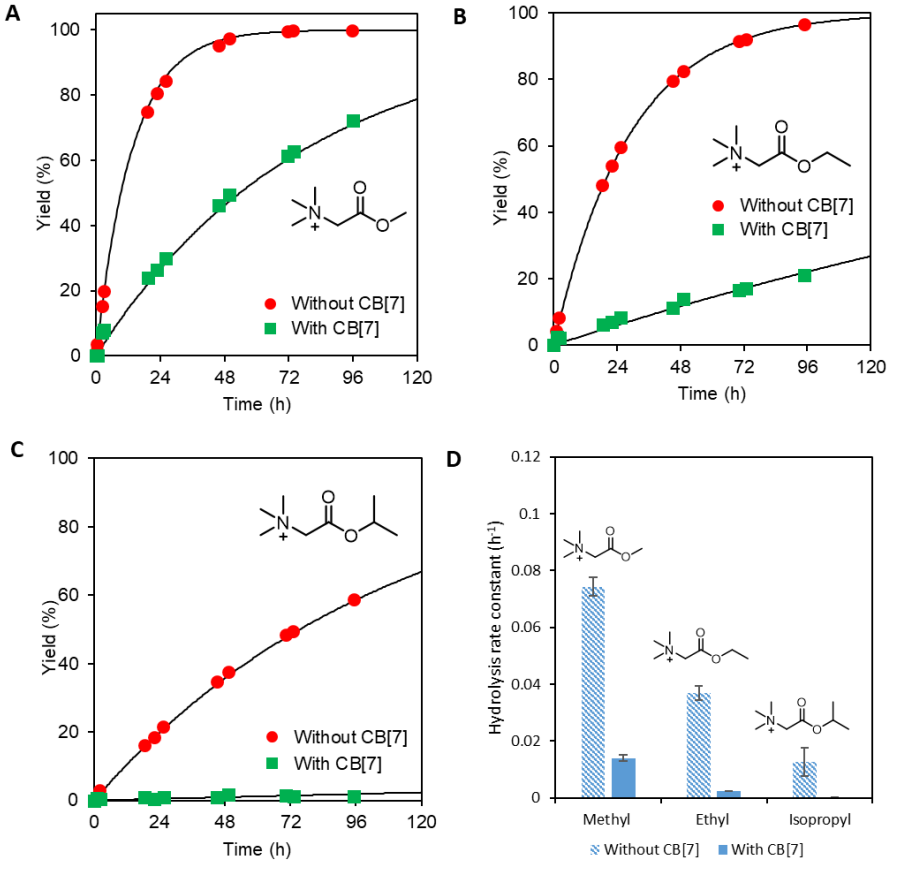

Figure S7.7: Ester hydrolysis profiles in the presence and absence of CB[7] as determined by ^{1}H NMR. **(A)**. Methyl ester **1**, **(B)**. Ethyl ester **2**, **(C)**. Isopropyl ester **3** and **(D)**. A summary of the corresponding hydrolysis rate constants (n=2). Conditions: esters (1 mM) (with 2 mM CB[7] for ethyl and isopropyl ester and 3 mM CB[7] for the methyl ester) in sodium phosphate buffer (100 mM, pH 7.5) at RT. The red and green symbols are the experimental data points as determined by ^{1}H NMR. The black line shows a first-order reaction rate model based on the rate constants shown in panel **(D)**.

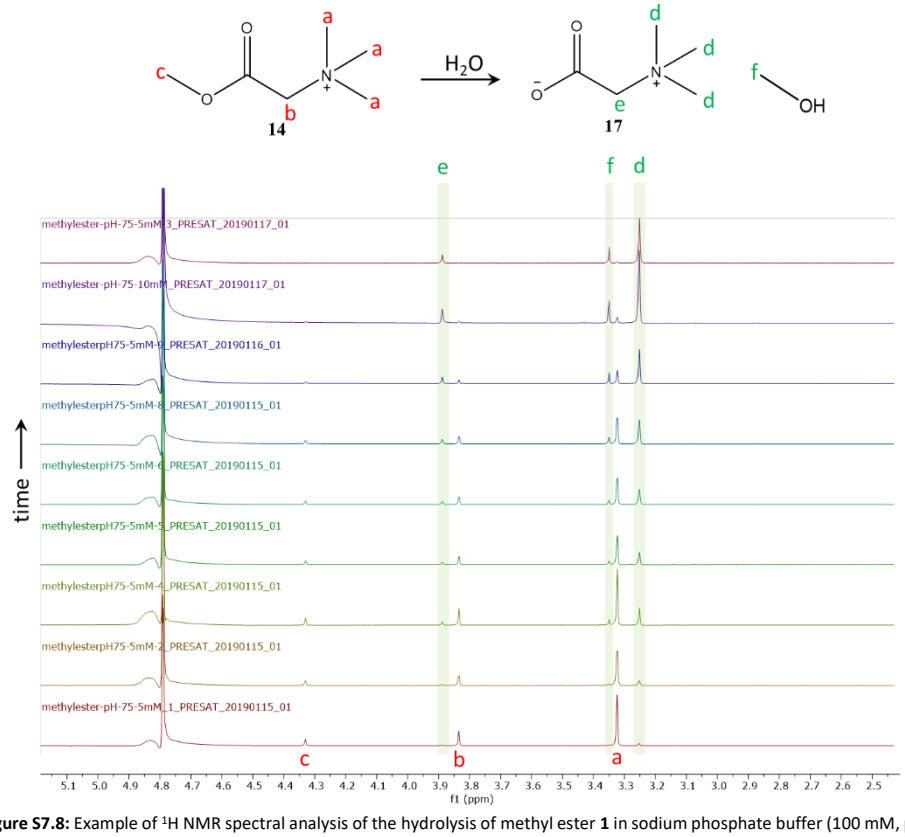

Figure S7.8: Example of ^{1}H NMR spectral analysis of the hydrolysis of methyl ester **1** in sodium phosphate buffer (100 mM, pH 7.5 with NMR solvent D_2O) at RT at different time intervals. The peaks corresponding to the ester vanish over time, meanwhile the product peaks (highlighted in green) intensify.

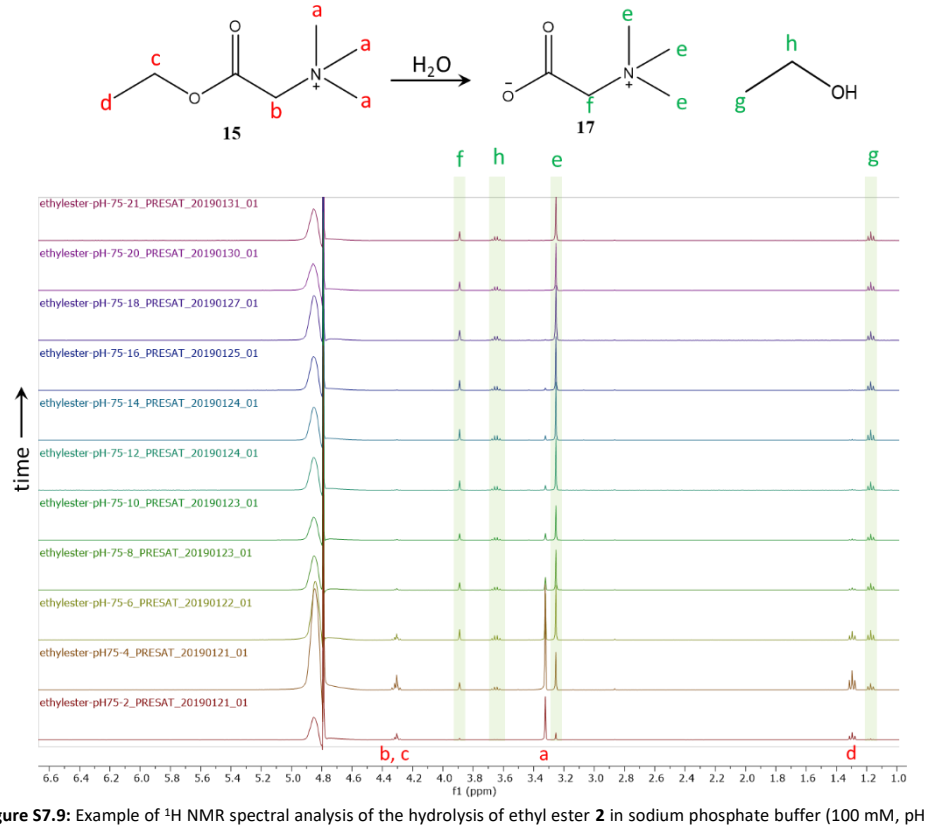

Figure S7.9: Example of ^{1}H NMR spectral analysis of the hydrolysis of ethyl ester **2** in sodium phosphate buffer (100 mM, pH 7.5 with NMR solvent D_2O) at RT at different time intervals. The peaks corresponding to the ester vanish over time, meanwhile the product peaks (highlighted in green) intensify.

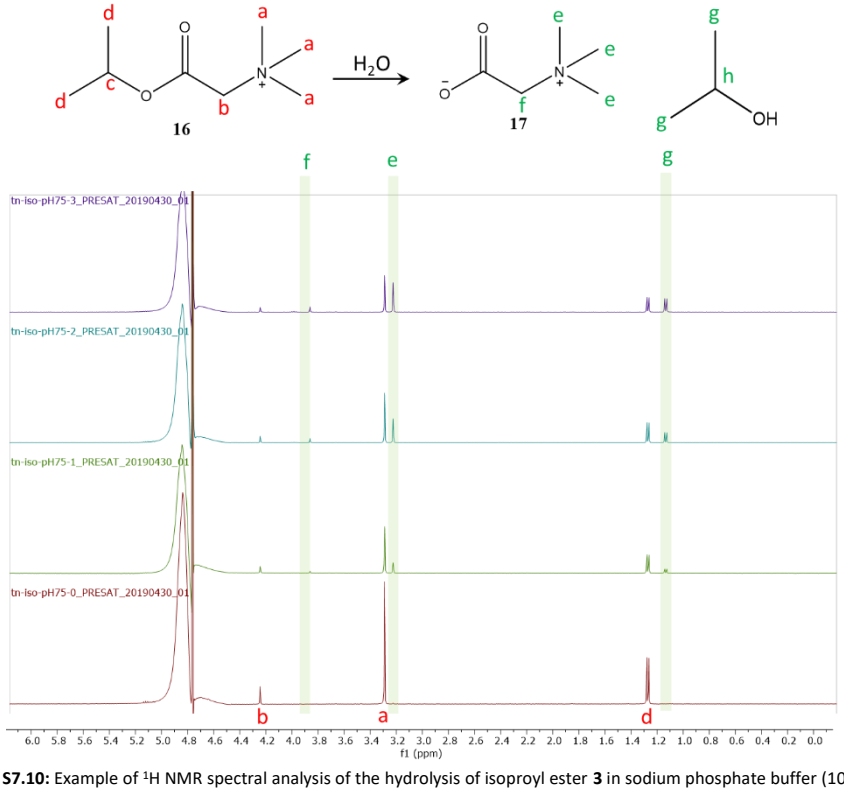

Figure S7.10: Example of ^{1}H NMR spectral analysis of the hydrolysis of isoproyl ester **3** in sodium phosphate buffer (100 mM, pH 7.5 with NMR solvent D_2O) at RT at different time intervals. The peaks corresponding to the ester vanish over time, meanwhile the product peaks (highlighted in green) intensify.

7.5.5 Dye CB[*7*] fluorescence spectra

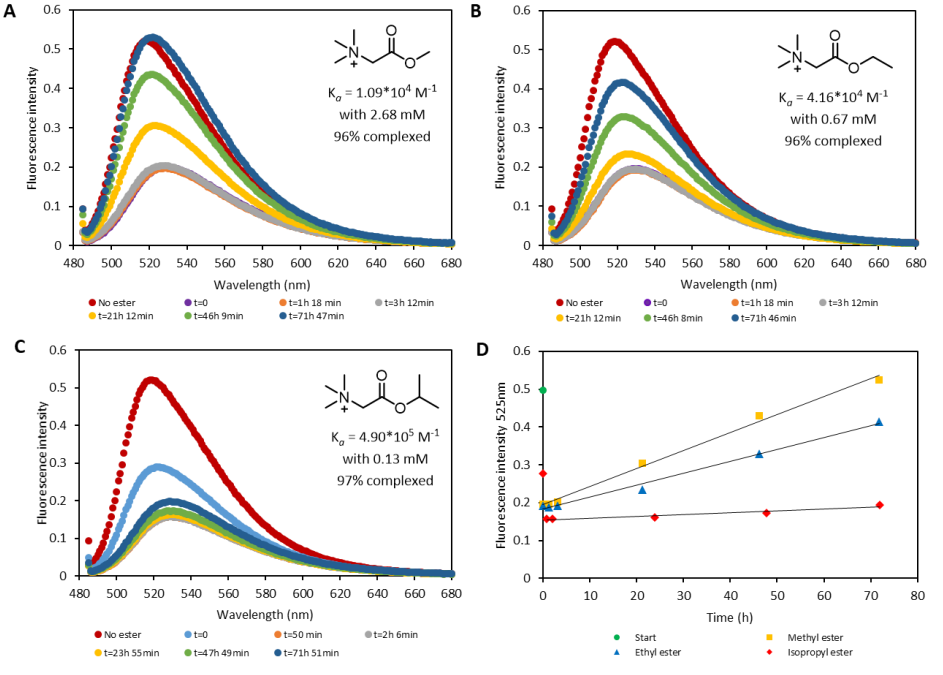

Figure S7.11: Acridine orange (AO) **5** fluorescence spectra over time in the presence of CB[7] and different esters. **(A)**. Methyl ester **1**, **(B)**. Ethyl ester **2**, **(C)**. Isopropyl ester **3** and **(D)**. Fluorescence intensity of AO **5** in and outside CB[7] over time at 525 nm (maximum in emission spectrum) with addition of different esters. Conditions: esters (methyl **1** 2.68 mM, ethyl **2** 0.67 mM and isopropyl **3** 0.13 mM) with 0.054 mM CB[7]and 0.027 mM AO **5** in sodium phosphate buffer (100 mM, pH 7.5) at RT. Samples were excited at wavelength 465 nm.

7.5.6 Hydrazone UV-VIS absorbance

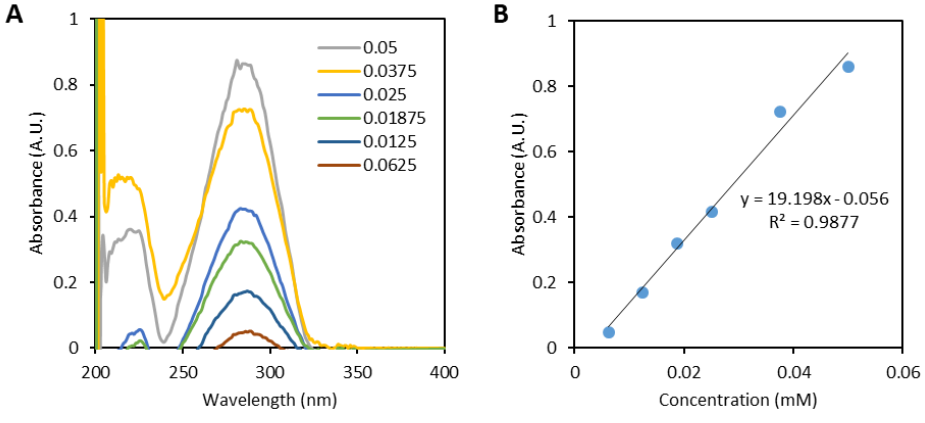

Figure S7.12: Extinction coefficient for hydrazone product **9** in sodium phosphate buffer (100 mM, pH 7.5) at 287 nm: 19.2 $mM^{-1}cm^{-1}$. **(A)**. UV-Vis absorbance spectra of hydrazone product **9** at different concentrations. **(B)**. Absorbance at 287 nm of hydrazone product **10** at different concentrations.

Using Lambert-Beer law:

$$A = \varepsilon l C$$

, where A is the absorbance of **9** at 287 nm, ε is the extinction coefficient, l is the path length and C is the concentration of hydrazone **9**, εl is the slope of plot in Figure S7.12B. Therefore, the extinction coefficient for hydrazone **9** at 287 nm is 19.2 mM^{-1} cm^{-1} at pH 7.5.

The yield of hydrazone product **9** is further calculated by determining the concentration from:

$$[C] = \frac{A}{\varepsilon l}$$

By monitoring the absorbance of product **9** peak at 287 nm, the yield of **9** as a function of time can be calculated. All graphs showing the yield of **9** in this chapter are calculated in this way.

7.5.7 Kinetic model

In this section the kinetic model is explained, which calculates the changing reaction rate constant for hydrazone formation during the fuel cycle. When the ester fuels are added to the reaction mixture, the catalyst is liberated from the CB[7] host and over time due to the hydrolysis of the esters the catalyst is captured again inside CB[7]. Consequently, the free catalyst concentration in the solution is changing as a function of time (and the catalytic rate constant). Overall, this can be modelled numerically with a set of differential equations. To do this, we will first explain the ester hydrolysis kinetics, hydrazone formation kinetics and equilibrium concentration calculations for host-guest complex formation. After that we assemble the kinetic model based on these individual parts and numerically calculate the concentration of the different species and the k-value.

Ester hydrolysis reaction kinetics

It is assumed that ester hydrolysis proceeds in a first-order rate:

$$Ester + Water \rightarrow Acid + Alcohol$$

$$\frac{d[E]}{dt} = -k_{hydrolysis}[E]$$

, where $k_{hydrolysis}$ is the hydrolysis rate constant and $[E]$ the time-dependent ester concentration. After integration, the rate law can be written as:

$$ln\left(\frac{[E]_t}{[E]_0}\right) = -k_{hydrolysis}t$$

, where $[E]_0$ is the initial ester concentration, $[E]_t$ the ester concentration at time *t* and $k_{hydrolysis}$ the hydrolysis rate constant. By following the ester vs acid concentration over time with ^{1}H NMR the hydrolysis rate constant can be determined by fitting the equation to a linear line (y = mx). The as such determined rate constants for ester hydrolysis at different pH and inside or outside CB[7] are provided in Figure S7.6-7.

Hydrazone formation reaction kinetics

The hydrazone formation reaction is assumed to be a second-order reaction. The reaction was performed at pseudo-first order conditions by using one of the reagents in excess. Unless stated otherwise, concentrations used in the hydrazone formation reaction were 0.2 mM aldehyde **7** and 0.02 mM hydrazide **8**.

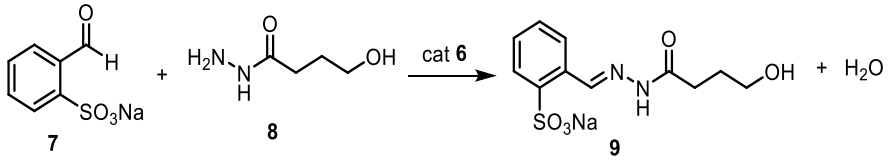

Initial	**t = 0**	$[A]_0$	$[A]_0$	0
	t = *t*	$[A]_t = [A]_0 - [C]_t$	$[B]_t = [B]_0 - [C]_t$	$[C]_t$

$[A]$ is the excess aldehyde **7** concentration, $[B]$ the concentration of hydrazide **8** and $[C]$ the hydrazone product **9**. The second order rate equation, assuming first-order in both A and B, can be expressed as:

$$\frac{d[C]}{dt} = k[A][B]$$

For $[A]_0 \neq [B]_0$ and using $[A]_t = [A]_0 - [C]_t$ and $[B]_t = [B]_0 - [C]_t$ the second-order rate equation after integration can be expressed as:

$$\ln\frac{[A]_t}{[A]_0} - ln\frac{[B]_t}{[B]_0} = k([A]_0 - [B]_0)t$$

Because A was used in excess, it can be assumed that:

$[A]_0 \gg [B]_0$ then $\frac{[A]_t}{[A]_0} \approx 1$ and$[A]_0 - [B]_0 \approx [A]_0$

Therefore, the rate equation can be written as:

$$\frac{[B]_t}{[B]_0} = e^{-k[A]_0 t}$$

$$ln\left(\frac{[B]_t}{[B]_0}\right) = -k[A]_0 t$$

$$ln\left(1 - \frac{[C]_t}{[B]_0}\right) = -k[A]_0 t$$

, where $[A]_0$ is the initial aldehyde **7** concentration, $[B]_0$ the initial hydrazide **8** concentration, $[C]_t$ the hydrazone **9** concentration at time t and k the reaction rate constant. Hence, by following the hydrazone product **9** concentration over time with

UV-VIS the rate constants of the pseudo-first order reactions can be determined by fitting this equation to a linear line (y = mx).

Equilibrium concentration calculation of dye/catalyst/ester⊂CB[7] complex

The calculation here is shown for the catalyst⊂CB[7] complex, but the same calculation applies for the dye⊂CB[7] and ester⊂CB[7] complex. The equilibrium concentrations can be calculated as follows:

	$[CB[7]]$	$[Cat]$	$[Cat{\subset}CB[7]]$
Initial	$[CB[7]_0] = a$	$[Cat]_0 = b$	0
Change	$-x$	$-x$	x
Equilibrium	$a - x$	$b - x$	x

, where $[CB[7]_0]$and $[Cat_0]$ are the CB[7] and catalyst concentrations that are added to the reaction mixture and x is the catalyst⊂CB[7] complex concentration. From this, the association constant is defined as:

$$K_a = \frac{k_f}{k_b} = \frac{[Cat{\subset}CB[7]]}{[Cat][CB[7]]} = \frac{x}{(a-x)(b-x)}$$

By solving this equation for x an expression for the catalyst⊂CB[7] complex concentration is obtained:

$$[Cat{\subset}CB[7]] = \frac{a \cdot K_a + b \cdot K_a + 1 - \sqrt{a^2 \cdot {K_a}^2 - 2a \cdot b \cdot {K_a}^2 + b^2 \cdot {K_a}^2 + 2 \cdot a \cdot K_a + 2 \cdot b \cdot K_a + 1}}{2 \cdot K_a}$$

$$= \frac{[CB[7]]_0 K_a + [Cat]_0 K_a + 1 - \sqrt{[CB[7]]_0{}^2 K_a{}^2 - 2[CB[7]]_0[Cat]_0 K_a{}^2 + [Cat]_0{}^2 K_a{}^2 + 2[CB[7]]_0 K_a + 2[Cat]_0 K_a + 1}}{2K_a}$$

From this, the free CB[7] and catalyst concentrations in solution can then be calculated as follows:

$$[CB[7]] = [CB[7]]_0 - [Cat{\subset}CB[7]]$$

$$[Cat] = [Cat]_0 - [Cat{\subset}CB[7]]$$

, where $[CB[7]]$ is the uncomplexed (free) CB[7] concentration and $[Cat]$ is the uncomplexed (free) catalyst concentration.

MATLAB numerical model of differential equations

Using the above relations and by determining the ester hydrolysis rate constants in and outside CB[7] with ^{1}H NMR, the catalyst in the solution as a function of time can be calculated and based on that the rate constant for hydrazone formation over time. Upon addition of the esters as chemical fuel, the esters will form a complex with CB[7] with a concentration of $\left[Ester{\subset}\mathrm{CB}[7]\right](t)$, which is a function of time (as the esters hydrolyse over time). The ester inside CB[7] hydrolyses slower than outside CB[7] this is taken into account in the model. Hence, to calculate the concentration profiles of all the species in the reaction mixture, we use the following equations and use the MATLAB function ode45 to calculate them numerically:

$$\frac{d[Ester]}{dt} = -k_{hydrolysis}[Ester] - k_f[E]\left[CB[7]\right] + k_b\left[Ester{\subset}CB[7]\right]$$

$$\frac{d[Ester{\subset}CB[7]]}{dt} = -k_{hydrolysis}\left[Ester{\subset}\mathrm{CB}[7]\right] + k_f[Ester]\left[CB[7]\right] - k_b\left[Ester{\subset}CB[7]\right]$$

$$\frac{d[Acid]}{dt} = k_{hydrolysis}[Ester] + k_{hydrolysis}\left[Ester{\subset}CB[7]\right]$$

$$\frac{d[Alcohol]}{dt} = k_{hydrolysis}[Ester] + k_{hydrolysis}\left[Ester{\subset}CB[7]\right]$$

$$\frac{d[Cat]}{dt} = -k_f[Cat]\left[CB[7]\right] + k_b\left[Cat{\subset}CB[7]\right]$$

$$\frac{d\left[Cat{\subset}CB[7]\right]}{dt} = k_f[Cat]\left[CB[7]\right] - k_b\left[Cat{\subset}CB[7]\right]$$

$$\frac{d[CB]}{dt} = -k_f[Ester]\left[CB[7]\right] + k_b\left[Ester{\subset}CB[7]\right] - k_f[Cat]\left[CB[7]\right] + k_b\left[Cat{\subset}CB[7]\right] + k_{hydrolysis}\left[Ester{\subset}CB[7]\right]$$

Finally, to calculate the rate constant as a function of time the catalyst concentration over time is used in the following equation:

$$k\,(t) = (k_0 + k_{cat}[cat](t) + k_1[CB[7]])$$

, where $k\,(t)$ is the total reaction rate constant that changes over time, k_0 the rate constant of the background reaction (uncatalysed hydrazone formation), k_1 the rate constant of CB[7] catalysed hydrazone formation, $[cat](t)$ the catalyst concentration over time and $[CB[7]]$ the total CB[7] concentration present. N.B. CB[7] has a minor background reaction taken into account with $k_1[CB[7]]$.

7.5.8 Control over hydrazone formation

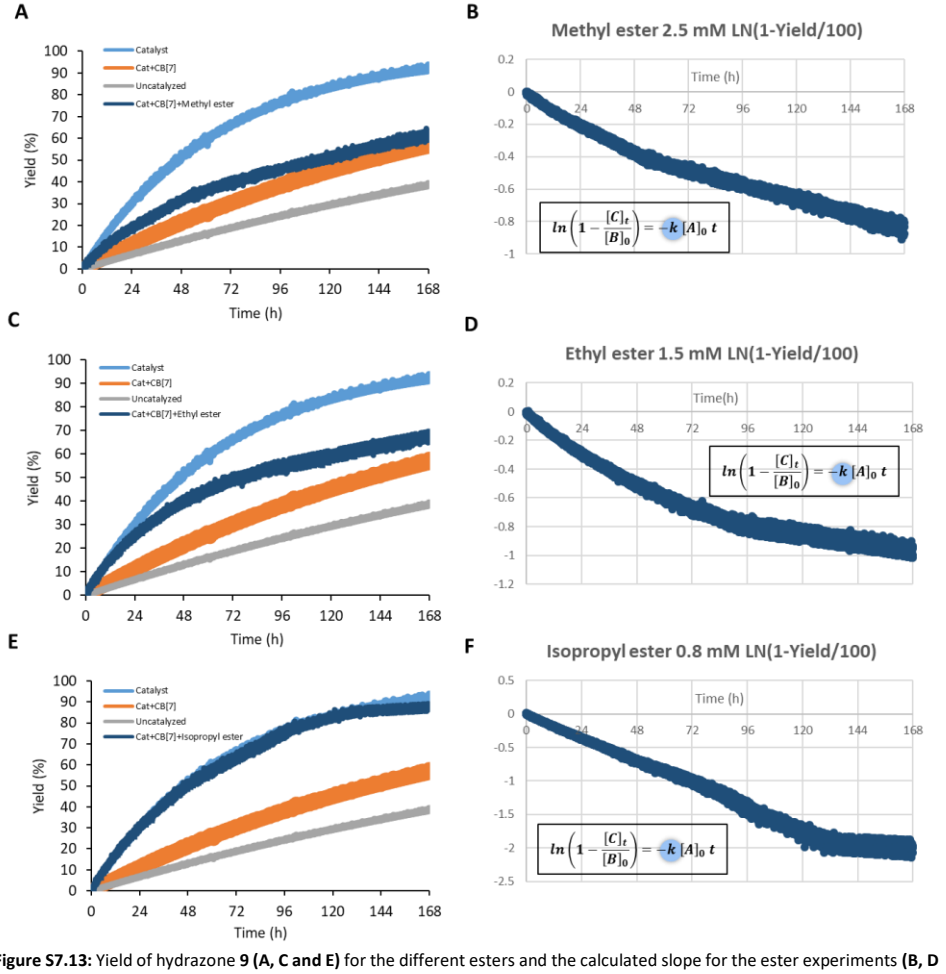

Figure S7.13: Yield of hydrazone **9 (A, C and E)** for the different esters and the calculated slope for the ester experiments **(B, D and F)**: **(A-B)**. Methyl ester **1**, **(C-D)**. Ethyl ester **2** and **(E-F)**. Isopropyl ester **3**. Conditions: 0.2 mM aldehyde **7**, 0.02 mM hydrazide **8**, 0.2 mM catalyst **6**, 0.6 mM CB[7] and 2.5 mM methyl ester **1** / 1.5 mM ethyl ester **2** / 0.8 mM isopropyl ester **3** in sodium phosphate buffer (100 mM, pH 7.5) at RT.

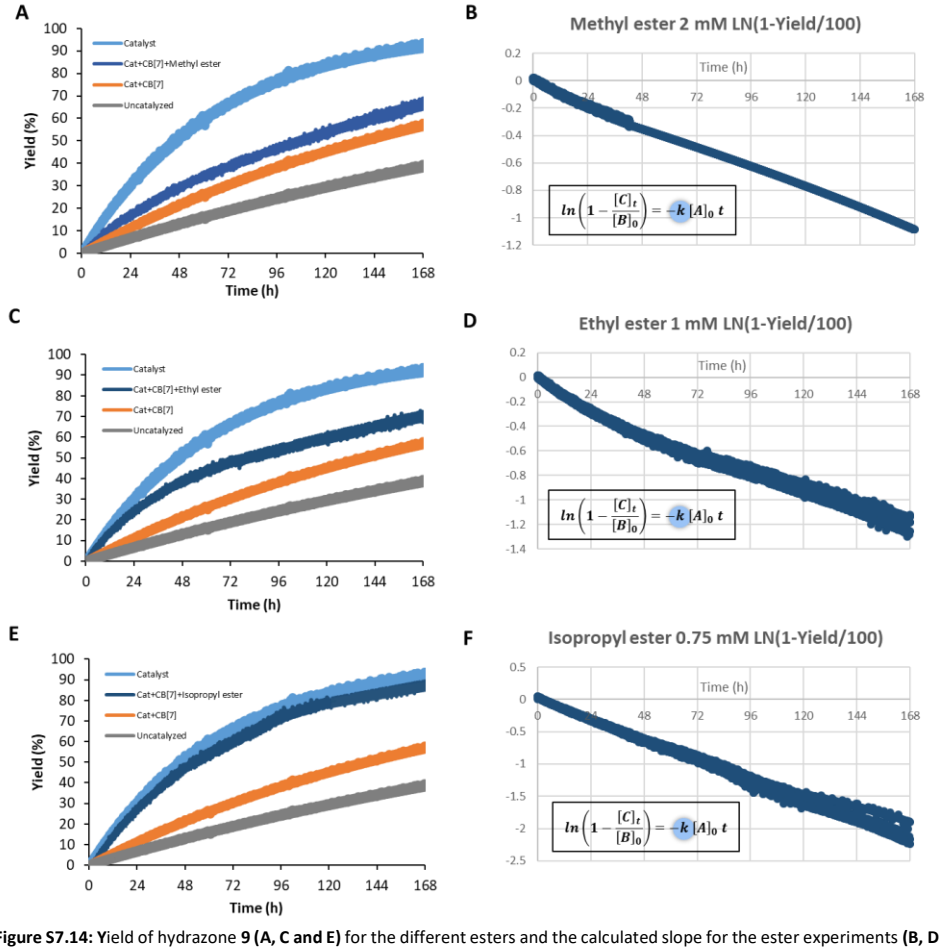

Figure S7.14: Yield of hydrazone **9 (A, C and E)** for the different esters and the calculated slope for the ester experiments **(B, D and F)**: **(A-B)**. Methyl ester **1**, **(C-D)**. Ethyl ester **2** and **(E-F)**. Isopropyl ester **3**. Conditions: 0.2 mM aldehyde **7**, 0.02 mM hydrazide **8**, 0.2 mM catalyst **6**, 0.6 mM CB[7] and 2 mM methyl ester **1** / 1 mM ethyl ester **2** / 0.75 mM isopropyl ester **3** in sodium phosphate buffer (100 mM, pH 7.5) at RT.

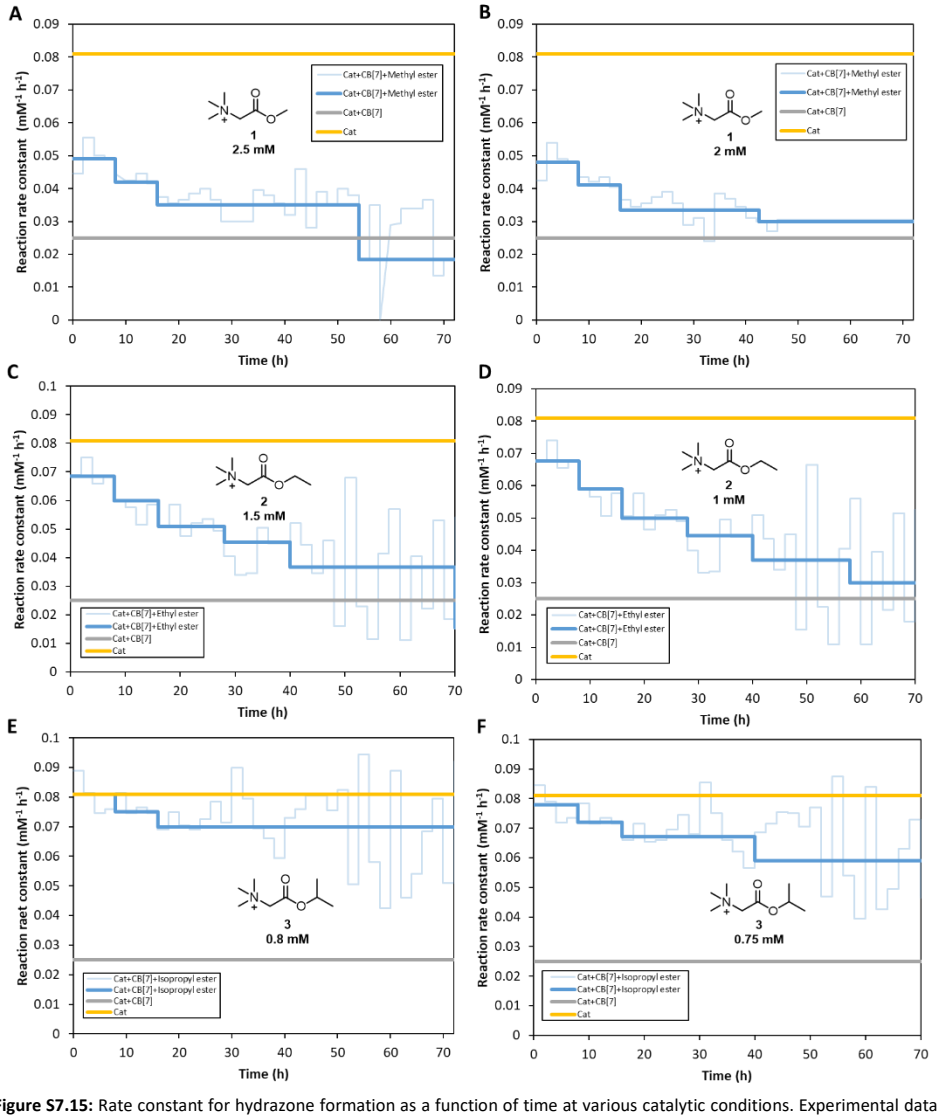

Figure S7.15: Rate constant for hydrazone formation as a function of time at various catalytic conditions. Experimental data with ester fuels at small (blue transparent lines) and large time intervals (blue thick lines): **(A)**. Methyl ester **1** 2.5 mM, **(B)**. Methyl ester **1** 2 Mm, **(C)**. Ethyl ester **2** 1.5 mM, **(D)**. Ethyl ester **2** 1 mM, **(E)**. Isopropyl ester **3** 0.8 mM, **(F)**. Isopropyl ester **3** 0.75 mM. Conditions: 0.2 mM aldehyde **7**, 0.02 mM hydrazide **8**, 0.2 mM catalyst **6** and 0.6 mM CB[7].

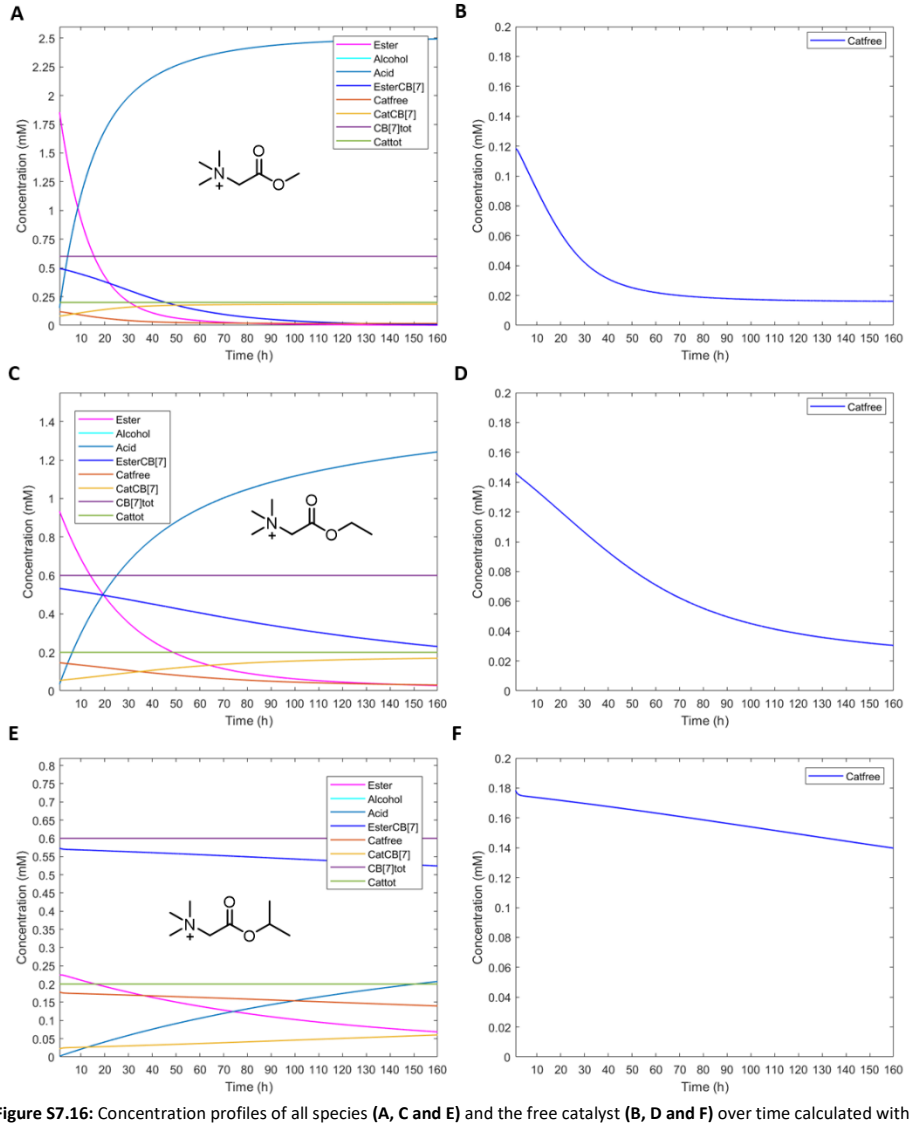

Figure S7.16: Concentration profiles of all species **(A, C and E)** and the free catalyst **(B, D and F)** over time calculated with the kinetic model in MATLAB: **(A-B)**. Methyl ester **1** 2.5 mM, **(C-D)**. Ethyl ester **2** 1.5 mM and **(E-F)**. Isopropyl ester **3** 0.8 mM.

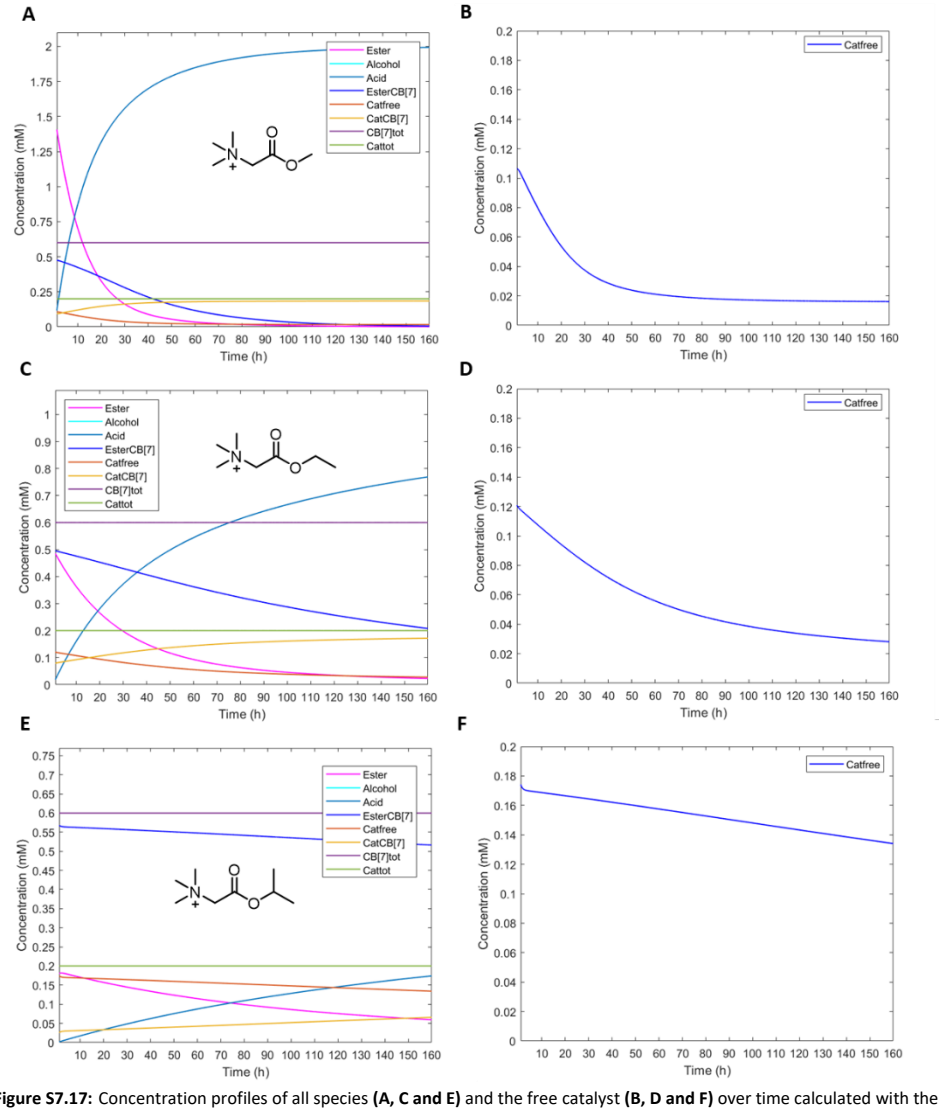

Figure S7.17: Concentration profiles of all species **(A, C and E)** and the free catalyst **(B, D and F)** over time calculated with the kinetic model in MATLAB: **(A-B).** Methyl ester **1** 2 mM, **(C-D)**. Ethyl ester **2** 1 mM and **(E-F)**. Isopropyl ester **3** 0.75 mM.

7.5.9 Ester blank reactions

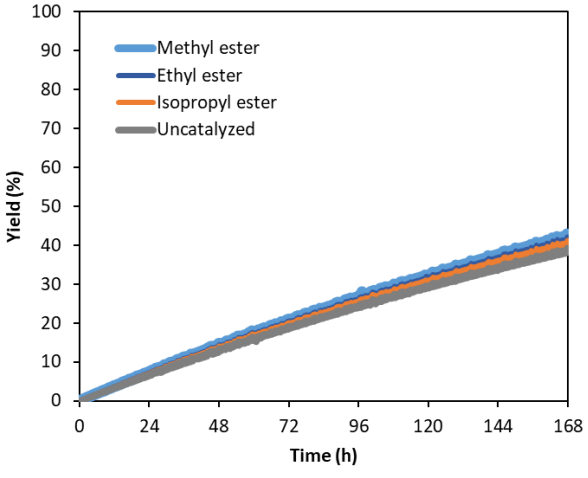

Catalyst system	Second order k_r [mM^{-1} h^{-1}]	$k_i/k_{uncatalyzed}$
Uncatalyzed	0.0135	1
Methyl ester	0.0140	1.04
Ethyl ester	0.0137	1.01
Isopropyl ester	0.0136	1.01

Figure S7.18: Hydrazone formation blank reactions with esters **1-3**. Conditions: 0.2 mM aldehyde **7**, 0.02 mM hydrazide **8** with methyl ester **1** 2.5 mM or ethyl ester **2** 1.5 mM or isopropyl ester **3** 0.8 mM in sodium phosphate buffer (100 mM, pH 7.5) at RT. Very similar trend to the uncatalysed reaction of yield vs time indicates that the esters do not catalyse the hydrazone formation reaction.

7.5.10 NMR and MS spectra

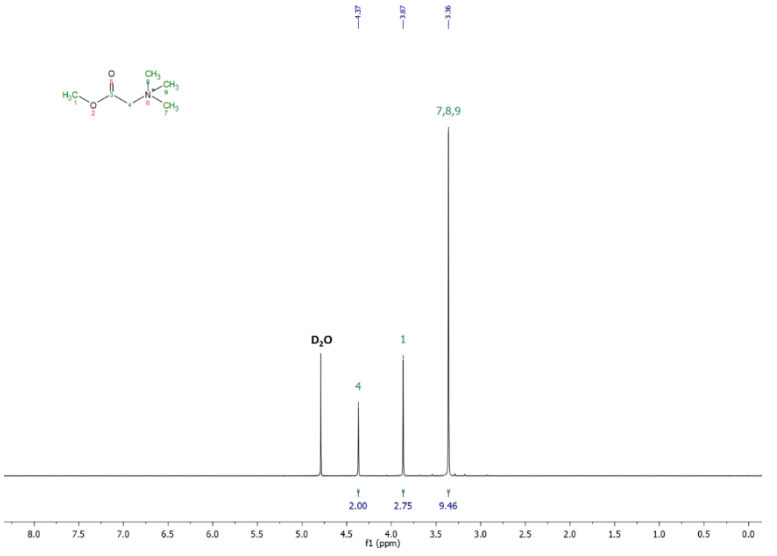

Figure S7.19: ^{1}H NMR spectrum of glycine betaine methyl ester **1** in D_2O.

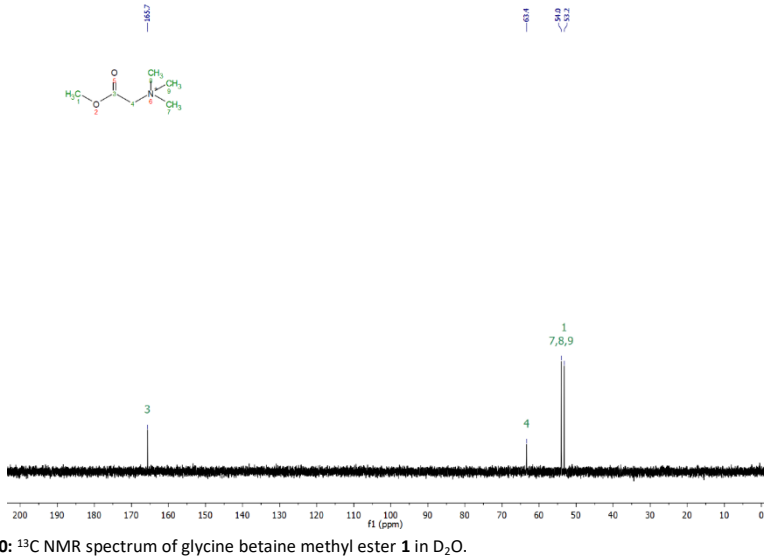

Figure S7.20: ^{13}C NMR spectrum of glycine betaine methyl ester **1** in D_2O.

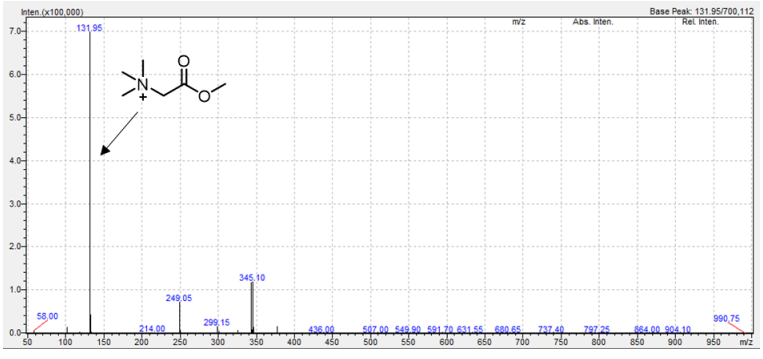

Figure S7.21: ESI-MS spectrum (positive mode) of glycine betaine methyl ester **1** in H_2O. m/z 132 is $[(M)^+]$ and 343/ 345 is $[(2M^+{+}Br^-)^+]$.

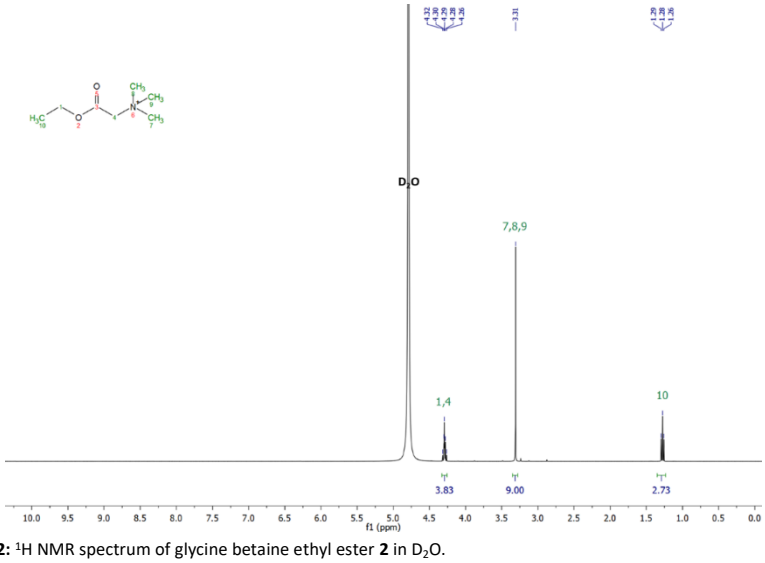

Figure S7.22: ^1H NMR spectrum of glycine betaine ethyl ester **2** in D_2O.

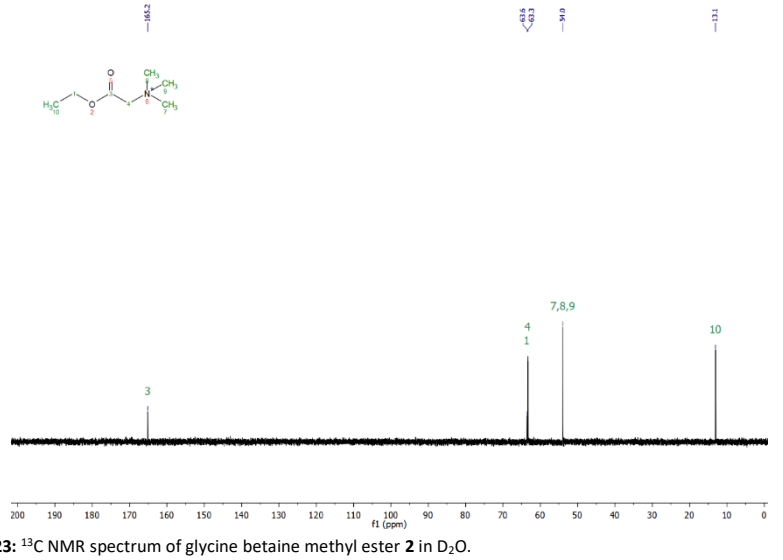

Figure S7.23: ^{13}C NMR spectrum of glycine betaine methyl ester **2** in D_2O.

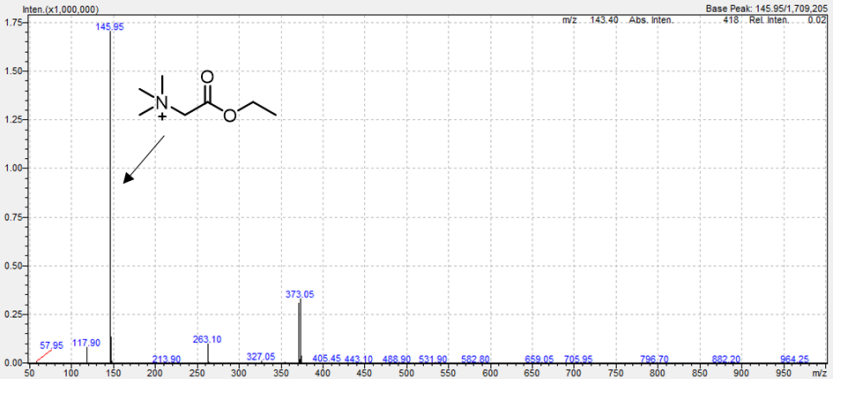

Figure S7.24: ESI-MS spectrum (positive mode) of glycine betaine ethyl ester **2** in H_2O. m/z 146 is $[(M)^+]$ and 371/ 373 is $[(2M^+ + Br^-)^+]$.

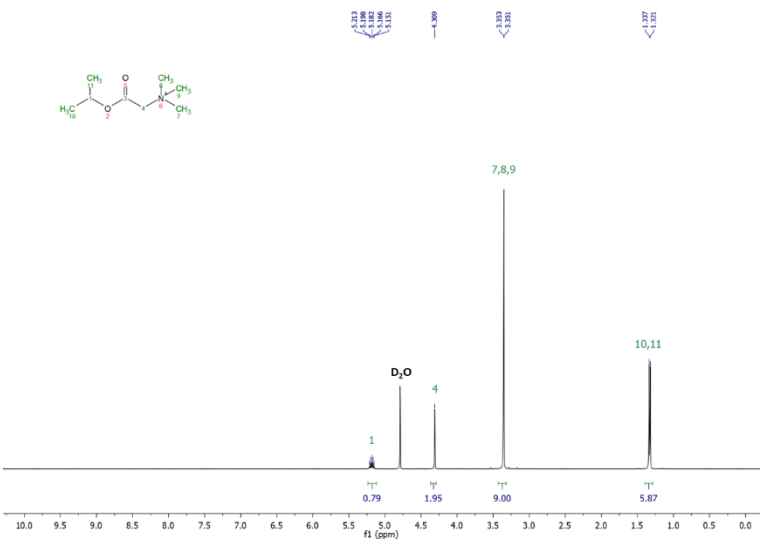

Figure S7.25: ^{1}H NMR spectrum of glycine betaine isopropyl ester **3** in D_2O.

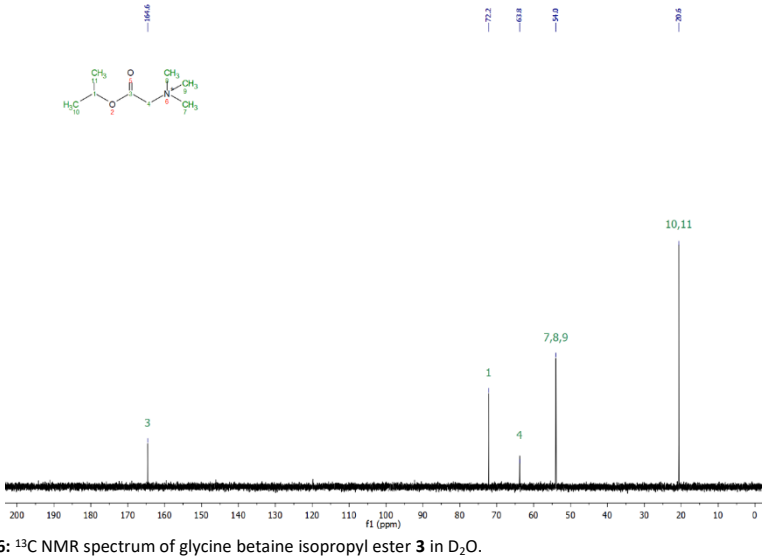

Figure S7.26: ^{13}C NMR spectrum of glycine betaine isopropyl ester **3** in D_2O.

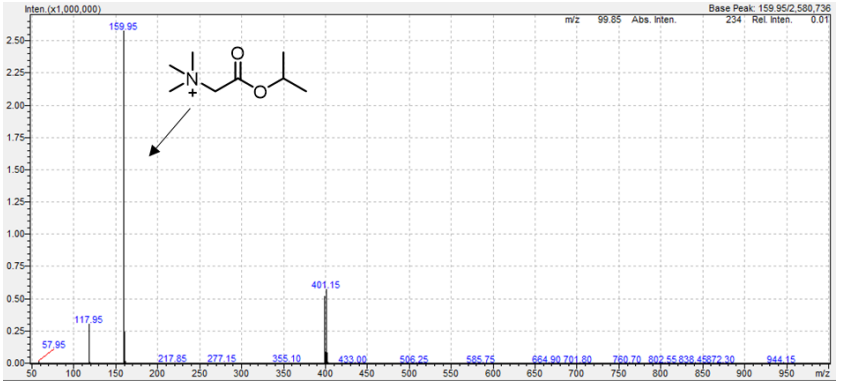

Figure S7.27: ESI-MS spectrum (positive mode) of glycine betaine isopropyl ester **3** in H_2O. m/z 160 is $[(M)^+]$ and 399/ 401 is $[(2M^+ + Br^-)^+]$.

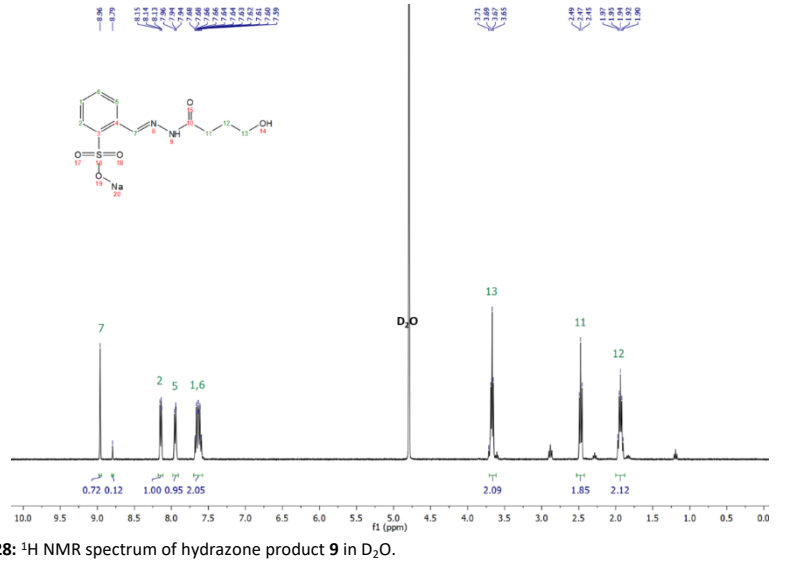

Figure S7.28: ^1H NMR spectrum of hydrazone product **9** in D_2O.

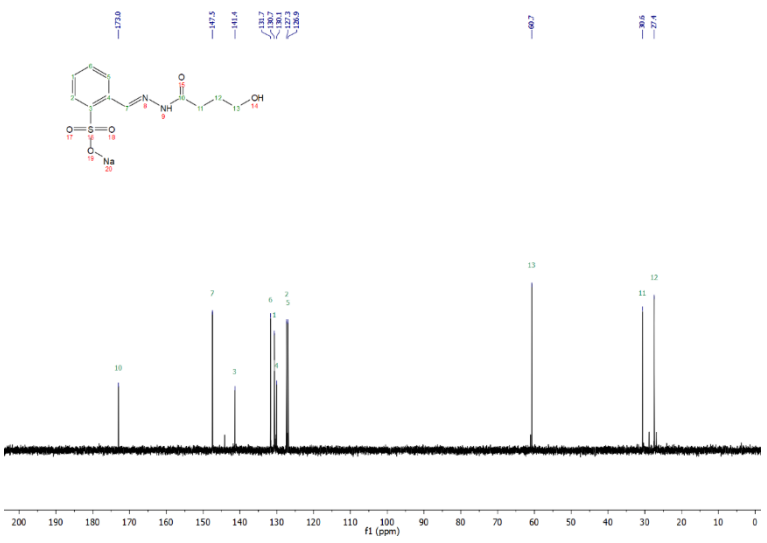

Figure S7.29: ^{13}C NMR spectrum of hydrazone product **9** in D_2O.

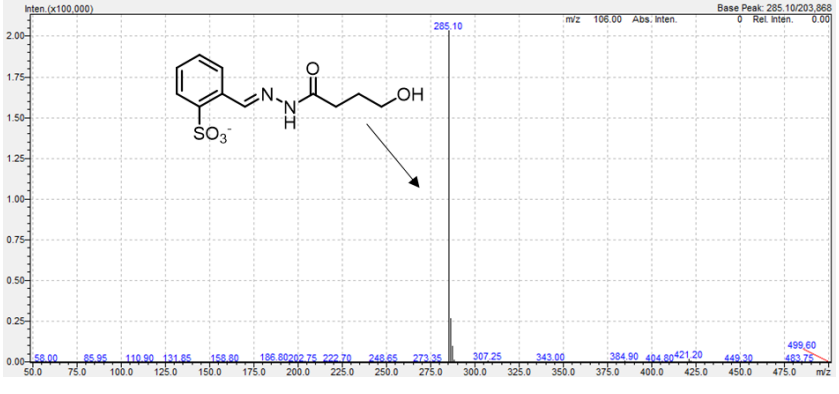

Figure S7.30: ESI-MS spectrum (negative mode) of hydrazone product **9** in H_2O. m/z 285 is $[(M\text{-}Na^+)^-]$.

7.5.11 Supplementary references

1. J. Novacek, L. Roiser, K. Zielke, R. Robiette and M. Waser, *Chem. Eur. J.*, 2016, **22**, 11422-11428.
2. G. L. Li, F. Trausel, M. P. van der Helm, B. Klemm, T. G. Brevé, S. A. P. van Rossum , M. Hartono, H. H. P. J. Gerlings, M. Lovrak, J. H. van Esch and R. Eelkema, *manuscript in preparation*, 2020.
3. M. Shaikh, J. Mohanty, P. K. Singh, W. M. Nau and H. Pal, *Photochem. Photobiol. Sci.*, 2008, **7**, 408-414.
4. J. Liu, N. Jiang, J. Ma and X. Du, *Eur. J. Org. Chem.*, 2009, **2009**, 4931-4938.

SUMMARY

The entire research described in this thesis is part of the larger field of Systems Chemistry. This field of chemistry deals with the understanding of the complexity of biology by mimicking biochemical reaction networks with emergent properties attributed to the entire system. In particular, this research focuses on the design of artificial non-equilibrium chemical reaction networks (CRNs) inspired by signal transduction pathways in living organisms. Specific attention is given to catalysis in such networks. For the design of the catalytic CRNs, organocatalysts are considered as the ideal candidates as they are simple, cheap, recyclable and robust compared to enzymes and frequently less toxic catalysts than metals. On top of that, since organocatalysts can operate under mild conditions, it can pave the way for future applications in biological environments.

First, in **Chapter 2** organocatalytic reactions in aqueous media are reviewed. Landmark contributions in organocatalysis are discussed followed by the different activation modes of organocatalysts. The reaction examples are limited to nucleophilic and base catalysis, which are also important for further chapters. Crucial considerations for organocatalysis to work in aqueous media are the characteristics of the catalyst (e.g. functional groups and pK_a values) and the reaction (e.g. the microenvironment surrounding the reaction intermediates). Based on the recent developments in this field, a bright future is expected for organocatalysis in biology with applications in chemical biology and biomedicine.

With regard to non-equilibrium CRNs, most work has been done in the field of supramolecular polymers. In **Chapter 3** chemically fuelled, transient supramolecular polymers are reviewed. Supramolecular polymerizations are part of molecular self-assembly and then specifically the formation of one-dimensional aggregates connected by non-covalent interactions. The non-covalent polymers form primarily via isodesmic and cooperative mechanisms. In analogy to biology, microtubule and actin filament assembly with non-linear features such as treadmilling and dynamic instability are discussed. Furthermore, different thermodynamic regimes of supramolecular polymers and the nature of the chemical fuel are discussed. These topics, as well as the polymerization mechanisms, come back in the comprehensive literature overview in this chapter. As it turns out, nucleoside triphosphates are highly popular fuels in combination with enzyme catalysis, next to redox chemistry and smart pH-switches. The next challenges in this field are the development of dynamic functions, the maintenance of the non-equilibrium state by continuous supply of chemical fuel and to obtain

increased controllability of the non-equilibrium system. All in all, non-equilibrium supramolecular polymers are considered as fundamental elements for the design of dynamic and tuneable systems with a great potential for future applications.

In **Chapter 4** the organocatalytic fuel-driven CRN designed during this research is presented. The network is a fuel-driven esterification CRN, where the yield and lifetime of the ester product can be controlled by two organocatalysts. Pyridine is the catalyst for the ester formation, while imidazole catalyses the backward ester hydrolysis. Experimental data of ester yields are corroborated by a kinetic model. Next, the fuel-driven strategy is applied to a responsive polymer system, where polymer conformation (coil vs globule) and aggregation can be regulated by changing fuel and catalyst levels. Overall, in this chapter organocatalysis is used as a tool to control an artificial fuel-driven system, resulting in a macromolecular superstructure change similar to natural non-equilibrium systems.

Chapter 5 builds on the work of **Chapter 4** and uses the transient polymer coil to globule transition to alter depletion interactions in a colloidal system. As random coil, the polymer is a depletant for silica colloids, stimulating colloidal aggregation, while in the compact globule conformation, the polymer is unable to deplete the colloids, leading to redispersion of the colloidal particles. In a full fuel cycle, the polymer undergoes cyclic transitions from coil to globule, directly influencing the colloidal aggregation and redispersion processes. In that way, a fuel-driven CRN on the molecular scale generates a microscopic response with a transient colloidal depletion cycle. All in all, the temporal propagation of non-equilibrium behaviour across length scales shows great promise for the design of responsive materials with life-like properties.

In order to gain better understanding of the impact of catalysis in CRNs in **Chapter 6** simulations in batch and flow systems are presented along with relevant literature comparisons. The simulations show that changes in the catalysts' concentrations in batch and flow result in responses in product yield, lifetime and steady states levels. For the flow system, product steady state levels can be altered by *in-situ* up or downregulation of catalysts' levels, whereas unusual concentration profiles and self-regulation can be obtained by incorporation of feedback elements. Eventually, expanding the scope of catalysis in non-equilibrium CRNs with small molecule and metal catalysis can promote the discovery of novel reaction networks and enhance the application potential in synthetic materials.

In **Chapter 7** a second fuel-driven CRN is presented, which deals with supramolecular encapsulation to regulate catalytic activity. Hydrolysable esters are used as chemical

fuels to form a transient complex with supramolecular host cucurbit[7]uril (CB[7]). The esters are only temporally stable in aqueous environment and disintegrate into acid and alcohol, which both do not bind to CB[7]. With dye release experiments the feasibility of the concept is demonstrated. Next, the fuel-driven transient complex formation is used to control the kinetics of a second chemical reaction, in which the fuel does not participate. By varying the ester structure and concentration different catalyst liberation times and free catalyst concentrations can be accessed, regulating the overall reaction rate. The system shows potential for the design of more complex non-biological networks and ultimately incorporation of signal transduction in organic materials.

In conclusion, in this research organocatalysis is used as a tool to control out-of-equilibrium fuel-driven CRNs. With comprehensive literature reviews, experiments and mathematical simulations we show how organocatalysis can be implemented in such networks and what the impact is on the behaviour of various reaction networks. Ultimately, increased understanding of the working principles of catalytically regulated non-equilibrium CRNs can form the basis for the development of man-made signal responsive and interactive materials.

SAMENVATTING

Het volledige onderzoek beschreven in deze thesis vormt een onderdeel van de chemie van systemen. Dit veld houdt zich bezig met het onderzoeken van de complexiteit van de biologie door biochemische reactienetwerken met bijzondere eigenschappen toegeschreven aan het volledige systeem na te bootsen. Dit onderzoek in het bijzonder richt zich op het ontwerpen van artificiële uit-evenwicht chemische reactienetwerken (CRNen) geïnspireerd op signaaltransductie cascaderoutes in levende organismen. Specifieke aandacht wordt gegeven aan katalyse in zulke netwerken. Voor het ontwerp van de katalytische CRNen worden organokatalysatoren beschouwd als de ideale katalysatorkandidaten omdat ze eenvoudig, betaalbaar, recyclebaar en robuust zijn vergeleken met enzymen en vaak minder toxisch dan metaal katalysatoren. Bovendien, omdat organokatalysatoren kunnen opereren onder milde omstandigheden, zijn ze veelbelovend voor toekomstige toepassingen in een biologische omgeving.

Als eerste, in **Hoofdstuk 2** worden organokatalytische reacties in waterige media besproken. Belangrijke bijdragen in de organokatalyse worden besproken gevolgd door de verschillende activeringsmodi van organokatalysatoren. De reactievoorbeelden worden beperkt tot nucleofiele en basische katalyse, die ook weer belangrijk zijn voor verdere hoofdstukken. De kenmerken van de katalysator (bijv. functionele groepen en pK_a-waarden) en de reactie (bijv. de micro-omgeving van de reactietussenproducten) zijn essentiële overwegingen voor organokatalyse om in waterige media hun werk te kunnen doen. Op basis van de recente ontwikkelingen in dit gebied wordt er een mooie toekomst verwacht voor organokatalyse in de biologie met toepassingen in de chemische biologie en de biogeneeskunde.

Met betrekking tot uit-evenwicht CRNen, is het meeste werk gedaan rondom supramoleculaire polymeren. In **Hoofdstuk 3** worden chemische brandstof-gedreven, eindige supramoleculaire polymeren besproken. Supramoleculaire polymerisaties maken onderdeel uit van moleculaire zelf-assemblage en dan specifiek de formatie van eendimensionale aggregaten verbonden door non-covalente interacties. De non-covalente polymeren vormen voornamelijk via isodesmische en coöperatieve mechanismen. Als biologisch voorbeeld wordt de assemblage van microtubuli en actine-filamenten met niet-lineaire kenmerken zoals “treadmilling” en “dynamische instabiliteit” besproken. Verder worden verschillende thermodynamische regimes van supramoleculaire polymeren en de aard van de chemische brandstof besproken. Deze onderwerpen, evenals de polymerisatiemechanismen, komen daarna terug in het uitgebreide literatuuroverzicht in dit hoofdstuk. Het blijkt dat nucleoside-trifosfaten

zeer populaire brandstoffen zijn in combinatie met enzymkatalyse, naast redoxchemie en slimme pH-schakelaars. De volgende uitdagingen in dit gebied zijn de ontwikkeling van dynamische functies in uit-evenwicht systemen, het in stand houden van de uit-evenwichtstoestand door continue aanvoer van chemische brandstof en het verkrijgen van een grotere controle over het niet-evenwichtssysteem. Alles bij elkaar worden uit-evenwichtig supramoleculaire polymeren beschouwd als fundamentele elementen voor het ontwerpen van dynamische en afstembare systemen met een groot potentieel voor toekomstige toepassingen.

In **Hoofdstuk 4** wordt de organokatalytische brandstof gestuurde CRN die tijdens dit onderzoek is ontworpen, gepresenteerd. Het netwerk bestaat uit een brandstof gestuurde CRN met een veresteringsreactie, waarbij de opbrengst en levensduur van het esterproduct kunnen worden gereguleerd door twee organokatalysatoren. Pyridine is de katalysator voor de esterformatie, terwijl imidazole de teruggaande esterhydrolyse katalyseert. Experimentele data van de esteropbrengsten worden ondersteund door een kinetisch model. Vervolgens wordt de brandstof gestuurde strategie toegepast op een responsief polymeersysteem, waarbij polymeerconformatie (spiraal versus bolletje) en aggregatie kunnen worden gereguleerd door het brandstof- en katalysatorniveau te veranderen. In het geheel wordt in dit hoofdstuk organokatalyse gebruikt als een hulpmiddel om een kunstmatig brandstof-gedreven systeem te reguleren, wat resulteert in een macromoleculaire verandering van een superstructuur vergelijkbaar met natuurlijke niet-evenwichtssystemen.

Hoofdstuk 5 bouwt voort op het werk van **Hoofdstuk 4** en gebruikt de eindige polymeer spiraal-bolletje overgang om depletie-interacties in een colloïdaal systeem te veranderen. Als willekeurige spiraal is het polymeer een depletiemiddel voor silica colloïden, waardoor colloïdale aggregatie wordt gestimuleerd. In de compacte bolletjesconformatie verliest het polymeer echter zijn depletiecapaciteit, wat leidt tot herdispersie van de colloïdale deeltjes. In een volledige brandstofcyclus ondergaat het polymeer cyclische overgangen van spiraal naar bolletje, wat een directe invloed heeft op de colloïdale aggregatie- en herdispersieprocessen. Op die manier genereert een brandstof gestuurde CRN op de moleculaire schaal een microscopische respons met een eindige colloïdale depletiecyclus. Al met al is de tijdelijke propagatie van uit-evenwichtsgedrag over lengteschalen een grote belofte voor het ontwerpen van responsieve materialen met levensechte eigenschappen.

Om een beter begrip te krijgen van de impact van katalyse op CRNen worden in **Hoofdstuk 6** simulaties in batch- en stroomsystemen gepresenteerd samen met relevante literatuurvergelijkingen. De simulaties laten zien dat veranderingen in de

concentraties van de katalysator in batch en flow resulteren in veranderingen in productopbrengst, levensduur en steady-state niveaus. Voor het stroomsysteem kunnen de steady-state-niveaus van het product worden gewijzigd door *in situ* op- of neerwaartse regulering van de katalysatorniveaus, terwijl ongebruikelijke concentratieprofielen en zelfregulatie kunnen worden verkregen door het opnemen van feedbackelementen in het systeem. Uiteindelijk kan het uitbreiden van de omvang van katalyse met kleine molecuul- en metaalkatalyse in niet-evenwichtige CRNen de ontdekking van nieuwe reactienetwerken bevorderen en het toepassingspotentieel in synthetische materialen vergroten.

In **Hoofdstuk 7** wordt een tweede brandstof gestuurde CRN gepresenteerd, waarbij supramoleculaire inkapseling wordt gebruikt om de katalytische activiteit te reguleren. Hydrolyseerbare esters worden gebruikt als chemische brandstoffen om een tijdelijk complex te vormen met de supramoleculaire gastheer cucurbit[7]uril (CB[7]). De esters zijn slechts tijdelijk stabiel in waterig milieu en vallen uiteen in zuur en alcohol, die beide niet binden aan CB[7]. Met kleurstofafgifte-experimenten wordt de haalbaarheid van het concept aangetoond. Vervolgens wordt de brandstof-gedreven, eindige complexvorming gebruikt om de kinetiek van een tweede chemische reactie, waaraan de brandstof niet deelneemt, te controleren. Door de esterstructuur en -concentratie te variëren, kunnen verschillende katalysatorafgiftetijden en vrije katalysatorconcentraties worden verkregen, waardoor de algehele reactiesnelheid kan worden beïnvloed. In het algemeen is het systeem veelbelovend voor het ontwerp van meer complexe niet-biologische netwerken en uiteindelijk voor het implementeren van signaaltransductie in organische materialen.

In conclusie, in dit onderzoek wordt organokatalyse gebruikt als een hulpmiddel om brandstof gestuurde uit-evenwicht CRNen te besturen. Met uitgebreid literatuuronderzoek, experimenten en wiskundige simulaties laten we zien hoe organokatalyse kan worden opgenomen in dergelijke netwerken en wat de impact is op het gedrag van verschillende reactienetwerken. Uiteindelijk kan een beter begrip van de werkingsprincipes van katalytisch gereguleerde niet-evenwichtige CRNen de basis vormen voor de ontwikkeling van door de mens gemaakte signaalgevoelige en interactieve materialen.

ACKNOWLEDGEMENTS

Doing science is oftentimes a collaborative effort and therefore I am very grateful to many people who have contributed in any way to the establishment of this thesis and the research described in it.

Dr. Rienk Eelkema (promotor and daily supervisor), I was very excited to start my PhD research under your supervision. Although I was mostly trained to work with enzymes, I am very grateful for the opportunity you gave me to work in your organic synthesis lab. Together we came up with many interesting projects, of which most are now part of this thesis. Thank you for sharing your scientific expertise with me, for being always approachable to talk in person or chat about research or other (science related) topics and for the very fast corrections and feedback.

Prof. dr. Jan H. van Esch (promotor), thank you for inspiring discussions and suggestions on improvements of experiments. The atmosphere in the group was always great and the Sinterklaas dinner at your place was really nice. Rienk and Jan, I am very thankful to both of you for supporting my personal development and career choices.

Apart from my two promotors, I would like to thank all the committee members (Prof.dr. Ulf Hanefeld, Prof.dr. Jan C. M. van Hest, Prof.dr. Andreas Walther, Prof.dr. Nathalie H. Katsonis, Prof.dr. Stephen J. Picken and Dr. Laura Rossi) for assessing my thesis and taking presence in the defence.

Dr. Laura Rossi and Dr. Eduardo Mendes, thank you for the great collaborations with the polymer and colloid projects. It was a pleasure and valuable experience working with you. Laura, your enthusiasm and critical thinking are much appreciated. Eduardo, your talks were always inspiring and maybe we meet again sometime at the Coffee Company.

Dr. ing. Ger Koper, I really enjoyed assisting you with Molecular Thermodynamics. I hope the retirement is doing you well.

Prof. dr. Ferdinand Grozema and Dr. ir. Volkert van Steijn, thank you for valuable scientific discussions outside my expertise area.

Prof. dr. Ulf Hanefeld, I am also very grateful for the time I spent at the TU in your group. Thank you for sharing your passion for research, especially in catalysis, with me. You motivated me to continue in academia and always get the best out of myself. Your friendliness and continued interest are much valued. I hope we can remain in contact.

Dr. Niels Galjart, I really enjoyed your course about protein quality control mechanisms and microtubules in particular. It was very inspiring for me to learn about non-equilibrium systems from a cell biology perspective. Maybe one day we can still set up a collaboration.

Susan, thank you for being a great colleague and friend. Working together in the UV-lab were the best days in the lab. I will always remember the silent disco at Chains and your preference for the Spice Girls songs. Peggy, thank you for cheering up the atmosphere in the office and for all the nice and helpful chats. With you it was always fun and never boring. I admire your perseverance and positive mindset. I hope we can stay in contact and continue to have our chats and dinners together with Susan. Tobias, thank you for all your help in the lab. Whenever my Schlenk line was clogged or the pump was not working you were always ready to help. You have been a great colleague and I loved our discussions about meat and pizza preparations. Angie, thank you for the nice times outside the lab with playing Frisbee and dancing Lindy Hop at the TU sports centre. ¡Que te vaya bien! Emma, it was always so nice to talk to you about all different kind of topics and meet your girls on many occasions. Fanny, thank you for introducing me to the lab in the beginning. Your passion for survival sports is truly admirable. Reece and Sarah, thank you very much for the help with the MATLAB particle counting coding. I wish you both all the best with your projects. Bowen, thank you for being a great help with the viscosity measurements and finalizing the paper. I hope your final experiments go well and you can soon finish your PhD. Guotai, it was great working with you on the fuel-driven systems and the CB projects. Your work ethics are outstanding. Irene, thank you very much for helping me out in the lab with the students. Benjamin Klemm, it was a great experience writing the review paper together. Besides, you are a great host for the BBQ dinners. Benjamin Spitzbarth, your organic synthesis skills are spectacular, no doubt you will excel at your PhD. Mariano, thank you for the smooth collaboration and helpful advices with synthetic procedures. Yongjun, it was always nice chatting with you about science and polymers(omes). Mark, we started at the same time with the MST Bachelor program and it is great to see us both pursuing a PhD. Hanan, catching up with you at the fellowship or at Chains was always very nice. I hope we can keep in touch. Cansel, Qian, Hendrik, Suellen, Elmira, Sahil, Tomasz, Serhii, Vasudevan, Matija, Vincent, Jos, Kai, Fan, Yu, Nancy, Juncheng, Ardeshir and Yiming thanks for the great time in the ASM group. I wish you all the best of luck in your projects and/ or careers. Lars van der Mee, Sietse Kuipers and Duco Bosma, thank you for your assistance in the lab and the nice chats. Veby, thank you for taking care of all the organizational matters and for being always so kind. Els, Caroline, Louw Florusse, Marcel de Puit, Stephen Picken, Wolter Jager, Marcel Bus, Ben Norder and Xiaohui Liu thank you for all the great Staff meetings, both offline and online. Stephen Eustace, thank you for helping me with NMR experiments. Wiel Evers, thanks for your valuable help with the TEM experiments.

I am honoured that I also got the chance to supervise many students during my PhD. This was a great experience and many of them did an amazing job, which makes me really proud. Muhamad Hartono (Tono), working with you was delightful. You are

intelligent and a hard-worker, a very strong combination. You really excelled in your Master project and part of your research is described in this thesis. Chang-Lin Wang (Wax), thank you for the amazing work you did. Together we had a great collaboration, which led to many very nice results, which are all described in this thesis. I wish you all the very best in your future career. Jennifer, you were very hardworking and I admire your patience with the organic synthesis part of your project. I hope you will do well in your PhD. Tuanke, you are brilliant when it comes to modelling and you did very well in your thesis.

Besides the professors and (ASM) colleagues, I would like to thank my friends, new colleagues and family. Gabie and Zoe, together we did the Bachelor and Master in Delft and Leiden. Thank you for being there for me during my entire studies and for all the nice Surinamese dinners (with Caroline as well)! We could always talk for hours about food. Caroline, it was so nice to see you coming back to the Netherlands. Thank you for all your prayers and for being a great friend and ever so sweet. Great friends Great ChemE: Jetsabel, Prajakta, Nilaya, Tanya, Dimas, Aaditya, thank you for all your support, nice dinners and chats throughout the Master and PhD.

Els, Elly and Laureen, it was always lovely to catch-up and share our experiences. Els, thank you for cheering me up with Pasteís de Nata and for your help with the proofreading. Elly and Laureen, I wish you all the best for the rest of your PhDs.

HMC colleagues, thank you for the warm welcome. Gabrielle, Joost, Anne, Rebecca, Elske, Niels and Rolf it is a pleasure working with you and I am very much looking forward to the coming years.

Daniella and Corinne, thank you being a constant source of strength and support. Daniella, thank you for all the fruitful discussions about the propositions and your advices for when I was stuck in the PhD project. Daniella and Enrico, I wish you success in all your future endeavours. Corinne, your upbringing has brought us this far and this milestone could not have been achieved without you. Peter, you taught me to follow passion and never give up, I am grateful for that. Ivonne and Marco, thank you for your support in difficult times. Ruben, Roland, Julia and Boris, it is amazing to see you all pursuing exciting jobs and studies. Opa en Oma, ik vind het geweldig dat jullie zo trots zijn en hoop dat jullie de verdediging mogen meemaken. Partha Pratim, Chandana and Ambarish Bose (Mishti Poribar), our calls have been very delightful and I am looking forward to meeting all of you.

Pritish, thank you for your help with the thesis cover and lay-out. I can always count on you and feel blessed to have you by my side.

CURRICULUM VITAE AUCTORIS

Michelle Petronella van der Helm was born on 19th of August, 1994 in Delft, the Netherlands. After finishing high school (*Gymnasium*) at Stanislascollege in Delft in 2012, she started the Bachelor program *Molecular Science & Technology* at both the TU Delft and Leiden University. After completion of the propaedeutic year, she received a Young Talent Award in Chemistry for the best grades in the academic year 2012-2013. In the third year of the Bachelor, she performed her final Bachelor thesis in the Biocatalysis group at the TU Delft under supervision of Prof. dr. Ulf Hanefeld. After graduating *summa cum laude* for the Bachelor she continued in 2015 with the Master program *Chemical Engineering* at the TU Delft, where she chose a major in Chemical Product Engineering. In 2017 she obtained her M.Sc. degree *cum laude* and she was appointed as the Best Graduate of the Faculty of Applied Sciences. In addition, for her Master thesis in Biocatalysis about "Enzyme reactions in monolithic microreactors" under supervision of Prof. dr. Ulf Hanefeld and in collaboration with the Silesian University of Technology, in Gliwice (Poland), she received the AkzoNobel graduation prize for Chemistry and Process Technology and the KNCV Golden Master Award. In the same year she started her PhD under Dr. Rienk Eelkema and Prof. dr. Jan H. van Esch in the Advanced Soft Matter group at the TU Delft. Her research was part of the *Signal transduction in organic materials* project and dealt with both organocatalysis and out-of-equilibrium systems.

LIST OF PUBLICATIONS

- van der Helm, M. P.; Hartono, M.; Eelkema, R., Transient host-guest complexation to control catalytic activity. *manuscript in preparation.*
- van der Helm, M. P.; de Beun, T.; Eelkema, R., On the use of catalysis to bias reaction pathways in out-of-equilibrium systems. *manuscript submitted.*
- van der Helm, M. P.; Wang, C.-L.; Lewis, R.W.; Schyck, S.; Rossi, R.; Eelkema, R., Transient colloid assembly by fuel driven modulation of depletion interactions. *manuscript submitted.*
- van der Helm, M. P.; van Esch, J.H.; Eelkema, R., Chemically fuelled, transient supramolecular polymers (*Book chapter). WILEY-VCH manuscript submitte*d.
- Li, G.; Trausel, F.; van der Helm, M. P.; Klemm, B.; Brevé, T.G.; Van Rossum, S.A.P.; Hartono, M.; Gerlings, H.H.P.J.; Lovrak, M.; van Esch, J.H.; Eelkema, R., Tuneable control over organocatalytic activity through host guest chemistry. *manuscript in preparation*.
- Zhou Y; Piergentili I.; Hong, J.; van der Helm, M. P.; Macchione, M; Li, Yao; Eelkema, R.; Luo, S., Indoline catalyzed acylhydrazone/oxime condensation under neutral aqueous conditions. *Organic Letters* **2020**, 22 (15), 6035–6040.
- van der Helm, M.P.; Wang, C.-L.; Fan, B.; Macchione, M.; Mendes, E.; Eelkema, R., Organocatalytic control over a fuel-driven esterification network. *Angewandte Chemie international edition* **2020**, 59 (46), 20604-20611.
- Brevé,T.G.; Filius, M.; Araman, C.; van der Helm, M.P.; Hagedoorn, P.-L.; Joo, C.; Kasteren, S.I.; Eelkema, R., Conditional copper-catalyzed azide–alkyne cycloaddition by catalyst encapsulation. *Angewandte Chemie international edition* **2020**, 59 (24), 9340-9344.
- van der Helm, M. P.; Klemm, B.; Eelkema, R., Organocatalysis in aqueous media. *Nature Reviews Chemistry* **2019**, 3 (18), 491-508.
- van der Helm, M. P.; Bracco, P.; Busch, H.; Szymańska, K.; Jarzębski, A. B.; Hanefeld, U., Hydroxynitrile lyases covalently immobilized in continuous flow microreactors. *Catalysis Science & Technology* **2019**, 9, 1189-1200.
- Chen, B.-S.; Médici, R.; van der Helm, M. P.; van Zwet, Y.; Gjonaj, L.; van der Geest, R.; Otten, L. G.; Hanefeld, U., Rhodococcus strains as source for ene-reductase activity. *Applied Microbiology and Biotechnology* **2018**, 102 (13), 5545-5556.